

Anderson Localization and Anomalous Transport of Ultrasound in Disordered Media

by

Laura A. Cobus

A Thesis submitted to the Faculty of Graduate Studies of

The University of Manitoba

in partial fulfilment of the requirements of the degree of

Doctor of Philosophy

Department of Physics and Astronomy

University of Manitoba

Winnipeg, Canada

March 2016

Copyright © 2016 by Laura A. Cobus

Abstract

Wave transport in strongly scattering, disordered media is investigated experimentally using ultrasonic techniques. Several cases of anomalous wave transport (deviations from conventional diffusion) are studied through experiments on aluminum mesoglass samples, which were designed and created for this purpose. The anomalous wave behaviour is contrasted with conventional diffusion, observed at some frequencies via both transmission and backscattering measurements on wide, thick, slab-shaped samples. The coherent backscattering (CBS) effect is measured experimentally for strongly scattered acoustic waves in three dimensions (3D), and is compared for the first time with theory for diffusive elastic waves in 3D to give an estimate of the diffusion coefficient. At other frequencies, an Anderson localization regime is observed, and is studied in detail. The first experimental study of CBS for localized elastic waves in 3D is presented. By comparing both backscattering and transmission measurements with predictions from a ‘local’ self-consistent theory of localization, the first experimental observation of a complete Anderson mobility gap for elastic waves in 3D is reported. In this mobility gap, large contributions to backscattered intensity from recurrent scattering were observed, enabling the first experimental study of recurrent scattering on its own. The time-dependence of the recurrent scattering, $R(t)$, is shown to agree with theoretical predictions in the diffuse and localized regimes. At the mobility edge, $R(t)$ shows a surprisingly slow decay, prompting further theoretical work. Localization and criticality are also investigated via statistical measurements of ultrasound from cubic mesoglasses of different sizes. Finite-size scaling of multifractal quantities is observed in these cubic samples, and a preliminary fit with theory to determine critical parameters of the Anderson transition is demonstrated. Finally, a sample which is a candidate to exhibit superdiffusion of ultrasound is studied via a range of experimental techniques, showing subtle deviations from diffusion and opening doors for the next steps in this study.

Acknowledgements

First and foremost, I would like to thank my supervisor, Dr. John. H. Page, for his boundless support and guidance, and for exemplifying the perserverance, judgement, and honesty that I hope to achieve as a research scientist.

I am also very grateful to have had the opportunity to be a part of the close-knit research group at the Ultrasonics Laboratory. I would like to thank all past and present members who have been helpful in my PhD work. In particular, thanks to Anatoliy Strybulevych for patiently teaching me so much when I first began at the lab, and to Kurt Hildebrand for countless brainstorming sessions and moral support.

I would like to thank my international collaborators, including Dr. Arnaud Derode, Dr. Sergey Skipetrov, and Dr. Bart van Tiggelen. Special thanks goes to Dr. Alexandre Aubry for leading the way in our study of recurrent scattering, and for many cheerful and helpful discussions.

Thank you also to the members of my examining committee: Dr. Can-Ming Hu, Dr. Byron Southern, and Dr. Arkady Major.

Finally, I would like to extend my heartfelt gratitude to my family and friends who have been there for me throughout. Thank you for your love and support.

Dedication

For my dad, who taught me to catch frogs, and thus to be captivated by the natural world.

Table of Contents

Abstract	i
Acknowledgements	iii
Dedication	iv
Table of Contents	v
List of Tables	x
List of Figures	xi
List of Copyrighted Material for which Permission was Obtained	xvi
1. Introduction	1
2. Background Theory and Concepts	6
2.1. Overview	7
2.2. Multiple scattering of waves in disordered media	7
2.2.1. Theory for wave propagation through a disordered medium	10
2.2.2. Intensity propagation through the disordered medium	15
2.2.3. Scattering theory revisited: diagrammatic perturbation theory	16
2.2.4. Calculating intensity propagation: approximations	24
2.2.5. Configurational averaging	27
2.3. Symmetry in scattering systems	28
2.3.1. The consequences of spatial reciprocity	29
2.3.2. The propagation matrix in backscattering	31
2.4. Introduction to coherent backscattering	32

2.4.1. Calculating the CBS effect	34
2.5. Introduction to Anderson localization.....	37
2.5.1. The scaling theory of localization.....	38
2.5.2. Renormalized diffusion and the self-consistent theory of localization.....	41
2.5.3. Experimental concept: discrimination between diffuse and localized regimes...	43
Appendix 2A : Enhancement factor calculation details	45
3. Experimental Techniques and Data Processing	47
3.1. Creation of slab mesoglasses L1 and L2	48
3.1.1. Sample brazing	48
3.1.2. Bead size measurement (L1 and L2).....	50
3.2. Experiments (slab samples).....	52
3.2.2. Transmission Experiments	55
3.2.3. Reflection Experiments.....	64
3.2.4. Frequency filtering.....	80
3.2.5. Ballistic Measurements	81
3.2.6. The transmission/reflection coefficient.....	95
Appendix 3A : Furnace heating profiles	97
4. Strong Diffusive Scattering	99
4.1. Introduction	100
4.2. Coherent backscattering in the diffuse regime	101
4.2.1. Theory for diffuse coherent backscattering in 3D	103
4.2.2. Corrections for experimental limitations.....	111
4.2.3. Experiment and data processing	114

4.2.4. Fitting procedure.....	114
4.3. Transmission.....	116
4.3.1. The time-of-flight profile	117
4.4. Results for backscattering and transmission at 1.65 MHz	123
4.5. Conclusion.....	126
Appendix 4A : Diffuse far-field simplification	127
5. The Anderson Mobility Gap	130
5.1. Introduction	131
5.1.1. The experimental search for localization of classical waves in 3D	132
5.2. The local self-consistent theory of localization	135
5.2.1. Outline of local SC theory calculations	136
5.3. Comparison of experimental data with self-consistent theory	139
5.3.1. SC theory for a very thick sample	140
5.3.2. Fortran and matlab calculations.....	140
5.3.3. Self-consistent theory fitting procedure.....	143
5.4. The Anderson mobility gap probed by coherent backscattering	148
5.4.1. Experimental backscattering measurements.....	149
5.4.2. Fitting dynamic CBS profiles with SC theory.....	151
5.5. Identification of Anderson mobility edges	155
5.5.1. Parabola-fitting method.....	156
5.6. Results for the Anderson mobility gap.....	158
5.6.1. The Boltzmann diffusion coefficient.....	159
5.6.2. Observations on thick samples	163

5.6.3. Critical exponent estimation.....	163
5.7. Conclusion.....	165
Appendix 5A : Anderson mobility gap probed by dynamic coherent backscattering	166
6. Recurrent Scattering.....	176
6.1. Introduction to recurrent scattering.....	177
6.2. Surface recurrent scattering effects on the coherent backscattering profile.....	180
6.2.1. Recurrent scattering and the memory effect.....	181
6.3. Recurrent scattering in the Anderson mobility gap.....	186
6.4. Statistics of the propagation matrix	190
6.5. Conclusion.....	193
Appendix 6A : Recurrent scattering and memory effect at the Anderson localization transition.....	194
7. Statistics and Multifractality Near the Mobility Edge	207
7.1. Introduction	208
7.2. Introduction to multifractality.....	208
7.2.1. Multifractality and finite-size scaling	211
7.3. Speckle statistics in a slab mesoglass	216
7.3.1. Field mapping	216
7.3.2. Variance from speckle maps.....	216
7.3.3. Multifractality	218
7.4. Experiments on cubic mesoglasses.....	222
7.4.1. Construction of brazed cubic samples.....	222
7.4.2. Measurements of vibrations on the sample surface	223

7.5. Speckle statistics from cubic mesoglasses	230
7.5.1. Variance	230
7.5.2. Noise discrimination	231
7.5.3. Multifractality and finite-size scaling	234
7.5.4. Critical exponent estimation.....	236
7.6. Conclusions and future directions.....	241
8. A Lévy Phononic Glass	242
8.1. Introduction	243
8.2. Slab sample L0.....	245
8.3. Transmission through the Lévy phononic glass.....	246
8.4. Speckle statistics of the Lévy phononic glass	254
8.5. Conclusions and future directions.....	258
9. Conclusions and future directions.....	259
References	265

List of Tables

Table 3.1: Details on setups for reflection experiments.	67
Table 3.2: Details on ultrasonic arrays used in reflection experiments.....	67
Table 5.1: Input parameters for SC Fortran calculations for sample L1.	142
Table 7.1: Starting values and results for free fit parameters from FSS model.....	240

List of Figures

Figure 2.1: Ultrasonic waves observed after an initial short pulse.	8
Figure 2.2: Two scattering paths: \vec{r}_1 to \vec{r}_3 and \vec{r}_3 to \vec{r}_4	15
Figure 2.3: Physical interpretation of the third diagram of $G(\vec{k}, \vec{k})$	17
Figure 2.4: Summation of ladder terms.....	23
Figure 2.5: The concepts of spatial reciprocity and time-invariance are linked.	29
Figure 2.6: Two interfering rays A and B.	33
Figure 2.7: Paths of a pair of advanced and retarded Green's functions.....	35
Figure 2.8: Summation of most-crossed diagrams.....	36
Figure 2.9: The behaviour of the scaling function β as a function of $\ln \gamma$	40
Figure 3.1: The stainless steel mold used to make samples L1 and L2	50
Figure 3.2: Distribution of diameters for aluminum beads comprising sample L1.	51
Figure 3.3: Sample L1.....	52
Figure 3.4: Raw transmitted field through sample L2 for $\rho = 0$ mm.....	53
Figure 3.5: Schematic of a Panametrics focussing transducer.....	55
Figure 3.6: Signal path through electronics and experimental setup.	57
Figure 3.7: Simple sketch of the vacuum, ballast and sample setup.....	59
Figure 3.8: Sample L2 in preparation for a water tank experiment.	61
Figure 3.9: The emission transducer (left) is attached to the cone by acrylic rods.....	63
Figure 3.10: The sample and sample holder are flush against the baffle.	63

Figure 3.11: Experimental setup for reflection measurements with an ultrasonic array.....	65
Figure 3.12: First step of acquisition sequence for an ultrasonic array of N elements.....	68
Figure 3.13: Backscattered field signals from sample L1	72
Figure 3.14: Backscattered field signals from a flat aluminum sheet.....	73
Figure 3.15: Reflected intensity from a flat aluminum sheet	76
Figure 3.16: Backscattered intensity from sample L2.....	76
Figure 3.17: Average transmitted wavefield through sample L1	86
Figure 3.18: Coherence criterion from a transducer centered at 500 kHz	87
Figure 3.19: Coherence criterion (narrowband frequency filtering, 200 - 600 kHz).....	88
Figure 3.20: Coherence criterion (broadband frequency filtering around 1 MHz).....	89
Figure 3.21: Coherence criterion (narrowband frequency filtering, 750 kHz – 1 MHz).	90
Figure 3.22: Average transmitted wavefield through sample L1	90
Figure 3.23: Estimates of velocity through sample L1 from ballistic measurements.....	93
Figure 3.24: Estimates of transport parameters through sample L1	94
Figure 3.25: Amplitude transmission coefficient of ultrasound through samples L1 and L2 ...	96
Figure 3A.1: Heating profile used to braze sample L1	97
Figure 4.1: Dynamic albedo measured with acoustic pulses.....	102
Figure 4.2 : Schematic for backscattering experimental geometry.....	104
Figure 4.3: Experimental CBS profiles (symbols) with fits from diffusion theory (lines)	115

Figure 4.4: An example of the method used to determine the diffusion coefficient.....	116
Figure 4.5: Diagram of the transverse confinement technique.....	118
Figure 4.6: Sketch of cross-shaped acquisition sequence	119
Figure 4.7: Transverse width measured from sample L1, at 250 kHz	121
Figure 4.8: TOF profiles for sample L1 (open circles) and fits with diffusion theory.....	122
Figure 4.9: Transverse width measured from sample L1, at 1.65 MHz.....	124
Figure 4.10: TOF profiles for sample L1 (open circles) and fits with diffusion theory.....	125
Figure 5.1: Transverse confinement results.....	144
Figure 5.2: Absorption time τ_A of ultrasound in sample L1 as a function of frequency.....	146
Figure 5.3: $w_\rho^2(t)$ profiles for sample L2	147
Figure 5.4: Experimental dynamic CBS profiles.....	150
Figure 5.5: Dynamic CBS profiles from samples L1 (top) and L2 (bottom)	152
Figure 5.6: The reciprocal of the square of the half width at half maximum of dynamic CBS profiles	154
Figure 5.7: χ_{red}^2 vs L/ξ for three different frequencies.....	157
Figure 5.8: Ratio of sample thickness L to the localization (correlation) length ξ	158
Figure 5.9: Localization (correlation) length ξ as a function of frequency.....	159
Figure 5.10: The diffusion time τ_D (a) and Boltzmann diffusion coefficient D_B (b)	160
Figure 5.11: On-axis time-of-flight profiles for samples L1 (a) and L2 (b).....	161

Figure 5.12: Energy velocity v_E estimated from the Boltzmann diffusion coefficient D_B ...	162
Figure 5.13: The localization (correlation) length ξ measured in transmission from L1.....	164
Figure 5.14: The localization (correlation) length ξ measured in backscattering.....	164
Figure 6.1: Backscattered intensity plotted against scattering angle.	179
Figure 6.2: Backscattered intensity profiles at time $t = 200 \mu s$ from sample L1.	181
Figure 6.3: Propagation matrices K for time $t = 15 \mu s$ (a) and $t = 200 \mu s$ (b).	182
Figure 6.4: Propagation matrices from L1 after the RS-MSF process.....	186
Figure 6.5: Time dependence of the RS to total intensity ratio $I_R(t)/I(t)$	187
Figure 6.6: Time dependence of the RS intensity $I_R(t)$	188
Figure 6.7: Time dependence of the RS intensity $I_R(t)$	190
Figure 6.8: ‘Hotspots’	192
Figure 7.1: For a fixed system size, the spatial structure of the transmitted speckle pattern can be probed by dividing up the speckle map into boxes of size b	209
Figure 7.2: The measured anomalous exponents Δ_q	211
Figure 7.3: Numerical simulations of the probability density	214
Figure 7.4: Variance of normalized transmitted intensity speckle maps for sample L1	217
Figure 7.5: Anomalous fractal exponents Δ_q	219
Figure 7.6: Anomalous fractal exponents Δ_2 as a function of frequency.	220
Figure 7.7: Anomalous exponent Δ_q calculated for matrices of pseudo-random values.	221

Figure 7.8: Cubic aluminum-sintered samples	223
Figure 7.9: The experimental setup for a representative 5 cm cube.	224
Figure 7.10: Average transmitted intensity through a 5 cm cube.....	226
Figure 7.11: Transmitted amplitude through a 5 cm cube measured by a laser interferometer.....	227
Figure 7.12: Average variance as a function of frequency.	231
Figure 7.13: Intensity maps of one 5 cm cube at 1.1538 MHz.....	232
Figure 7.14: Intensity maps one 5cm cube at 1.1538 MHz after intensity thresholding.	233
Figure 7.15: Probability Density Functions.....	235
Figure 7.16: Anomalous exponents Δ_q are very low even for the diffuse regime.....	236
Figure 7.17: Experimentally-measured mean PDF values, α	240
Figure 8.1: Sample L0, shown in its acrylic holder for ultrasonic experiments.....	246
Figure 8.2: Amplitude transmission coefficient for sample L0	247
Figure 8.3: Average time-of-flight profiles through sample L0.....	248
Figure 8.4: Average transmitted intensity through sample L0 at 1 MHz.	250
Figure 8.5: $I(\rho)$ for three different times	251
Figure 8.6: Transverse width divided by sample thickness squared for sample L0.....	252
Figure 8.7: Experimental lifetime of transmitted intensity through sample L0.....	253
Figure 8.8: Speckle maps of transmitted intensity through sample L0 at 1 MHz.	255
Figure 8.9: Variance of transmitted intensity speckle maps through sample L0.	257

List of Copyrighted Material for which Permission was Obtained

Figure 2.3: Physical interpretation of the third diagram of $G(\vec{k}, \vec{k})$	17
Figure 3.5: Schematic of a Panametrics focussing transducer.....	55
Figure 4.1: Dynamic albedo measured with acoustic pulses.....	102
Figure 4.5: Diagram of the transverse confinement technique.....	118
Figure 6.1: Backscattered intensity plotted against scattering angle.	179
Figure 7.3: Numerical simulations of the probability density	214

1. Introduction

Wave propagation is central to many areas of physics, and has been studied in depth for centuries. Special attention has more recently been focussed on waves in complex media, where waves leaving the medium look very different to those that entered. Having been enthusiastically researched for several decades, this subject remains at the frontier of science. This is partly due to the difficulty of characterizing waves in a disordered medium, theoretically or experimentally, but also to the great promise of such work, whether for imaging, communication, controlling naturally-occurring catastrophes, or other applications yet to be devised. The variety and complexity of the remaining problems make it an exciting time to work in this field.

One of the great interests in studying waves in complex media is that one can observe anomalous wave behaviour, i.e. waves that behave differently to what is expected in the majority of situations. Typically, waves propagate through a medium of random scattering objects via *diffusive transport*. This occurs for a system where size (L) is larger than a few *mean free paths*, the average distance travelled by a wave between scattering events (ℓ). For a dense enough system where wavelength λ is comparable to ℓ , the propagating waves interact with many different scatterers, becoming *multiply scattered*. For a large enough L , the waves become randomized by the random positions of the scatterers, eventually losing their coherence with the original input wave. Then, the wave propagation can be very accurately modeled by the *diffusion approximation*. This theory describes the energy transport of multiply scattered waves in probabilistic terms, instead of keeping track of each possible individual wave path through the sample (an impossible task). I refer to transport which is well-described by the diffusion approximation as *conventional diffusion*. Other types of wave phenomena, where this theory fails or breaks down altogether in a multiple scattering medium, are referred to as anomalous.

In the diffusion approximation, interference effects between individual waves are

unimportant. This means that if one averages the phase of the diffusing waves over different positions of the source and/or detector (*configurational averaging*), the result should approach zero. However, certain measurable quantities can survive this average despite the randomizing effect of the scattering medium. These quantities are not included in the diffusion approximation, but can be explained with a more comprehensive theory of wave scattering. They thus provide valuable insight into the details of wave scattering inside the medium, at a deeper level than is possible using the diffusion approximation. Perhaps the most extreme example of anomalous wave behaviour is *Anderson localization*, where waves are ‘trapped’ inside the medium due to the disorder of the scatterers, and the diffusion approximation breaks down completely. Such major deviations from diffusion are usually observed in the *strong scattering regime*. This is a regime where the scatterer size d is comparable to λ , so that ℓ is small and waves are very sensitive to the presence and arrangement of the scatterers. Experimentally, this is a difficult regime to access, especially for three-dimensional (3D) media, so the observation and characterization of phenomena such as localization are still uncommon in 3D. The experimental study of anomalous wave transport of elastic waves in 3D, and Anderson localization in particular, is the focus of my work in this thesis.

Since the rare phenomena which I would like to study are caused by interference effects, acoustic waves are a natural choice for experiments, as the *phase* of the waves can be measured as well as amplitude; in contrast, the rapidity of the oscillations of light waves make phase measurements extremely difficult. The impedance mismatch between scattering particles and the surrounding medium can also be made larger for sound than it can for light. This could potentially enhance strong scattering effects, facilitating the observation of exotic phenomena such as localization. The Ultrasonics Laboratory has been a world leader in studying

conventional diffusion with ultrasound (Page et al. 1995; Page et al. 1996; Schriemer et al. 1997), and more recently reported the first unambiguous observation of 3D Anderson localization (Hu et al. 2008). The goal of my research for this thesis is to, building on this previous work, investigate new avenues of exploration for exotic wave phenomena. I have engineered and created all of the samples presented in this thesis to show specific types of anomalous wave behaviour. All of the experiments presented in this thesis were also carried out by me.

Proof that a certain wave phenomenon is present is not a trivial matter. Sometimes only subtle deviations are observed from typical behaviour, or else multiple processes may be present which can confuse the interpretation of experimental results. There also tends to be a significant grey area between ‘conventional’ wave behaviour and the rare phenomena that I am searching for. The most reliable approach is to measure several different aspects of wave propagation, and to carefully compare the experimental results to appropriate theoretical predictions. This is the approach that I take in this thesis. Chapter 2 outlines the background concepts and theory necessary to plan and interpret my experiments. Chapter 3 explains in detail the experimental techniques which I used to study ultrasound in complex media in this thesis. Each of the subsequent chapters presents a study of a different wave phenomenon, all of which are interrelated by the concepts in Chapter 2.

Most of the research of this thesis is for ultrasound in the strong scattering regime, where diffuse transport can be observed, but where there is also a good likelihood of anomalous wave behaviour. My experimental observations begin with Chapter 4, where both conventional diffusion and the beginnings of deviations from diffusion are studied. Notably, this work includes reflection data which are compared to as-yet unpublished theory for reflected acoustic waves from a 3D medium. The results suggest that subdiffusion, the slowing of wave spreading due to

disorder, is prevalent in my system at some frequencies. Since, in this thesis, subdiffusion can be seen to be a precursor to localization, this work is a natural lead-in to my research on Anderson localization, which begins in Chapter 5. There I present the first ever experimental measurement of an Anderson *mobility gap*, which also constitutes the first ever experimental observation of localization of elastic waves in 3D in reflection. Chapter 5 is supplemented by a manuscript (included as an Appendix) that I have submitted for peer-review on this work. Chapter 6 presents the first experimental study of *recurrent scattering*, a process that is fundamental to Anderson localization but which has not, until this work, been examined on its own. A submitted publication is also appended to this thesis.

Chapters 7 and 8 focus more on the use of statistical measurements to measure deviations from diffusion. Chapter 7 presents experimental results aimed at studying critical behaviour (the transition between diffusion and localization) in different sizes of cubic samples. Localization can be observed and quantified simply by changing the sample size, but this is very difficult experimentally for 3D samples. These measurements are the first of their kind for 3D samples. Finally, Chapter 8 presents a study of a sample which could potentially show *superdiffusion* of ultrasound. Although it is always possible to make some guesses based on theory and experience, how ultrasound behaves inside this unique sample was mostly unknown, a priori. This chapter presents the combination of several different experimental techniques, introduced in the previous chapters, to probe this wave behaviour.

The signatures of anomalous wave behaviour that are studied in this thesis can seem very different from each other. However, they are different manifestations of similar wave scattering processes. It is the goal of this thesis to, via experimental study, advance the current knowledge on a few of these topics, and more broadly, to illustrate some parallels between them.

2. Background Theory and Concepts

2.1. Overview

The theory of wave scattering has been reviewed in detail in several past works (e.g. Sheng 2006; Akkermans and Montambaux 2007; Ishimaru 1977). The goal of this chapter is to provide an intuitive understanding of the scattering processes to be experimentally investigated in this thesis, along with a description of the theory with which experimental results are compared. Each section presents a concept using (1) a heuristic introduction, (2) a treatment of the same concept with diagrammatic scattering theory, and (3) a discussion of experimental aspects in the context of this thesis. The scattering theory allows for an understanding of how different scattering processes contribute to what is observed experimentally; effects which may appear quite different from each other can be seen to arise from very similar principles.

2.2. Multiple scattering of waves in disordered media

The description of energy transport of waves through a multiple scattering medium is often treated as a random walk process. Each possible trajectory through the sample is imagined as a random path from scatterer to scatterer, with equal probability of scattering into all directions. The transport through the system is described by the *probability* of a walker travelling a distance \vec{r} through the sample. This amounts to performing a statistical average, also called an *ensemble average* or *configurational average*, over all possible paths. Despite neglecting interferences between different possible paths through the sample, this classical picture can describe wave transport through inhomogeneous media remarkably well. However, there are some cases which defy this classical picture. This can be illustrated by a simple example of wave propagation through an inhomogeneous medium:

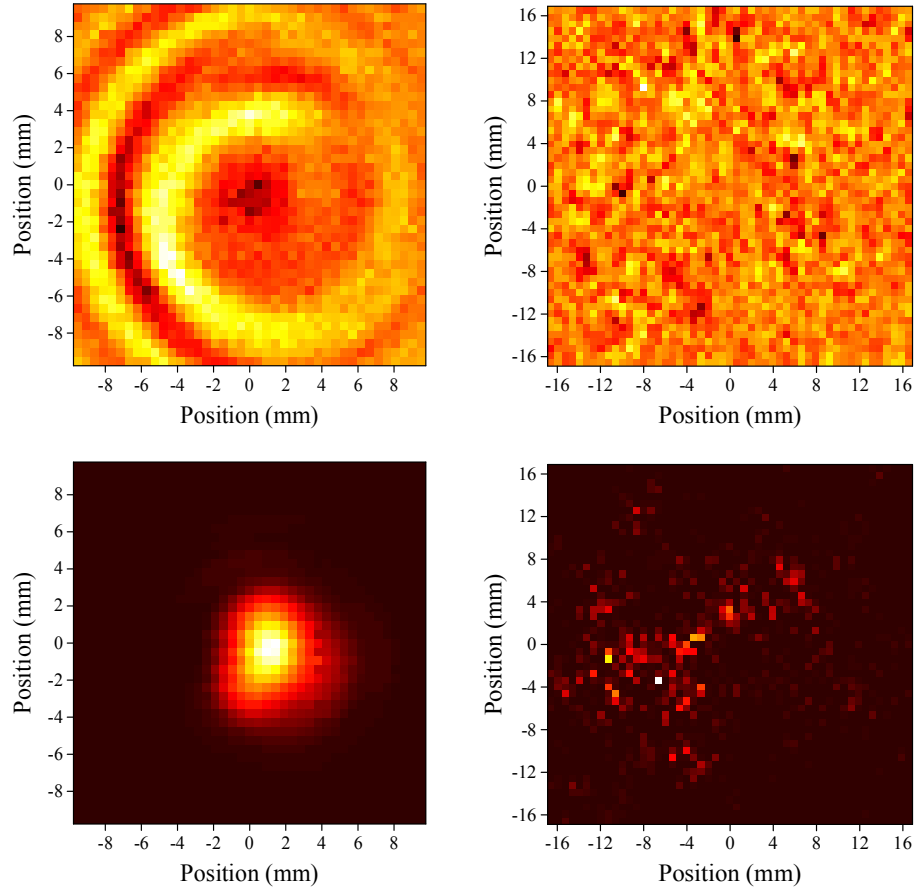


Figure 2.1: Ultrasonic waves observed after an initial short pulse. The left plots show ultrasound transmitted through water. The right plots show ultrasound transmitted through a multiple scattering medium (sample L1, introduced in this thesis in Section 3.1.1.2). The top plots show the transmitted field at a time shortly after the initial pulse was emitted; the diffraction pattern on the left is a sharp contrast to the field speckle pattern on the right, where waves appear to have lost all coherence with the source pulse. (Note that the field on the top left is spiral-shaped, instead of having concentric circles, due to a slight misalignment of source and detector.) The bottom plots show the transmitted amplitude in the frequency domain (at 1 MHz); the amplitude speckle pattern (right) retains no spatial coherence with the initial pulse (left).

Waves travelling through a homogeneous material retain their coherence, resulting in simple diffraction patterns such as that shown in Figure 2.1. In this case, a wave has scattered at most once from something in the medium – for these *single scattering* processes, the scattered wave retains its coherence with the source. In contrast, coherence is not necessarily maintained for a wave travelling through a disordered material, for example light in a medium with a

randomly-varying dielectric, or sound in a medium with randomly-ordered scatterers. Then, the resulting transmitted or reflected signals viewed in the far field forms a *speckle pattern* with randomly-varying bright and dark spots of intensity as shown in Figure 2.1. This is the result of *multiple scattering*, where the wave has scattered more than once inside the sample.

Speckle can seem completely random, but actually contains detailed information about the scattering medium. The study of wave propagation in random media consists of extracting information from quantities such as speckle. This is difficult experimentally because the disorder of the scatterers randomized the path lengths of the waves, which means that phase and amplitude are also randomized. If an average is performed over a sufficient number of *configurations of disorder*, i.e. different distributions of scatterers in the medium, then the speckle pattern disappears. Such an effect has indeed been observed turbid media such as milk, where the positions of scatterers change with time, so a time-averaged speckle will disappear if one waits long enough. However, there are some cases in which coherence remains even after this configurational averaging process. These phenomena, such as *coherent backscattering* and *recurrent scattering*, provide experimental proof that classical transport theory cannot fully describe wave propagation in random media. They also provide excellent opportunities to study waves in disordered media, as will be shown in this thesis.

Theory describing waves in random media can be divided up into two types: *analytical theory* and *transport theory* (Ishimaru 1977). Analytical theory begins with basic differential equations such as the wave equation, and gives as a result differential or integral equations for statistical quantities. It is thus possible to take into account all multiple scattering and interference effects, but impossible to yield an exact result, making comparison with experiment difficult. Examples of analytical theories include the Dyson and Bethe-Salpeter equations.

Transport theory describes the transport of energy through the scattering medium more heuristically, and is generally less mathematically rigorous than an analytical theory. One of the major transport theories, called radiative transport theory, is based on a differential equation called the *equation of transport*, which is analogous to the Boltzmann's equation used in the kinetic theory of gases. Transport theories generally ignore the phase and fluctuations of wave fields in random media, which may become important when the wave is scattered many times.

2.2.1. Theory for wave propagation through a disordered medium¹

Presented is a 'microscopic' treatment of wave propagation in a homogeneous medium, which is then extended to include the presence of scatterers.

Scalar waves of frequency ω propagating through a homogeneous medium obey the Helmholtz equation:

$$\nabla^2 \phi + \kappa_0^2 \phi = 0, \quad (2.1)$$

where $\kappa_0^2 = \omega^2/v_0^2$, and v_0 is the wave velocity. If at $t = 0$, the system is excited by a pulse localized at $\vec{r} = \vec{r}'$, then this wave equation becomes

$$(\nabla^2 + \kappa_0^2) G_0(\omega, \vec{r}, \vec{r}') = \delta(\vec{r} - \vec{r}'). \quad (2.2)$$

where \vec{r}' denotes the source position. The Green's function, $G_0(\omega, \vec{r}, \vec{r}')$, describes the response of the medium at \vec{r} , in frequency and spatial domains, of a delta-function source excitation. For a uniform medium, the system response does not depend on the source position, only on the distance between source and detector, so the Green's function is $G_0(\omega, \vec{r}, \vec{r}') = G_0(\omega, \vec{r} - \vec{r}')$. In real space in three dimensions, there are two solutions: the retarded (G^+) and advanced (G^-) Green's functions, which represent outgoing and incoming spherical waves:

¹ (Sheng 2006; Tourin 1999)

$$G_0^\pm(\omega, \bar{R}) = -\frac{\exp(\pm i\kappa_0 R)}{4\pi R}, \quad (2.3)$$

where $R = |\vec{r} - \vec{r}'|$ is the distance between source and detector. Note that $G^- = (G^+)^*$. In the frequency domain, the Green's function is

$$G_0(\omega, \bar{k}) = \frac{1}{\kappa_0^2(\omega) - k^2}. \quad (2.4)$$

To study the effects of scatterers, we introduce a term $\sigma(\vec{r})$ denoting deviations from homogeneity, like an effective potential in the analogous quantum mechanics situation. Equation (2.2) becomes

$$(\nabla^2 + \kappa_0^2)G(\omega, \vec{r}, \vec{r}') = \delta(\vec{r} - \vec{r}') + \sigma(\vec{r})G(\omega, \vec{r}, \vec{r}'). \quad (2.5)$$

The solution to Equation (2.5) is the recursive relation

$$G(\omega, \vec{r}, \vec{r}') = G_0(\omega, \vec{r} - \vec{r}') + \int G_0(\omega, \vec{r} - \vec{r}_1) V(\vec{r}_1) G(\omega, \vec{r}_1, \vec{r}') d\vec{r}_1 \quad (2.6)$$

where the impurity potential operator $V(\vec{r})$ has elements $V_{r_1, r_2} = (\delta r)^d \sigma(\vec{r}_1) \delta_{r_1, r_2}$. In wave vector space,

$$G(\bar{k}, \bar{k}') = G_0(\bar{k}, \bar{k}') + \int G_0(\bar{k}) V(\bar{k} - \bar{q}) G(\bar{q}, \bar{k}') d\bar{q}. \quad (2.7)$$

The Green's function, being the solution to the wave equation (Equation (2.2) or (2.5)), completely describes the propagation of an acoustic wave in the medium. However, just like in the classical picture which averages over many random walks through the sample, the knowledge of a single Green's function is not sufficient to describe overall wave transport. Only by averaging over all possible configurations of disorder (arrangements of scatterers) can we determine useful information about wave propagation. Importantly, though, the Green's function explicitly includes phase, while the random walker picture does not.

The next goal is the average Green's function $\langle G \rangle$, which describes the average field inside

the medium. Here we outline the calculation of the average of Equation (2.7), and see what quantities we can measure from it.

It is convenient to continue in matrix notation. Note that we really only desire to calculate $G(\vec{k}, \vec{k})$, since it is the only part that will resist the process of configurational averaging. Equation (2.7) may be written as

$$\mathbf{G} = \mathbf{G}_0 + \mathbf{G}_0 \mathbf{V} \mathbf{G}. \quad (2.8)$$

Substituting \mathbf{G} back into Equation (2.8) gives

$$\mathbf{G} = \mathbf{G}_0 + \mathbf{G}_0 \mathbf{T} \mathbf{G}_0. \quad (2.9)$$

Whereas \mathbf{V} represents just the first order of multiple scattering (single scattering), the scattering matrix \mathbf{T} is a sum of *all* orders of multiple scattering, and is defined as the matrix power series summation

$$\mathbf{T} = \mathbf{V} + \mathbf{V} \mathbf{G}_0 \mathbf{V} + \mathbf{V} \mathbf{G}_0 \mathbf{V} \mathbf{G}_0 \mathbf{V} + \dots \quad (2.10)$$

When the medium is randomly varying in space and/or time, the waves in the medium also vary randomly in phase and amplitude, and must therefore be described in terms of statistical quantities. Thus, as discussed above, the goal is to calculate the configurationally averaged Green's function

$$\bar{\mathbf{G}} = \mathbf{G}_0 + \mathbf{G}_0 \bar{\mathbf{T}} \mathbf{G}_0, \quad (2.11)$$

where

$$\bar{\mathbf{T}} = \left\langle \mathbf{V} (1 - \mathbf{G}_0 \mathbf{V})^{-1} \right\rangle \quad (2.12)$$

We now define an operator Σ as

$$\bar{\mathbf{G}}^{-1} = \mathbf{G}_0^{-1} - \Sigma \quad (2.13)$$

and

$$\Sigma = \bar{\mathbf{T}}(\mathbf{I} - \bar{\mathbf{T}}\mathbf{G}_0)^{-1}. \quad (2.14)$$

Equation (2.13) is known as the Dyson equation, and Σ as the self-energy operator. It follows that

$$\bar{\mathbf{G}}(\omega, \vec{k}) = \frac{1}{\kappa_0^2(\omega) - k^2 - \Sigma(\omega, \vec{k})}. \quad (2.15)$$

All non-trivial information about $\bar{\mathbf{G}}$ is contained in the self-energy $\Sigma(\omega, \vec{k})$.

2.2.1.1.1. Coherent propagation (the Coherent Potential Approximation)

When wavelength is large compared to scatterer size (Rayleigh scattering), mean field approximations such as the Coherent Potential Approximation (CPA) are appropriate, but they only take into account particle-particle correlations in a limited way. The idea is that the effect of the scatterers in the sample is simply to renormalize the wave propagation, and thus parameters describing the medium are renormalized. The description becomes that of an effective, homogenized, medium. The renormalization occurs when considering the Green's function which includes the self-energy, as in Equation (2.15). If the self-energy is \vec{k} -independent, then it renormalizes the Green's function, so that $\kappa_e^2(\omega) = \kappa_0^2(\omega) - \Sigma(\omega)$, and the new, effective-medium (e) configurationally-averaged Green's function is

$$\langle \mathbf{G}_e \rangle_c(\omega, \vec{k}) = \frac{1}{\kappa_e^2(\omega) - k^2}. \quad (2.16)$$

Correspondingly, for a 3D continuous effective medium, the Green's function in real space is

$$\langle G_e \rangle_c = -\frac{\exp(i\kappa_e R)}{4\pi R}. \quad (2.17)$$

This homogenization of the medium results in the replacement of subscript 0 in $\bar{\mathbf{G}}_0$ with e .

Mean-field theories such as the CPA generally focus on calculating the real part of the self-energy (i.e. the real part of κ_e^*), which gives information about effective properties of a homogenized medium such as the effective dielectric constant. For scattering theory, it is more interesting to calculate the imaginary part of the self-energy, as we will see below:

It can be shown (Sheng 2006) that the local density of states at \vec{r} is related to the Green's function:

$$\text{DOS}(\omega, \vec{r}) = \frac{2\omega}{v_0^2} \left(\frac{1}{\pi} \text{Im} G(\omega, \vec{r} = \vec{r}') \right) \quad (2.18)$$

where v_0 is the phase velocity in the uniform medium. For the system to be physical, we require $\text{Im}(\bar{G}^+) < 0$. Now, if κ_e^* has a positive imaginary part, then \bar{G}^+ decays exponentially, as shown by Equation (2.17). What physical mechanism is responsible for this spatial decay of \bar{G}^+ ? The answer can be inferred from the optical theorem:

$$O = -\frac{1}{\kappa_0} \text{Im} \langle \kappa_0 | t^+ | \kappa_0 \rangle \quad (2.19)$$

where the total scattering cross-section O is related to the imaginary part of t^+ , which is the average scattering matrix (Equation (2.12)) for a single scatterer. The scattering matrix is in turn related to $\text{Im}(\kappa_e^*)$ via Equation (2.14). Thus, the loss of a unique propagation direction (the decay of \bar{G}^+), is a result of *scattering* loss. This (intensity) decay length is usually denoted by $1/\text{Im}(\kappa_e^*) = 2\ell_s$, and ℓ_s as the scattering mean free path. Note that since Equation (2.17) is not a transport equation, ℓ_s is not a *transport* mean free path, but is an extinction length of the averaged disordered medium.

The exponential decay of this $\langle G \rangle$ due to scattering from the forward direction implies a loss of coherence past this length scale. This makes sense, since averaging together many completely uncorrelated fields would yield a result of zero. Thus, we can see that the average

field propagating in the medium, $\langle G \rangle$, describes the coherent behaviour of wave propagation. Several quantities can be measured from $\langle G \rangle$, and are described in more detail in Section 3.2.5.

2.2.2. Intensity propagation through the disordered medium²

The intensity of a wave field ψ is proportional to the product of the fields: $I \propto \psi\psi^*$. Thus, just as $\langle G \rangle$ gives us information about the average field in the medium, $\langle GG^* \rangle$ gives us information about the average intensity transport. Define the *intensity Green's function* as the tensor product

$$\mathbf{G}_2(\vec{r}_1, \vec{r}_2, \vec{r}_3, \vec{r}_4) \equiv \mathbf{G}(\vec{r}_1, \vec{r}_3) \otimes \mathbf{G}^*(\vec{r}_2, \vec{r}_4) \quad , \quad (2.20)$$

where incident and outgoing directions are \vec{r}_1 (\vec{r}_2) and \vec{r}_3 (\vec{r}_4), respectively, as sketched in Figure 2.2.

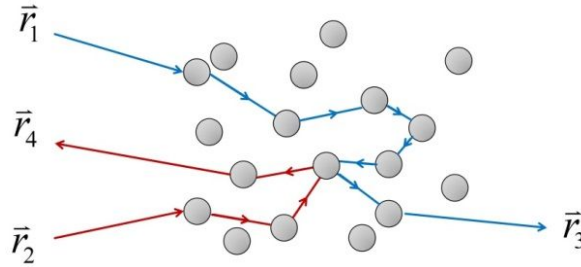


Figure 2.2: Two scattering paths: \vec{r}_1 to \vec{r}_3 and \vec{r}_2 to \vec{r}_4 .

The intensity of a pulse in a random medium, averaged over all configurations of disorder, is

$$I = \langle G_2 \rangle \quad (2.21)$$

(Sheng 2006). The Green's functions in the random medium are related to those defined for homogeneous media by

² (van der Mark, van Albada, and Lagendijk 1988; Tourin 1999; Sheng 2006).

$$\begin{aligned}\mathbf{G} &= \mathbf{G}_0 + \mathbf{G}_0 \mathbf{T} \mathbf{G}_0 \\ \mathbf{G}^* &= \mathbf{G}_0^* + \mathbf{G}_0^* \mathbf{T} \mathbf{G}_0^*\end{aligned}\quad , \quad (2.22)$$

where the subscript for \mathbf{G}_0 denotes the Green's function defined relative to the homogeneous medium in which the scatterers are embedded. After configurational averaging,

$$\bar{\mathbf{G}}_2 = \mathbf{G}_0 \otimes \mathbf{G}_0^* + (\mathbf{G}_0 \otimes \mathbf{G}_0) \mathbf{\Gamma} (\mathbf{G}_0^* \otimes \mathbf{G}_0^*) \quad (2.23)$$

where the *vertex function* $\mathbf{\Gamma} = \langle \mathbf{T} \otimes \mathbf{T}^* \rangle$ represents all multiple scattering processes. Defining a new vertex function \mathbf{U} as

$$\mathbf{\Gamma} = \mathbf{U} + \mathbf{U} (\mathbf{G}_0 \otimes \mathbf{G}_0^*) \mathbf{\Gamma}, \quad (2.24)$$

we have in analogy with the self-energy,

$$\bar{\mathbf{G}}_2 = \bar{\mathbf{G}} \bar{\mathbf{G}}^* + \bar{\mathbf{G}} \bar{\mathbf{G}}^* \mathbf{U} \bar{\mathbf{G}}_2 \quad (2.25)$$

(tensor multiplication notation is from now on implicitly assumed). Equation (2.25), with the definitions of $\mathbf{\Gamma}$ and \mathbf{U} , is the *Bethe-Salpeter (BS) equation* – the intensity Green's function analog of the Dyson Equation. The physical meaning is significant: \mathbf{U} incorporates all wave scattering processes into $\bar{\mathbf{G}}_2$. The Bethe-Salpeter equation is the microscopic equivalent of the radiative transport equation used in a transport theory approach, which is discussed in Section 2.2.4.1.3.

2.2.3. Scattering theory revisited: diagrammatic perturbation theory

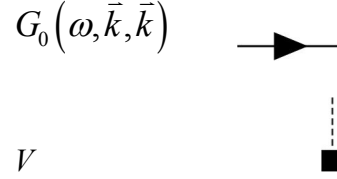
2.2.3.1. Diagrammatic derivation of the Dyson equation and self-energy³

A derivation using diagrammatic notation is presented for the Dyson equation and the self-energy. While this is a longer method of obtaining Equation (2.13), the physical meaning of the

³ Much of the theory in this section is from reference (Tourin 1999).

results is more easily understood. The method also forms the basis for calculations in following sections.

We will adopt the following Feynman diagram conventions:



A horizontal line with an arrow represents the homogeneous Green's function, and a dotted line ending in a solid square represents one scattering. Then $G(\vec{k}, \vec{k})$, as expressed in Equations (2.9) and (2.10), is

$$G(\omega, \vec{k}, \vec{k}) = \text{---}\!\!\!\rightarrow + \text{---}\!\!\!\rightarrow \text{---}\!\!\!\rightarrow + \text{---}\!\!\!\rightarrow \text{---}\!\!\!\rightarrow \text{---}\!\!\!\rightarrow + \dots$$

$V(\vec{q}=0) \quad V(\vec{q}) \quad V(-\vec{q})$

Here, \vec{q} represents a scattering vector. For example, the interpretation of the third diagram is as follows: a wave with direction \vec{k} is scattered by potential $V(\vec{q})$ (Figure 2.3), changing its direction to $\vec{k} + \vec{q}$. The wave then encounters potential $V(-\vec{q})$ and leaves in direction $\vec{k} + \vec{q} - \vec{q} = \vec{k}$.

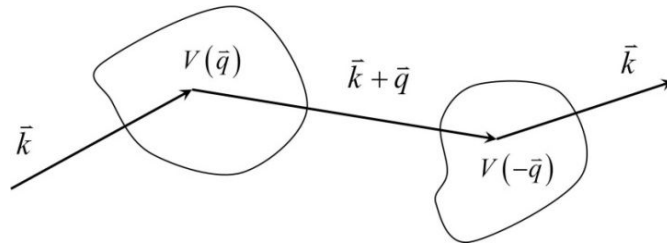


Figure 2.3: Physical interpretation of the third diagram of $G(\vec{k}, \vec{k})$. Used with permission (Tourin 1999).

In general, these diagrams represent all possible chains of events which result in $\vec{k} = \vec{k}'$.

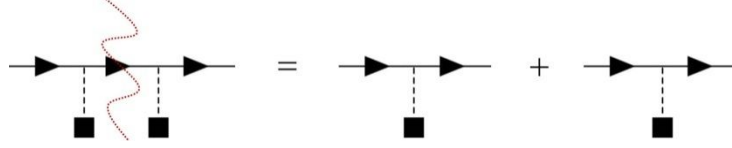
Equations (2.9) and (2.10) may be written more explicitly in terms of \vec{k} and \vec{q} as

$$G(\vec{k}) = G_0(\vec{k}) + G_0(\vec{k})V(0)G_0(\vec{k}) + \sum_{\vec{q}} G_0(\vec{k})V(\vec{q})G_0(\vec{k} + \vec{q})V(-\vec{q})G_0(\vec{k}) \dots \quad (2.26)$$

We want to average Equation (2.26) over all realizations of disorder. Assuming that there are N randomly placed scatterers with no correlations between their positions, it may be shown that the average of Equation (2.26) is a sum of terms with increasing orders of N (Tourin 1999):

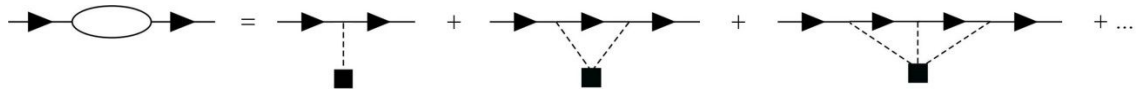
$$\begin{aligned} \langle G(\vec{k}, \vec{k}) \rangle &= G_0(\vec{k}, \vec{k}) + G_0(\vec{k})NV_1(0)G_0(\vec{k}) \quad \longrightarrow \quad + \begin{array}{c} \vec{k} \quad \vec{k} \\ \longrightarrow \quad \longrightarrow \\ | \\ \blacksquare \\ | \\ V(\vec{q}=0) \end{array} \\ &+ G_0(\vec{k})NV_1(0)G_0(\vec{k}) \quad + \begin{array}{c} \vec{k} \quad \vec{k} + \vec{q} \quad \vec{k} \\ \longrightarrow \quad \longrightarrow \quad \longrightarrow \\ | \quad \quad | \\ \blacksquare \quad \blacksquare \\ | \quad \quad | \\ V(\vec{q}) \quad V(-\vec{q}) \end{array} \\ &+ N \sum_{\vec{q}} G_0(\vec{k})V_1(\vec{q})G_0(\vec{k} + \vec{q})V_1(-\vec{q})G_0(\vec{k}) \quad + \begin{array}{c} \vec{k} \quad \vec{k} + \vec{q} \quad \vec{k} \\ \longrightarrow \quad \longrightarrow \quad \longrightarrow \\ \diagdown \quad \diagup \\ | \quad \quad | \\ \blacksquare \\ | \\ V(\vec{q}) \quad N \quad V(-\vec{q}) \end{array} \\ &+ G_0(\vec{k})NV_1(0)G_0(\vec{k})NV_1(0)G_0(\vec{k}) \quad + \begin{array}{c} \vec{k} \quad \vec{k} \quad \vec{k} \\ \longrightarrow \quad \longrightarrow \quad \longrightarrow \\ | \quad \quad | \\ \blacksquare \quad \blacksquare \\ | \quad \quad | \\ NV_1(\vec{q}=0) \quad NV_1(\vec{q}=0) \end{array} \\ &+ \dots \quad + \dots \end{aligned}$$

Looking at the scattering diagrams, we can see that the sum in the third term has had the effect of ‘entangling’ the involved scattering processes, since the sum can not be factorized. The diagonal dotted lines represent the fact that the final wave direction depends on *both* of the scattering processes involved. Another way of describing this concept is to note that there are two basic types of diagrams: *reducible* and *irreducible*. A reducible diagram is one where a vertical cut may be made without intersecting any dotted lines, e.g.

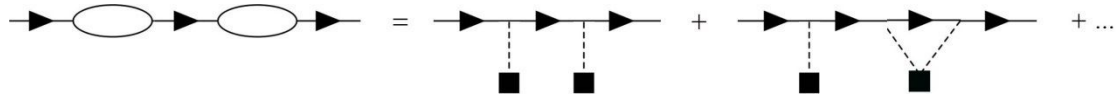


A diagram which may not be cut in this way is irreducible; in the above expression, the diagrams on the right-hand-side are both irreducible.

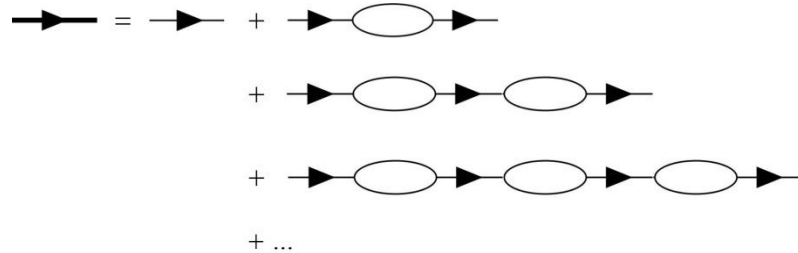
Grouping the diagrams as a function of the number of irreducible diagrams they contain, the diagrams with *one* irreducible diagram are



i.e. each term on the right contains *one* irreducible diagram. Similarly, the sum of all diagrams containing *two* irreducible diagrams is



etc. Thus, we may write the average homogeneous Green's function (the average of Equation (2.26)) as

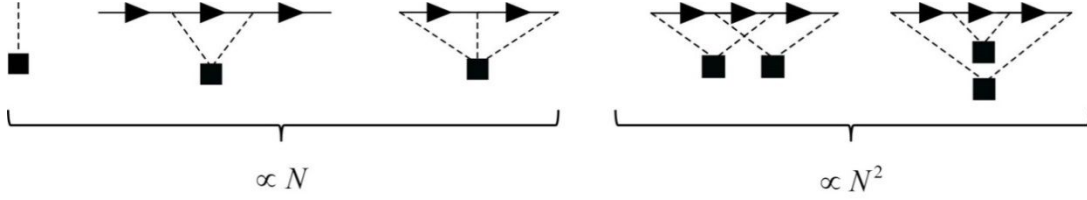


Multiplying each term by $\rightarrow \text{loop} \rightarrow$, we may directly derive the Dyson equation:



Identifying terms between Equation (2.14) and the diagrammatic representation, written above, it is clear that the self-energy Σ is the sum of all irreducible diagrams, $\rightarrow \text{loop} \rightarrow$.

These diagrams include all those proportional to N , but also those proportional to higher orders of N :



It is common to only include some of the terms of the self-energy in subsequent calculations. Our diagrammatic description of self-energy will show the physical consequences of such approximations.

2.2.3.2. Intensity transport

Diagrammatic perturbation theory is presented here for $\bar{\mathbf{G}}_2$ just as it was for self-energy in Section 2.2.3.1. In the diagrammatic representation, one scattering event is represented by a cross (x), and Green's functions by horizontal lines. Thus,

$$\mathbf{G} = \mathbf{G}_0 + \mathbf{G}_0 \mathbf{T} \mathbf{G}_0 = \text{---} + \text{---} \times \text{---} + \text{---} \times \times \text{---} + \text{---} \times \times \times \text{---} + \dots \quad (2.27)$$

To write $\mathbf{G}_2 = \mathbf{G} \mathbf{G}^*$ in terms of diagrams, the elements of \mathbf{G} (outgoing propagation) are placed on the top, and the elements of \mathbf{G}^* (incoming propagation) on the bottom. Identical scatterers are connected by dashed lines. For example, the average product of the third terms of \mathbf{G} and \mathbf{G}^* is:

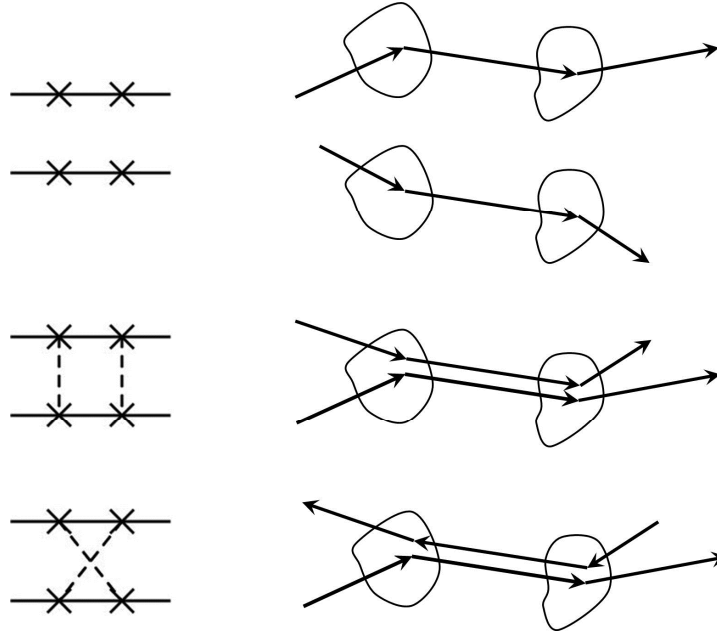
$$\left\langle \begin{array}{c} \text{---} \times \times \text{---} \\ \text{---} \times \times \text{---} \end{array} \right\rangle = \begin{array}{c} \text{---} \times \times \text{---} \\ \text{---} \times \times \text{---} \end{array} + \begin{array}{c} \text{---} \times \times \text{---} \\ \text{---} \times \times \text{---} \\ \text{---} \times \times \text{---} \end{array} + \begin{array}{c} \text{---} \times \times \text{---} \\ \text{---} \times \times \text{---} \end{array}$$

All of the possibilities for a chain of two scattering events are represented. Writing the same thing in matrix notation is much more work:

$$\begin{aligned}
& \left\langle \sum_i \sum_{i \neq j} G_0 t_i G_0 t_j G_0 \otimes \sum_k \sum_{l \neq k} G_0^* t_k^* G_0^* t_l^* G_0^* \right\rangle = \left\langle \sum_i \sum_{i \neq j} G_0 t_i G_0 t_j G_0 \otimes \sum_{\substack{k \neq i \\ k \neq j}} \sum_{\substack{l \neq k \\ l \neq i}} G_0^* t_k^* G_0^* t_l^* G_0^* \right\rangle \\
& + \left\langle \sum_i \sum_{i \neq j} G_0 t_i G_0 t_j G_0 \otimes \sum_{\substack{k \neq i \\ k \neq j}} \sum_{\substack{l \neq k \\ l \neq i}} G_0^* t_k^* G_0^* t_l^* G_0^* \right\rangle + \left\langle \sum_i \sum_{i \neq j} G_0 t_i G_0 t_j G_0 \otimes \sum_{\substack{k \neq i \\ k \neq j}} \sum_{\substack{l \neq k \\ l \neq i}} G_0^* t_k^* G_0^* t_l^* G_0^* \right\rangle \quad (2.28)
\end{aligned}$$

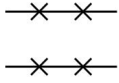
Here, t_k are elements of the scattering matrix \mathbf{T} , representing scattering from *one impurity only*.

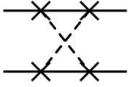
Yet another way of representing the third term of \mathbf{G}_2 is shown below, by interpreting it as symbolizing pairs of paths through groups of scatterers:

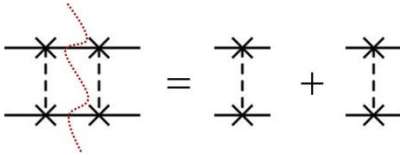


(Tourin 1999). The first diagram represents two paths with no scatterer in common. The second path represents two paths which encounter the scatterers in the same order. The third path represents two paths which encounter the same scatterers, but in an inverse order. We can see that the order in which the scatterers are encountered by the waves is important; this is the only difference between the last two terms.

There are three basic types of diagrams:

1) Non-connected:  contributing to the first term of the BS equation, $\bar{\mathbf{G}} \otimes \bar{\mathbf{G}}^*$.

2) Irreducible: 

3) Reducible : 

We will represent all irreducible diagrams with one irreducible diagram as:

$$\text{Diagram with two horizontal lines and a shaded square in the middle} = \text{Diagram with two horizontal lines and a dashed line connecting the 'x' marks} + \text{Diagram with two horizontal lines and a dashed line connecting the 'x' marks} + \text{Diagram with two horizontal lines and a dashed line connecting the 'x' marks}$$

So $\bar{\mathbf{G}}_2$, being a collection of all reducible and irreducible diagrams, may be written as

$$\langle G(\bar{r}, \bar{r}_0) G^*(\bar{r}', \bar{r}'_0) \rangle = \text{Diagram with two horizontal lines} + \text{Diagram with two horizontal lines and a shaded square in the middle} + \text{Diagram with two horizontal lines and two shaded squares in the middle} + \dots \quad (2.29)$$

where, for example, the third term is the sum of all reducible diagrams which each contain *two* irreducible diagrams. In analogy with the Dyson equation, comparing terms of the above diagrammatic equation with Equation (2.25) shows that the sum of *all connected diagrams* (without the incoming and outgoing Green's functions) is

$$\Gamma = \text{Diagram with two horizontal lines and a shaded square in the middle} + \text{Diagram with two horizontal lines and two shaded squares in the middle} + \dots$$

Γ is called the *reducible vertex function* Γ , and gives information on the *total* scattered wave intensity. From Equations (2.6), (2.9), and (2.10), the averaged scattering intensity may be expressed as

$$\left\langle \left| \psi_s(\bar{R}) \right|^2 \right\rangle_c \propto \int G_0(\bar{r}_1, \bar{R}) G_0^*(\bar{r}_2, \bar{R}) \Gamma(\bar{r}_1, \bar{r}_2, \bar{r}_3, \bar{r}_4) G_0(\bar{r}_3, \bar{R}) G_0^*(\bar{r}_4, \bar{R}) d\bar{r}_1 d\bar{r}_2 d\bar{r}_3 d\bar{r}_4 \quad (2.30)$$

for incident wave ϕ and scattered wave amplitude ψ_s (Sheng 2006).

From the definition of Γ given by Equation (2.24), the sum of all irreducible diagrams may be recognized as the *irreducible vertex function*, \mathbf{U} :

$$U \equiv \boxed{} = \begin{array}{c} \times \\ \vdots \\ \times \end{array} + \begin{array}{c} \times \\ \text{---} \times \\ \text{---} \times \\ \text{---} \times \end{array} + \begin{array}{c} \times \times \\ \text{---} \times \times \\ \text{---} \times \times \\ \text{---} \times \times \end{array} + \dots \quad (2.31)$$

As shown by Equation (2.25), \mathbf{U} is involved in the successive recalculation of the scattering intensity due to wave scattering processes. Thus, \mathbf{U} is most useful for finding information about wave transport and the diffusion coefficient (van Tiggelen 1999; Akkermans et al. 1988; Sheng 2006).

At this point, it is useful to look at the vertex functions more closely. We will define the first term in Equation (2.31) as l . The irreducible vertex \mathbf{U} is sometimes called the *generator* of Γ , as it successively generates Γ according to Equation (2.24). For example, if we let $\mathbf{U} \rightarrow l$, then Equation (2.24) becomes

$$\Gamma_l = l + l \cdot \mathbf{G} \otimes \mathbf{G}^* \cdot \Gamma_l \equiv \mathbf{L} \quad (2.32)$$

where \mathbf{L} is the sum of all so-called *ladder diagrams*, shown in Figure 2.4. In other words, l (the first term in Equation (2.31)) generates *all* of the ladder diagrams. This approximation (letting $\mathbf{U} \rightarrow l$) is called the *ladder diagram approximation*, and is discussed in Section 2.2.4.1.2.

$$\boxed{\mathbf{L}} \equiv \begin{array}{c} \times \\ \vdots \\ \times \end{array} + \begin{array}{c} \times \times \\ \text{---} \times \times \\ \text{---} \times \times \\ \text{---} \times \times \end{array} + \begin{array}{c} \times \times \times \\ \text{---} \times \times \times \\ \text{---} \times \times \times \\ \text{---} \times \times \times \end{array} + \dots$$

Figure 2.4: Summation of ladder terms.

Without approximation, the full reducible vertex is

$$\Gamma = \mathbf{U} + \mathbf{R} \quad (2.33)$$

where \mathbf{R} is the sum of all reducible diagrams. These include many higher-order diagrams,

making it difficult to work with the full expression for $\mathbf{\Gamma}$ when calculating intensity. Thus, most of the diagrams of \mathbf{R} are often ignored. We will use this treatment in the following sections, as it applies very well to most (weakly-scattering) systems. Only for very strong scattering is a more complete description required; this issue is discussed in Section 2.5.2.

2.2.4. Calculating intensity propagation: approximations

Just as with $\bar{\mathbf{G}}$, exact solutions for $\bar{\mathbf{G}}_2$ are generally not possible in the presence of disorder, due to the difficulty of summing the terms in \mathbf{U} and $\mathbf{\Gamma}$ exactly. For weak scattering systems, it is possible to obtain accurate theoretical predictions using approximations which break down in the strong scattering regime. The two most common approximations employed by multiple scattering theories are: i) particle-particle correlations are neglected, and ii) paths in which the wave interacts with the same scatterer more than once are neglected. These assumptions break down for high densities of scatterers in the sample. Some useful approximations are summarized in this section.

2.2.4.1.1. The Independent Scattering Approximation⁴

The Independent Scattering Approximation (ISA) consists of keeping only first-order terms in the diagrammatic expansion of the self-energy (also called the Born approximation). It is appropriate for dilute systems with low density of scatterers.

Keeping only the first-order terms for the self-energy, i.e. all terms proportional to the impurity concentration (the diagrams of the self-energy are given in Section 2.2.3.1), gives

$$\Sigma(\omega, \vec{k}) = N t_{\vec{k}}, \quad (2.34)$$

⁴ (Ishimaru 1977; Tourin 1999; van der Mark, van Albada, and Lagendijk 1988; Sheng 2006).

where N is the number of scatterers, and elements t_k were defined previously. Now, if the scatterers are randomly positioned and are pointlike (relative to λ) then $\Sigma(\omega, \vec{k})$ becomes \vec{k} -independent. In this case, the Green's function in the ISA takes the form of Equation (2.17).

The contribution to self-energy from the second order in N depends on λ/ℓ_s , where ℓ_s is the scattering mean free path (see Section 2.2.1.1.1) and is thus negligible for very dilute systems. However, contributions from higher orders may become important for time-dependant scattering and for the coherent backscattering effect.

2.2.4.1.2. The Ladder Diagram Approximation (a.k.a. Boltzmann approximation)

As discussed in Section 2.2.2, including only the first term for the irreducible vertex function is called the *ladder diagram approximation*. This is equivalent to making a dilute medium approximation. It may be shown that, in this case,

$$U_k^{(1)} = N t_k, \quad (2.35)$$

where N and t_k were defined previously. The reducible vertex function Γ now only contains ladder diagrams (Equation (2.32)). All intensity transport is carried out through the processes shown in Figure 2.4, where only pairs of Green's functions involving identical paths contribute. The replacement of \mathbf{U} by $U_k^{(1)}$ is also commonly known as the Boltzmann approximation.

2.2.4.1.3. The Radiative Transfer Equation⁵

The radiative transfer approach is equivalent to that of the ladder diagram approximation; only weak scattering is taken into account. However, transport theory enables the calculation of theoretical predictions to compare with experimental quantities.

All theory on radiative transfer employs the ISA and the Boltzmann approximation. We

⁵ See, e.g., (Lagendijk and van Tiggelen 1996).

begin by interpreting the Bethe-Salpeter equation, without approximation, as the following type of transport equation:

$$\left[\frac{\partial}{\partial t} + \vec{\nabla} \cdot \vec{\nabla} + \text{losses} \right] I_u(\vec{r}, t) = \text{sources} + \text{scattering}, \quad (2.36)$$

where $I_u(\vec{r}, t)$ is the average propagating intensity for waves of velocity \vec{v} . If both the dilute medium approximation (ISA) (taking Equation (2.34) for $\Sigma(\omega, \vec{k})$), and the Boltzmann approximation (taking Equation (2.35) for \mathbf{U}) are made, it can be shown (Lagendijk and van Tiggelen 1996) that $I_u(\vec{r}, t)$ obeys the *radiative transfer equation*:

$$\frac{1}{v_p} \frac{\partial \bar{I}_u(\vec{r}, t)}{\partial t} + \vec{v} \nabla \bar{I}_u(\vec{r}, t) = -\frac{1}{l_s} \bar{I}_u(\vec{r}, t) + n \int d\bar{\Omega}'_u \frac{d\sigma}{d\Omega}(\vec{v}' \rightarrow \vec{v}) \bar{I}_u(\vec{r}, t) + \text{source}, \quad (2.37)$$

where v_p is the phase velocity of the wave in the effective medium. The left side of the equation represents variations in time and space along the direction of \vec{u} . The first equation on the right represents the energy loss in the incident direction due to scattering in other directions. The second right-hand-side equation represents the energy gain in the incident direction due to scattering events in direction \vec{u} towards the incident direction \vec{u} .

2.2.4.1.4. The Diffusion Approximation (a.k.a. the Boltzmann approximation)⁶

The exact radiative transfer equation can only be solved numerically, making it difficult to treat strong scattering processes, and thus the diffusion approximation is often preferred. The common procedure is to replace an exact transport equation with a diffusion equation, optionally incorporating appropriate boundary conditions. We may write the diffusion equation as

$$\frac{\partial W(r, t)}{\partial t} - D_B \nabla^2 W(r, t) = \delta(r) \delta(t), \quad (2.38)$$

⁶ (Tourin 1999; Akkermans et al. 1988).

where $W(r, t)$ is the local energy density, and D_B is the Boltzmann diffusion coefficient, defined as

$$D_B = \frac{1}{d} v_E \ell^* . \quad (2.39)$$

Parameter v_E is the energy (or transport) velocity. The transport mean free path ℓ^* describes the distance the waves travel before the direction of propagation is randomized, and is given by

$$\ell^* = \frac{\ell_s}{1 - \int \cos(\vec{u}, \vec{u}') \frac{d\sigma}{d\Omega} d\Omega} = \frac{\ell_s}{1 - \cos \theta} \quad (2.40)$$

where \vec{u} and \vec{u}' were previously defined. The solution of the diffusion equation in an infinite medium is

$$W(r, t) = \frac{1}{(4\pi D_B t)^{d/2}} e^{-\frac{r^2}{4D_B t}} . \quad (2.41)$$

Here we can recognize the expression for a random walk whose number of steps goes to infinity. Thus, intensity propagation in the diffusive medium is analogous to a random walk between scattering events. Like the ladder diagram approximation, the diffusion approximation does not take into account interference effects between different possible paths through the sample, and hence breaks down for very strong scattering. It is only valid on length scales larger than ℓ^* .

2.2.5. Configurational averaging

As introduced in Section 2.2.1, waves in a random medium have randomly-varying phase and amplitude – an effect that occurs even for weak scattering. To extract information from this type of system, two main approaches may be employed: analysis of speckle statistics such as variance, or the calculation of configurationally-average quantities. Experimentally, an average over *all* possible configurations of randomly-positioned scatterers is not possible, but enough

configurational averaging can be performed to obtain good measurements of the desired quantities such as average transmitted intensity as a function of time (c.f. Equations (2.11) and (2.23)). Configurational averaging in experiment is typically achieved by physically changing the medium through which waves propagate, i.e. by using a medium which changes slowly with time, or by creating a great many different samples, and then averaging the desired quantity over all times/samples.

2.3. Symmetry in scattering systems

A scattering system in which energy is conserved may exhibit *reciprocity* and/or *time-reversal symmetry*. It is useful to discuss these properties here, as they are fundamental to understanding both the theory and real-world applications of wave scattering.

A spatially reciprocal system is one which is invariant upon interchange of source and detector (Figure 2.5, top). Time-reversal invariance is a related property in which, for every wave pulse $\psi(\vec{r}, t)$ diverging from a source, there exists a set of waves $\psi(\vec{r}, t)$ that can be ‘time-reversed’, i.e. retrace all of the paths taken by the partial waves of pulse $\psi(\vec{r}, t)$, to converge back at the original source. This process is illustrated in Figure 2.5 (bottom); imagine that a pulse is sent into a medium from point a , and the scattered signal is detected some time later at point b . Then, if that detected signal is time-reversed (a ‘first-in, last-out’ operation) and emitted from point b , the original pulse should be detected at point a . The concept of time-reversal is at the heart of the scattering theory presented in this thesis, as can be seen by the *two* Green’s function solutions to the wave equation (Equation (2.2)). For each causal solution, there exists an anti-causal solution which is simply a time-reversed copy of the causal one. If energy conservation in the system is obeyed, then the conditions of reciprocity and time-reversal invariance are equivalent (Carminati et al. 2000).

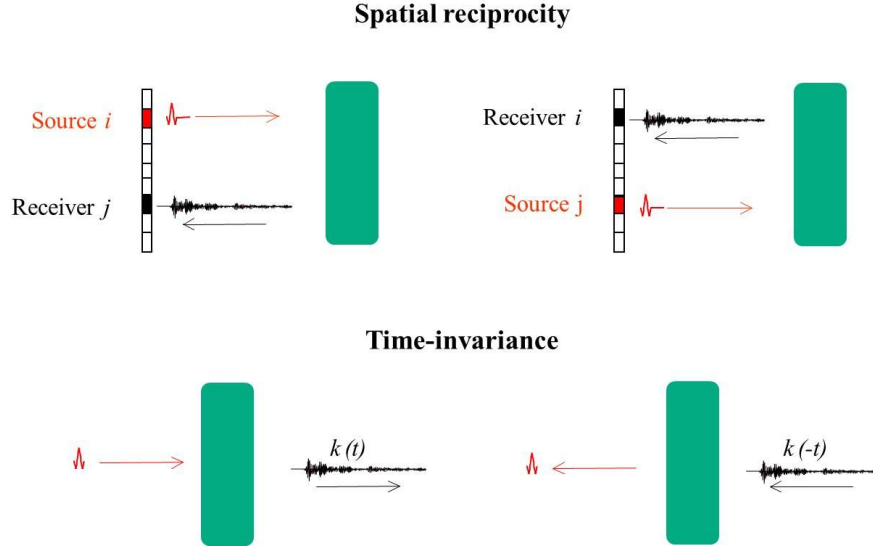


Figure 2.5: The concepts of spatial reciprocity and time-invariance are linked. Each is obeyed for any input/output geometry (shown here are reflection, top, and transmission, bottom, for slab-shaped samples). Top: A pulsed emission from i results in a multiply-scattered pulse at j . For a spatially reciprocal system, a pulsed emission at j will result in the *same* multiply-scattered pulse at i . Bottom: A pulse sent through a spatially reciprocal system results in a multiply-scattered signal being detected on the other side. If this multiply-scattered signal is time-reversed and sent back into the medium, the resulting transmitted signal will be the original source pulse.

2.3.1. The consequences of spatial reciprocity

Reciprocity applied to diagrammatic scattering theory can show why classical transport theory should not be used to describe very strongly scattering systems (Akkermans et al. 1988; van Tiggelen, Lagendijk, and Wiersma 2001). Recall that the reducible vertex, $\mathbf{\Gamma}$, represents *all* of the scattering processes of the intensity Green's function. Written without approximation (Equation (2.33), reproduced here) it is:

$$\mathbf{\Gamma} = \mathbf{U} + \mathbf{R}$$

where \mathbf{U} holds all irreducible diagrams, and \mathbf{R} holds all reducible diagrams. Spatial reciprocity imposes the following relation for the intensity Green's function:

$$\Gamma(\vec{r}_1, \vec{r}_2, \vec{r}_3, \vec{r}_4) = \Gamma(\vec{r}_2, \vec{r}_1, \vec{r}_4, \vec{r}_3) = \Gamma(\vec{r}_1, \vec{r}_2, \vec{r}_4, \vec{r}_3) \quad (2.42)$$

(van Tiggelen, Lagendijk, and Wiersma 2001). The first identity is a well-known classical reciprocity relation also obeyed by radiative transfer (Section 2.2.4.1.3). The second identity consists of reversing directions either from $1 \rightarrow 3$ or $2 \rightarrow 4$, but not both. This identity is obeyed by $\mathbf{\Gamma}$, but not by \mathbf{U} or \mathbf{R} on their own. The reason for this is the following:

The interchange of source and receiver for either \mathbf{G} or \mathbf{G}^* is equivalent to reversing the direction of either the top or bottom of the diagrams shown in Section 2.2.3.2. Clearly, this process can convert *any* reducible diagram into an irreducible one (for a proof see van Tiggelen and Maynard (1998)):

$$R(\bar{r}_1, \bar{r}_2, \bar{r}_3, \bar{r}_4) = C(\bar{r}_1, \bar{r}_2, \bar{r}_4, \bar{r}_3) \quad (2.43)$$

where new vertex \mathbf{C} represents all crossed diagrams which may be constructed from reducible diagrams with the bottom replaced by its adjoint. However, \mathbf{C} does not make up the entire set of diagrams in \mathbf{U} ; there is another set of irreducible diagrams that we will write as \mathbf{S} .

$$\mathbf{U}(\bar{r}_1, \bar{r}_2, \bar{r}_3, \bar{r}_4) = \mathbf{S}(\bar{r}_1, \bar{r}_2, \bar{r}_3, \bar{r}_4) + \mathbf{C}(\bar{r}_1, \bar{r}_2, \bar{r}_3, \bar{r}_4). \quad (2.44)$$

The set \mathbf{S} is a set of (irreducible) scattering diagrams that transforms into itself;

$$S(\bar{r}_1, \bar{r}_2, \bar{r}_3, \bar{r}_4) = S(\bar{r}_1, \bar{r}_2, \bar{r}_4, \bar{r}_3). \quad (2.45)$$

The vertex \mathbf{S} describes so-called “super single-scattering”. It contains not only the single scattering diagram l , but also all “loop” events, which are paths which begin and end at the same place (or, more accurately, within ℓ_s of each other) (van Tiggelen, Wiersma, and Lagendijk 1995). These “loop” events are also called *recurrent scattering*.

By approximating $\mathbf{U} \sim l$ the classical treatment of wave scattering ignores the entire set of crossed diagrams \mathbf{C} as well as the recurrent scattering diagrams. Thus radiative transfer (and therefore the diffusion approximation) *does not obey reciprocity!* The importance of the crossed diagrams was first suggested by Götze, and was subsequently demonstrated by Vollhardt and

Wölfle for the renormalization of wave diffusion (Götze 1979; Vollhardt and Wölfle 1980b; Vollhardt and Wölfle 1992). The crossed diagrams give rise to the *coherent backscattering effect* (introduced in Section 2.4), which was in fact the first experimental evidence that the radiative transfer theory is incomplete for light, and by extension, other classical waves. The recurrent scattering diagrams become important for systems with very strong scattering, and are discussed in Chapter 6.

2.3.2. The propagation matrix in backscattering

In a real-world system, time-invariance is never perfectly obeyed since this assumption requires, for example, a completely lossless medium in which the velocity of individual scatterers is much less than the velocity of the waves in the medium. However, the time-invariance and interference effects with which it is associated may be remarkably robust for classical waves (shown, for example, by Fink et al. (2000)). There are powerful experimental methods based on this concept. A ubiquitous example is ultrasonic imaging, which employs multiple sources and detectors to capture a matrix of signals, containing the responses between each source and detector. This *propagation matrix* contains all relevant information about the system, and thus is ideal for the characterization of the material through which the waves have travelled. The beauty of this approach is its simplicity; once a propagation matrix is measured for a particular system, all imaging and extraction of information from the matrix can be performed after the experiment has been finished. For a reciprocal system, *iterative time-reversal* can be used for, for example, selective target detection through an aberrating layer (Prada et al. 1996; Popoff et al. 2011) and wave focussing across a highly scattering slab (Popoff et al. 2010; Kim et al. 2012). Coherent backscattering and recurrent scattering effects can also be calculated (following sections). In this thesis, all experiments in the backscattering configuration consist of

the measurement of the propagation matrix and its subsequent analysis.

2.4. Introduction to coherent backscattering

Coherent backscattering (CBS) is an interference effect that is seen in the configurationally averaged intensity of backscattered waves from a disordered medium. CBS can occur for any type of wave, and in fact was first reported independently in two different fields: for electrons in dirty metals (Langer and Neal 1966) and for light waves in a turbulent atmosphere (de Wolf 1971). Coherent backscattering of light was first measured experimentally by three different groups: in 1984 by Kuga and Ishimaru using dense latex microspheres as a scattering medium, and in 1985 by van Albada and Lagendijk, and by Wolf and Maret with polystyrene spheres (Kuga and Ishimaru 1984; van Albada and Lagendijk 1985; Wolf and Maret 1985). The first observation of dynamic (time-dependent) coherent backscattering was reported for light waves (Vreeker et al. 1988). However subsequent experiments highlighted the advantages of acoustics for CBS, where time information is readily available (femtosecond pulses are needed in optics) (Tourin et al. 1997; Bayer and Niederdränk 1993).

The CBS effect can be understood in a basic way by considering the schematic of Figure 2.6. Two ray paths in a scattering medium are shown. Both paths A and B have amplitude A_i at some far-off source point \mathbf{R}_0 and wave vector k_i . After path A experiences n elastic scatterings it leaves the front surface with k_f . Ray path B undergoes the same n scatterings, but in the opposite order, and also exits with k_f . The outgoing rays, A_0 and B_0 , are detected at some far-off position \mathbf{r}_0 .

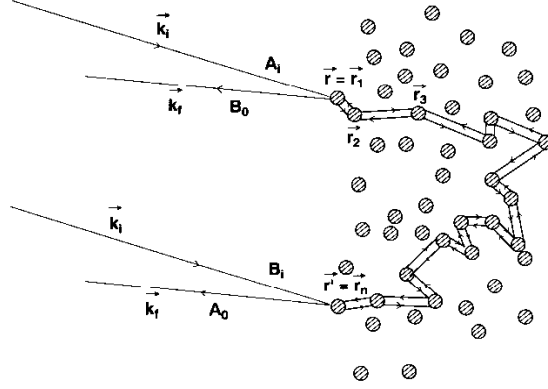


Figure 2.6: Two interfering rays A and B. Ray B may be regarded as ray A propagating backwards in time (Sheng 2006).

The outgoing and initial ray amplitudes are related to each other by a product of Green's functions, i.e.

$$A_0 = A_i G_A \exp \left[i \vec{k}_i \cdot (\vec{r}_1 - \vec{R}_0) + i \vec{k}_{1,2} \cdot (\vec{r}_2 - \vec{r}_1) + \dots + i \vec{k}_{n-1,n} \cdot (\vec{r}_n - \vec{r}_{n-1}) + i \vec{k}_f \cdot (\vec{r}_0 - \vec{r}_n) \right], \quad (2.46)$$

where $k_{n-1,n}$ is the wave vector of ray propagation between scatterers $n-1$ and n , and G_A is a factor that accounts for the scattering strength of each scatterer. Similarly for ray path B, since $B_i = A_i$,

$$B_0 = A_i G_B \exp \left[i \vec{k}_i \cdot (\vec{r}_n - \vec{R}_0) + i \vec{k}_{n,n-1} \cdot (\vec{r}_{n-1} - \vec{r}_n) + \dots + i \vec{k}_{2,1} \cdot (\vec{r}_1 - \vec{r}_2) + i \vec{k}_f \cdot (\vec{r}_0 - \vec{r}_1) \right], \quad (2.47)$$

where $G_B = G_A$ since all scatterers involved are identical. Since $k_{n-1,n} = -k_{n-1,n}$, the sum of all phase factors between the first and last terms is the same for both rays A and B. Thus, for a coherent beam incident on the surface of a random medium, backscattered intensity from A and B is

$$|A_0 + B_0|^2 = |A_0|^2 + |B_0|^2 + A_0 B_0^* + A_0^* B_0 = 2 \left\{ 1 + \cos \left[(\vec{k}_i + \vec{k}_f) \cdot (\vec{r} - \vec{r}') \right] \right\} |A_0|^2. \quad (2.48)$$

The constant term inside the curly brackets is due to incoherent scattering (paths that do not interfere with each other constructively on average), and the cosine term is due to the constructive interference between reciprocal paths A and B. This interference causes an enhancement in backscattered intensity; this is the coherent backscattering effect. The coherence is maximum for $k_i + k_f = 0$, where the backscattered intensity is enhanced by a factor of 2. This

reciprocal paths argument rests on the condition of spatial reciprocity; for every path α there exists a *time-reversed* path β , where the wave encounters the same scatterers in exactly the reverse order (and vice versa).

The CBS effect is also often called *weak localization*, and occurs in even the most weakly-scattering systems. All that is needed to produce coherent backscattering is a reciprocal medium where waves may be multiply scattered (i.e. the existence of reciprocal paths like the ones shown in Figure 2.6). Note that the term *backscattering* is different than *reflection*; backscattered waves have not simply reflected off of the sample surface, but have entered the sample, interacted with *at least* one scatterer, and then exited the sample via the same side they entered.

2.4.1. Calculating the CBS effect

Here, as in other sections, we will calculate the CBS effect using diagrammatic scattering theory. Since coherent backscattering is seen in the backscattered intensity from a multiple scattering system, we can use Equation (2.30), reproduced here:

$$\left\langle \left| \psi_s(\vec{R}) \right|^2 \right\rangle_c \propto \int G_0(\vec{r}_1) G_0^*(\vec{r}_2) \Gamma(\vec{r}_1, \vec{r}_2, \vec{r}_3, \vec{r}_4) G_0(\vec{r}_3) G_0^*(\vec{r}_4) d\vec{r}_1 d\vec{r}_2 d\vec{r}_3 d\vec{r}_4$$

Equation (2.30) can be used to calculate the backscattered intensity from any system, so long as the Green's functions between source and medium and between medium and detector $G_0(\vec{r}, \vec{R})$, and the reducible vertex $\Gamma(\vec{r}_1, \vec{r}_2, \vec{r}_3, \vec{r}_4)$ are known. Of these, the most difficult to compute is Γ , as it requires the summing of a huge number of scattering diagrams. To obtain an expression for $\langle |\psi_s(\vec{R})|^2 \rangle$ which is comparable to real-world measurements, some kind of approximation must be employed. The diagrammatic method of calculation helps to determine which types of scattering processes to include and which can be ignored.

The first consequence of averaging over all realizations of disorder (the integral in

Equation (2.30)) is that the interference between paths of the type shown in Figure 2.7a average to zero (this is why the first term in Equation (2.29) is not included in the irreducible vertex).

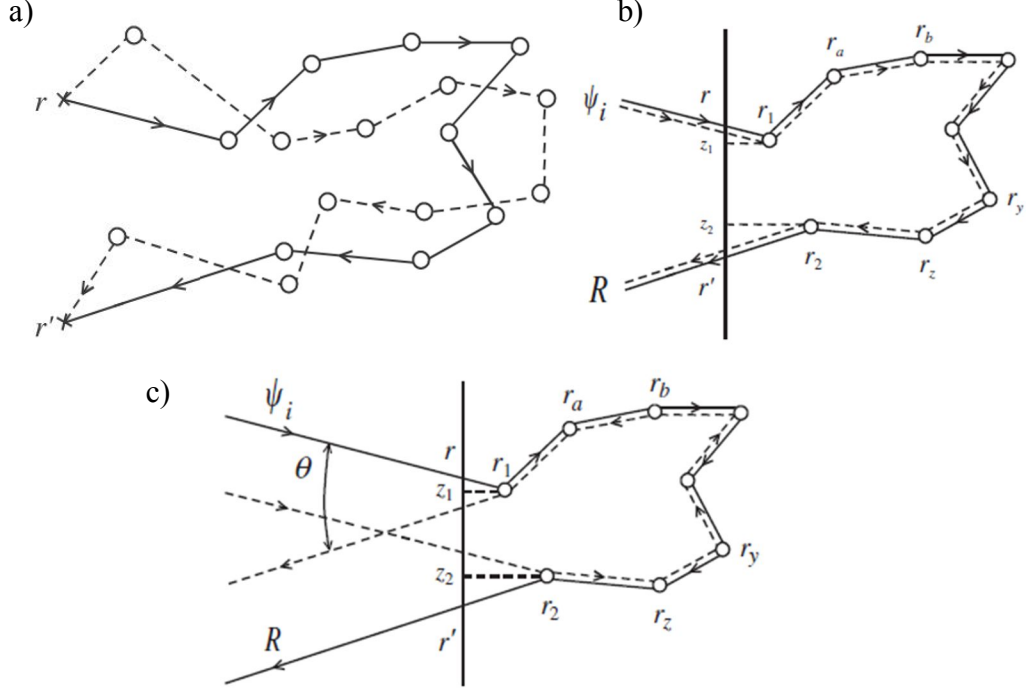


Figure 2.7: Paths of a pair of advanced and retarded Green's functions. a) Paths which do not interfere constructively, b) Identical paths with propagation along the same direction, and c) Identical paths with propagation along opposite directions (Akkermans and Montambaux 2007).

Now, the simplest approach to calculate $\langle |\psi_s(\vec{R})|^2 \rangle$ is to use the ladder diagram approximation. As discussed in Sections 2.2.3.2 and 2.2.4.1.2, this means that the vertex $\Gamma(\vec{r}_1, \vec{r}_2, \vec{r}_3, \vec{r}_4)$ is composed of the sum of all ladder diagrams (Figure 2.4). The backscattered intensity is now

$$I_{inc}(\vec{R}) = \int G_0(\vec{r}_1, \vec{R}) G_0^*(\vec{r}_2, \vec{R}) L(\vec{r}_1, \vec{r}_2, \vec{r}_3, \vec{r}_4) G_0(\vec{r}_3, \vec{R}) G_0^*(\vec{r}_4, \vec{R}) d\vec{r}_1 d\vec{r}_2 d\vec{r}_3 d\vec{r}_4 \quad (2.49)$$

and corresponds to the structure in Figure 2.7b. As previously stated, this is equivalent to the diffusion approximation. Wave transport is represented as a statistical probability, taking into account all possible scattering paths through the sample. However, interference between those

different paths (i.e. accounting for the fact that they are all, in effect, occurring at the same time) is not included. For this reason, the backscattered intensity under the ladder approximation is often called the *incoherent contribution* to the backscattering intensity profile.

As we have seen in the beginning of this section, the ladder diagrams on their own can not account for the CBS effect. The CBS effect is due to reciprocal paths through the sample; the types of paths shown in Figure 2.7c. If we want our system to obey reciprocity, we need to include all of the diagrams that result from an interchange of source and detector for the ladder diagrams. In other words, we enforce the reciprocity relation

$$\mathbf{L}(\vec{r}_1, \vec{r}_2, \vec{r}_3, \vec{r}_4) = \mathbf{C}_M(\vec{r}_3, \vec{r}_2, \vec{r}_1, \vec{r}_4) \quad (2.50)$$

where the new vertex \mathbf{C}_M contains the sum of all *most-crossed* diagrams. Diagrammatically, this corresponds to flipping the bottom (or top) of each ladder diagram, with dotted lines remaining connected to the same scatterers, resulting in a sum of most-crossed diagrams as shown in Figure 2.8. Thus, we have calculated the paths of Figure 2.7c using the ladder diagrams, simply by the interchange of source and detector.

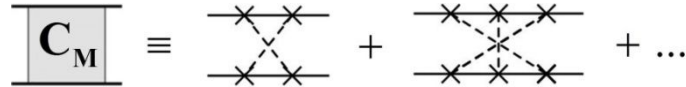


Figure 2.8: Summation of most-crossed diagrams. The first scatterer encountered on the top (incoming) path corresponds to the last scatterer encountered on the bottom (outgoing) path.

Since each path pair in both \mathbf{L} and \mathbf{C}_M starts and ends at the same particle (or, more accurately, within a region about the size of a mean free path), we can expect dependence on only two \vec{r} positions (van der Mark, van Albada, and Lagendijk 1988):

$$\begin{aligned} L(\vec{r}_1, \vec{r}_2, \vec{r}_3, \vec{r}_4) &\propto \delta(\vec{r}_1 - \vec{r}_2) \delta(\vec{r}_3 - \vec{r}_4) F(\vec{r}_1, \vec{r}_3) \\ C_M(\vec{r}_1, \vec{r}_2, \vec{r}_3, \vec{r}_4) &\propto \delta(\vec{r}_3 - \vec{r}_2) \delta(\vec{r}_1 - \vec{r}_4) F(\vec{r}_1, \vec{r}_3) \end{aligned} \quad (2.51)$$

where the propagator $F(\vec{r}_1, \vec{r}_3)$, is the Green's function for the incoherent intensity at \vec{r}_3 from a source at \vec{r}_1 . $F(\vec{r}_1, \vec{r}_3)$ can be found by solving a transport equation; on length scales larger than the transport mean free path, this reduces to a diffusion equation (van Tiggelen, Lagendijk, and Wiersma 2001).

The contribution of most-crossed diagrams to backscattered intensity is often called the *coherent contribution*, and is given by

$$I_{coh}(\vec{R}) = \int G_0(\vec{r}_1, \vec{R}) G_0^*(\vec{r}_2, \vec{R}) C_M(\vec{r}_1, \vec{r}_2, \vec{r}_3, \vec{r}_4) G_0(\vec{r}_3, \vec{R}) G_0^*(\vec{r}_4, \vec{R}) d\vec{r}_1 d\vec{r}_2 d\vec{r}_3 d\vec{r}_4. \quad (2.52)$$

For most systems (i.e. where the diffusion approximation holds), $\Gamma \approx \mathbf{L} + \mathbf{C}_M$ is sufficient to describe the backscattered intensity.

2.5. Introduction to Anderson localization

The concept of Anderson localization is that strong disorder can inhibit the propagation of waves, resulting in the spatial localization of wavefunctions. First proposed by P.W. Anderson in 1958 (Anderson 1958) for quantum spin diffusion (and charge diffusion), the theory was extended to classical waves decades later (Anderson 1985; John, Sompolinsky, and Stephen 1983; John 1984). For classical waves, the idea is that interference effects between scattered waves in a disordered medium cause the slowing, and eventually absence of, wave transport. In the localization regime waves remain localized inside the medium on a length scale given by the localization length ξ (van Tiggelen, Wiersma, and Lagendijk 1995; Anderson 1958; Sheng 2006). Between diffusive and localized states a true transition occurs at the so-called *mobility edge*, and exists only in three dimensions (3D) (E. Abrahams et al. 1979).

2.5.1. The scaling theory of localization⁷

One way of defining localization is that, for an infinite system, almost all states are exponentially localized in space. This spatial confinement of modes could be measured by imagining a sample which is divided up into many smaller subsamples. In each subsample a delta function excitation is placed at the centre, and the response at each subsample surface is measured. By varying this procedure for different subsample sizes L , it is possible to distinguish between localized and *extended* (diffuse) states: If states are localized, then the response decreases with increasing L , but for extended states the response should be constant with L .

Another way of stating the concept above is that a localized wavefunction becomes insensitive to the presence of sample boundaries when $L > \xi$, where *localization length* ξ is the spatial extent of the wavefunction. This is the basis of the *Thouless criterion of localization*, first put forth in the 1970s by Thouless et al. (Edwards and Thouless 1972; Thouless 1974; Licciardello and Thouless 1975). The fundamental ideas are outlined below using the terminology of classical waves.

Here we will take a time scales approach to identifying localization. We wish to measure the time it takes for a change at one sample boundary to be communicated to the other side. We define this time as the *Thouless time* τ_H , and the frequency width of the mode associated with this energy transport as

$$\delta\omega = \frac{1}{\tau_{TH}} \quad (2.53)$$

In the diffusion regime the Thouless time is equal to the diffusion time τ_D , which is the typical time for wave energy to propagate diffusively across the sample:

⁷ See (Sheng 2006; van Tiggelen 1999).

$$\tau_D = \frac{L^2}{\pi^2 D} \quad (2.54)$$

where D is the diffusion coefficient. Thus $\delta\omega \propto L^{-2}$ for extended states. For a localized state where $L > \xi$, $\delta\omega$ can only couple evanescently to the boundary, and therefore has exponential dependence on system size: $\delta\omega \sim \exp(-L/\xi)$.

To make a measure of the change in $\delta\omega$ with system size, we must compare it with the average frequency separation $\Delta\omega$ between neighbouring eigenvalues. We define the dimensionless ratio

$$\gamma = \frac{\delta\omega}{\Delta\omega}. \quad (2.55)$$

$\Delta\omega$ is inversely proportional to the density of states, which is proportional to sample volume, so

$$\Delta\omega \propto L^{-d} \quad (2.56)$$

for both extended and localized states. Thus the Thouless criterion is given by

$$\begin{aligned} \gamma &\propto L^{d-2} && \text{for extended states} \\ \gamma &\propto \exp(-L/\xi) && \text{for localized states } L > \xi. \end{aligned} \quad (2.57)$$

It is clear that there should be some transitional point between extended and localized states. Furthermore, for $d = 3$ this point should be a critical one, where γ switches from increasing with L to decreasing with L . This argument is the basis for *the scaling theory of localization*, which was proposed in the context of phase transitions in 1979 (E. Abrahams et al. 1979). Defining

$$\beta \equiv \frac{d \ln \gamma}{d \ln L}, \quad (2.58)$$

the problem can now be framed with a single scaling parameter. Figure 2.9 is a schematic of the behaviour of β as a function of $\ln \gamma$ and of dimensionality of the system.

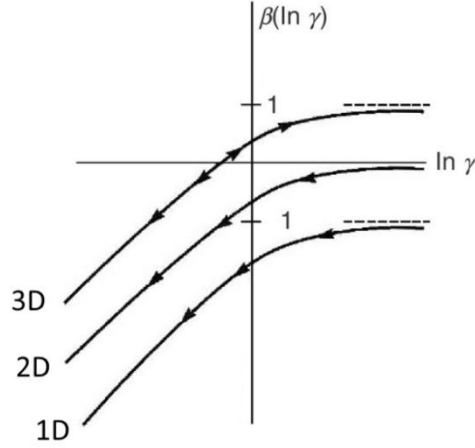


Figure 2.9: The behaviour of the scaling function β as a function of $\ln \gamma$. It is assumed that β is continuous. The arrows indicate the direction in which $\ln(\gamma)$ varies as L increases (Sheng 2006).

Several interesting observations immediately present themselves. Of particular interest for this thesis is the existence of an unstable critical point at γ_c , from which the direction of variation of $\beta(\ln \gamma)$ points away. This critical point, also known as the mobility edge, *exists only in 3D*, as is clear from Figure 2.9. The system behaviour near the mobility edge can be described using the slope of β , defined here as ν . In the localization regime near the mobility edge, the localization length behaviour depends on ν as

$$\xi \propto |\mathcal{E}|^{-\nu} \quad (2.59)$$

where \mathcal{E} is a measure of the distance between γ and γ_c (Sheng 2006). Thus, the single parameter ν governs the localization transition. This demonstrates an important advantage of the scaling theory, which is that its predictions can be experimentally tested by varying a sole parameter of the system, and keeping all other variables constant. Experimentally, this parameter is typically either sample size L , or ‘degree of disorder’ of the medium. For wave scattering, this disorder can be altered by changing either the medium itself (e.g. scatterer size, type, and position) and keeping frequency of the waves constant, or vice versa. If frequency of the waves

is changed (and sample conditions kept constant), then, since γ depends on frequency ω , we have

$$\xi \propto |\omega - \omega_c|^{-\nu} \quad (2.60)$$

While a value of $\nu = 1$ was initially predicted from scaling arguments (Wegner 1979), subsequent numerical simulations raised doubts about this prediction, which was finally proven untrue (Kramer et al. 2010). Since then, the value of ν has been estimated with higher precision and for a variety of systems. For 3D disordered systems belonging to the orthogonal universality class⁸, new results from systems including (but not limited to) disordered phonon simulations (Pinski and Roemer 2011), cold-atom quantum kicked rotors (Lemarié et al. 2009; Lopez et al. 2012), and numerical scaling calculations (Slevin and Ohtsuki 2014; Ghosh et al. 2015) have led to a current, widely-accepted estimate of $\nu \sim 1.6$.

Although it was an extremely important advance in the field of localization, the scaling theory does not include fluctuations of the wavefunctions (γ in Eq. (2.55) is a configurationally averaged quantity), and so is not a complete description of wave propagation near the critical regime.

2.5.2. Renormalized diffusion and the self-consistent theory of localization

In the 1980s, a powerful reformulation of scaling theory, the *self-consistent theory of localization*, was developed by Vollhardt and Wölfle (Vollhardt and Wölfle 1980a; Vollhardt and Wölfle 1980b; Vollhardt and Wölfle 1992). This diagrammatic model describes the

⁸ This is a class of systems which obey time-reversal symmetry (and spin-rotation symmetry, for quantum systems), which is probably the most appropriate case for classical waves. It is worth noting that a different estimate of $\nu \approx 1.89$ was obtained for simulations of elastic waves, wherein it was suggested that such systems are of a different universality class, but this has not since been verified (Sepehrinia, Tabar, and Sahimi 2008).

renormalization of diffusion processes due to the disorder of the medium. Theoretically, in an infinite disordered system, diffusion coefficient $D \rightarrow 0$ in the localization regime. In a finite system with open boundaries, as is usually the case experimentally, waves are free to propagate out of the sample, so transport can not be fully suppressed by localization. However, the description of a diffusion coefficient which decreases due to disorder is still a relevant one, and is outlined here. A ‘local’ version of this theory (Skipetrov and van Tiggelen 2006; Cherroret, Skipetrov, and van Tiggelen 2010) has been successful at describing Anderson localization of classical waves near a mobility edge (Hu et al. 2008), and is presented in the context of experimental measurements in Section 5.1.1.

The diffusion coefficient may be obtained from the irreducible vertex \mathbf{U} (Sheng 2006). In the ISA, where ordinary single scattering is the only contribution to \mathbf{U} , the Boltzmann diffusion coefficient D_B is obtained (that of Equation (2.39)). As scattering strength increases, the transport of wave energy begins to deviate from this simple picture. We have shown, using diagrammatic theory, how the intensity Green’s function is renormalized by multiple scattering events (Equation (2.25)). Equations such as (2.24) and (2.25) make it clear that a complete description of wave propagation in random media needs to be *self-consistent*. This is the basic idea of the self-consistent theory of localization. The idea is to successively calculate \mathbf{U} from the sum $\mathbf{U} = l + \mathbf{C}$.

A more detailed summary of self-consistent theory calculations is presented in Section 5.1.1. Here, we can estimate the effect of the renormalization of \mathbf{U} on the diffusion coefficient by writing the maximally-crossed diagrams \mathbf{C} as a *correction* to $\mathbf{U} = l$. This results in a *correction* to the diffusion coefficient:

$$D \cong D_B - \delta D \tag{2.61}$$

where D_B is known as the Boltzmann diffusion coefficient, the same as that of Equation (2.38).

The correction to diffusion is, in the weak scattering limit,

$$\delta D = \frac{1}{\pi} \frac{v}{k^{d-1}} \begin{cases} L - \ell & 1\text{D} \\ \ln(\ell/L) & 2\text{D} \\ 1/\ell - \ell/L & 3\text{D} \end{cases} \quad (2.62)$$

where d is the system dimension and L is the system size (Sheng 2006). Here we assume isotropic scattering, i.e. $\ell_s = \ell_B^*$. The absence of diffusion, $D = 0$, coincides with the presence of localized states. The critical system size for localization is the *localization length* ξ . Setting $D = 0$ and $L = \xi$ in Equation (2.62),

$$\xi \cong \begin{cases} (1 + \pi)\ell & 1\text{D} \\ \ell \exp(\pi k \ell / 2) & 2\text{D} \\ (1/\ell - \pi k^2 \ell / 3)^{-1} & 3\text{D} \end{cases} \quad (2.63)$$

This gives the so-called Ioffe-Regel criterion for localization (Ioffe and Regel 1960; Mott 1974),

$$k\ell < \sqrt{3/\pi} \cong 1. \quad (2.64)$$

Note that this *correction* to the diffusion coefficient is not the same thing as what is being calculated by the self-consistent theory, which calculates \mathbf{U} more directly, instead of adding a correction to it.

2.5.3. Experimental concept: discrimination between diffuse and localized regimes

Due to its universal nature, Anderson localization has been explored experimentally in a wide range of areas including quantum physics (Sapienza et al. 2010), ultracold atoms (Jendrzejewski et al. 2012), ultrasound (Hu et al. 2008), optics (Segev, Silberberg, and Christodoulides 2013), seismology (Friedrich and Wegler 2005), and even cosmology (Bershadskii 2003). Much of this work has focussed on 1D, quasi-1D, and 2D systems, in which

there is always some degree of localization. In 3D the presence of Anderson localization is much more difficult to verify. One needs to achieve (1) strong enough scattering, and (2) the right combination of disorder, frequency, etc. to induce localization of waves in the sample. The discrimination between diffuse and localized regimes remains an ongoing problem in the field of wave scattering. As discussed in Section 2.5.1, a prevailing approach in many studies is to vary one parameter such as system size or frequency while keeping all others constant. The behaviour of the system is then studied as a function of that parameter. Some quantity is measured which is theoretically predicted to depend on whether wave transport is diffuse or localized. Several such localization criteria have been proposed, including:

1. The Ioffe-Regel criterion of Equation (2.64), often interpreted as $k\ell_s \sim 1$, and relatedly, a small mean free path which denotes ‘strong’ disorder. A definite indication of very strong scattering, the Ioffe-Regel criterion is generally accepted as an *approximate* criterion for localization of waves in 3D.

2. The exponential decay of eigenmodes at large distances (van Tiggelen 1999). This may not hold, however, for finite media with open boundaries since waves can propagate through the boundaries out of the sample. It is also difficult to distinguish this criterion from absorption.

3. A vanishing density of states (DOS) (van Tiggelen 1999). This implies that localization is more likely near a frequency gap of the scattering medium.

4. A vanishing diffusion coefficient D . As shown by the self-consistent theory of localization, this does not hold for a medium with open boundaries; the diffusion coefficient can never really vanish, but at the mobility edge D scales as $1/L$ (Anderson 1958; van Tiggelen and Kogan 1994).

5. The Thouless criterion $g = \text{constant} \approx 1$. Here, g is the dimensionless conductance which is given approximately by $g \equiv \delta\omega/\Delta\omega$.

6. Variance of transmitted intensity $\text{var}(I) = 2\text{var}(T) + 1 = 4/3g + 1 = 7/3$, where $g = 1$ is the dimensionless conductance at the mobility edge, and T is total transmission through the sample. This criterion has been used for photons in quasi 1D (Chabanov, Stoytchev, and Genack 2000) but could hold for other dimensions.

Care must be taken when relying on just one of these criteria to demonstrate the presence of localization, as most are approximate and must be interpreted based on the specific experimental conditions. A more accurate approach may be to combine one or a few of the above criteria with measurements of spatial or temporal dependence of transmitted or reflected waves from the disordered medium. This is the approach taken in this thesis. The experimental strategies are introduced in Chapter 4 in the context of conventional diffusion, and extended to localization and anomalous transport in Chapters 5, 7, and 8.

Appendix 2A : Enhancement factor calculation details⁹

Any ladder diagram may be converted to a most-crossed diagram by reversing the direction of the adjoint Green's function, and vice versa. In terms of individual diagrams, the reciprocity identity between ladder and most-crossed diagrams is:

$$\begin{array}{c} \vec{k} \quad \vec{k}' \\ \longrightarrow \quad \longrightarrow \\ \diagdown \quad \diagup \\ \longleftarrow \quad \longleftarrow \\ \vec{k}' \quad \vec{k} \end{array} = \begin{array}{c} \vec{k} \quad \vec{k}' \\ \longrightarrow \quad \longrightarrow \\ | \quad | \\ \longrightarrow \quad \longrightarrow \\ -\vec{k} \quad -\vec{k}' \end{array} + \begin{array}{c} -\vec{k}' \quad -\vec{k} \\ \longleftarrow \quad \longleftarrow \\ | \quad | \\ \longleftarrow \quad \longleftarrow \\ \vec{k}' \quad \vec{k} \end{array}$$

This may be written in terms of contributions to the intensity Green's function $\mathbf{G}_2 =$

⁹ (Akkermans and Maynard 1985)

$\mathbf{G}_2^{(C)} + \mathbf{G}_2^{(L)}$ as

$$G_2^{(C)}(k\hat{s}, k\hat{s}'; k\hat{s}, k\hat{s}') = \frac{1}{2} \left[G_2^{(L)}(k\hat{s}, k\hat{s}'; -k\hat{s}', -k\hat{s}) + G_2^{(L)}(-k\hat{s}', -k\hat{s}; k\hat{s}, k\hat{s}') \right] \quad (2A.1)$$

where \hat{s} is a unit vector indicating wave vector direction. This is an identity which is very useful when performing calculations involving crossed diagrams. In the special case of exact backscattering, $\vec{s}' = -\vec{s}'$,

$$G_2^{(C)}(k\hat{s}, -k\hat{s}; k\hat{s}, -k\hat{s}) = G_2^{(L)}(k\hat{s}, -k\hat{s}; k\hat{s}, -k\hat{s}), \quad (2A.2)$$

and thus

$$G(k\hat{s}, -k\hat{s}; k\hat{s}, -k\hat{s}) = 2G_2^{(L)}(k\hat{s}, -k\hat{s}; k\hat{s}, -k\hat{s}). \quad (2A.3)$$

Thus, the total probability of backscattering is twice the incoherent multiple scattering probability. This is a well-known result.

3. Experimental Techniques and Data Processing

3.1. Creation of slab mesoglasses L1 and L2

To study the propagation of ultrasound in strongly scattering media, I have created two slab-shaped ‘mesoglass’ samples. The samples consist of spherical aluminum beads which are connected by thin aluminum ‘necks’, forming an elastic network. This section presents details of how the samples were created. Section 3.2.5.5 gives more detailed properties of the samples as determined from ultrasonic measurements.

3.1.1. Sample brazing

The aim of the brazing process described below is to create a solid 3D network of individual aluminum beads. In this network, adjoining beads are connected to each other by thin ‘necks’, while the spherical structure of each individual bead is preserved.

The aluminum (Al) beads are brazed together in a furnace, using silicon (Si) powder and a potassium fluoroaluminate flux called NOCOLOK¹⁰. The NOCOLOK flux enables the silicon and aluminum to form a eutectic alloy - at a temperature lower than the melting temperature of aluminum, the alloy flows between beads which are in contact, forming bonds. This brazing process has been well-covered in references (Hu 2006; Bobowski 2001; Baldantoni et al. 1994). Here I summarize the brazing technique and include details on the creation of my specific samples.

3.1.1.1. General brazing process

The oxide layer on the surfaces of the aluminum beads is removed by briefly immersing the beads in a dilute solution of sodium hydroxide. The beads are rinsed with reverse osmosis

¹⁰ NOCOLOK is a registered trademark of Alcan Aluminum Ltd (Baldantoni et al. 1994).

water, and placed into a slurry of silicon powder, NOCOLOK powder, and reverse osmosis water. The ratio of Si:NOCOLOK:Al beads was 1:2:400 by weight. By heating and stirring the aluminum beads/slurry mixture, the water is evaporated and the beads become evenly coated with a Si/NOCOLOK mixture.

The coated beads are then poured into a stainless steel mold, shown in Figure 3.1. To encourage random positioning of the beads, the mold has dimples which are randomly placed parallel to the mold bottom, and whose depth in the mold is also random¹¹ (see Figure 3.1, right, for a close-up). The bead-filled mold is placed inside an airtight stainless steel retort, which is inside a furnace. The retort is closed and sealed. The air in the retort is evacuated, after which the retort is filled with nitrogen to a pressure of 10 psi. The furnace and retort are heated to 650-655°C. The exact heating profile depends on the amount of aluminum being brazed (heating profiles for my samples are given in Appendix 3A). Nitrogen is allowed to flow out of the retort at a very slow rate throughout the heating process to maintain a slight over-pressure, and to remove some of the by-products of the brazing. At around 650°C, the NOCOLOK flux removes any oxide layer from the aluminum beads, and enables the silicon and aluminum to form a eutectic alloy. The alloy flows between beads which are in contact, forming bonds. This process takes around five to ten minutes. The furnace is then cooled back to room temperature.

¹¹ A disordered, but fairly close-packed, pattern of holes was calculated using code with the following type of strategy; first, several ‘seed’ holes are randomly-placed. Then new holes are added near each seed hole, and the program continues to add holes near (randomly selected) existing holes, until no space remains which can accommodate a new hole. Distance between holes is randomly selected from a range of typically [-1,4] mm. Each hole is assigned a depth value randomly between 0.2 and 2 mm. ‘Random’ values are determined using built-in functions of the coding language, such as IGOR’s *enoise* function. A separate pattern of disordered holes was created for each detachable piece of each mold (bottom, sides, and top). A Faculty of Science machinist then punched the holes into the flat metal mold pieces, and was able to automate the process to follow each pattern accurately.

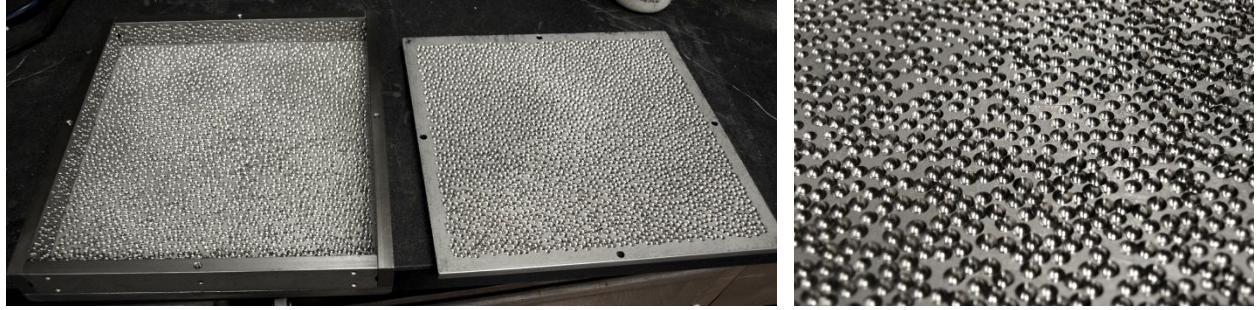


Figure 3.1: The stainless steel mold used to make samples L1 and L2, with its top (left). The side walls shown are those used for sample L1; those for L2 are taller. A close-up of the mold surface is shown on the right.

Finished samples are cleaned of any by-products of brazing by successive rinses in NaOH solution, or for small samples, by placing them in a dilute solution of NaOH in a ultrasonic cleaner.

3.1.1.2. Slab samples L1 and L2

Samples L1 and L2 are polydisperse, in order to discourage the formation of a complete band gap in the frequency region which might show Anderson localization (Lee 2014). This would be most effective with a continuous distribution of bead diameters around a mean value of $\lesssim 4$ mm. To approximate this distribution, 4.11 mm diameter Al beads were etched with hydrochloric acid (HCl) until they attained the desired size; etching time corresponds roughly to the decrease in bead size. The size distribution of beads destined for sample L1 was measured (see Section 3.1.2), and was found to correspond nicely with the above goals. Samples L1 and L2 were then brazed as described above.

3.1.2. Bead size measurement (L1 and L2)

In order to characterize the polydispersity of samples L1 and L2, the distribution of bead sizes was measured. This analysis was performed after the beads were etched, and before they were brazed together to form samples. Since the process was time-consuming, it was performed

only for beads which were then used to create sample L1; however, since etching and brazing procedures for both samples were the same, the bead size distribution should hold for both samples L1 and L2. I determined the distribution of bead sizes using the following steps:

1. Photos were taken of most of the beads which were ultimately included in the sample. For each photo, the mean radius of a few beads was measured with calipers, and this value was recorded along with their position in the picture. A graticule was included in each photo.

2. The photos were loaded into ImageJ and processed: the image was converted to binary, and the ‘watershed’ option was used to create small boundaries between particles. After calibrating the scale/units of the image using the graticule, the ‘Analyze Particles’ method was used to measure the size of every ellipse in the image at the same time.

3. For each ellipse, the measurements of major and minor radii were averaged together for an estimate of bead radius (for all beads, measured circularity was 0.9 or higher). Then all measurements from all images were combined.

Figure 3.2 shows the probability density of all measured bead diameters.

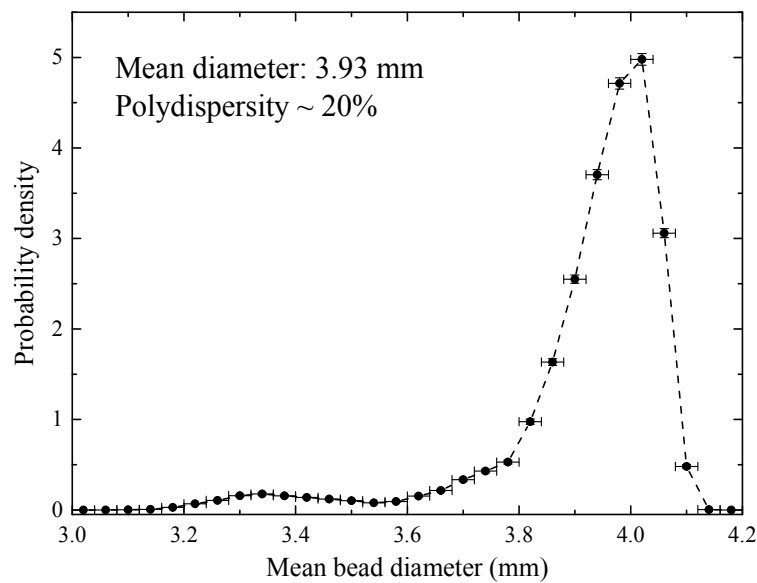


Figure 3.2: Distribution of diameters for aluminum beads comprising sample L1.

Figure 3.3 shows sample L1. Each slab sample has a cross-section of $230 \times 250 \text{ mm}^2$ which is much larger than sample thicknesses $L_1 = 25 \pm 2 \text{ mm}$ for sample L1, and $L_2 = 38 \pm 2 \text{ mm}$ for sample L2. Such a large sample ‘face’ (the broad side of a sample) is important when conducting experiments with ultrasonic arrays, as the array can be placed far away from the sample and still not ‘see’ waves which have contacted sample boundaries. A large thickness is also advantageous for reflection measurements, as the contributions from the far side of the sample are limited. Both L1 and L2 are similar to those previously studied for strong scattering phenomena, including localization (Hu et al. 2008; Hildebrand et al. 2014), but instead of being monodisperse they have a mean bead size diameter of 3.93 mm with a polydispersity of around 20%. This polydispersity encourages random positioning between beads (Figure 3.3, right).



Figure 3.3: Sample L1. Left: complete sample, slab ‘face’ shown. Right: The bead structure of sample L1. Bead neck sizes are slightly larger than those from previous monodisperse samples (Hu et al. 2008), indicating a stronger amount of brazing.

3.2. Experiments (slab samples)

3.2.1.1. Overview

Experiments performed on all slab-shaped samples consisted of sending an acoustic pulse into one sample face, and then detecting the transmitted (reflected) field that escapes the sample on the opposite (same) face. The primary goal of these measurements is the transmitted (reflected)

field as a function of time. Time $t = 0$ is defined as the time that the input pulse arrives at the sample surface. This time is often measured directly by acquiring an input signal at the position of the input sample face, and determining the arrival time of the input pulse intensity (proportional to the square of the envelope of the field). The smaller additional time shift due to propagation in water between the sample output surface and the hydrophone is also taken into account. The time before $t = 0$ is called the ‘pretrigger’ signal. Transmitted fields are acquired with a long pretrigger (see Figure 3.4) to be able to determine the background noise level due to the equipment setup:

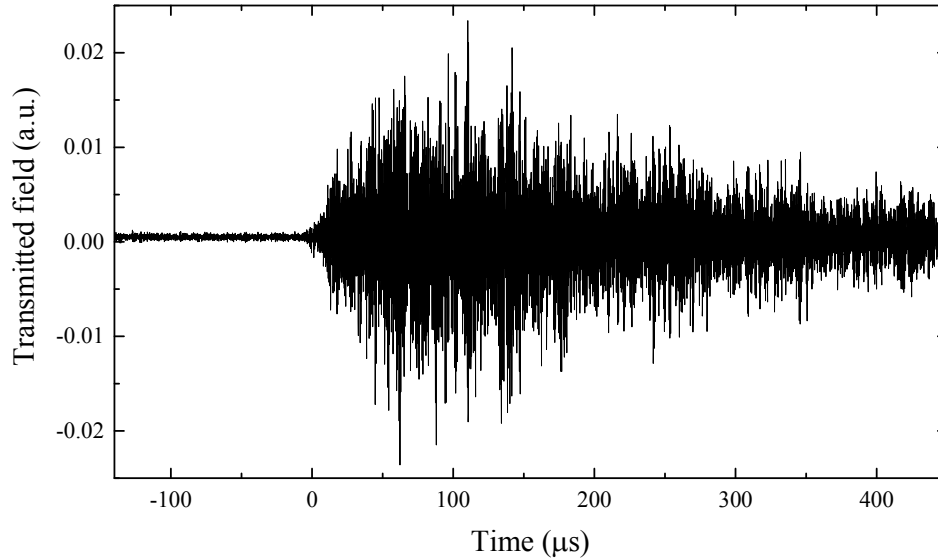


Figure 3.4: Raw transmitted field through sample L2 for $\rho = 0$ mm. Time $t = 0$ is the time that the input pulse arrives at the sample. A long pretrigger signal is acquired before $t = 0$.

To reduce the noise in the detected field, the receiving electronics for all experiments described in this section (both in transmission and reflection) are capable of repeatedly sampling the wave field. In other words, the same pulse is emitted many times very rapidly (but with the time between emissions much longer than the record length) and an average is taken over the resulting transmitted (reflected) fields. Intensity, or at least a quantity proportional to it, is

determined in the same way as for the input pulse intensity, by calculating the square of the envelope of the transmitted field. These proportionality factors are unimportant for the quantities that I examine in this thesis, so this quantity will henceforth be referred to simply as intensity.

3.2.1.2. Configurational averaging

For every experiment, configurational averaging is required due to the disorder and strong scattering nature of my samples. For my large slab samples, configurational averaging is performed in the following way; after all acquisitions for a single source point are completed, the sample is translated in the plane parallel to its face, and the acquisition sequence is repeated, with the waves propagating through a different region of the sample. Intensity is averaged over all of these different configurations, giving a more statistically accurate picture of the wave transport. For reflection measurements on strongly scattering media, it is possible to increase the number of possible array positions by, for example, flipping or rotating the sample and repeating the acquisition sequence with the array.

3.2.1.3. General experimental setup

All experiments were performed in a water tank, with the source, sample and detector immersed in water. Ultrasound is transmitted efficiently through water, and is also coupled easily between water and aluminum. In general, immersion ultrasonic transducers were used, having impedances such that ultrasound is well-coupled to water (specific properties are discussed in later sections).

The water tank setup eliminates any need for direct contact between sample and transducers, and thus avoids the variable coupling issues that contact bonds often present. The water tank used in the following experiments was made out of plexi-glass. A steel frame was built above the tank in order to mount equipment above and inside the tank. To be able to move

the sample and/or transducers around during the experiment, controllable motorized stages were placed on the metal frame.

The details of the experimental setup and method vary depending on what I expected to measure. The following sections describe the different types of experiments performed on slab-shaped samples.

3.2.2. Transmission Experiments

3.2.2.1. Ultrasonic emission and detection

For the experiments discussed below, either piezoelectric immersion transducers or miniature hydrophones (for detection only) were used to emit and receive ultrasonic fields. Piezoelectric focussing transducers made by Panametrics were used to create a good approximation of a point source. They have a field pattern sketched in Figure 3.5. In practice, the -6dB envelope can produce side lobes, and thus a cone-shaped aperture was added whenever a good point source was desired (discussed further in Section 3.2.2.3). Each transducer has a central frequency with a nominal bandwidth of $\approx 80\%$. Experimentally, it is often possible to get very good quality signal at the edges or even outside of this frequency range.

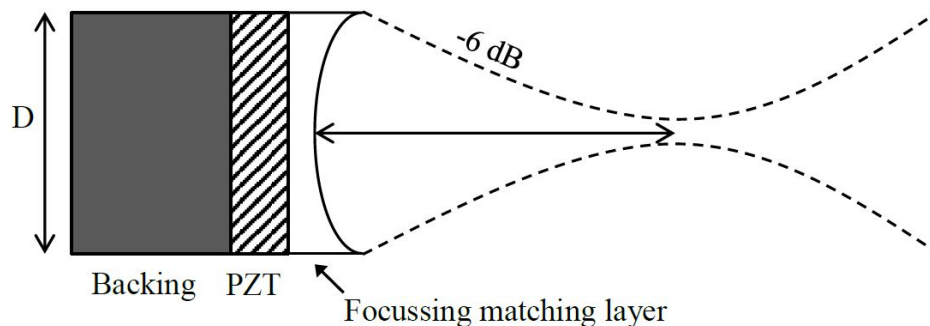


Figure 3.5: Schematic of a Panametrics focussing transducer. The position of the focal spot is different for transducers of different central frequency. Used with permission (Hildebrand 2015).

3.2.2.1.1. Miniature hydrophone detector

For point-source detection, an Onda HNC-0400 needle hydrophone was used. The piezoelectric element of the hydrophone has a diameter $\sim 400\mu\text{s}$, which is much smaller than the wavelength of sound at the frequencies which it is designed to detect. It has an approximately Gaussian angular acceptance width of $\sigma \approx 30^\circ$. It can therefore give an accurate measurement of scattered field at a certain position, and is assumed, by the theory described in this thesis, to be a perfect point-detector. There is a known finite-size effect on measurements of the dynamic transmitted intensity profile (Hu 2006), and which is negligible for all data presented in this thesis. The hydrophone has a dedicated pre-amplifier to boost the detected signal before it is sent to the receiving electronics.

3.2.2.2. Experimental Setup

In the transmission geometry, a short pulse was generated by an ultrasonic transducer on one side of the sample. On the other side of the sample either a transducer or a miniature hydrophone detected the transmitted field. The general experimental setup is presented in Figure 3.6. As various experiments were performed over an extended time period, several different electronic amplifiers and receivers were used, based on availability. Specific equipment used was:

Arbitrary Waveform Generator Model 33220A

Ritec Gated Amplifier Model GA-2500A

E&I Instruments continuous wave amplifier Model 2200L

Stanford Research Systems Pulse Generator Model DG535

Panametrics High Voltage Pulser/Receiver Model 5058PR (operating in receiver mode)

Ritec Broadband Receiver Model BR640A

Textronix Oscilloscope Model TDS5032B

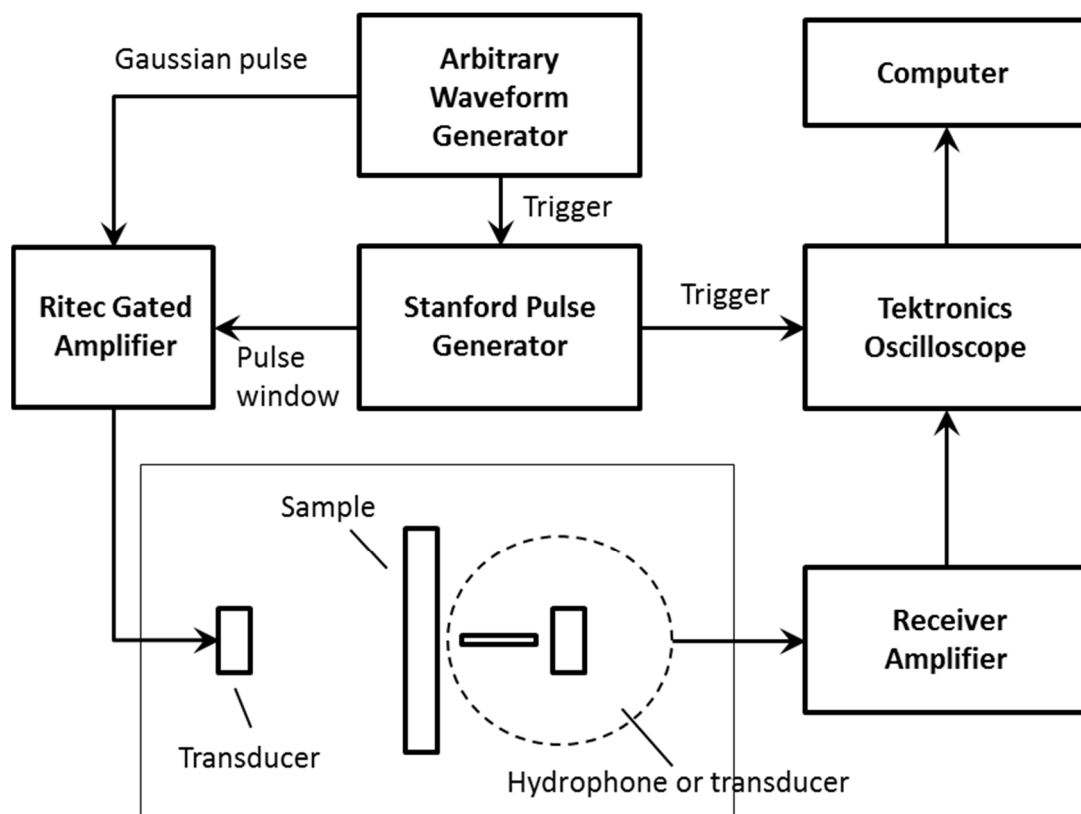


Figure 3.6: Signal path through electronics and experimental setup.

The Arbitrary Waveform Generator (AWG) sends out an electrical pulse which describes a Gaussian-modulated sinusoidal pulse. The central frequency of the pulse is chosen to exactly or nearly match that of the transmitting and receiving transducers. The pulse is then amplified by a power amplifier, and finally converted to an ultrasonic vibration by the emitting transducer. While the E&I amplifier did not require a gating input, the Ritec Gated Amplifier was used in conjunction with gating electronics as shown in Figure 3.6. The gating function of the Ritec Gated Amplifier was employed to ensure a clean, brief input pulse (i.e. eliminate any straggling signals caused by reflections from cables or amplifying electronics). The Stanford Pulse Generator was programmed to define a discrete window in time, which was sent to the Ritec amplifier and used to window the pulse, which was then output to the transducer.

On the other side of the sample, either a miniature hydrophone with a preamplifier or a

transducer was used to detect the transmitted acoustic field and to convert it into an electrical signal. This signal was amplified by the Receiver, and then recorded by the oscilloscope. A personal computer captured and saved the data from the oscilloscope. This computer was also used to command the motorized stage controllers to move the sample and the transducers/hydrophone.

3.2.2.2.1. Sample holder, waterproofing and vacuum setup

For all transmission experiments, I constructed a holder for each sample. At the top of each support, a steel rod was attached which in turn attached to the motorized stage running above the water tank. The holder could be sealed water-tight with the sample inside, enabling the air in the pores of the sample to be evacuated. The sample remained under low pressure relative to atmosphere (around 20-25 inHg below atmospheric pressure) for the entirety of the experiment to ensure that sound was only propagating through the aluminum bead structure. The main component of each holder was an acrylic support made by the Faculty of Science machinist, either rectangular or ring-shaped depending on the shape of the sample into which the sample was placed. The sample was secured in the support with a thin layer of silicone or acrylic (the type used for household sealing purposes). To enable the air surrounding the sample to be evacuated using a conventional vacuum pump, I used one of two methods:

1. 'Gluing method': Thin plastic sheets were glued to either side of the acrylic support, with the sample sandwiched in between. Air was vacuumed from between the sheets via a small hole running through the edge of the acrylic, connected by a thin tube to a vacuum chamber and pressure gauge.

2. 'Bag method': The sample was placed into a bag which I constructed out of a type of plastic commonly used to keep food under vacuum. Air was removed from this bag via a thin

tube at one end of the bag, carefully sealed against air and water leakage. The sample and bag were then placed into the acrylic support .

I developed this second method of vacuum-sealing the samples because the gluing stage of the first method is difficult and time-consuming. For both methods, a very thin layer of vacuum grease was applied between the plastic walls and sample surface to help couple sound through the plastic layer.

To evacuate the air from a sample and to keep it at low pressure, it was connected via poly-flo tubing to a vacuum pump and ballast apparatus as shown in Figure 3.7. First, the vacuum pump is used to place the ballast (a large empty drum) under reduced pressure, to between 20-25 inHg below atmospheric pressure. The pump is then turned off. When completely closed, the ballast is able to remain at the same stable pressure for weeks at a time. The valve between the ballast and sample is then slowly opened, so that all of the air was evacuated from the sample, and the sample eventually comes to be the same pressure as the ballast. A sample sealed in its holder can remain close to the same stable pressure, connected to the ballast, for the entirety of an experiment (sometimes several weeks). While an experiment is running, the sample and ballast setup is checked every day for any rise in pressure, and vacuumed out slightly if needed.

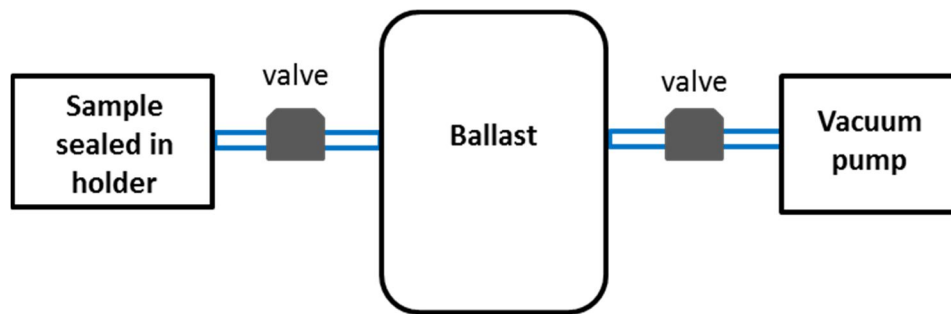


Figure 3.7: Simple sketch of the vacuum, ballast and sample setup. The valve between the sample and ballast remains open for the duration of an experiment, enabling the sample to remain at a stable reduced pressure.

3.2.2.2.2. Extraneous reflection elimination (baffles)

Some of the transmission measurements performed are sensitive to very small transmitted signals, which may arrive long after the initial pulse has been sent. Thus, it is important to eliminate the possibility of sound arriving at the receiver via any path except through the sample. To this end, a baffle was constructed to block any sound propagating through the tank between source and receiver. The baffle is a thin sheet of flexible plastic, wrapped in several layers of Teflon tape, placed in the center of the tank (shown in Figure 3.9 and Figure 3.10). A hole in the center of the baffle allows sound to pass, and this is where the sample is placed, ideally completely covering the hole. When placing the baffle in the tank before an experiment, I tested it by blocking the hole (with another plastic piece wrapped in Teflon tape) and sending a pulse into the tank with the emitting transducer. The receiver was moved around the tank attempting to detect any signals transmitted through or around the baffle.

During the actual experiment, there is the possibility of sound coming around the edges of the sample or through the acrylic support. This possibility is very small for samples L1 and L2, since they are wide enough to block the baffle hole completely, and I placed them in the tank such that the sample surface makes firm contact with the baffle itself. However, to be safe, I attached thin ‘wings’ to the edges of the acrylic support, and covered them and the support with Teflon tape, to trap and absorb any stray signals. Figure 3.8 shows sample L2 in various stages of experimental setup.

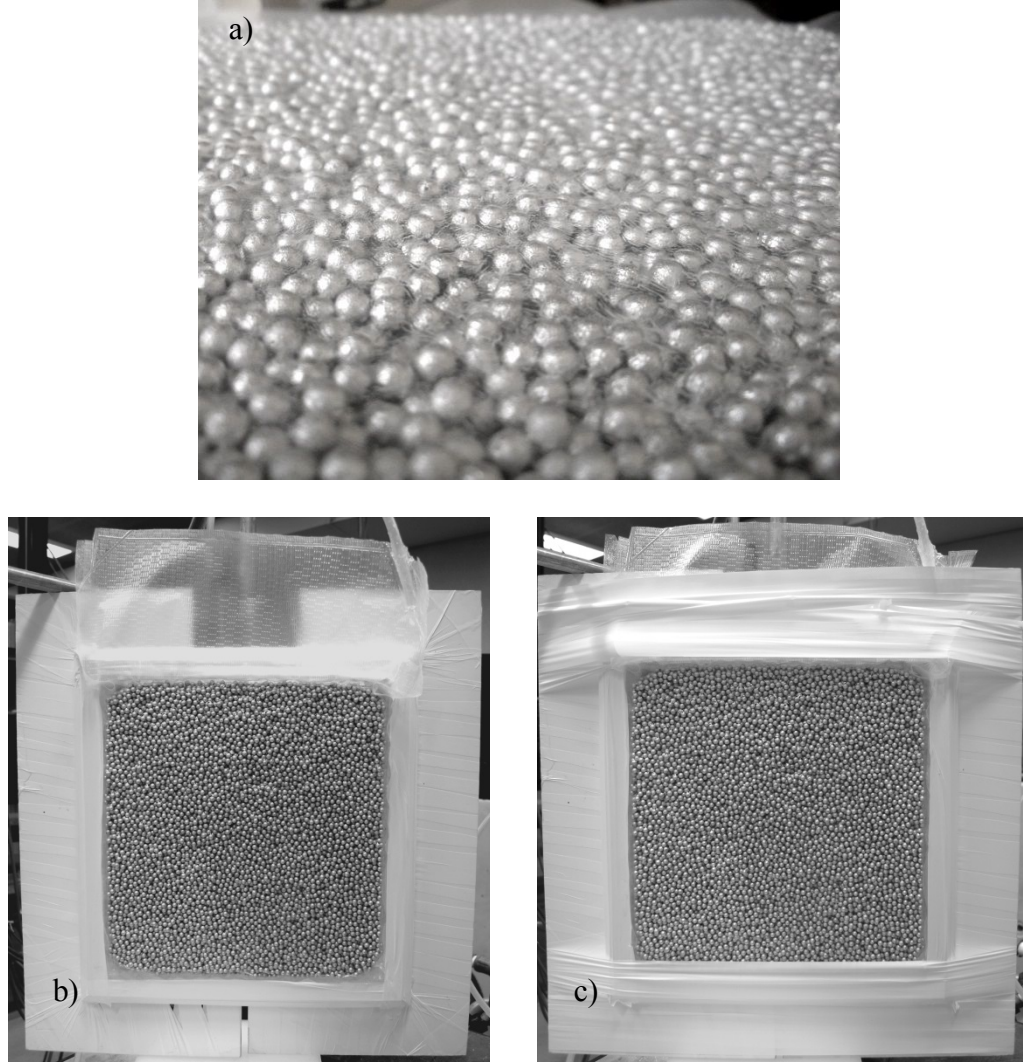


Figure 3.8: Sample L2 in preparation for a water tank experiment. (a) Close-up of the sample surface when sealed in a plastic bag. There is a thin layer of vacuum grease between the plastic and the sample surface, and air has been evacuated from the bag. (b,c) The sample in its holder, with ‘wings’ attached to the holder sides. The top of the plastic bag extends upwards above the sample. (b) The poly-flo tube that is connected to the vacuum-ballast setup is visible in the top right corner. (c) The entire sample/holder is then wrapped in Teflon tape.

3.2.2.3. Measurement Techniques and Geometries

This section describes the transmission experiments that I performed on my slab-shaped samples using a quasi-point-like source and detector. For most experiments discussed in this thesis, the desired measurement is configurationally-averaged intensity. Thus, the source and

detector must be small (quasi-point-like) so that the spatial averaging is only performed *after* intensity is calculated from the acquired field. The goal when setting up the experiment is to have both source and detector are approximately point-like, and positioned in the near-field of the sample.

For the source, a focusing ultrasonic transducer is positioned in the tank, separated from the sample by approximately the focal length of the transducer. A cone made of thin plastic, wrapped in Teflon tape, is positioned very close to the sample surface (in the near-field, approximately 2 mm away) to help couple the focussed sound into the sample at only a small spot. The cone is connected to the transducer via rigid plastic rods and a flat bar, as shown in Figure 3.9. By making slight adjustments to how the rods are connected to the plastic bar, the relative positioning of the transducer and the cone may be changed. This enables the alignment of the transducer and the cone on dry land. The apparatus is positioned with the cone pointing upwards, and a plumb line is hung through the hole in the cone tip to the transducer face. The apparatus is aligned when the plumb line points exactly in the middle of the transducer face. By performing this alignment before placing the apparatus in the tank, a very tight and bright focal spot may be achieved.

A miniature sub-wavelength hydrophone is used for detection. In my experiments, the hydrophone tip is positioned as close as possible to the sample without contacting it, approximately 2-3 mm away in the near-field (Figure 3.10).

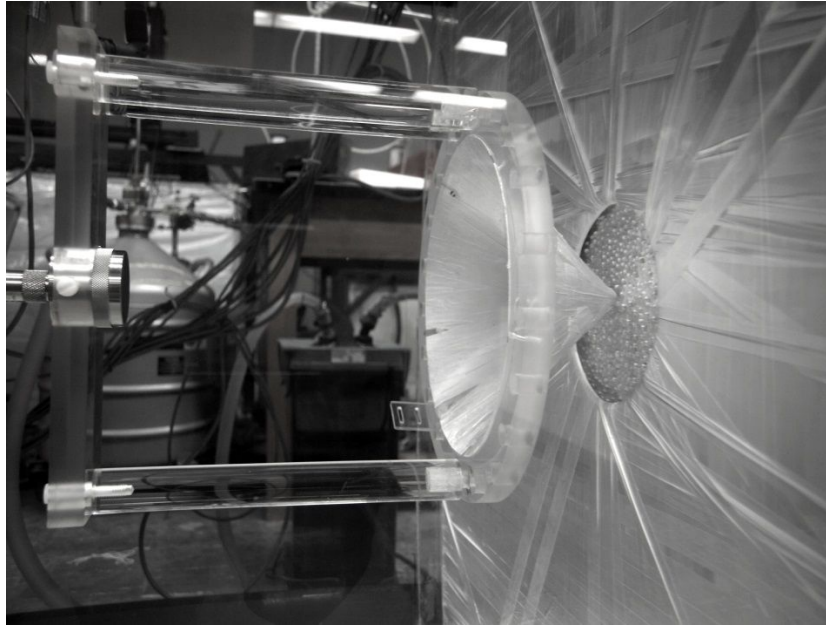


Figure 3.9: The emission transducer (left) is attached to the cone by acrylic rods. The cone tip is a few millimetres from the sample input surface. The sample face is on the opposite side of the baffle; some of the sample face is visible through the hole in the baffle.

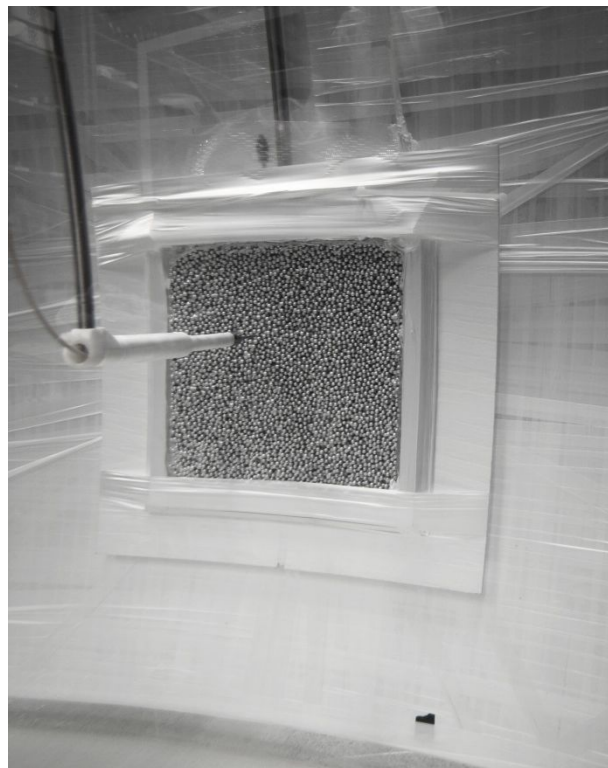


Figure 3.10: The sample and sample holder are flush against the baffle. The hydrophone tip is positioned millimeters away from the sample output surface. In this photograph the baffle is the large white surface covering most of the image background.

For all quasi-point-source experiments, the source is kept stationary and the hydrophone detector scans the opposite face of the sample in the near field. The transmitted intensity as a function of transverse distance from the source, ρ is measured. I performed two types of point-source experiments, which differed from each other only in the number and spacing of detector positions: a) the dynamic transverse intensity profile, introduced in Section 4.3.1.1, and b) ‘field maps’, introduced in Section 7.3.1.

3.2.2.4. Source characterization

To complete the analysis of this data as described in Sections 4.3.1.1 and 7.4, a map of the source must be acquired. The sample is simply removed and the hydrophone moved closer to the source so that it is in the plane previously occupied by the input face of the sample. By scanning the hydrophone in a grid, and recording the wavefield over many positions on this grid, a map of the source spot or plane wave is acquired.

3.2.3. Reflection Experiments

3.2.3.1. Experimental Setup

In the reflection geometry, an ultrasonic array was used to send short pulses into the sample, and detect the signal which is reflected and/or backscattered from the same side of the sample. An ultrasonic array is a collection of small transducer elements which can each emit and receive wavefields independently of the other elements.

The experimental setup is shown in Figure 3.11.

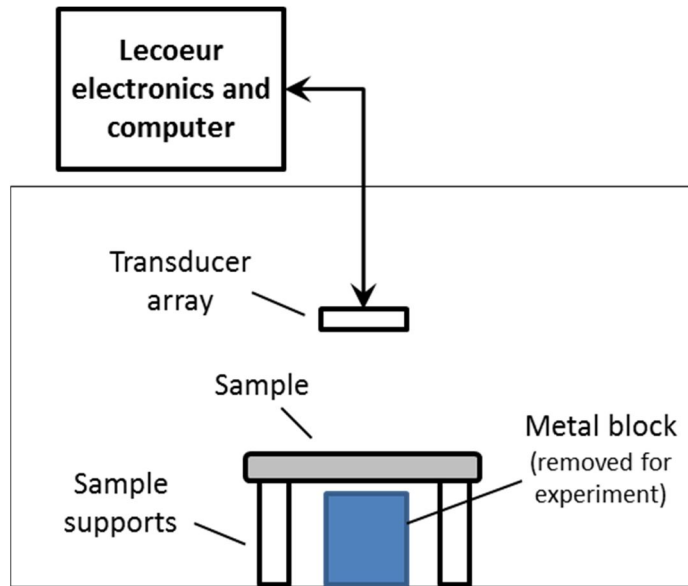


Figure 3.11: Experimental setup for reflection measurements with an ultrasonic array. The array is suspended in the tank by a metal rod attached to the motorized stage. The sample is supported by acrylic blocks (shown in white). The metal block is used to test for reflections between the sample and the tank bottom, and is removed before the actual experiment is started.

All pulse generation, amplification, and data acquisition for ultrasonic arrays is carried out by a dedicated multi-channel electronics system (produced by Lecoeur Electronique). The system has a separate digital channel for each array element, and can amplify signals through each of these channels in both transmission and reception. A personal computer controls and saves data acquired by the electronics. The computer also controls the motorized stages above the tank to move the transducer array around in the tank.

For setup simplicity, reflection measurements were conducted with the array pointing downwards at the sample. The sample rests on two or more supports with one of its wide faces parallel to the bottom of the tank. The array is translated parallel to the sample face to record backscattered signal from different spots on the sample surface. For some experiments, additional configuration averaging was achieved by flipping the sample so that the sample face initially facing the tank bottom now faces the array, and repeating the experiment.

It is conceivable that unwanted contributions to backscattered field could arise from the signal travelling through the sample, reflecting off either a sample support or the tank bottom, and travelling back through the sample. A test for this effect was carried out during the setup before each experiment. A block of metal was placed under the sample, on the bottom of the tank, with its top very close to or touching the bottom sample face (Figure 3.11). The array was used to record backscattered field from the sample with and without this block, with a large amount of averaging, and the signals compared. The block was never detectable using this method, but was always removed anyway before the start of each experiment; waves reflected from the tank bottom and back into the sample arrive later and would be weaker than waves reflecting from a block very near to the bottom sample surface.

3.2.3.2. Ultrasonic array specifications

Reflection measurements on samples L1 and L2 were performed at either the Institut Langevin in Paris, France, or at the Ultrasonics Laboratory in Winnipeg, Manitoba. Like single-element transducers, each ultrasonic array emits a pulse centered at a certain characteristic frequency, so different arrays were used order to gather data over a wide frequency range. Table 3.1 contains the main parameters of each reflection experiment discussed in this thesis. Besides the experiments performed on samples L1 and L2, additional measurements were carried out on two other samples: ‘H4’, an aluminum-sintered slab sample with a disc-shaped face, which, like those studied by Hu et al. (Hu et al. 2008; Hu 2006), has previously shown signatures of localization of ultrasound, and ‘GB’, a sample of (unsintered) glass beads, which are known to show only diffusion of ultrasound. Results from these experiments are not reported in this thesis, as it was found that the sample faces were not wide enough to make edge effects insignificant (this issue is discussed further in Section 3.2.3.4).

Sample	Sample-array separation (mm)	Number of array positions	Central frequency of transducer array (MHz)	Number of elements used	Laboratory in which experiment was performed
L1	146	91	3.2	64	Institut Langevin
L2	187	117			
Glass	84.5	50			
L1	182	302	1.6	64	Institut Langevin
H4	67	40			
L2	136	66	1.0	128	Ultrasonics Laboratory

Table 3.1: Details on setups for reflection experiments. Note that the arrays at the Institut Langevin actually had 128 elements, but the number of elements used was 64 because only 64 channels of the Lecoeur electronics system were operating correctly.

All arrays used were manufactured by Imasonic. Table 3.2 contains important specifications of each array used for reflection experiments. Note that, similarly to the transducers used in transmission, good signals are possible at the edges and outside of the -6dB bandwidth, especially at the low-frequency end. Notably, the 1.5 MHz array displayed excellent signal (and at least $\text{SNR} > 4$) all the way down to 0.6 MHz (c.f. Figure 3.25).

Central freq. (MHz)	Bandwidth (-6dB) (MHz)	Number of elements	Pitch (mm)	Inter-element separation (mm)	Element height (mm)	Homogeneity in sensitivity (\pm dB)	Cross-talk (dB)
3.2	2 - 3.8	64	0.417	0.03	10		
1.5	1.2 - 1.9	128	0.5	0.25	12	3	Nominal: ≤ -35 Experimental: ≈ -45.9
1.0	0.7 - 1.4	128	0.9	0.35	15	3	≤ -35

Table 3.2: Details on ultrasonic arrays used in reflection experiments. Pitch refers to the center-to-center distance of individual elements. Unknown values are left blank. The nominal central frequency of the 1.6 MHz array was 1.5 MHz, according to Imasonic, but testing in the laboratory showed it to be closer to 1.6 MHz. The experimentally-determined bandwidth of this array also greatly exceeded that given by the manufacturer (see text).

3.2.3.3. Measurement Techniques and Geometries

What is essentially desired in my reflection experiments is a measure of backscattered field as a function of time, and of distance between source and receiver. To acquire this information the experimental procedure technique shown in Figure 3.12 is employed. A short pulse is emitted by the first element in the array, and the backscattered field is detected with all N elements. Then the same pulse is emitted by the second element, and the backscattered field recorded with all N elements. This sequence is repeated, emitting with all N elements in turn. The data acquired in this way forms an $N \times N$ *response matrix*, which represents the wavefield responses between each emitter and detector. The response matrix holds a huge amount of information about the medium, and in particular about wave behaviour inside the medium. It is a powerful tool with which to perform analyses such as, for example, beamforming (Aubry et al. 2007; Aubry and Derode 2007). Simply by changing the relative delay times between sources and emitters, and then summing wavefields, an image of the material's surface may be produced just as if focused beamforming had been done in real time.

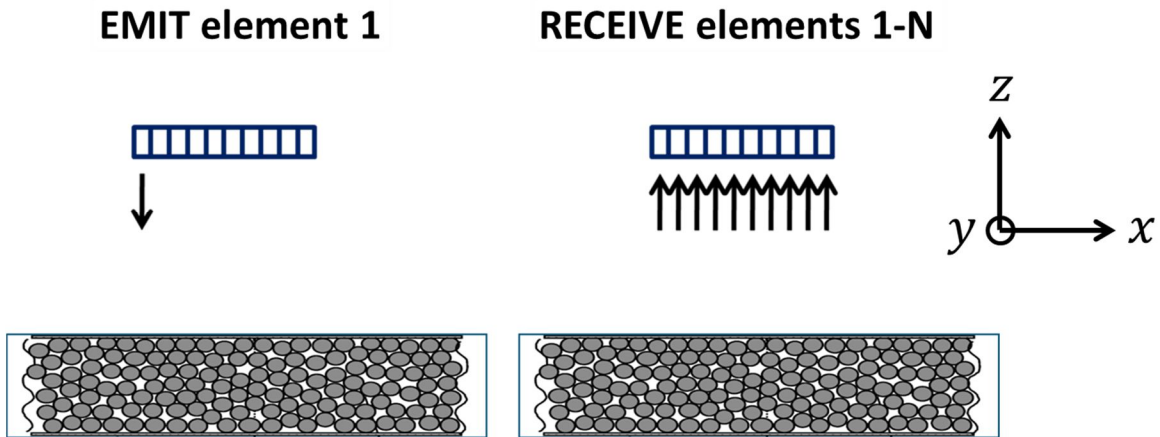


Figure 3.12: First step of acquisition sequence for an ultrasonic array of N elements. To complete the sequence, this step is repeated but with element 2 emitting, then element 3... up to element N .

The response matrix should reflect the properties of the medium under investigation, and not be unduly influenced by the properties of the measurement apparatus. Each experiment presents its own set of setup challenges, mainly due to the properties of the array and associated electronics, the desired length of time to be recorded, and the desired amount of configurational averaging. The most significant of these challenges, and their solutions in the context of my experiments, are discussed in the following sections (3.2.3.4 - 3.2.3.7.2).

3.2.3.4. Long-time signals vs configurational averaging

A main goal of my reflection experiments is to measure time-dependent quantities such as the dynamic coherent backscattering effect, and to observe wave scattering behaviour at as late times as possible. Besides signal-to-noise issues (discussed later), the limiting factor in recording long times in reflection is the separation between source and sample. Waves that are reflected from the sample surface, travel back to the array, are reflected off of the array and then travel back to the sample can interfere with those waves that are already scattering around inside the sample. By convention, we set time $t = 0$ to be the time it takes a pulse to travel twice the sample-array distance (the first arrival time of reflected signals at the transducer array). Thus, the longest possible time that should be used for analysis is $t' = 2d$, where d is the sample-array distance. By placing the array far from the sample, longer times may be investigated. However, this goal conflicts with the aim of minimizing the amount of signal from the edges of the sample that is seen by the array. Ideally, the only backscattered signal we would like to record is that which has not interacted with the edges of the sample, and so the array should be kept nearer to the center of the sample. In principle it is unlikely that no signal coming from the sample sides will be recorded by the array, especially the outer array elements, but these effects are probably negligible if they are very weak compared to the signal coming from the center of the sample.

In summary, there is something of a trade-off between long-time acquisition and amount of independent array positions (i.e. amount of configurational averaging).

3.2.3.5. Alignment

It is important that the ultrasonic array be parallel to the sample surface, in both x and y dimensions (where z is the plane running through both array and sample face, as indicated in Figure 3.12). During experimental setup, alignment of the array was performed by hand, by making slight adjustments to the position of the array in the array holder, and observing reflected signals from some flat surface. Alignment in the direction of the height of each element (parallel to y in Figure 3.12) was performed by adjusting the array until the largest reflected signal is achieved. Alignment along the length of the array (parallel to x in Figure 3.12), to ensure that each element is equidistant from the reflecting surface, is achieved by ensuring that reflected signals from the flat surface arrive at the same time for all elements. For a well-aligned array, a signal sent and received by the first element should have the exact same travel time as one sent and received by the last element¹².

3.2.3.6. Calibration

During an experiment, each array element is connected to one channel of the Lecoer electronics system. Thus, for clarity in the following discussion, we will call a system of one array element coupled to its dedicated electronic channel *one channel* of the experimental

¹² Often, misalignment along x may be corrected for in post-processing, by correcting the relative delay times between source and receivers so that the first reflected signals arrive at the same time. However, since the surfaces of my samples are rather bumpy, the specular signal differs slightly in phase and amplitude depending on the spot on the surface from which waves were reflected, and it is often not easily discerned from other backscattered signals. This means that the alignment of sample and array is especially important during the setup of the experiment, as it can not be perfectly corrected in post-processing.

measurement system.

Ideally, each channel sends and receives signals in exactly the same way. If, for example, a uniform plane wave is detected by the array, the recorded signal from a particular channel should be the same as from each other one. One way to observe this effect is by looking at the reciprocity of the measured response matrix. If the system obeys reciprocity, and if all channels are behaving in exactly the same way, then the signal sent from, for example, channel 1 to 64 should be exactly the same as that sent from channel 64 to channel 1.

My scattering samples L1 and L2 are reciprocal systems as described in Section 2.3. The response matrices measured in experiments at the Institut Langevin show remarkably good reciprocity, indicating that each channel was behaving very similarly in both emission and reception. As Figure 3.13 shows, even between the farthest-separated array elements, and through the strongly-scattering sample L1, reciprocity is well-obeyed for this system. Note that no calibration of the system, other than the built-in internal calibration of the Lecoeur electronics system, was performed during experimental setup.

At the time that I performed my experiments, the reciprocity of the array/electronics apparatus used at the Ultrasonics Laboratory was not as good. Figure 3.14 shows backscattered signals from a flat aluminum sheet, measured at the Ultrasonics Laboratory. Here, calibration in emission has been applied (see below for details), but not in reception. The sheet was used to illustrate that the non-reciprocal nature of the signals was due almost entirely to the array/electronics system. There is no phase shift between reciprocal signals, which is good. Between elements that are close together, reciprocal signals are similar (left plot), but there is a systematic amplitude difference noticeable. Between elements that are farther from each other (right plot), there is a huge difference in amplitude between reciprocal signals. The inset of each

plot shows the attempt to correct for these differences, before performing the actual experiment. Results are not perfect, but do bring reciprocal signals much closer together. The procedure for applying this correction, or calibration of measurement apparatus, is outlined below.

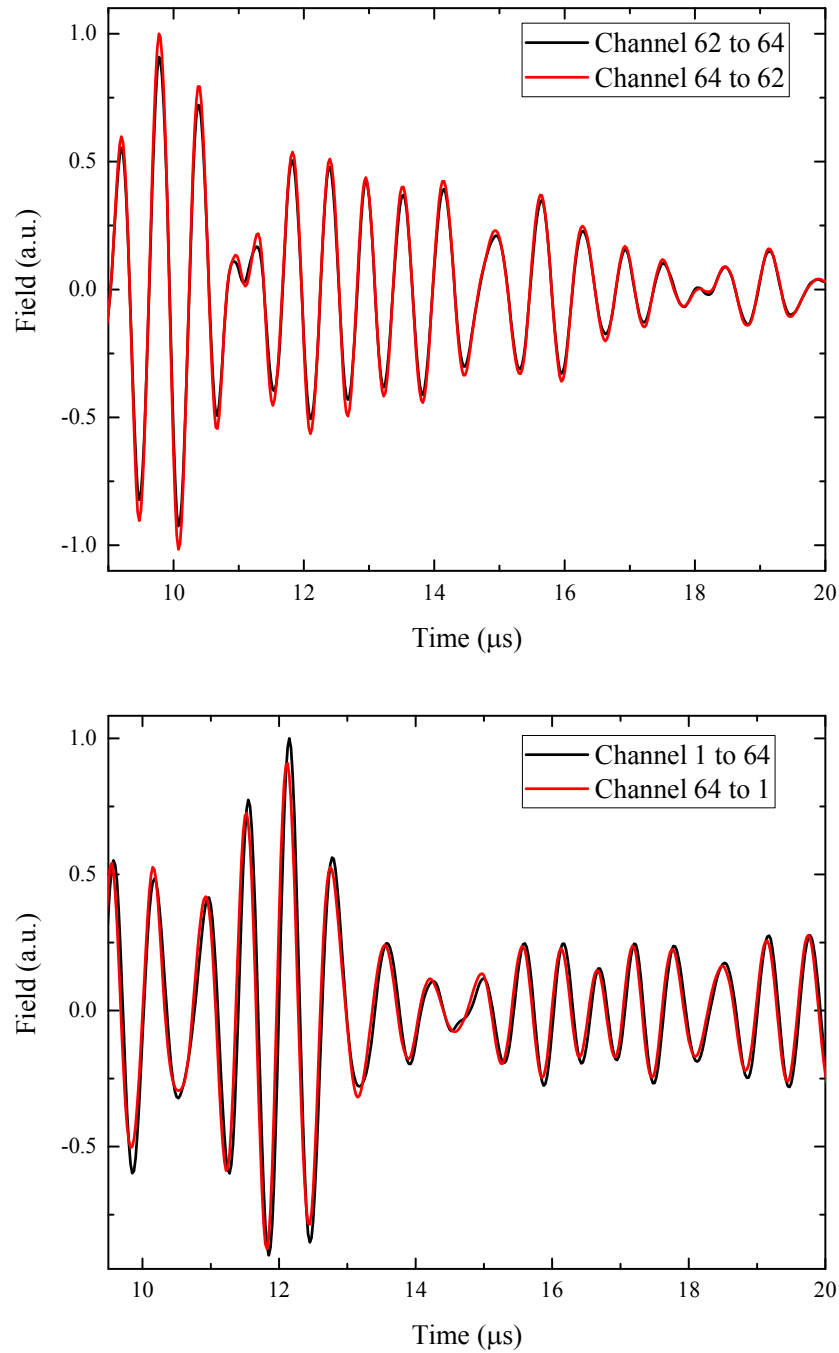


Figure 3.13: Backscattered field signals from sample L1, measured with array and electronics at the Institut Langevin.

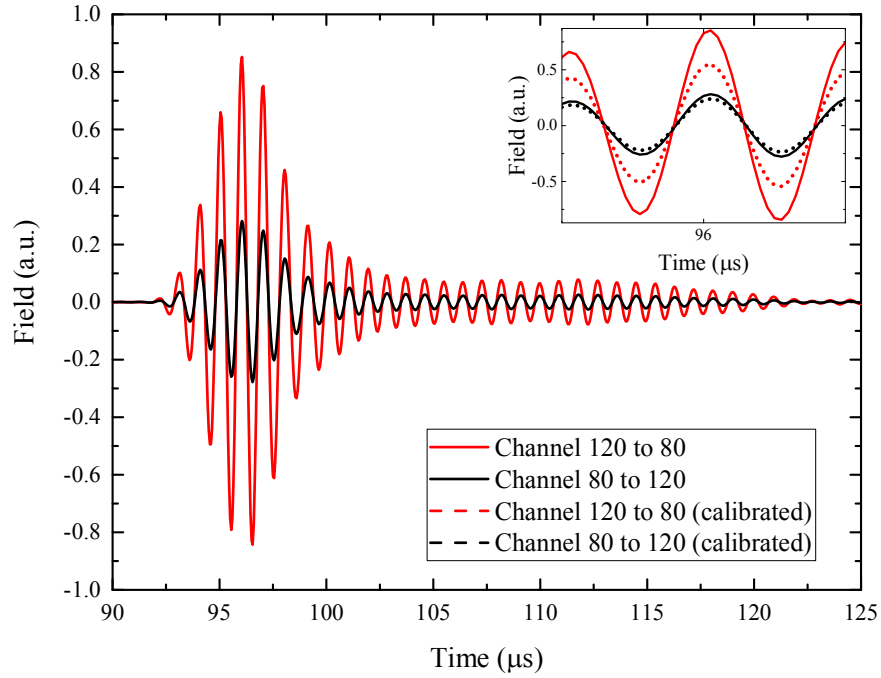
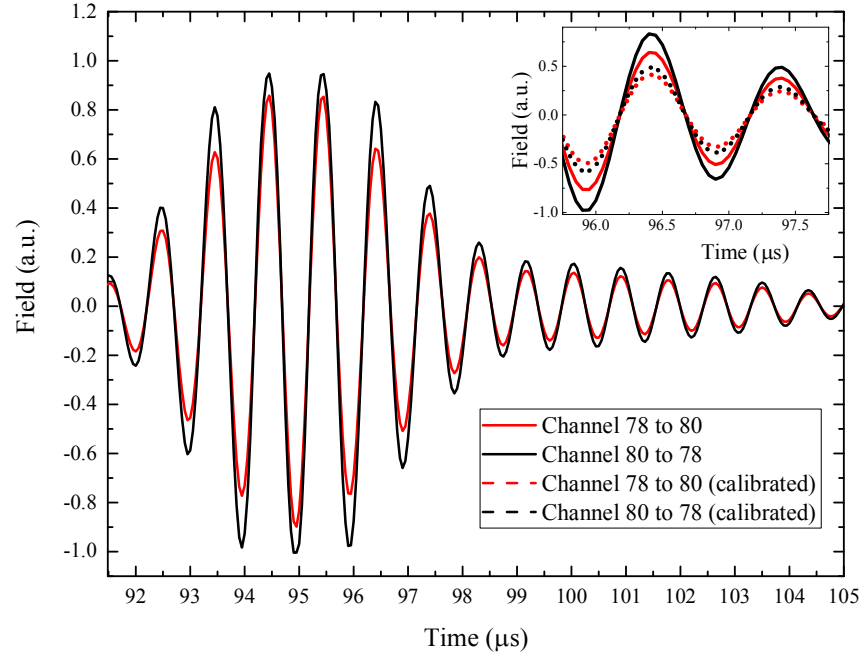


Figure 3.14: Backscattered field signals from a flat aluminum sheet, measured at the Ultrasonics Laboratory. Solid lines represent signals which have been corrected in emission to account for the non-reciprocity of this measurement system, but not in reception. Dotted lines in insets represent signals which have been corrected in reception (via calibration 'masks').

Calibration must always be performed for the array and Lecoeur electronics apparatus together rather than separately. If the array is disconnected from the electronics and then connected again, or even if the initialization of the electronics is performed again, the amplitude differences in reception and emission from element-to-element change completely, in a seemingly random way. Also, which elements are ‘bad’ (emit/receive disproportionately noisily) changes. These ‘bad’ elements are detected in post-processing, and their contributions are not used in subsequent analysis.

After the array is positioned in the water tank as shown in Figure 3.11, the array/electronics system is calibrated using the following steps:

Calibration in reception: with the goal that each channel records the same pulse with the same amplitude.

- Set up a single transducer in approximately the same area as the sample will be placed during the experiment, facing up (facing the array). The transducer emits a single pulse centered at the central frequency of the array (connected to a single channel of the Lecoeur electronics).
- The array begins with its first element centered over the transducer. That first element records the pulse from the transducer. The array is translated parallel to the transducer a distance equal to the inter-element distance of the array, so that the second element is centered over the transducer, in the exact position that the first element was.
- The second element records the pulse from the transducer.
- The process is repeated until each array element has recorded, in principle, the exact same pulse.

- A ‘mask’ to correct for differences in amplitude between signals is constructed. To apply this reception calibration, all experimental data should be multiplied by these correction factors (one for each channel) in post-processing.

Calibration in emission: with the goal that, when each channel is directed to emit the same pulse, the actual pulses that are physically emitted have the same amplitude.

- Replace the single transducer with some flat reflecting surface. It is easy and convenient for later setup steps to put the sample in place now, with some kind of hard reflecting sheet (I used aluminum) laid over top of it.
- Emit and receive with each individual element (emit with 1, receive with 1, then emit with 2, receive with 2, etc.).
- Apply the reception calibration mask to recorded signals appropriately. Any differences in recorded amplitude should be, in principle, due to differences in the operation of the array/electronics in emission only.
- A ‘mask’ to correct for differences in amplitude between signals is constructed. To apply this emission calibration, the pulses to be emitted are defined in matlab and then multiplied by these correction factors (one for each channel). Then these corrected pulses are sent to the Lecoeur electronics to be emitted by the array¹³.

As well as being closer in amplitude as shown for some examples in Figure 3.14, the overall backscattered wave field appears smoother and has less variations across different channels. Backscattered intensity measured at the Ultrasonics Laboratory is shown in, for both pre- and post-calibration in reception. The initial pulse was emitted by channel 64 (in the center

¹³ Another, possibly better, way to perform this calibration could be to iteratively change the amplitude of the pulse sent to a particular channel until the emitted pulse has the desired amplitude, and then repeat this for each channel.

of the 128-element array).

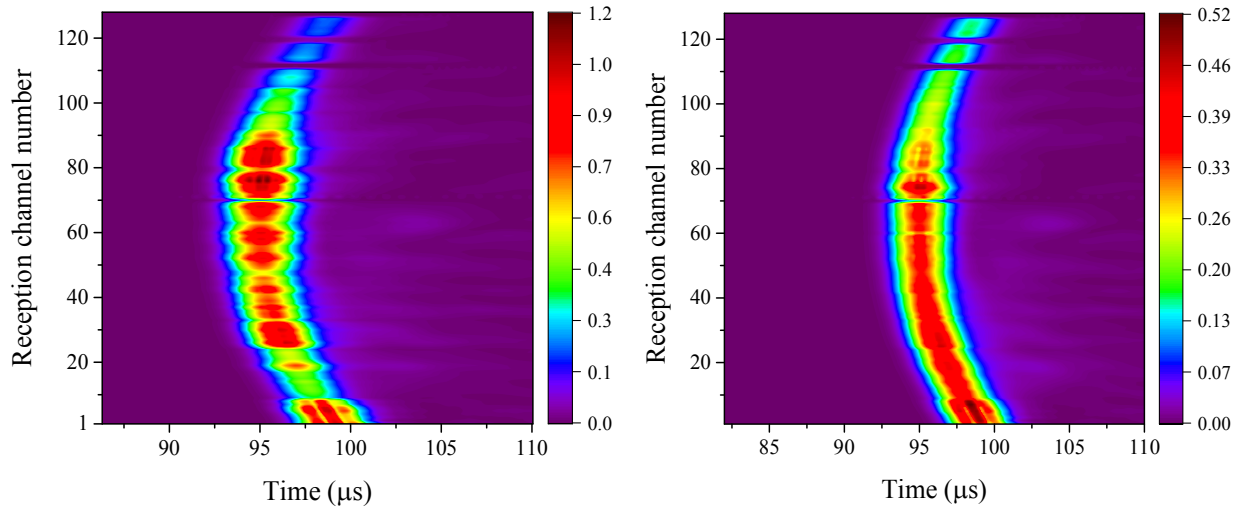


Figure 3.15: Reflected intensity from a flat aluminum sheet, measured at the Ultrasonics Laboratory. The initial pulse was sent from channel 64, with emission calibration applied. Left: reception calibration has not been applied. Right: reception calibration has been applied.

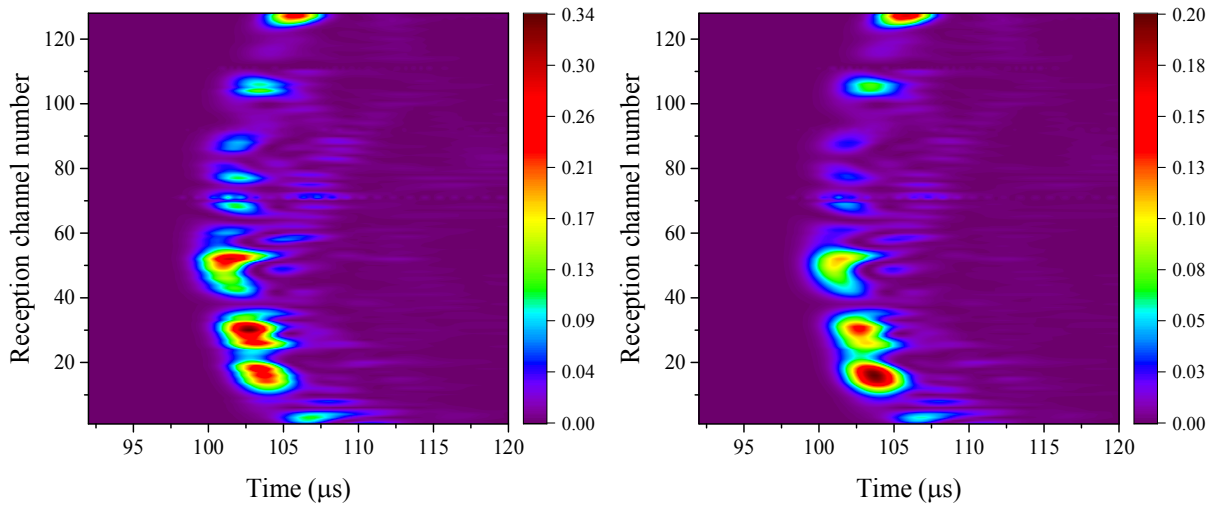


Figure 3.16: Backscattered intensity from sample L2, measured at the Ultrasonics Laboratory. The initial pulse was sent from channel 64, with emission calibration applied. Left: reception calibration has not been applied. Right: reception calibration has been applied.

Although the resulting signals after calibration still exhibit some irregularity (Figure 3.15), this was the best that could be done at the time, and did result in cleaner data. It is important to

note that the less-than-ideal reciprocity of this system should not have an important impact on the experimental results presented in this thesis (i.e. the backscattering results for sample L2). This is because the desired measurements are quantities of averaged intensity. The large amount of spatial and configurational averaging involved should compensate for the asymmetry caused by imperfect functioning of the array system described above. However, this raw experimental data is less appropriate for other potential analyses that are very sensitive to differences in each detected field, such as correlations (e.g. Hildebrand et al. 2014; Knothe and Wellens 2015).

3.2.3.7. Data acquisition techniques and details

3.2.3.7.1. Signal-to-noise issues

To measure backscattered field at long times after the initial pulse was input to the sample, a good signal-to-noise (SNR) ratio is needed. Here I define ‘good’ SNR as having $|\varphi_{\text{signal}}(t)|/|\varphi_{\text{noise}}(t)| \geq 4$. To improve SNR, averaging is performed so that for N successive averages the noise is reduced by \sqrt{N} assuming that noise is uncorrelated from one acquisition to the next. However, this operation also increases the acquisition time per emission (and N accompanying acquisitions) by a factor of N .

At the Institut Langevin, onboard averaging was not enabled for the Lecoeur system, meaning that multiple averaging had to be performed ‘manually’, by recording many signals and averaging them with the personal computer. This process takes much more time than would internal averaging by the Lecoeur system (or by an oscilloscope, as is done with transmission measurements), and can greatly increase the total time of an experiment. Already, experiments may take up to several weeks, so methods to decrease the experimental running time are needed.

The next section details one such method, called the Hadamard method (Lingevitch 2002). This technique was introduced to me at the Institut Langevin, and was used for the

backscattering experiment with sample L1 centered at 1.6 MHz (Dec 17, 2010). I did not use it for the subsequent experiment on L2 (Oct. 30, 2013), as I found that the onboard averaging was just as fast as using the Hadamard method, and does not rely on the linearity of array elements.

3.2.3.7.1.1. The Hadamard method

The idea behind this technique is that instead of acquiring the response matrix ‘directly’ as outlined in Section 3.2.3.3, the acquisition can be performed ‘indirectly’ by the emission of a more complicated form, from all array elements. The following explanation is a summary of the technique¹⁴:

The Hadamard matrix is a square matrix composed of vectors which are all orthogonal with each other, and has all coefficients equal to ± 1 . Thus, its row (or column) vectors obey

$$\sum_{j=1}^N \mathbf{E}_{ij} \mathbf{E}_{kj} = N \delta_{i,k} \quad (3.1)$$

where \mathbf{E}_i is the i th vector ($n = 1 \dots N$) of the Hadamard base. This property may be exploited to improve SNR in the following way; instead of the normal ‘direct’ method of emission and reception (outlined in previous sections), the vectors \mathbf{E}_i of a Hadamard matrix are emitted one after another from the entire array:

Emission 1: \mathbf{E}_1 is emitted with all N elements participating simultaneously, each with a weight coefficient of \mathbf{E}_{1j} ($j = 1 \dots N$). The received signal on element n is therefore $\sum_{j=1}^N \mathbf{E}_{1j} \mathbf{K}_{nj}(t)$, where $n = 1 \dots N$.

Emission 2: \mathbf{E}_2 is emitted with all N elements participating simultaneously, each with a weight coefficient of \mathbf{E}_{2j} ($j = 1 \dots N$). The received signal on element n is therefore $\sum_{j=1}^N \mathbf{E}_{2j} \mathbf{K}_{nj}(t)$, where $n = 1 \dots N$.

¹⁴ This is a summary of a personal communication with Arnaud Derode.

Etc. The N^2 received signals $\mathbf{M}_{ni}(t)$ can therefore be expressed as $\mathbf{M}_{ni}(t) = \sum_{j=1}^N \mathbf{E}_{ij} \mathbf{K}_{nj}(t)$ or, in matrix notation,

$$\mathbf{M} = \mathbf{K} \mathbf{E}^T \quad (3.2)$$

where i denotes the emission element, and n the reception element. It is simple to recover the signal matrix (i.e. the response matrix) \mathbf{K} , due to the orthogonality of the Hadamard vectors. For example, to obtain the signal received by element n if the element p had emitted by itself, we write $\mathbf{K}_{np}(t) = \sum_i \sum_j \mathbf{E}_{ip} \mathbf{E}_{ij} \mathbf{K}_{nj}(t) = \frac{1}{N} \sum_i \mathbf{K}_{nj}(t) \sum_j \mathbf{E}_{ij}^T \mathbf{E}_{ip}$ or, in matrix notation (and substituting in Equation (3.2)),

$$\mathbf{K} = \frac{1}{N} \mathbf{K} \mathbf{E}^T \mathbf{E} = \frac{1}{N} \mathbf{M} \mathbf{E} . \quad (3.3)$$

Equation (3.3) shows us that for the same emission amplitude, the obtained signal $\mathbf{S} = \mathbf{E} \mathbf{M}$ is a factor N times higher than that which would have been obtained via the ‘direct’ measurement method. Thus, in the presence of (assumedly uncorrelated) electronic noise, we obtain *without averaging* the same SNR as if we had used the ‘direct’ procedure and averaged N times. Therefore for the same acquisition time, we gain SNR. Or inversely, for the same SNR, we can perform the experiment much more rapidly.

The main drawback of this method is that it rests on the linearity of the entire acquisition system (transducer array + emission/reception electronics). No apparatus is perfectly linear, and thus careful testing is required before an experiment to ensure that the recovered signal (e.g. a reference pulse) is acceptable, i.e. almost identical to that obtained using more standard methods.

3.2.3.7.2. Time-gain control

Amplification of the detected field is needed to be able to have enough signal at long times.

In backscattering, this can prove challenging because the initial backscattered field, being made up of mostly specular reflection, is very large compared to the field at longer times. If gain applied to the detected field is too large it would saturate the field at early times (amplify it above the input voltage range of the recording electronics).

In all experiments performed at the Institut Langevin this issue was a significant concern. The solution I employed (developed by researchers prior to my arrival) was to acquire the backscattered signal three separate times, with different time delays. Then, different gain could be applied to each acquired signal, so that the initial signals had low gain and the long-time signals had high gain. After the experiment, the sections of signal were ‘stitched’ back together, correcting for differences in amplitude caused by differing applied gain. This technique, although very effective when no other solution is available, requires three times the acquisition time, so is not ideal. For experiments performed at the Ultrasonics Laboratory, this ‘stitching’ method was not required, probably due to changes made to the Lecoeur system since the fabrication of the version used at the Institut Langevin. Improvements that apply here are a wider range of amplitudes that can be recorded, and better onboard averaging capabilities to increase SNR at long times.

3.2.4. Frequency filtering

For temporal and frequential analysis, data (both transmitted and reflected) were filtered in the frequency domain with a narrow Gaussian filter of the form

$$\exp\left[-\frac{(f-f_c)^2}{w^2}\right], \quad (3.4)$$

where f_c is the central frequency of the filter and w is the filter width. The Fourier-transformed field is multiplied by the Gaussian filter, and the resulting product is inverse Fourier

transformed back into the time domain, and the envelope of the time-domain signal squared to obtain intensity. By performing these steps many times, changing the central frequency of the Gaussian filter, frequency- and time- dependent data are obtained. The frequency filter is applied before any other data processing is done (before the RS-MSF and CBS calculations, for backscattering measurements).

3.2.5. Ballistic Measurements

3.2.5.1. Ballistic transport

Wave propagation through a strongly scattering medium contains both coherent and incoherent contributions. The incoherent contribution arises from the interference of multiply scattered partial waves. The coherent signal, which we also refer to as the *ballistic* signal, is one which has propagated through the sample without scattering away from the forward direction, and thus maintains a definite phase relation to the incident pulse.

Fundamental to the description of ballistic transport is the dispersion relation, which relates wavelength λ with frequency f . A medium is non-dispersive when the relationship between wavevector $k = 2\pi/\lambda$ and angular frequency $\omega = 2\pi f$ is linear. The velocity at which the oscillation of waves travel is called the *phase velocity*, defined as $v_p = \omega/k$, and is constant in a non-dispersive medium. In a *dispersive* medium the relationship between frequency and wavevector is not necessarily linear, so phase velocity is frequency-dependent. Wave pulses are then made up of components of different frequencies, each of which travels at its own phase velocity. These components interfere to produce a pulse, which is well-defined in time if the frequency range is narrow enough. The pulse envelope travels at the *group velocity*, defined

mathematically as $v_g \equiv \left. \frac{d\omega}{dk} \right|_{k_0}$.

Experimentally, both phase and group velocities may be determined using the general relation $v = L/\Delta t$, where L is the sample thickness and Δt is the time that a wave takes to travel through the sample. For group velocity, Δt_{group} is the time required for the peak of the envelope of a pulse to propagate through the material. This means that experimentally, the frequency range needs to be narrow enough to have a well-defined pulse. To obtain frequency dependence, the pulse is filtered in frequency with a narrow bandwidth (10% of the central frequency of the input transducer). For phase velocity, Δt_{phase} is found by measuring the phase difference $\Delta\phi$ between the FFTs of the ballistically-transmitted pulse and an input pulse through water, using the relation $\Delta t_{phase} = \Delta\phi/\omega = \Delta\phi/2\pi f$ (see, e.g., (Hu 2006)).

The amplitude of a wave pulse is also affected by propagation through a dispersive medium. Due to both scattering and absorption losses, a wave pulse would be expected to decay exponentially as it travels through the sample. This loss of ballistic intensity is described by the parameter the extinction mean free path, ℓ_e . Both the scattering mean free path ℓ_s and the absorption length ℓ_a contribute to the extinction mean free path:

$$\frac{I(x)}{I(0)} = \exp\left(-\frac{x}{\ell_s}\right) \exp\left(-\frac{x}{\ell_a}\right) = \exp\left(-\frac{x}{\ell_e}\right) \quad (3.5)$$

i.e.

$$\frac{1}{\ell_e} = \frac{1}{\ell_a} + \frac{1}{\ell_s} \quad (3.6)$$

For strongly scattering samples, scattering losses will dominate those from absorption, and thus the extinction mean free path may be often considered essentially equal to the scattering mean

free path¹⁵. Experimentally, ℓ_e (and thus ℓ_s) may be found by measuring the total attenuation α of the wave pulse through the medium, since $\ell_e = 1/\alpha$.

In the following sections, wave transport parameters including v_p , v_g , and ℓ_s are measured and results given. Calculations are based on the preceding explanations; further details may be found in the 1996 and 1997 works of Page et al.

3.2.5.2. Measurement of the ballistic pulse

Experiments with both plane-wave source and detector were carried out to measure the average transmitted field as a function of time. A disordered, strongly scattering medium will have ‘dark spots’ where very little signal may be coupled in or out. In contrast with the experiments presented earlier, here the goal is to measure the average *field* to be transmitted directly through the sample. Thus, a plane-wave source may be more effective than a point-source, as it couples signal into the medium over a wider area. Similarly, a transducer measures the average field across its entire surface, so while it is not sensitive to small-scale fluctuations of transmitted wave fields, a wide, flat-face transducer is a good choice for the measurement of average transmitted field (not intensity).

Transducers used were similar to those described in Section 3.2.2.1, but have a flat face to create an approximate plane-wave. For convenience, these transducers will be referred to as ‘plane-wave transducers’ in this thesis. Since a plane-wave transducer emits ultrasound from many points on its face, the overall intensity varies along the beam due to interference between

¹⁵ For example, for sample L1 we have at most $\ell_a \sim v_p \tau_a \approx (2.7 \text{ mm}/\mu\text{s})(200 \mu\text{s}) \sim 540 \text{ mm}$, where τ_a is the absorption time, measured as detailed in Section 3.2.5) and v_p is measured from the ballistic pulse (this result presented in Section 3.2.5.5). In contrast, $\ell_s \sim 1 \text{ mm}$ was estimated from the ballistic pulse. Thus, absorption is entirely negligible for the ballistic pulse, and $\ell_s \approx \ell_e$ is an excellent approximation for samples L1 and L2.

these emitted partial waves. The variations in the beam are substantial nearer to the source, in an area called the *near-field* of the beam. The zone beyond the near field where the beam is more uniform is called the *far-field*. The beam has the least fluctuations and the highest amplitude at the transition between near- and far-field, often called the *natural focus* of an unfocused transducer. In my experiments, the plane-wave transducer and the sample were separated by roughly the natural focus of the transducer. If need be, the separation distance may be larger and wider than the natural focus to produce a wider beam.

I performed what I call a plane-wave experiment to measure the average transmitted wavefield through sample L1 for the frequency range 0.7 – 1.5 MHz. The goal of this experiment was to measure the ballistic pulse. Thus, long-time signals are of little importance, so the baffle and sample-holder ‘wings’ (discussed in Section 3.2.2.2.2) were not used. Both source and detector were plane-wave transducers with a central frequency of 1 MHz. The source transducer face had a diameter of 0.5” (1.27 cm), and was placed approximately 21.6 cm from the sample center. The detector had a face 1” (2.54 cm) in diameter, and was placed approximately 21.8 cm from the sample center. In both cases the sample-transducer distance was larger than the natural focus.

For a medium in which multiple scattering dominates, the ballistic signal may not be visible over the scattered signal in any single transmitted waveform. However, the spatially-averaged total wavefield may make the ballistic field measureable due to the phase sensitivity of ultrasonic transducers. The ballistic pulse maintains its phase coherence with the input signal, regardless of the exact arrangement of scatterers. In contrast, the scattered wave arrives at the detector with a phase shift that depends on the different possible paths through the sample from source to detector. By averaging together waves which are transmitted through different regions

of a disordered sample, the incoherent contributions cancel each other out, while the coherent contributions interfere constructively. For large-diameter transducers this is achieved experimentally by fixing the positions of the transmitting and receiving transducers, and translating the sample in a plane perpendicular to the sample surface. In this way, the transmitted field was measured over a grid of 31x31 points, separated by 5 mm, across the sample surface. To reduce electronic noise, the detected signal was averaged over many repetitions of the input waveform. The experimental configurations used are discussed in Section 3.2.5.4, below.

3.2.5.3. Coherence criterion

The dominance of strong scattering at some frequencies, which is exacerbated by the thickness of samples L1 and L2, make ballistic experiments especially challenging. It is not obvious whether the first signal to be transmitted is only ballistic, or whether it includes scattered signals which have not been completely cancelled by the various averaging techniques. Thus, a criterion was established (by Kurt Hildebrand and myself) to determine help with this determination. The quantity under consideration is the square of the average field divided by the average intensity:

$$\hat{\psi}(t) \equiv \langle \psi(t) \rangle^2 / \langle \psi(t)^2 \rangle \quad (3.7)$$

This ratio is a statistical measure of the amount of fluctuations of the set of wavefunctions from the average. If all $\psi(t)$ are completely independent of each other, then $\hat{\psi}(t) = 1/N$. If signals are completely coherent (all the same), then $\hat{\psi}(t) = 1$. In a practical sense, if our ballistic signal is mostly coherent, then we should expect $\hat{\psi}(t) \gg 1/N$ over the range of times spanned by the ballistic pulse. In this context, intensity $\psi^2(t)$ was found by squaring the envelope of the waveform.

3.2.5.4. Extraction of the ballistic pulse

Experiments to measure the ballistic pulse were carried out for the frequency range of 0.25 – 1.5 MHz. This was done using two different input transducers centered at 500 kHz and 1 MHz. For lower frequencies below 750 kHz, where $\lambda \gg a$ (a is bead size), scattering is not very strong, and much of the initial detected signal is coherent. Thus, the ballistic signal could be extracted from existing transverse confinement data performed with a central frequency of 500 kHz. This experiment used a point-source input and output: The ballistic pulse was found by averaging all transmitted wavefunctions for which source and detector were directly opposite each other ($\rho = 0$). The average transmitted wavefunction is shown in Figure 3.17.

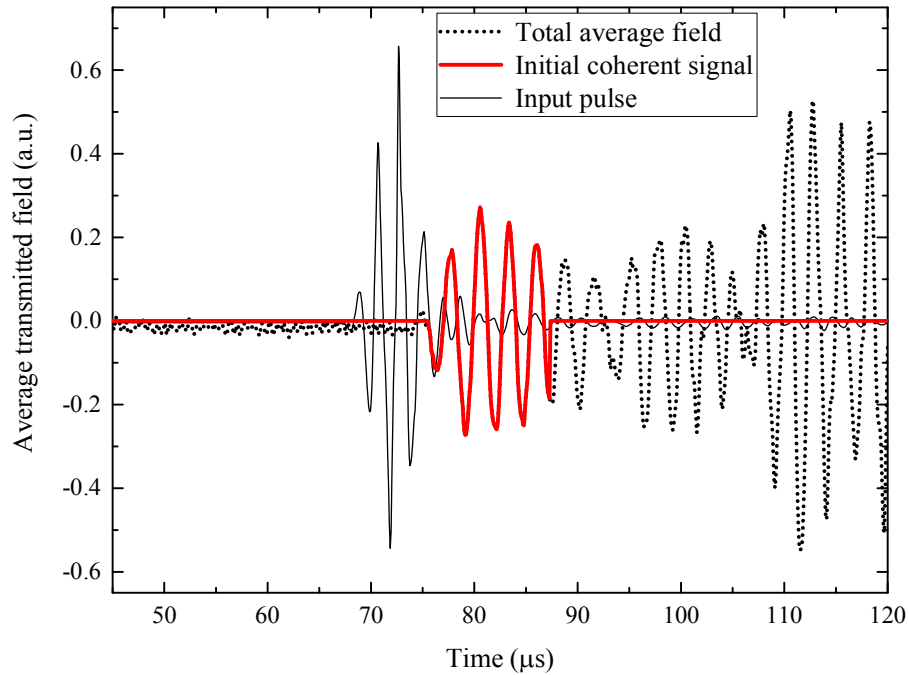


Figure 3.17: Average transmitted wavefield through sample L1 (dotted line) (broadband frequency filtering around 500 kHz). Due to the time it takes to travel through the sample, the coherent part of the average field (red thick solid line) arrives much later than the input pulse (black thin solid line).

To determine the range of time over which the transmitted pulse is coherent (i.e. to identify the ballistic signal), $\hat{\psi}(t)$ was calculated. The result is shown in Figure 3.18.

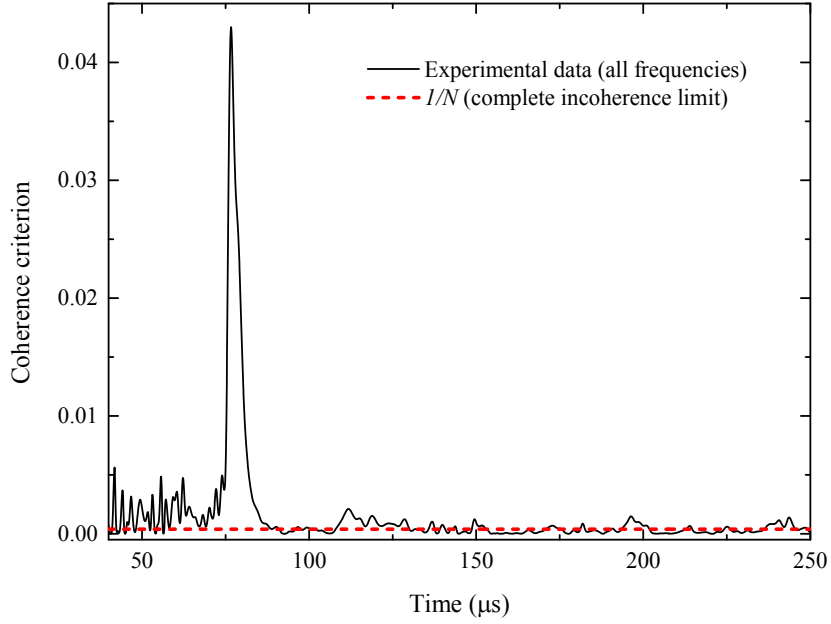


Figure 3.18: Coherence criterion applied to average transmitted field through sample L1, from a transducer centered at 500 kHz, with no frequency filtering applied.

The dashed line shows the theoretical value for $\hat{\psi}(t)$ if all detected waves were completely incoherent. It is clear between around 77-89 μs , the transmitted field is much more coherent than at any other time, and that during these times $\hat{\psi}(t) \gg 1/N$. There is some coherence in the noise before the signal begins, indicating that the noise is not purely random. Thus the coherence criterion, applied to the data shown in Figure 3.18, indicates the presence of a clear ballistic signal, and gives us an estimate of its extent in time. This ballistic pulse is highlighted in Figure 3.17 (solid line).

The ballistic signal includes all frequencies in the bandwidth of the input pulse. However, not all frequencies contribute equally to this pulse. Near the band gap at 500 kHz, there may not even be any coherent propagation at all. Thus, we would like to apply the coherence criterion as a function of frequency, as well as time. To do this, we filter the transmitted wavefields in frequency as discussed in Section 3.2.4 with a width of $w = 0.1$ MHz. By varying the central frequency of Gaussian frequency filter, $\hat{\psi}(t)$ was calculated over a range of frequencies. Figure

3.19 shows that the coherent signal is largest around 250 kHz. However, $\hat{\psi}(t) \gg 1/N$ for all frequencies between 200-550 kHz. Thus, we can have confidence that parameters measured using the ballistic pulse are reliable between around 200 kHz and 450 kHz.

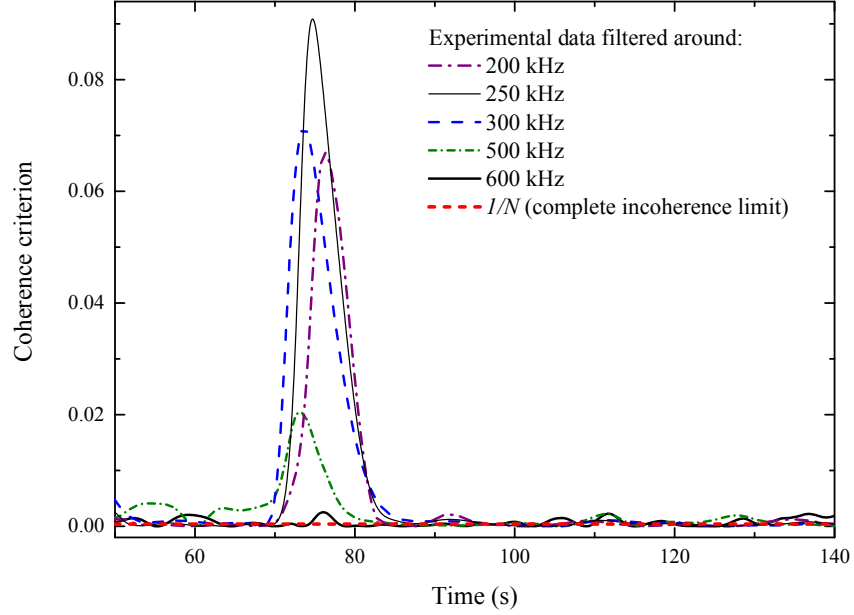


Figure 3.19: Coherence criterion applied to average transmitted field through sample L1 (narrowband frequency filtering, 200 - 600 kHz).

In the strong scattering regime where $\lambda \sim a$, closer to 1 MHz, the ballistic signal was much more difficult to observe. I attempted to extract the ballistic pulse from existing measurements for calculating the dynamic transverse profile with a point-source and detector centered at 1 MHz (see Section 4.3.1.1), but this data failed the coherence criterion completely. Thus, a separate experiment with a plane-wave source and detector was performed to measure the ballistic pulse.

The experimental setup and equipment are presented in Section 3.2.2. The transmitting and receiving transducers were fixed in place, and the sample was translated parallel to the transducers to enable a measurement of transmitted field through different parts of the sample. Transmitted waveforms were recorded over a grid of 10x10 points, separated by 5mm.

The coherence criterion was applied to these plane-wave data. Without frequency filtering,

$\hat{\psi}(t)$ includes the entire bandwidth of the input pulse (0.7 – 1.5 MHz), and is shown in Figure 3.20. An initial coherent signal may be observed between around 32 – 37 μs , although it is not more coherent than signals arriving later on in time. This may indicate a lack of sufficient averaging to completely cancel out scattered signals.

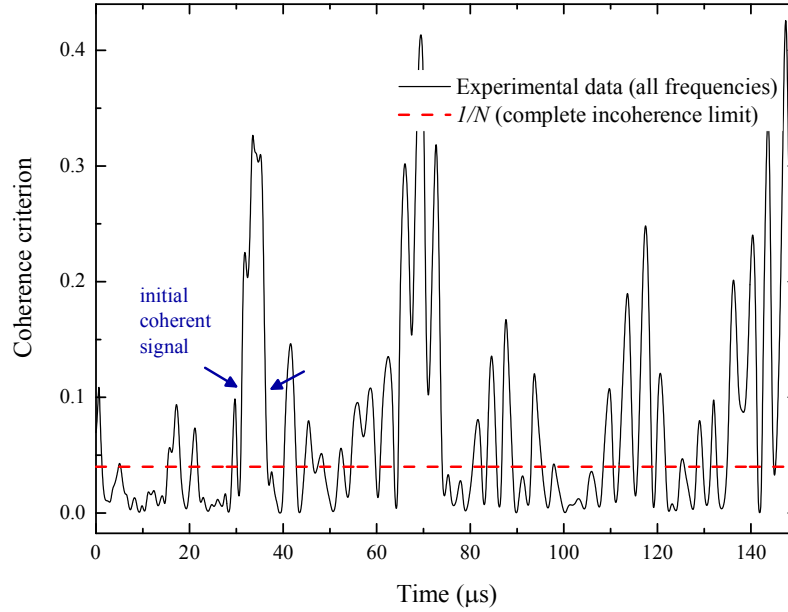


Figure 3.20: Coherence criterion applied to average transmitted field through sample L1 (broadband frequency filtering around 1 MHz).

Figure 3.21 shows $\hat{\psi}(t)$ with a narrow frequency filter ($w = 0.08$) of varying central frequency applied. Only for 800-900 kHz is the initially-arriving pulse more coherent than the rest of the signal at later times. We thus only have confidence that transport parameters measured using this ballistic pulse are reliable between 800-900 kHz. However, it does seem as though the initially-arriving transmitted signal is at least somewhat coherent over a frequency range of around 750 kHz to 900 kHz. This lends additional support to the identification of the ballistic signal between 25 and 28 μs . The average transmitted signal is shown in Figure 3.22 (dotted line), with the initial coherent contribution highlighted (red thick solid line).

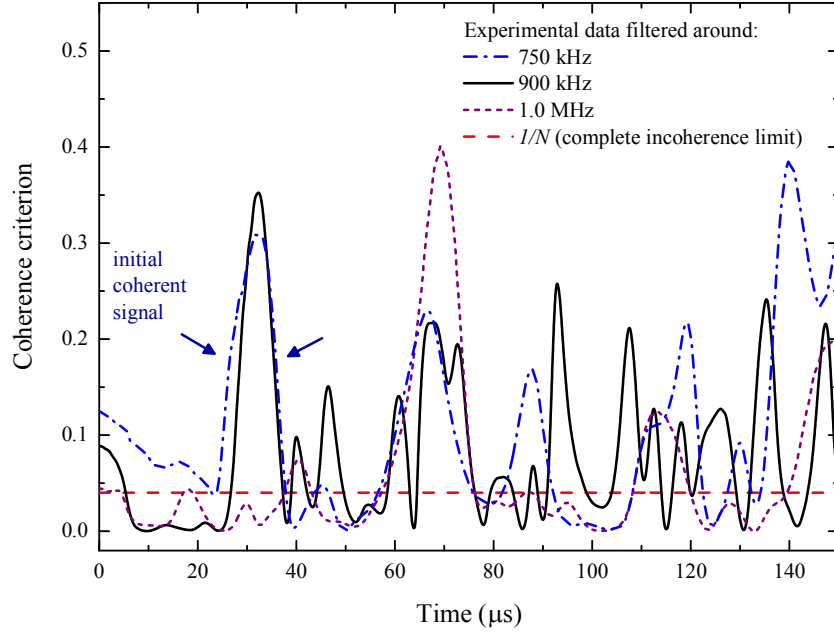


Figure 3.21: Coherence criterion applied to average transmitted field through sample L1 (narrowband frequency filtering, 750 kHz – 1 MHz).

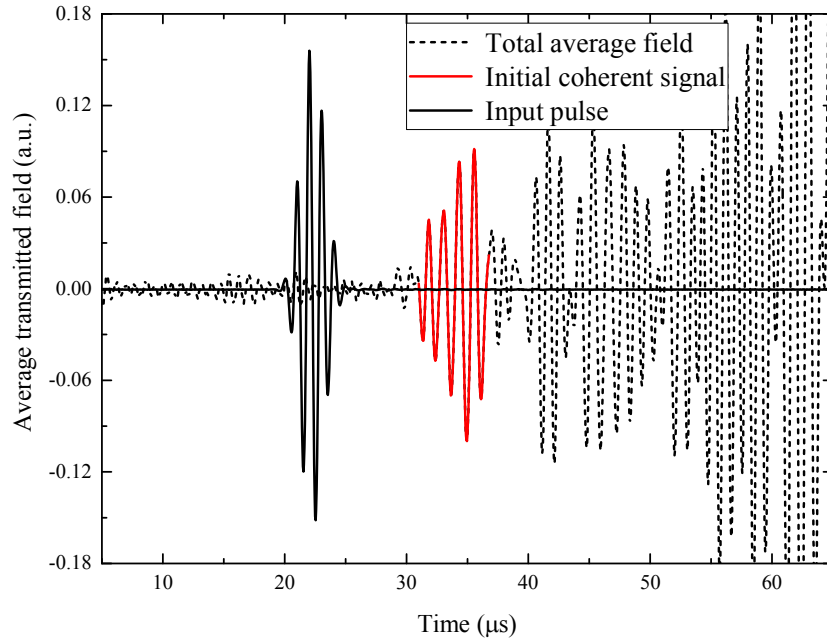


Figure 3.22: Average transmitted wavefield through sample L1 (dotted line) (broadband frequency filtering around 1 MHz). Due to the time it takes to travel through the sample, the coherent part of the average field (red thick solid line) arrives much later than the input pulse (black thin solid line). This effect is more drastic than for the data taken at 500 kHz (Figure 3.17).

3.2.5.5. Results

The thickness of sample L2 prohibits the use of many conventional methods of sample characterization which were employed to study L1, such as ballistic measurements. However, the samples were created with very similar techniques, so estimates of v_p , v_g , ℓ_s , and $k\ell_s$ from coherent measurements on L1 can be expected to be good approximations for L2. By comparing the ballistic pulse to the reference pulse (taken without the sample in place) (this calculation described in Hefei Hu's 2006 thesis), the following parameters were determined:

At 250 kHz:

Phase velocity $v_p = 3.4 \text{ mm}/\mu\text{s}$

Group velocity $v_g = 4.0 \text{ mm}/\mu\text{s}$

Wavelength = 14 mm

Scattering mean free path, $\ell_s = 1.8 \text{ mm}$

$k\ell_s = 0.83 \approx 0.8$

$R = 0.68$ (assuming $v_s = 0.5 v_L$)

$R = 0.75$ (assuming $v_s = v_L/\sqrt{2}$)

The calculation for the internal reflection coefficient R for multiply scattered waves has been summarized for acoustic waves by (Schriemer 1997) and for elastic waves by (Beck 1999). I used a program called 'crbar.c' (written by James Beck) to calculate R . Inputs include longitudinal and shear velocities. To estimate shear velocity it is necessary to assume a model for the ratio of longitudinal and shear modes. I used the estimate $v_L/v_s = \sqrt{2}$, which is the result of predictions from elasticity percolation near the percolation threshold (which we are not near). This ratio has been observed experimentally for porous glass sinter samples (Schriemer, Pachet, and Page 1996).

At 450 kHz:

Phase velocity $v_p = 3.2 \text{ mm}/\mu\text{s}$

Group velocity $v_g = 3.0 \text{ mm}/\mu\text{s}$

Wavelength $= 7.2 \text{ mm}$

Scattering mean free path, $\ell_s = 1.3 \text{ mm}$

$k\ell_s = 1.10 \approx 1.1$

$R = 0.70$

Between 800-900 kHz (values are averaged over this range):

Phase velocity $v_p = 2.78 \approx 2.8 \text{ mm}/\mu\text{s}$

Group velocity $v_g = 2.696 \approx 2.7 \text{ mm}/\mu\text{s}$

Wavelength $\approx 3.3 \text{ mm}$

Scattering mean free path, $\ell_s = 1.233 \approx 1.2 \text{ mm}$

$k\ell_s = 2.48 \approx 3$ (upper bound)

$R \approx 0.67$

Complete frequency-dependent results for v_p , v_g , ℓ_s , and $k\ell_s$ are shown in Figure 3.24 and Figure 3.24. The range of values which are most reliable, according to the coherence criterion, are highlighted (solid circles).

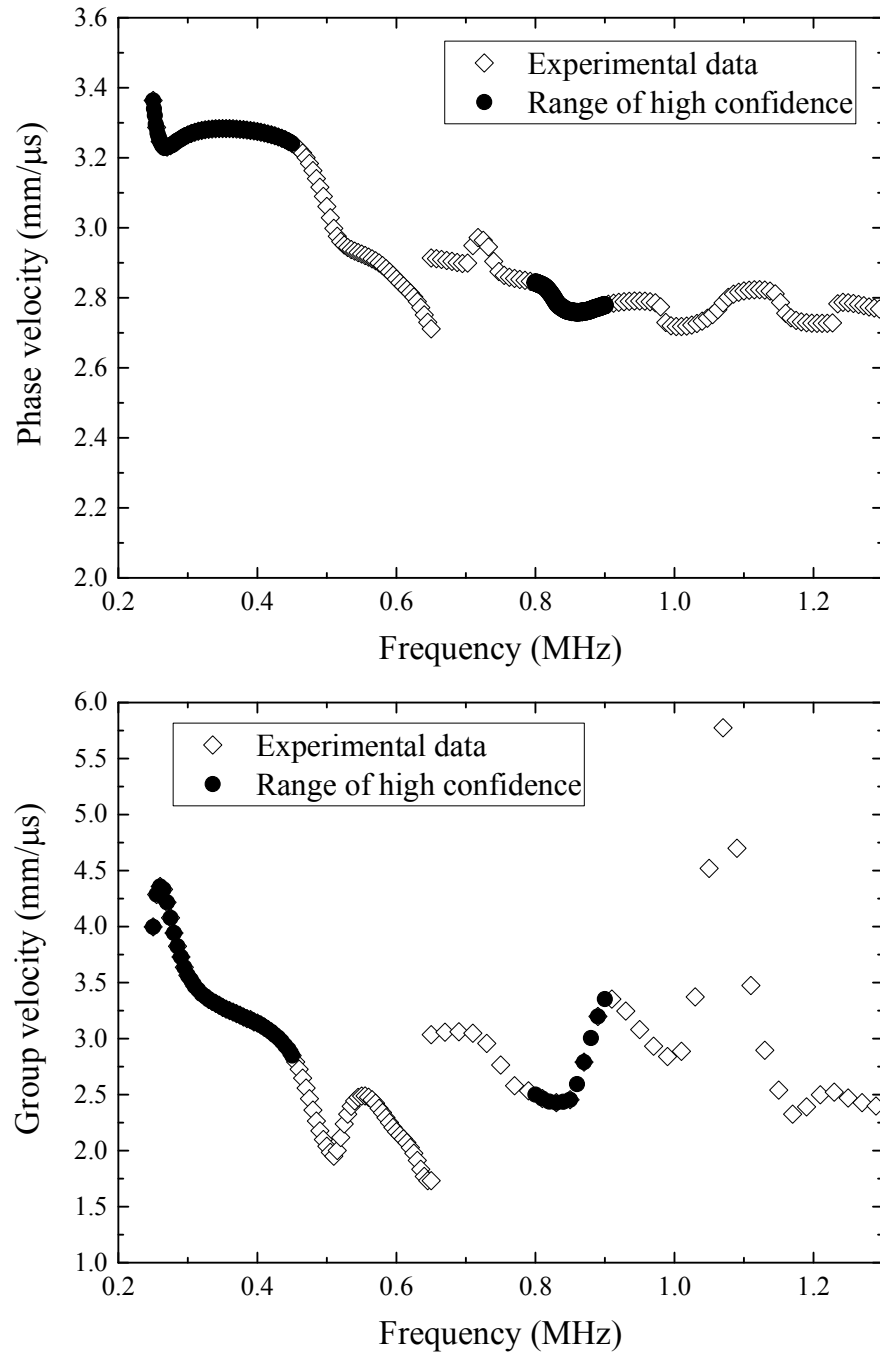


Figure 3.23: Estimates of velocity through sample L1 from ballistic measurements. Shown are v_p (top) and v_g (bottom). Solid circles indicate data which is most reliable according to the coherence criterion.

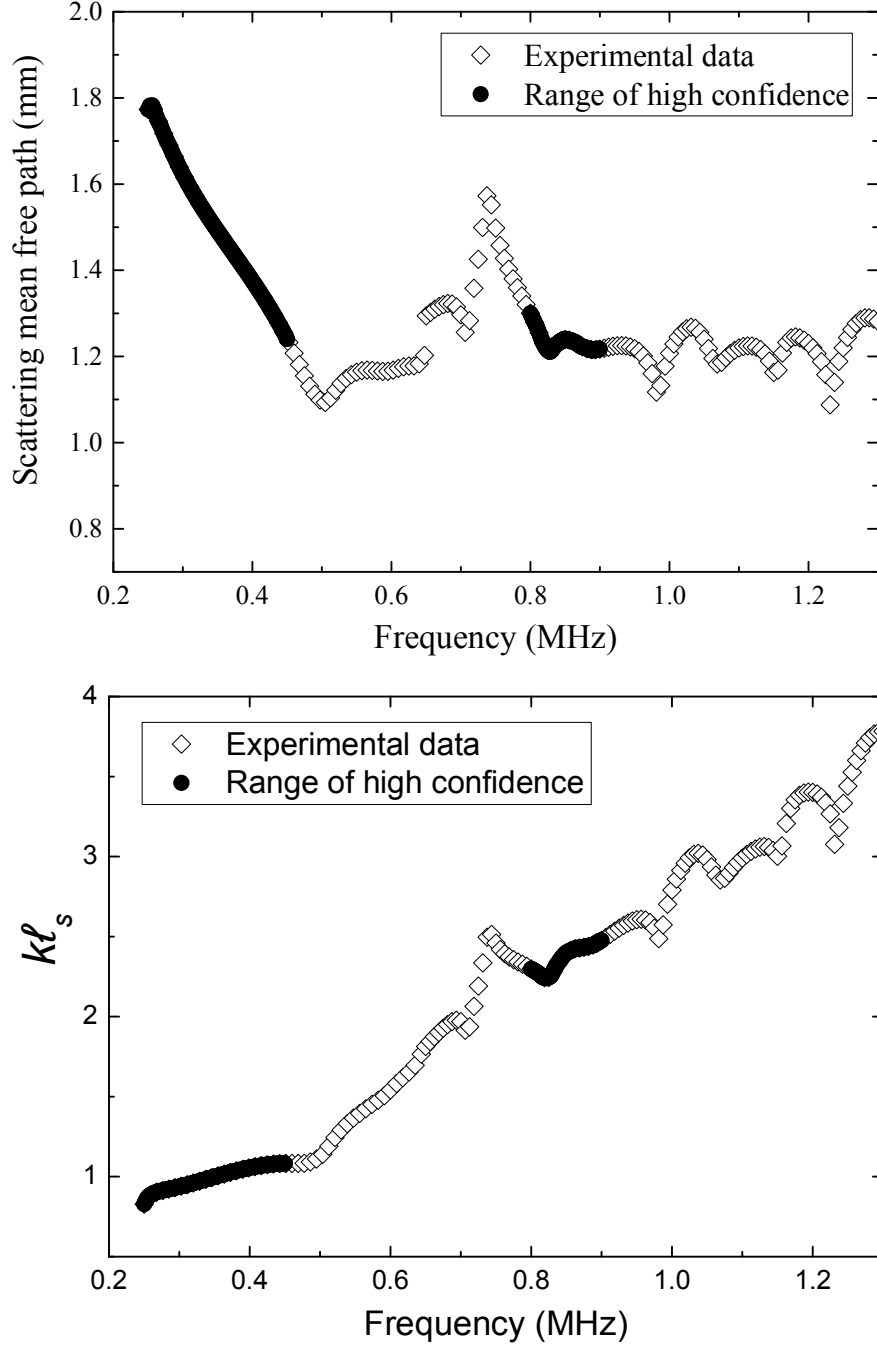


Figure 3.24: Estimates of transport parameters through sample L1 from ballistic measurements. Shown are: ℓ_s (top), and $k\ell_s$ (bottom). Solid circles indicate data which is most reliable according to the coherence criterion.

The measurement of $k\ell_s \sim 1 - 4$ indicate that ultrasound is strongly scattered in sample L1, over the frequency range of 0.25 MHz to 1.3 MHz.

3.2.6. The transmission/reflection coefficient

One of the first quantities that is usually evaluated for a new sample is the *amplitude transmission coefficient* $T(f)$, defined as the ratio of the average FFT of the transmitted signal and that of the reference:

$$T(f) = \frac{|\psi(f)_{transmitted}|}{|\psi(f)_{reference}|} \quad (3.8)$$

In this thesis, the transmission coefficient is determined in the following way. The numerator of Equation (3.8) is found by calculating the configurationally-averaged *on-axis* transmitted intensity through the sample. The reference signal is the same quantity through water, measured simply by removing the sample and repeating the same measurement for one on-axis position.

Figure 3.25 shows the spectrum of transmitted amplitude, $T(f)$, through samples L1 and L2. These results were calculated using (on-axis) data from the experiments which were performed to measure the dynamic transverse intensity profile. With this method of measuring $T(f)$, not *all* the transmitted signal is measured, so the total transmitted amplitude is underestimated. However, the relative frequency dependence of the transmitted amplitude is the desired quantity here, which is accurately determined. Note that no correction has been made to account for reflections at the two interfaces. The amplitude transmission reflection coefficient $R(f)$ is also shown in Figure 3.25. This quantity is calculated similarly to $T(f)$, but the measurement of a reference is trickier. Probably the best approximation would be to employ a smooth reflecting surface similar to that of the sample component material (i.e. metal). Another possibility is to use the initial, specularly reflected signal (that which only interacted with the sample surface before being reflected). This second approach is used here, as a reference signal was not recorded at the time of the experiment. This approach probably overestimates the

amplitude of $R(f)$ compared to $T(f)$, but does show similar frequency dependence.

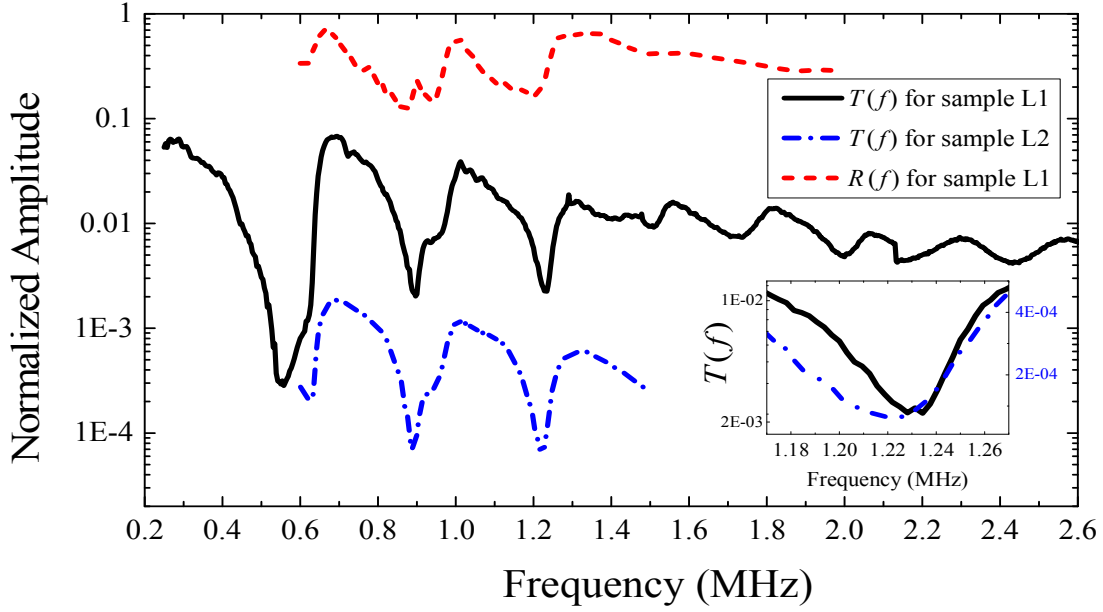


Figure 3.25: Amplitude transmission coefficient of ultrasound through samples L1 and L2 as a function of frequency, and amplitude reflection coefficient $R(f)$ from sample L1. $T(f)$ was only measured for a limited range of frequencies for L2, but its frequency dependence is expected to be similar to that of L1. Inset: a close-up of $T(f)$ around the 1.2 MHz pseudo-gap. This is the frequency range that is closely studied to observe the Anderson localization regime. In the inset the left vertical axis represents the data from sample L1 (black line), and the right vertical axis represents the data from sample L2 (blue dash-dot line).

In Figure 3.25 one can observe regions of high transmission, called *pass-bands*, which are due to the coupling of individual bead resonances (Turner, Chambers, and Weaver 1998; Lee 2014; Hu et al. 2008). If the coupling is not too strong, there will also be regions of low transmission, called *band gaps*, which are due simply to the absence of pass bands. These gaps are not the same as the complete gaps observed in the transmission spectra of crystalline media, which are due to Bragg scattering.

Appendix 3A : Furnace heating profiles

The following are the heating profiles that were programmed into the furnace. They consist of segments; each segment has a heating/cooling section at a certain rate ('Rate'), up to a target temperature ('Temp'), and then holds at that temperature for a time ('Hold'). The actual temperature inside the furnace was recorded with thermocouple wires extending from the top and bottom of the sample inside the furnace to an external recording device. An example of the programmed and actual heating profile is shown in Figure 3A.1.

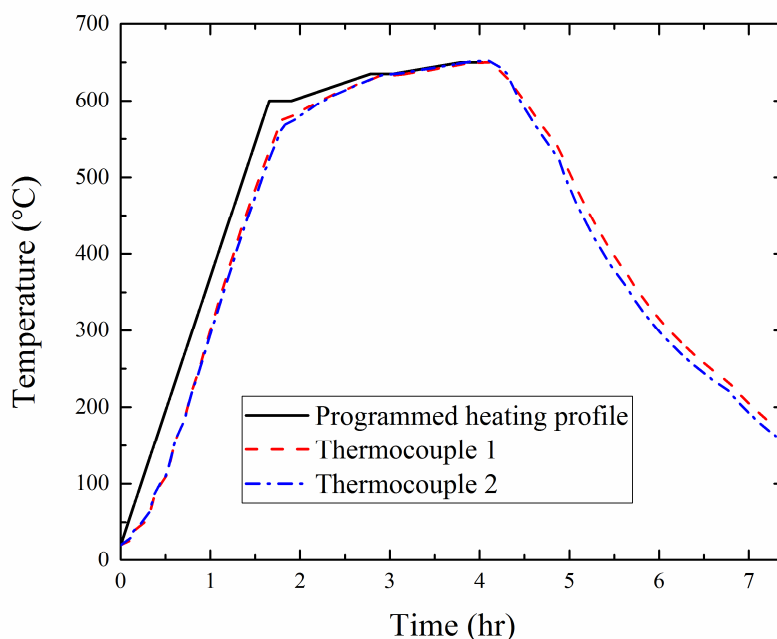


Figure 3A.1: Heating profile used to braze sample L1. The temperature inside the furnace (dotted lines) matches the programmed profile (solid line) near peak temperature, where the brazing results are most sensitive to temperature changes. At around 4 hr the furnace stops heating. Just before 5 hr the door of the furnace was opened to hasten cooling.

Sample L1

Segment	Rate (°C/hr)	Temp (°C)	Hold (min)
1	350	600	15
2	40	635	15
3	20	650	15

Sample L2

Segment	Rate (°C/hr)	Temp (°C)	Hold (min)
1	300	600	15
2	40	635	15
3	20	650	22

Sample L3 (see Chapter 8 for more details on this sample)

Segment	Rate (°C/hr)	Temp (°C)	Hold (min)
1	475	610	65

Sample L3 is a highly polydisperse sample that is investigated in Chapter 8. This sample was made using the brazing technique described in Section 3.1.1.1. However, it was found that this technique was not reliable to produce samples such as L0. Unlike samples like L1 and L2, which could be reproduced consistently using the same heating profiles, the heating profile used to produce L3 failed to produce other similarly polydisperse samples. The reason for this is probably due to the high degree of polydispersity of L0. Due to differences in surface area, different sizes of beads likely require different ratios of Si:NOCOLOK:Al beads. The ratio used for L3 was the same as that used for L1 and L2 (1:2:400 by weight), which was optimized for 4.11-mm diameter beads (Hu 2006). Subsequent difficulties in brazing small (1 and 2 mm) beads can almost certainly be solved by adjusting the coating based on bead surface area (Match 2015). Finally, note that the mold used for this sample had a flat, not dimpled surface.

Cubic samples (see Chapter 7 for more details on these samples)

Segment	Rate (°C/hr)	Temp (°C)	Hold (min)
1	350	610	90

4. Strong Diffusive Scattering

4.1. Introduction

To investigate departures from diffusion, it is necessary to first identify the signatures of conventional diffusion. To this end, this chapter presents a study of conventional diffusion of ultrasound in the slab mesoglass L1. The absorption-independent techniques which are used to observe localization in Chapter 5, both in reflection and transmission, are introduced here in the context of conventional diffusion. In reflection, I demonstrate experimentally the dynamic coherent backscattering effect from a strongly scattering 3D medium, in the diffuse regime. Data are compared to theory written by B. A. van Tiggelen in 2002 for CBS of diffuse classical waves in a 3D slab sample (van Tiggelen 2002). Fitting functions for this procedure were written by Matthew Hasselfield (Hasselfield 2003). I have adapted these functions to my own uses, written several more, and made several adjustments to both theory and fitting procedures. In this chapter I report a comparison of experiment to this theory. Such a comparison was performed once before (Hasselfield 2003), but was not published due to limitations in data quality. My analysis and results have obtained much better agreement and have extended the theory to more closely match the experimental setup.

I support my results with transmission measurements of the same samples. Included in this chapter are results from fitting transmission data from my sample L1 with theory, in the diffuse regime. These are presented as both a verification of some measured parameters for my sample (like velocity and mean free path), and as a verification of the result for the diffusion coefficient D_B measured via the CBS effect in the diffuse regime.

4.2. Coherent backscattering in the diffuse regime

The coherent backscattering (CBS) effect was introduced in Section 2.4, where it was shown that CBS occurs due to the constructive interference of waves travelling reciprocal paths inside the medium. For decades, the CBS effect has been used to measure characteristics of disordered media. For various types of diffuse waves and scattering media, the width of the static (time-integrated) CBS profile is commonly used to measure the transport mean free path, ℓ^* (Tourin et al. 1997; Jonckheere et al. 2000; Wolf et al. 1988; Bayer and Niederdränk 1993). The *dynamic* (time-dependent) CBS profile can be used to give an experimental measure of the Boltzmann diffusion coefficient D_B . At each time, the CBS profile typically has a rounded cone-shape. In the diffusive regime, the width of the dynamic CBS profile (the half width at half maximum) evolves as $\Delta\theta^{-2}(t) \propto Dt$. From this we can understand that the cone becomes *narrower* as time increases. This is because higher orders of scattering, i.e. longer path lengths, contribute more to small angles of the CBS cone (Akkermans et al. 1988). As the waves spend more time in the medium, they make longer and longer path lengths, which contribute more and more to small angles of the backscattered intensity profile.

The first experimental measurement of the dynamic CBS profile for acoustics was reported in 1997 by Tourin et al. for a 2D scattering medium (Tourin et al. 1997). Figure 4.1 shows how the diffusion coefficient was directly measured from the dynamic CBS profile, by plotting cone width vs time and fitting the results with a straight line.

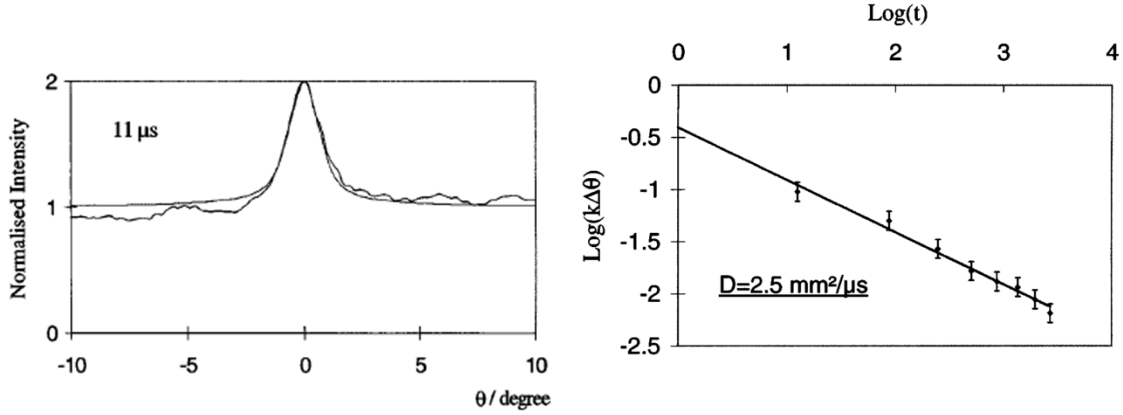


Figure 4.1: Left: Dynamic albedo measured with acoustic pulses for one representative time. Right: Cone width versus time. Smooth lines show theoretical predictions for a 2D scattering medium. Used with permission (Tourin et al. 1997).

Traditionally, the backscattered intensity profile has been assumed to have a Gaussian cone shape at every time, and one looks for the behaviour of the cone width in time (such as in the work of Tourin et al.). In 2D (in a far-field, plane-wave approximation), the half width at half maximum (HWHM) is expected to depend on time t as $\Delta\theta^{-2}(t) = \frac{tk^2D_B}{\Gamma}$, where Γ is a factor that depends on the transducers' directivity (Mamou 2005). As will be shown in this chapter, the expression is similar in 3D. It is therefore tempting to simply plot the experimentally-measured $\Delta\theta^{-2}(t)$ versus time, and fit a straight line to it. However, my CBS data in the diffuse regime show fluctuations despite a large amount of configurational averaging, which is perhaps not surprising considering the strong scattering nature of my samples. Deviations of the cone shape from exactly Gaussian at a certain time can only worsen fluctuations of $\Delta\theta(t)$. Fitting the entire intensity profile with theory can, to a certain extent, compensate for fluctuations in time and in space. The calculation of the $\theta^{-2}(t)$ depends on variables such as mean free path and velocity, so it is not much less difficult than calculating theory for the intensity profile. Thus, in this chapter, the dynamic CBS profiles are fit with theory for all space and time, simultaneously, to

obtain estimates of D_B and other parameters.

4.2.1. Theory for diffuse coherent backscattering in 3D

Section 2.4.1 demonstrates how to calculate the dynamic CBS profile, in general (by expressing the vertices \mathbf{L} and \mathbf{C} as solutions to the *time-dependent* diffusion equation). This section applies this method to produce theory which corresponds to my specific experimental geometry. Presented is a scattering theory developed by B. A. van Tiggelen for acoustic CBS from a 3D medium in the diffusion regime, similar to that presented for 2D by Tourin et al. (Tourin et al. 1997; van Tiggelen 2002). Some steps in the following derivation are excluded for brevity, but all relevant assumptions and references are included.

The geometry of the system is shown in Figure 4.2. The problem is assumed to be symmetric in ϕ , so the detector is taken to be at $(0, -\rho, -a + w)$ where ρ and w represent the difference in source-detector positions parallel and perpendicular to the slab surface, respectively. Ideally, in an experiment one attempts to have $w = 0$, i.e. the array and sample surface as parallel as possible.

The source, assumed to be monochromatic, emits:

$$\psi_{in}(\vec{R}) = -\frac{e^{ik\sqrt{a^2+R^2}}}{4\pi\sqrt{a^2+R^2}} \quad . \quad (4.1)$$

The first scattering event happens not exactly on the surface but somewhere inside the sample, after the extinction length ℓ_s (the ‘skin layer’) (Sheng 2006). In the following calculations we will neglect any phase shift which might occur in the skin layer. Additional assumptions are that $ka \gg 1$ and $a \gg \ell_s$.

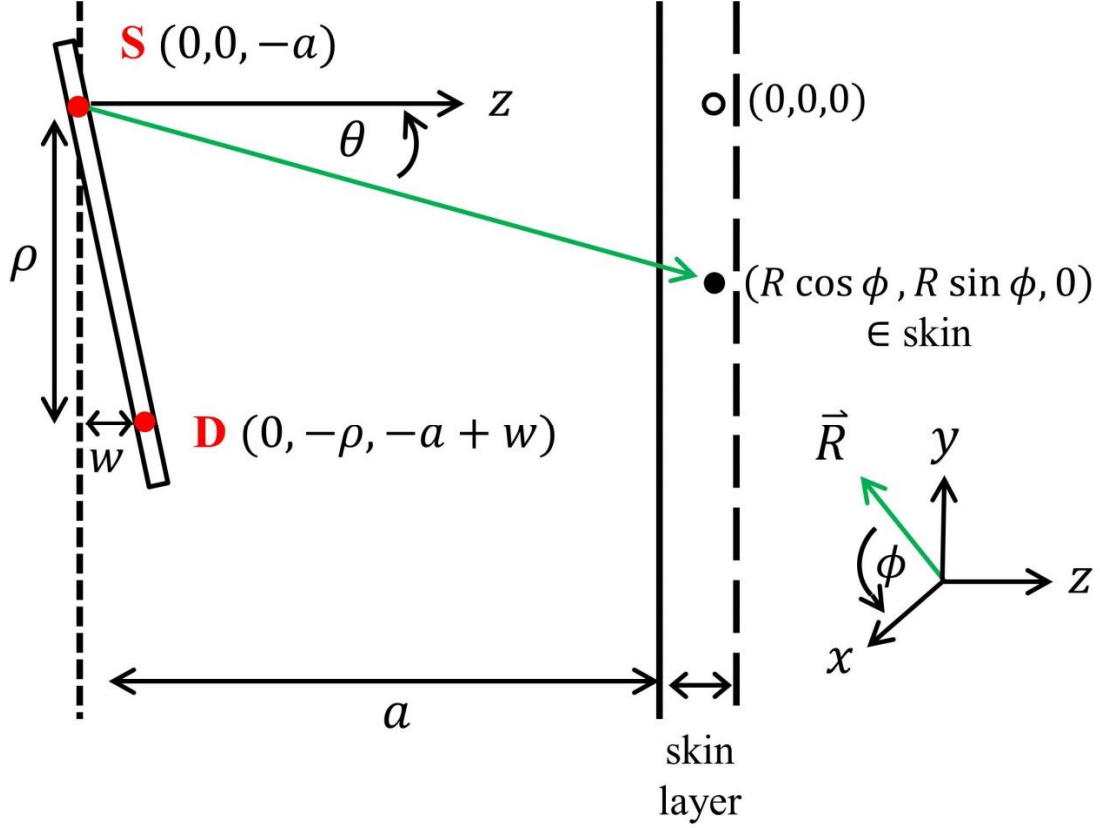


Figure 4.2 : Schematic for backscattering experimental geometry. Source S and detector D are separated in the z direction by a small distance w , which is exaggerated in this diagram for clarity. For a well-aligned experiment (see, for example, the discussion in Section 3.2.3.5), w should be near zero. Inside the sample the scattering is described by the coordinate system in the upper right. Vector \vec{R} is in the xy plane, parallel to the sample surface.

For the basic form of the calculation we refer back to the basic CBS theory of Section 2.4.1.

The general expression for intensity output from a scattering medium is Equation (2.30), reproduced here:

$$\left\langle \left| \psi_s(\vec{R}) \right|^2 \right\rangle_c \propto \int G_0(\vec{r}_1) G_0^*(\vec{r}_2) \Gamma(\vec{r}_1, \vec{r}_2, \vec{r}_3, \vec{r}_4) G_0(\vec{r}_3) G_0^*(\vec{r}_4) d\vec{r}_1 d\vec{r}_2 d\vec{r}_3 d\vec{r}_4 \quad (4.2)$$

where propagation between the source and the sample is given by $G_0(\vec{r}_1) = G_0(S, \vec{R})$ and $G_0(\vec{r}_2) = G_0(S, \vec{R})$, and propagation between the sample and detector is given by $G_0(\vec{r}_3) = G_0(D, \vec{R})$ and $G_0(\vec{r}_4) = G_0(D, \vec{R})$. The subscripts 1,2,3 and 4 refer to the various incoming and

outgoing waves, and can be understood by referring back to Figure 2.2.

As discussed in Section 2.2.3.2, the reducible vertex $\Gamma(\vec{r}_1, \vec{r}_2, \vec{r}_3, \vec{r}_4)$ describes all of the scattering processes inside the medium between \vec{r}_1 and \vec{r}_3 , and between \vec{r}_2 and \vec{r}_4 . Since we are considering the diffuse regime where the diffusion approximation holds, the approximation of $\Gamma \approx \mathbf{L} + \mathbf{C}_M$ will be applied. Both \mathbf{L} and \mathbf{C}_M are found using Equation (2.51), i.e. by solving the diffusion approximation for our particular experimental geometry. We therefore require the ‘3D ladder kernel’ $F(\vec{r}_1, \vec{r}_3)$, given by the solution to the diffusion equation for energy density:

$$\frac{\partial W(r, t)}{\partial t} = D_B \nabla^2 W(r, t) \quad (4.3)$$

in the region $0 < z < L$, where $W(r, t)$ is the local energy density, and D_B is the Boltzmann diffusion coefficient. In 3D, $D_B = v_E \ell^* / 3$, where v_E is the energy velocity (c.f. (Schriemer et al. 1997)). The Green’s function for Eq. (4.3) is that introduced in Eq. 2.41; the energy density in an infinite medium from a point source of unit strength at $t = 0$ at $(x, y, z) = (x', y', z')$:

$$G(x, y, z, t) = \frac{1}{8(\pi D_B t)^{3/2}} e^{-[r^2 + (z - z')^2] / 4 D_B t} \quad (4.4)$$

where $r^2 = (x - x')^2 + (y - y')^2$ (Carslaw and Jaeger 1995). For our experimental geometry, the most appropriate solution would be that of a slab-shaped medium with partial reflection of energy at the boundaries. The boundary conditions are therefore:

$$\begin{aligned} I + z_0 \frac{\partial I}{\partial z} &= 0, \quad z = L \\ I - z_0 \frac{\partial I}{\partial z} &= 0, \quad z = 0 \end{aligned} \quad (4.5)$$

with

$$z_0 = \frac{2}{3} \frac{1 + R_{\text{refl}}}{1 - R_{\text{refl}}} \ell^* \quad (4.6)$$

where here R_{refl} refers to the reflectivity of the sample. Physically, the *extrapolation length* z_0 is the distance outside the sample where the intensity decreases to zero. This leads to an effective increase in sample thickness

$$L_{\text{eff}} = L + 2z_0. \quad (4.7)$$

To simplify the problem, we can now change from the case of partially reflecting boundaries at $z = 0$ and $z = L$ to that of non-reflecting boundaries at $z = -z_0$ and at $z = L + z_0$. This is achieved with a linear extrapolation of conditions (4.5) to the interfaces, giving $I = 0$ at $z = -z_0$ and at $z = L + z_0$. The solution to equation (4.3) is then given by (Carlslaw and Jaeger 1995)

$$F_{3D}(\vec{r}, z_1, z_2, t) = (\text{const.}) \frac{e^{-r^2/4D_B t}}{D_B t} \sum_{m=1}^{\infty} e^{\frac{-m^2 \pi^2 D_B t}{L_{\text{eff}}^2}} \left[\cos\left(\frac{\pi m(z_1 - z_2)}{L_{\text{eff}}}\right) - \cos\left(\frac{\pi m(z_1 + z_2 + 2z_0)}{L_{\text{eff}}}\right) \right] \quad (4.8)$$

Now that the propagator is known, the backscattered intensity will be calculated from Equation (4.2). Here, as is commonly done, the derivation will be performed separately for the incoherent and coherent contributions to backscattered intensity.

4.2.1.1. Incoherent contribution to backscattered intensity

For the incoherent intensity, using Equations (2.30) and (2.51), we have

$$\begin{aligned} I_{\text{inc}}(\vec{R}) &= \int G_0(\vec{r}_1, \vec{R}) G_0^*(\vec{r}_2, \vec{R}) \delta_{1,2} \delta_{3,4} F(\vec{r}_1, \vec{r}_3) G_0(\vec{r}_3, \vec{R}) G_0^*(\vec{r}_4, \vec{R}) d\vec{r}_1 d\vec{r}_2 d\vec{r}_3 d\vec{r}_4 \\ &= \int \left| G_0(\vec{r}_1, \vec{R}) \right|^2 F(\vec{r}_1, \vec{r}_3) \left| G_0(\vec{r}_3, \vec{R}) \right|^2 d\vec{r}_1 d\vec{r}_3 \end{aligned} \quad (4.9)$$

The Green's functions in Equation (4.9) are the same as those in Equation (2.3). At this point two assumptions are made: that $k\ell_s \gg 1$ (the Ioffe-Refel criterion for diffusion), and the

Fraunhofer approximation that $|\vec{R} - \vec{r}_2| \rightarrow \infty$. Then, the Green's functions may be expanded as

$$G\left(S \rightarrow (\vec{R}, z) \in \text{skin}\right) = -\frac{e^{ik\sqrt{a^2 + R^2}}}{4\pi\sqrt{a^2 + R^2}} e^{\frac{z}{2\mu\ell_s}} \quad (4.10)$$

with $\mu = \cos \phi = a/\sqrt{a^2 + R^2}$ (Akkermans and Montambaux 2007). To properly express the intensity drop due to propagation from the last point in the sample at, e.g., (\vec{R}_3, z_3) , to detector D, the term in the denominator of Equation (4.10) will be expressed as

$$\frac{1}{(a^2 + R^2 + \rho^2 - 2\rho R \cos \phi)} \quad (4.11)$$

when referring to propagation between sample and detector, instead of $1/(a^2 + R^2)$ as is used when referring to propagation between source and sample. The task is now to substitute Equations (4.8) and (4.10) into the incoherent intensity of Equation (4.9). In cylindrical coordinates, this is

$$I_{inc}(\vec{R}) = \int dz_1 \int dz_2 \int dR_1 R_1 \int dR_2 R_2 \int d\phi_1 \int d\phi_2 \times \frac{e^{\frac{-z_1}{\mu_1 \ell_s}} e^{\frac{-z_2}{\mu_2 \ell_s}}}{(a^2 + R_1^2)(a^2 + R^2 + \rho^2 - 2\rho R \cos \phi)} F_{3D}(\vec{r}, z_1, z_2, t) \quad (4.12)$$

where the propagator $F_{3D}(\vec{r}, z_1, z_2, t)$ is defined in Equation (4.8). The z integrals in Equation (4.12) are the same as in the 2D theory given by Tourin (Tourin 1999) with some differences in the denominators. The final result, in cylindrical coordinates, is a 4D integral:

$$I_{inc}(\vec{R}) = \int_0^\infty dR_1 R_1 \int_0^\infty dR_3 R_3 \int_0^{2\pi} d\phi_1 \int_0^{2\pi} d\phi_3 \times \frac{\exp\left(-\frac{R_1^2 + R_3^2 - 2R_1 R_3 \cos \phi_{13}}{4D_B t}\right)}{(a^2 + R_1^2)(a^2 + R_3^2 + \rho^2 - 2\rho R_3 \cos \phi_3)} \sum_{m=1}^\infty e^{\frac{-m^2 \pi^2 D_B t}{L_{eff}^2}} L_m(\mu_1, \mu_3) \quad (4.13)$$

where the L_m terms are (Tourin 1999)

$$L_m(\mu_1, \mu_3) = \frac{2(A_1 + B_1)(A_3 + B_3)}{(a_1^2 + b^2)(a_3^2 + b^2)} \quad (4.14)$$

where $a_i = 1/l_s \mu_i$, $b = \pi m/B$, and

$$\begin{aligned} A_i &= \sin(bz_0) a_i \left(1 + (-a)^m e^{-a_i L}\right) \\ B_i &= \cos(bz_0) b \left(1 + (-a)^m e^{-a_i L}\right) \end{aligned} \quad (4.15)$$

4.2.1.2. Coherent contribution to backscattered intensity

Referring back to Equation (4.2), the coherent contribution to backscattered intensity is, for the geometry of Figure 4.2,

$$I_{coh}(\vec{R}) = \int G_0(\vec{r}_1, \vec{R}) G_0^*(\vec{r}_2, \vec{R}) \delta_{3,2} \delta_{1,4} F(\vec{r}_1, \vec{r}_3) G_0(\vec{r}_3, \vec{R}) G_0^*(\vec{r}_4, \vec{R}) d\vec{r}_1 d\vec{r}_2 d\vec{r}_3 d\vec{r}_4 \quad (4.16)$$

The integration over z is the same as in the incoherent calculation, but the rest of the calculation can *not* be simplified like the incoherent part could. This makes intuitive sense; the incoherent contribution contains only ladder diagrams, whereas the coherent contribution contains scattering processes that can not be ‘unentangled’ from one another. The complex exponential factors in the Green’s functions (Equation (4.10)) cancel each other out in the incoherent intensity calculation, but not in the coherent case. Now we must explicitly write them out. We have $\vec{R}_i = (R_i \cos \phi_i, R_i \sin \phi_i, 0)$, $S(0,0,-a)$, and $D(0,-\rho,-a+w)$, so the propagation between S and the first scatterer is

$$G_0(\vec{r}_i) \propto \exp\left(ik\sqrt{a^2 + R_i^2}\right), \quad (4.17)$$

and between the last scatterer and D,

$$G_0(\vec{r}_i, \vec{R}) \propto \exp\left(-ik\sqrt{(a-w)^2 + (R_i \sin \phi_i - \rho)^2 + R_i^2 \cos^2 \phi_i}\right), \quad (4.18)$$

and similarly for $G_0(\vec{r}_3)$ and $G_0(\vec{r}_4)$. The argument of the square root in (4.18) can be

simplified:

$$\begin{aligned}
& \sqrt{(a-w)^2 + (R_i \sin \phi_i - \rho)^2 + R_i^2 \cos^2 \phi_i} \\
&= \sqrt{a^2 + R_i^2 - 2aw - 2R_i \rho \sin \phi_i + \dots} \\
&= \sqrt{a^2 + R_i^2} \left(1 - \frac{aw + R_i \rho \sin \phi_i}{a^2 + s_i^2} + O(w^2 \rho^2) \right) \\
&= \sqrt{a^2 + R_i^2} - (\mu_i w + s_i \rho \sin \phi_i)
\end{aligned} \tag{4.19}$$

where $\mu_i \equiv \cos \theta_i = a / \sqrt{a^2 + R_i^2}$ and $s_i \equiv \sin \theta_i$. In (4.19), terms have been neglected due to the approximations $w \ll \sqrt{a^2 + R_i^2}$ and $\rho \ll \sqrt{a^2 + R_i^2}$. The definitions of (4.17) and (4.18), and the simplification of (4.19), now introduce the following phase factor into the integral:

$$\exp(ik[\mu_1 - \mu_2]w) \exp(ik[s_1 \sin \phi_1 - s_2 \sin \phi_2]) \tag{4.20}$$

The result for the integral for the coherent contribution to backscattered intensity is

$$\begin{aligned}
I_{coh}(\vec{R}) &= \int_0^\infty dR_1 R_1 \int_0^\infty dR_3 R_3 \int_0^{2\pi} d\phi_1 \int_0^{2\pi} d\phi_3 \cos[k(\mu_1 - \mu_3)\omega + k(s_1 \sin \phi_1 - s_3 \sin \phi_3)\rho] \\
&\quad \times \frac{\exp\left(-\frac{R_1^2 + R_3^2 - 2R_1 R_3 \cos \phi_{13}}{4D_B t}\right)}{(a^2 + R_1^2)(a^2 + R_3^2 + \rho^2 - 2\rho R_3 \cos \phi_3)} \sum_{m=1}^\infty e^{-m^2 \pi^2 D_B t / L_{eff}^2} L_m(\mu_1, \mu_3)
\end{aligned} \tag{4.21}$$

where $s_i = \sin \theta_i = \sqrt{1 - \mu_i^2}$.

4.2.1.3. Diffuse far-field assumption

At this point it is useful to introduce the *diffuse far-field* assumption to partially evaluate the integral. We will assume that backscattered phonons leave the sample at a point which is close to where they entered, i.e.

$$a^2 \gg 4D_B t \tag{4.22}$$

It is important to consider carefully whether the data to be compared with theory obey this

assumption. In my experiments I collect relatively long times, up to $\sim 315 \mu\text{s}$. This is necessary since for my strongly scattering samples it is the long-time behaviour that is the most illuminating when discriminating between diffuse and non-diffuse behaviour. However, transmission measurements on the same sample L1 reveal that the diffusion coefficient D_B is quite small ($D_B < 1.5 \text{ mm}^2/\mu\text{s}$) for the frequencies under consideration (shown in Chapter 4), so the approximation of Equation (4.22) holds in this case.

Mathematically, we can assume that the dominant contributions to the integral are from points (R_1, ϕ_1) and (R_3, ϕ_3) separated by distances that are small compared to a . The second point R_3 can be expanded as a first order displacement $(\Delta x, \Delta y)$ from $(R_1, \phi_1) = \vec{R}$. This is equivalent to a change of variables $(\vec{R}_1, \vec{R}_3) \rightarrow (\vec{R}, \vec{\Delta R})$. The full simplification is given in Appendix 4A. The result, applied to Equation (4.21) is

$$I_{coh}(\vec{R}) = C \int_0^\infty dR R \int_0^{2\pi} d\phi \frac{\exp\left(\mu_1^2 \frac{(k\rho)^2 D_B t}{a^2} [s^4 \sin^2 \phi + 1 - 2s^2 \sin^2 \phi]\right)}{(a^2 + R^2)(a^2 + R_3^2 + \rho^2 - 2\rho R_3 \cos \phi_3)} \quad (4.23)$$

$$\times \sum_{m=1}^\infty e^{\frac{-m^2 \pi^2 D_B t}{L_{eff}^2}} L_m(\mu_1, \mu_3)$$

where C is a multiplicative factor.

The shape of the CBS dynamic cone is determined by the dimensionless parameter $k\rho\sqrt{Dt}/a$, when $a^2 \gg Dt$. Thus, at each time the CBS intensity profile as a function of ρ has an almost Gaussian shape, with a width $(k\rho)_{FWHM}$ that depends on $(k\rho)_{FWHM} \sim a^2/Dt$. There is also some weak dependence on ρ from the denominator. The coherent contribution to total intensity sits on a uniform incoherent background given by Equation (4.13), and is equal in magnitude to the background level when $\rho = 0$.

This relation of $\Delta\theta^{-2}(t) \propto D_B t$ is commonly-used in other systems as well, notably for coherent backscattering in 2D (Mamou 2005; Tourin 1999). As discussed, $\Delta\theta^{-2}(t)$ plotted versus time can give an estimate of D_B . Here I will use a similar technique, but will base my measurement of D_B on a fit of the entire backscattered intensity profile.

4.2.1.4. Static CBS profile

The static (time-integrated) CBS profile (introduced in Section 2.4) may be calculated by integrating Equation (4.26) over all time. This calculation is in principle also possible for my experimental data, but there are not enough late times available experimentally to be able to compare my experimental data with theory. As time progresses, long paths contribute more and more to the static profile, typically giving it a narrow, peaked look. In my experiments, I do not have access to enough times to even approximate a CBS profile that has been integrated over *all time*, especially since in my strongly-scattering samples, the CBS profiles are wide, and narrow very slowly compared to other media. In addition, the earliest times (before around $15\ \mu\text{s}$) are not very reliable for my experimental data due to specular reflections which are difficult to completely exclude from my experimental data, especially since the sample surfaces are not smooth. Any filtering in frequency will also affect the earliest time data, as discussed in Section 3.2.4. Early times contribute the most to time-integrated intensity, and thus need to be measured very accurately for an accurate measure of the static CBS profile.

4.2.2. Corrections for experimental limitations

As detailed in Sections 3.2.3 and 4.2.3, coherent backscattering from my slab samples is measured using ultrasonic arrays, which are placed in the far-field of the sample. For an accurate

comparison of theory with experimental data, I apply several corrections to the theory, based on my specific experimental geometry. The matlab code for these corrections was written by M. Hasselfield in 2003.

4.2.2.1. Ultrasonic array directivity

Individual transducer array elements are quite narrow, and so emitted waves experience a certain amount of spreading out like diffraction of light through a slit. To characterize this effect the *transducer directivity* can be measured, which is the directional dependence of transducer efficiency (emitted intensity as a function of angle).

Directivity can be directly measured (e.g. with a laser interferometer), but when this data is not available, the ideal directivity provides a reasonable estimate (Mamou 2005). For a rectangular transducer of width W in 1D, field at angle θ varies in the far field as a sinc function of angle of incidence/emission (Hasselfield 2003):

$$\psi(\theta) = \psi(0) \text{sinc}\left(\frac{\pi W \sin \theta}{\lambda}\right) \quad (4.24)$$

The same expression can be used to correct for transducer height (y-direction), so total angular sensitivity (in the far field) is

$$\Omega(\theta_x, \theta_y) = \text{sinc}^2(\pi W \sin \theta_x / \lambda) \text{sinc}^2(\pi H \sin \theta_y / \lambda) \quad (4.25)$$

The directivity of the transducers is incorporated into theory calculations:

$$I_{coh}(\vec{R}) = \int_0^\infty dR \int_0^{2\pi} d\phi \Omega(\theta_{x,S}, \theta_y) \Omega(\theta_{x,D}, \theta_y) \times \frac{\exp\left(\mu_1^2 \frac{(k\rho)^2 D_B t}{a^2} [s^4 \sin^2 \phi + 1 - 2s^2 \sin^2 \phi]\right)}{(a^2 + R^2)(a^2 + R_3^2 + \rho^2 - 2\rho R_3 \cos \phi_3)} \sum_{m=1}^\infty e^{\frac{-m^2 \pi^2 D_B t}{L_{eff}^2}} L_m(\mu_1, \mu_3) \quad (4.26)$$

where

$$\begin{aligned}
\tan(\theta_{x,S}) &= \frac{R \cos \phi}{a} \\
\tan(\theta_{x,D}) &= \frac{R \cos \phi - \xi}{a} \\
\tan(\theta_y) &= \frac{R \sin \phi}{a}
\end{aligned} \tag{4.27}$$

I use this ideal directivity approximation for my theory calculations, as experimentally-measured transducer array directivity is not available.

4.2.2.2. Large transducer height

The transducer directivity correction included in Equation (4.26) is only concerned with width of individual transducer elements. The finite height of the elements means that signal is being collected over a larger area in space than is accounted for by the theory, which assumes point-sources and detectors. At the array surface, the size of the backscattered speckle is large enough that interference cancellation is not important¹⁶. Thus, an integration over backscattered intensity (instead of field) is sufficient to account for the influence of the finite height of the elements. An explicit integration of Equation (4.26) can be performed over all source points S on the emitting transducer and all detection points D on the receiving transducer:

$$I_{corrected}(\vec{R}) = \int_{-H/2}^{H/2} dy_1 \int_{-H/2}^{H/2} dy_2 I_{coh}(\vec{R}) \tag{4.28}$$

where $I_{coh}(\vec{R})$ is that from Equation (4.26). While this correction does not have a huge effect on the resulting theory (Hasselfield 2003), there is a small effect, so it is used for all theory presented in this thesis.

¹⁶ Defining $W \approx \sqrt{D_B t}$ as the spatial extent of the wave spreading in the sample, in the diffusion approximation (see also Section 6.2), the individual speckle size at the array surface is $\sim \lambda a / W \sim 3 * 182 / \sqrt{1.65 * 350} = 22$ mm (this D_B value taken from Section 4.4). This is larger than the array element height of 12 mm.

4.2.3. Experiment and data processing

An ultrasonic array was used to measure backscattered field from sample L1. The array had a central frequency of 1.6 MHz, and was positioned 182 mm from the sample surface. The experiments measure the *response matrix* (similar to the propagation matrix introduced conceptually in Section 2.3.2), which holds the responses between each emitter and detector. Once the response matrix has been acquired, the CBS profiles may be directly calculated from it by summing the intensity (envelope of the amplitude squared) over the same source-receiver separation. (This is equivalent to summing the *diagonals* of the intensity response matrix shown in Figure 6.3.) The final result is configurationally-averaged backscattered intensity as a function of angle between source and receiver, time, and frequency; $I(\theta, t, f)$. The experimental details to obtain the response matrices are given in Section 3.2.3. Examples of resulting CBS profiles are shown in Figure 4.3.

As will be shown in this chapter, wave transport is diffusive near 1.65 MHz. Nevertheless, there was a non-trivial recurrent scattering contribution to the data. This observation, and its significance, is discussed in Chapter 6. Here, the recurrent scattering contribution was removed from the total backscattered intensity to simplify the comparison with our diffusive theory. For details on this procedure see Chapter 6.

4.2.4. Fitting procedure

To begin fitting theory to data, I calculate several sets of theoretical dynamic cones from Equation (4.28), varying parameters which are unknown or imprecisely-known such as ℓ^* and R . I then compare each set of theory calculations to experimental data using nonlinear least squares fitting. This analysis is carried out using Matlab code, most of which was initially written by M. Hasselfield and subsequently adapted by me, and the rest of which was written by

me. Coherent and incoherent intensity contributions are normalized independently to achieve a more realistic fit. Each theory set contains a wide range of values of $D_B t$, and at each time index $t_{\text{experiment}}$ in the data, the best fit value of $D_B t$ from the theory set was determined (see Section 5.5.1 for details). An example of such fits is shown in Figure 4.3, where data are shown for several different times, along with the best-fit result at each time for a certain theory set.

The level of background intensity, although theoretically 0.5, was allowed to vary during the fitting. In reality, the background level deviates from 0.5 for times before around 100 μs . This is probably the result of challenges involved in the removal of the recurrent scattering contribution to background intensity. However, for the diffuse frequencies presented in this chapter the cones are narrow enough, and range of angles collected wide enough, that the background level can be fairly easily determined just by the shape of the cones.

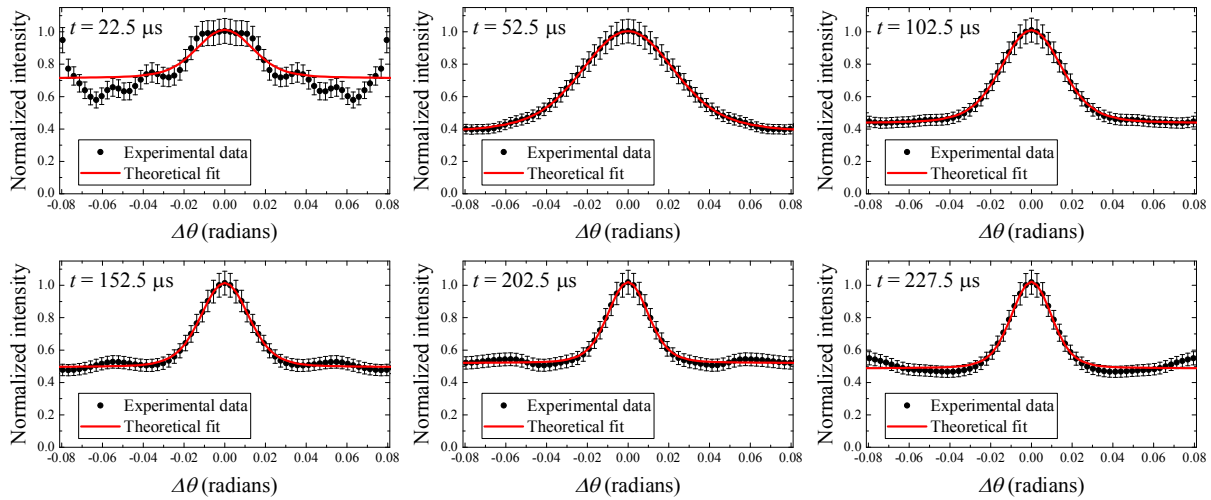


Figure 4.3: Experimental CBS profiles (symbols) with fits from diffusion theory (lines) for several representative times: 22.5 μs , 52.5 μs , 102.5 μs , 152.5 μs , 202.5 μs , and 227.5 μs .

An overall value of D_B is determined either by taking the (weighted) average value of $D_B t_{\text{theory}}/t_{\text{experiment}}$ or by plotting theoretical $D_B t$ values vs experimental t , and taking a (weighted) linear fit. The linear fit option provides a graphical representation of the data where

deviations from linearity are immediately obvious to the eye, so I prefer this option. Figure 4.4 shows D_B vs $t_{\text{experiment}}$ with a weighted linear fit. Error bars are given by the value of $D_B t$ needed to change reduced χ^2 (goodness of fit) by 1. More results from the fitting of CBS data with theory are presented and discussed in Section 4.4.

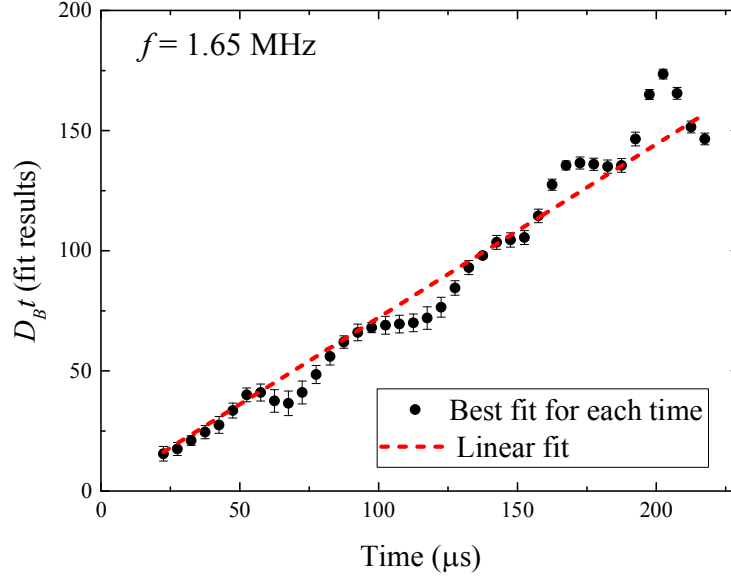


Figure 4.4: An example of the method used to determine the diffusion coefficient that best describes wave propagation at a particular frequency. Shown here are the $D_B t$ values obtained from the best fit of the theory to the experimental CBS profiles (for 1.65 MHz) at each experimental time $t_{\text{experiment}}$, plotted versus $t_{\text{experiment}}$ (symbols). The dashed line is a weighted linear fit to the data. Notable parameters used to calculate this theory are $\ell_s = 1.1 \text{ mm}$, $\ell^* = 8 \text{ mm}$, and $R = 0.75$, giving a value of $D_B = 0.72 \pm 0.02 \text{ mm}^2/\mu s$.

4.3. Transmission

The diffusion approximation (introduced in Section 2.2.4.1.4) is widely used to characterize multiple scattering media in transmission. Here I follow the methods of Page et al. to apply the diffusion approximation to strongly scattered ultrasound from a 3D medium (Page et al. 1995).

4.3.1. The time-of-flight profile

The configurationally-average transmitted intensity as a function of time is often called a *time-of-flight* (TOF) profile. To measure the TOF profile, a point source (or, a good approximation of one) is placed near the sample surface, and the transmitted intensity is measured on the other side of the sample with a point detector (see Section 3.2.2.3 for experimental details). The time-of-flight profiles are well-described by solutions to the diffusion equation for acoustic energy density in a slab of thickness L with infinite transverse extent, with appropriate boundary conditions (similarly to the propagation kernel for backscattered intensity profiles). This solution has been described in references (Page et al. 1995; Schriemer 1997) and will not be reproduced here. A fitting program in c has been developed (initially written by Art Bailey and subsequently modified by John H. Page and Hefei Hu) to perform non-linear least-squares fitting of experimental TOF profiles with this theory. For more accurate results, I modified this program slightly to take into account experimentally measured uncertainties in transmitted intensity. Inputs to the fitting function are: group velocity v_g , reflection coefficient R , (these are determined from ballistic experiments: see Section 3.2.5) the spatial width of the input pulse (to correct for the point-source assumption) σ (measured directly from the source map), and transport mean free path ℓ^* . Parameters determined by the fitting function are D_B , absorption time τ_A , and an arbitrary amplitude parameter.

Of all the input parameters, ℓ^* is the only one which is unknown. Thus, I performed fitting for a wide range of ℓ^* values. As shown in the proceeding sections, the possible range of ℓ^* can then be constrained to those values of ℓ^* which gave reasonable fits.

4.3.1.1. The dynamic transverse intensity profile

The measurement of the dynamic transverse intensity profile was first developed by Page

et al. to study wave scattering in the diffuse regime (Page et al. 1995). This experimental technique measures the spreading of waves in slab-shaped samples, in the transmission geometry. The experimental setup is shown in Figure 4.5. The quasi-point source is kept stationary, and a subwavelength detector scans the opposite face of the sample in the near field. By translating the detector a distance ρ parallel to the axis of the source, the transmitted intensity as a function of transverse distance from the source, ρ , is measured. (Further experimental details are given in Section 3.2.2.)

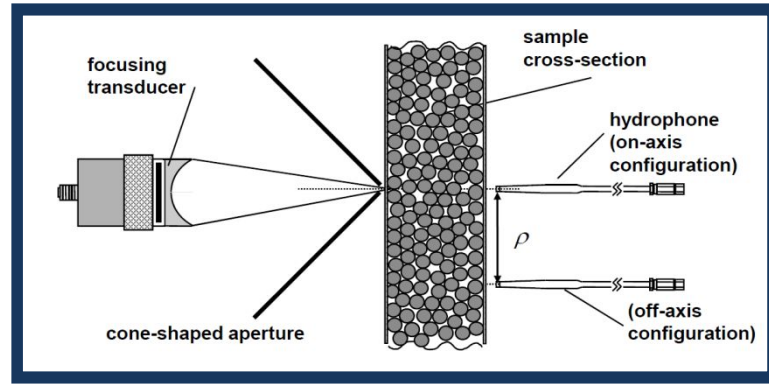


Figure 4.5: Diagram of the transverse confinement technique. Used with kind permission of Società Italiana di Fisica (Page 2011). Copyright (2011) by the Italian Physical Society.

This off-axis transmitted intensity is decreased by $\exp(-\rho^2/4Dt)$ due to the fact that at each time, fewer paths contribute to the intensity measured at ρ . By measuring the ratio of off-axis/on-axis transmitted intensity a transverse width $w_\rho(t)$ can be defined as

$$I(\rho, t) / I(0, t) \equiv \exp[-\rho^2 / w_\rho^2(t)] \quad (4.29)$$

Since all paths arriving at the same time have travelled the same distance in the sample, they are affected equally by absorption, so any absorption factor $\exp(-t/\tau_A)$ cancels out in Equation (4.29). Thus, this ratio is independent of absorption and is a direct measure of the spread of the energy outwards from the source. In the diffuse regime, the spatial profile is Gaussian, and the

transverse width is independent of ρ . Then, $w_\rho^2(t)$ evolves linearly with time as

$$w_\rho^2(t) = 4D_B t \quad (4.30)$$

Thus, for purely diffusive wave transport, the measurement of $w_\rho^2(t)$ can yield a relatively simple measurement of D_B *which does not depend on absorption or other any other parameters* (Page et al. 1995). Here, this method is applied to my transmission measurements of L1.

In my experiments, transmitted field was acquired at three off-axis distances: $\rho = [15, 20, 25]$ mm. Many (typically 3025) source positions were acquired by translating the sample. For each source position, the detector was scanned in a cross-shape as shown in . This was done so that transmitted intensity could be averaged over the same ρ distance, for improved configurational averaging.

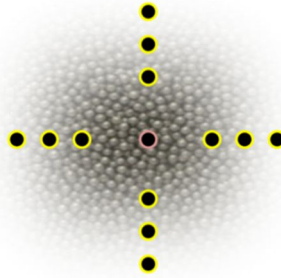


Figure 4.6: Sketch of cross-shaped acquisition sequence carried out by the detection hydrophone for transverse confinement experiments. Shown are the 13 acquisition positions for one source position. There is one acquisition point for $\rho = 0$ (red, centre), and 3 of each off-axis position (yellow, along the arms of the cross).

After filtering in the frequency domain (section 3.2.4), data are averaged over all source positions to obtain intensity as a function of detector position and time: $I(\rho, t)$. The background noise level is estimated by a linear fit of pretrigger intensity as a function of time, and this (constant) level was subtracted from the entire time-dependent intensity. Then, $I(\rho, t)$ taken at the same $|\rho|$ value were averaged together, and $w_\rho^2(t)$ calculated according to Equation (4.30).

For a demonstration of the use of TOF and $w_\rho(t)$ to determine D_B in the diffusive regime, I report here results for transmitted intensity through sample L1 at 250 kHz. For such a low frequency, the wavelength in the sample is more than twice the mean scatterer size, ($\lambda_{L1} \sim 14$ mm, bead diameter $\simeq 3.9$ mm), so localized behaviour is less likely. More importantly, 250 kHz is well below the lowest frequency pseudogap where localization effects are the least likely to appear. In addition, the relatively large wavelength means that ballistic propagation is relatively easily measured. Thus, parameters such as velocity and scattering mean free path were unambiguously determined, enabling straightforward fitting of TOF with diffusion theory. Interestingly, we measure a value of $k\ell_s \approx 0.8$; such a low value indicates the presence of very strong scattering, and are *below* the oft-used criterion for localization of $k\ell_s < 1$. Since here I find that there is unequivocally no localized behaviour, this is an example of the need to be cautious when relying on this approximate criterion for localized behaviour.

I have measured both TOF and transverse width $w_\rho(t)$ from L1 using the technique described in this section. Data are filtered in frequency with a Gaussian filter centered at 250 kHz, with a width of 35 kHz. Figure 4.7 shows $w_\rho^2(t)$. These data are independent of ρ , as expected in the diffuse regime. A linear fit (from 75 to 250 μs) of $w_\rho^2(t)$ for all ρ values gives an average diffusion coefficient of $D_B = 1.516 \pm 0.002$ mm²/ μs . The discrepancy at early times (before around 50 μs) is due to the effect of the finite-size frequency filter width (discussed in Section 3.2.4). On-axis transmitted intensity as a function of time is shown in Figure 4.8.

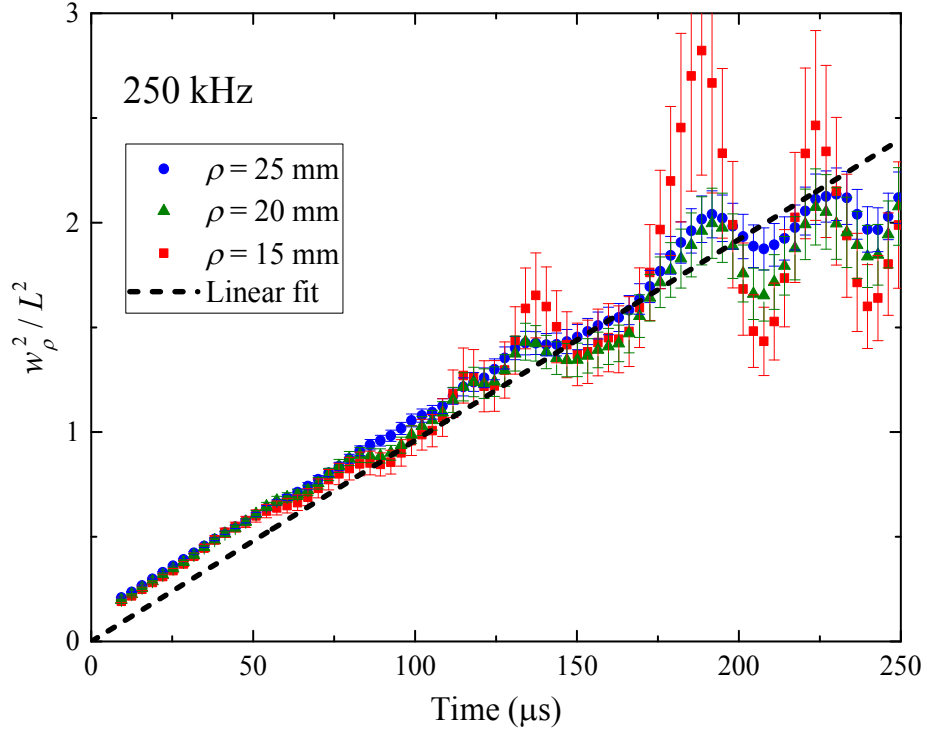


Figure 4.7: Transverse width measured from sample L1, at 250 kHz, with experimental uncertainty. Frequency filter width is 35 kHz. Error bars represent the uncertainty in the configurational average. Only every 40th data point is shown for clarity. Data for $\rho = 20$ mm is fit with a straight line (dashed line), with the y-intercept at zero. The fitting was performed for data after 50 μs , because convolution with the finite width of the frequency filter distorts the data slightly at early times. An average over fits for all ρ values gives a measure of $D = 1.516 \pm 0.002 \text{ mm}^2/\mu\text{s}$.

By fitting with a range of ℓ^* values we may estimate the most appropriate one. For 250 kHz (frequency filter width = 35 kHz) the best fit (i.e. lowest chi-squared value) is obtained for $\ell^* = 6$ mm. The fit giving a diffusion coefficient that best agrees with the estimate of $D_B \cong 1.51 \text{ mm}^2/\mu\text{s}$ from the $w_\rho^2(t)$ linear fit (within the nearest $0.01 \text{ mm}^2/\mu\text{s}$) is $\ell^* = 7.6$ mm.

Thus, the transverse width and time-of-flight profiles may be used in conjunction to find D_B and ℓ^* in the diffuse regime, even for very strong scattering. This method is only applicable when $w_\rho^2(t)$ is linear, which is an unambiguous signature of the diffuse regime.

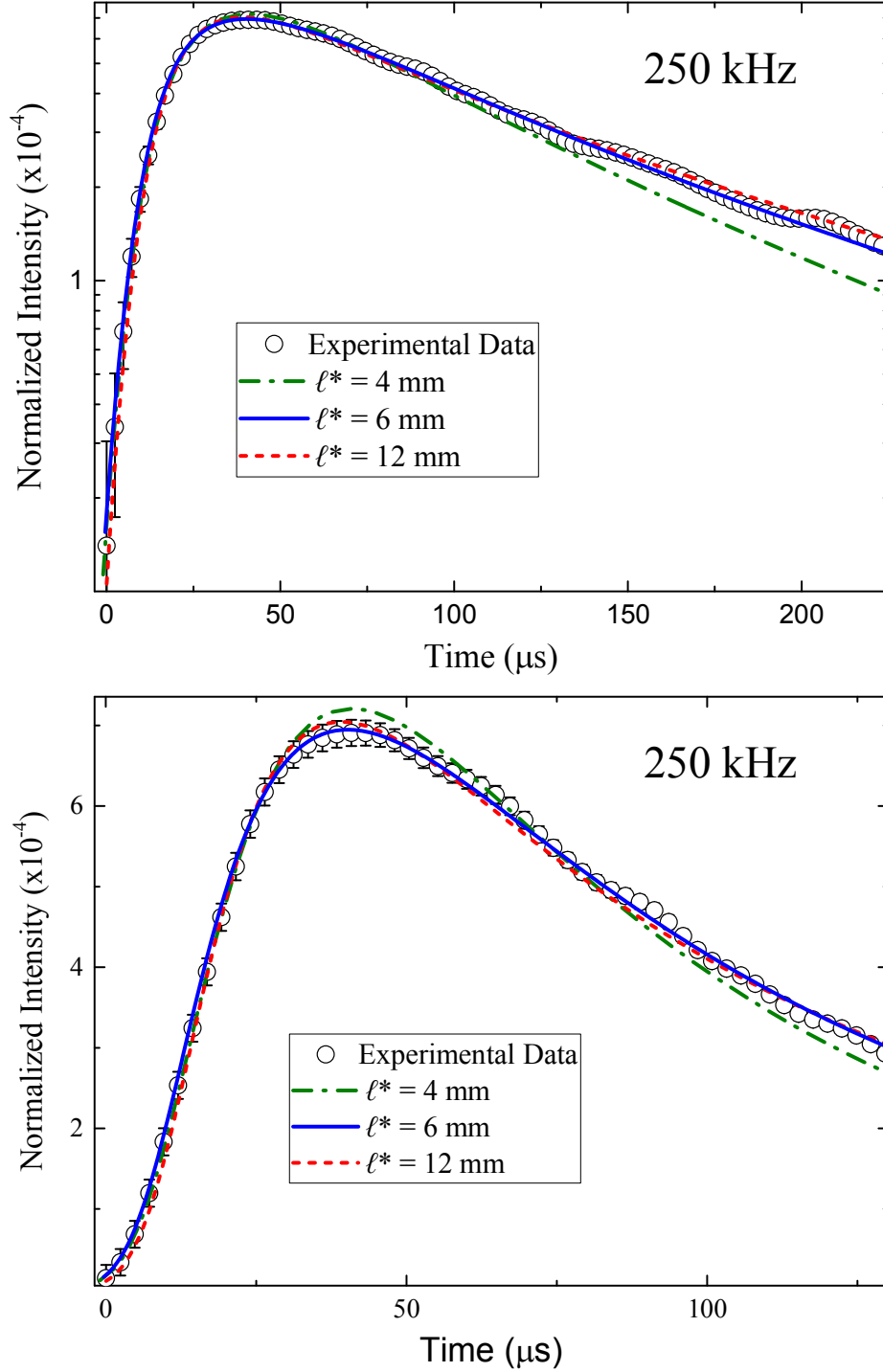


Figure 4.8: TOF profiles for sample L1 (open circles) and fits with diffusion theory. The fit for $\ell^* = 4$ mm (green dash-dot line) is an example of an ℓ^* value that is too low. Fits for $\ell^* = 6 - 8$ mm overlap almost completely; shown is the fit for $\ell^* = 6$ (blue solid line). These fits ($\ell^* = 6 - 8$ mm) give diffusion coefficients of $D_B = 1.44 - 1.80$ mm²/μs. The fit for $\ell^* = 12$ mm (red dashed line) also looks good, but returns a higher χ^2 value than the $\ell^* = 6 - 8$ mm fits. For data and fits shown here, $t = 0$ is defined as the time at which diffusion begins inside the medium.

4.4. Results for backscattering and transmission at 1.65 MHz

I have measured backscattering and transmission through sample L1 at 1.65 MHz. This frequency was chosen because, out of the range of frequencies at which I have data for both backscattering and transmission for sample L1 (around 0.75 – 2.5 MHz) the data appear qualitatively to be diffusive. At this frequency, scattering is very strong (we estimate $k\ell_s \approx 3$). In contrast to $f = 250 \mu\text{s}$, here there is no observable ballistic propagation through the sample, implying even stronger scattering (there may also be absorption losses, but as discussed, these are expected to be dominated by scattering losses). Thus, parameters measured from ballistic experiments (i.e. R and ℓ_s) are less certain at 1.65 MHz than they are at 250 kHz.

The transverse width is shown in Figure 4.9. Data are independent of ρ , as expected in the diffuse regime. However, $w_\rho(t)$ does not cross through (0,0). This behaviour has been observed for other frequencies and for other samples, often nearer to strong scattering regimes, and I am not sure what the cause is. A linear fit (from 50 to 350 μs) of $w_\rho^2(t)$ for all ρ values gives an average diffusion coefficient of $D_B = 0.706 \pm 0.002 \text{ mm}^2/\mu\text{s}$. This fit (the diffusion approximation prediction) describes the data well; allowing the linear fit to have a y-offset only changes this value to $D_B = 0.71 \pm 0.01 \text{ mm}^2/\mu\text{s}$ (slightly increased because the offset is actually slightly negative for two of the ρ values).

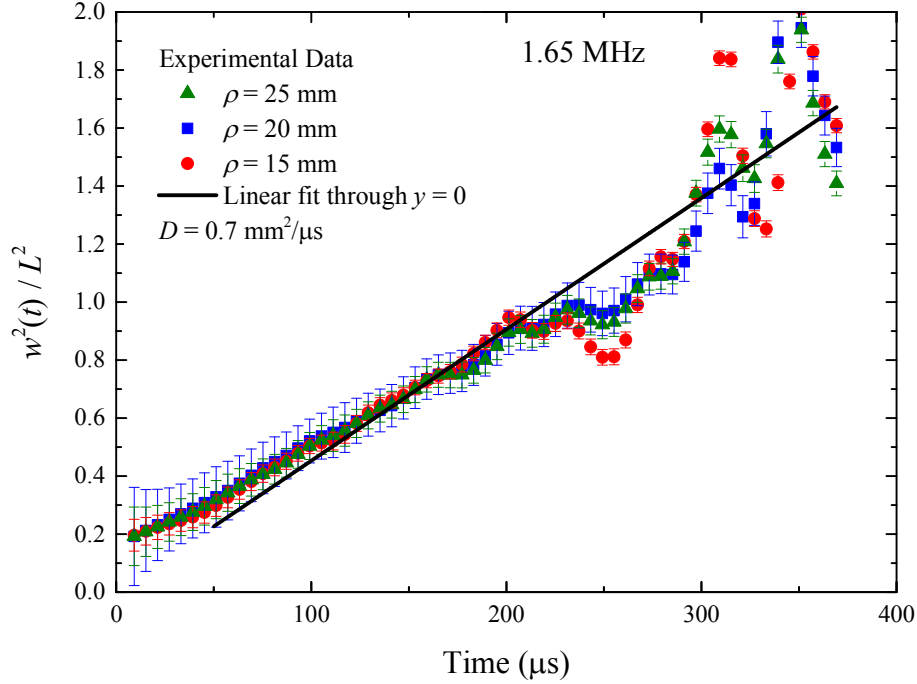


Figure 4.9: Transverse width measured from sample L1, at 1.65 MHz, with experimental uncertainty. Frequency filter width is 35 kHz. Error bars represent the uncertainty in the configurational average. Only every 150th data point is shown for clarity. Data is fit with a straight line, with the y-intercept either held at zero (black solid line) or allowed to vary (not shown as the fit result overlaps almost completely with the black solid line). For fits through $y = 0$, an average over all ρ values gives an estimate of $D_B = 0.706 \pm 0.002 \text{ mm}^2/\mu\text{s}$.

Experimental time-of-flight profiles at 1.65 MHz are shown with several theoretical fits in Figure 4.10. Clearly, changing the transport mean free path impacts the best fit value of D_B . In fact, this is the parameter that has the most impact on D_B ; for instance, changing R to 0.45 and keeping all other parameters constant only changes D_B by $0.005 \text{ mm}^2/\mu\text{s}$. A similar observation was made by Page et al. (Page et al. 1995). From the above plots it looks as though the best fits are for $\ell^* \sim 4 \text{ mm}$ and $D_B \sim 1.3 \text{ mm}^2/\mu\text{s}$. However, this is contradicted by the results from the $w_\rho(t)$, which gives an estimate of $D \sim 0.7 \text{ mm}^2/\mu\text{s}$. A reasonable choice for final parameters from both TOF and $w_\rho^2(t)$ fitting is $\ell^* = 8 \text{ mm}$ and $R = 0.75$, which gives $D_B = 0.805 \pm 0.004 \text{ mm}^2/\mu\text{s}$ and $\tau_A = 133 \pm 2 \mu\text{s}$.

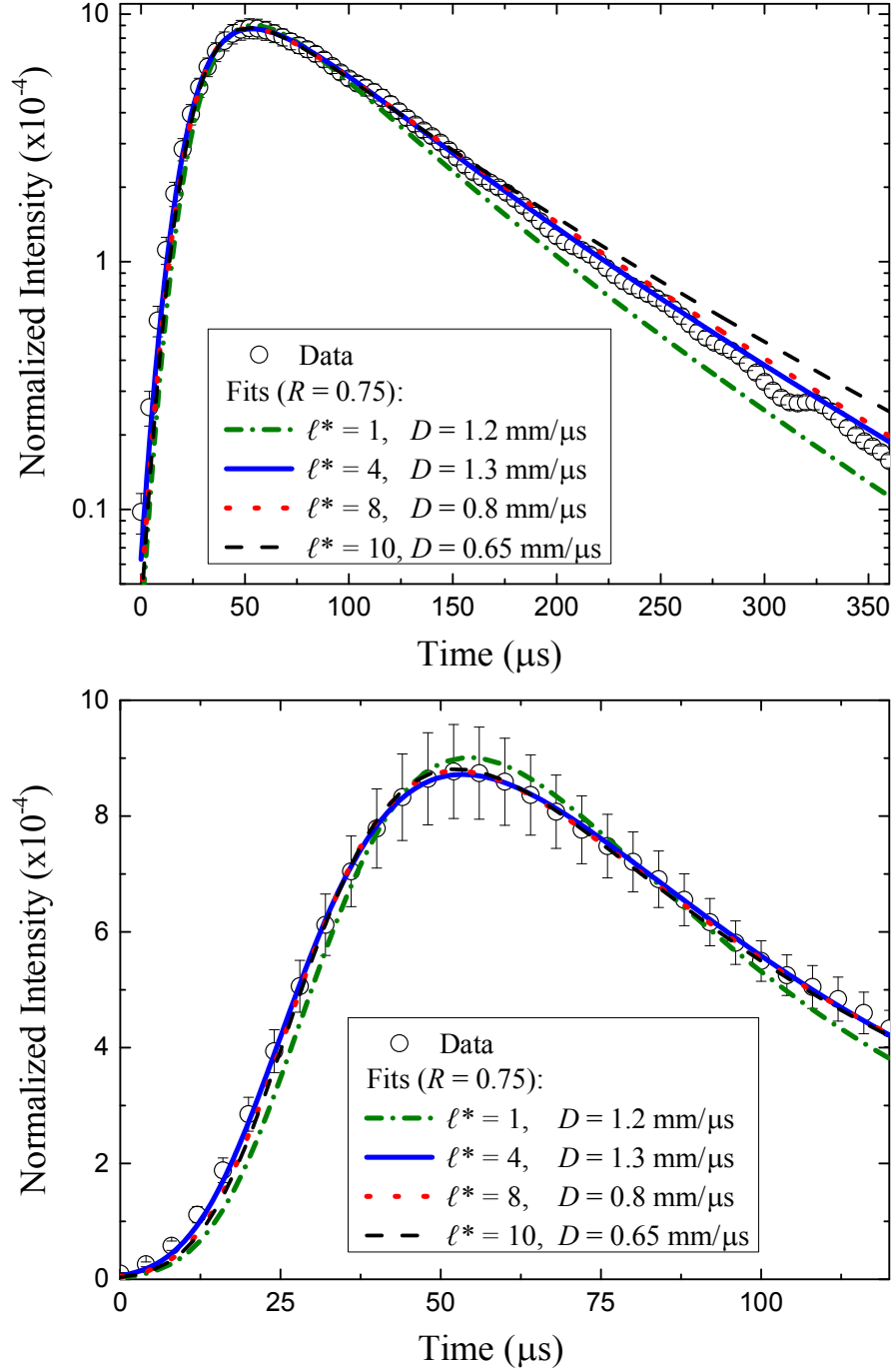


Figure 4.10: TOF profiles for sample L1 (open circles) and fits with diffusion theory. Plots are shown with intensity on a logarithmic scale to illuminate the long-time behaviour (top) and a linear scale to highlight early-time behaviour (bottom). The fit for $\ell^* = 1 \text{ mm}$ (green dash-dot line) is an example of an ℓ^* value that is too low. The fit for $\ell^* = 10 \text{ mm}$ (black dashed line) is an example of an ℓ^* value that is probably too high. Fits for $\ell^* = 4 - 8 \text{ mm}$ overlap almost completely. These fits ($\ell^* = 4 - 8 \text{ mm}$) give diffusion coefficients of $D_B = 0.8 - 1.3 \text{ mm}^2/\mu\text{s}$. Here, $t = 0$ is the time at which diffusion starts.

In backscattering, changing the value of R also does not make much difference; over a range of $R = 0.65 - 0.85$ with all other parameters constant, D_B only changes by $\sim 0.1 \text{ mm}^2/\mu\text{s}$. In fact, the best-fit value of D_B at 1.65 MHz was found not to depend as much on most input parameters such as velocity or mean free path, ranging from around $0.65 - 0.75 \text{ mm}^2/\mu\text{s}$ over a wide range of ℓ_s , ℓ^* , and R values. For example, choosing $\ell_s = 1.1 \text{ mm}$, $\ell^* = 8 \text{ mm}$, and $R = 0.75$ gave a best-fit value of $D_B = 0.72 \pm 0.02 \text{ mm}^2/\mu\text{s}$. Changing ℓ^* to 4 or 10 mm gives $D_B = 0.72 \pm 0.02 \text{ mm}^2/\mu\text{s}$ or $D_B = 0.73 \pm 0.02 \text{ mm}^2/\mu\text{s}$, respectively. Thus, even with the uncertainty related to measuring R and ℓ^* , I can state that backscattering measurements give $D_B = 0.7 \pm 0.2 \text{ mm}^2/\mu\text{s}$. This value agrees within error with the linear fit of $w_p^2(t)$, but not with the result from the TOF fitting.

It seems that we could use this result to narrow down the ‘real’ value of ℓ^* . Since we are reasonably sure of our measurement of $D_B = 0.7 \pm 0.1 \text{ mm}^2/\mu\text{s}$ from both the CBS and $w_p(t)$ fitting, we could choose a fit result for the TOF curves that gives a similar value of D_B . For the 1.65 MHz data presented here this would give a result of $\ell^* \sim 9 \pm 2 \text{ mm}$.

4.5. Conclusion

I have observed conventional diffusion of ultrasound in sample L1 at 250 kHz and likely at 1.65 MHz. Using both transmission and backscattering measurements, I have measured $D_B = 0.7 \pm 0.2 \text{ mm}^2/\mu\text{s}$ at 250 kHz. The theory presented for CBS from a 3D medium in the diffuse regime was shown to describe the experimental data very well, and gave results which are consistent with results from the established methods of measuring D in transmission. This constitutes the first experimental verification of this theory.

Some ambiguities in the analysis at 1.65 MHz remain, both in reflection and transmission.

Slightly subdiffusive behaviour may be complicating the comparison of experiment and theory in transmission, i.e., at later times, the diffusion coefficient may be becoming slightly renormalized from its initial value D_B . This hypothesis is supported by the observation of recurrent scattering at 1.65 MHz, even though we have established that wave behaviour is mostly diffusive at this frequency (this is discussed in Chapter 4).

Appendix 4A : Diffuse far-field simplification

This section contains details of how the diffuse far-field approximation simplifies Equation (4.21), which is reproduced here:

$$I_{coh}(\vec{R}) = \int_0^\infty dR_1 R_1 \int_0^\infty dR_3 R_3 \int_0^{2\pi} d\phi_1 \int_0^{2\pi} d\phi_3 \cos[k(\mu_1 - \mu_3)\omega + k(s_1 \sin \phi_1 - s_3 \sin \phi_3)\rho] \\ \times \frac{\exp\left(-\frac{R_1^2 + R_3^2 - 2R_1 R_3 \cos \phi_{13}}{4D_B t}\right)}{(a^2 + R_1^2)(a^2 + R_3^2 + \rho^2 - 2\rho R_3 \cos \phi_3)} \sum_{m=1}^\infty e^{-m^2 \pi^2 D_B t / L_{eff}^2} L_m(\mu_1, \mu_3)$$

The exponential containing the \vec{R} dependence rapidly kills off all contributions for which $(\vec{R}_1 - \vec{R}_2) > \sqrt{4Dt}$, which is the size of the diffuse halo. If this size is $\ll a$ (the diffuse far-field approximation), then $\sqrt{a^2 + R_i^2}$ does not vary much. Thus, we can write

$$I_{coh}(\vec{R}) = \int_0^\infty d^2 \vec{R}_1 \int_0^\infty d^2 \vec{R}_3 \frac{\exp\left(-\frac{R_{13}^2}{4D_B t}\right)}{(a^2 + R_1^2)(a^2 + R_1^2 + \rho^2 - 2\rho R_1 \cos \phi_1)} \\ \times \cos[k(\mu_1 - \mu_3)\omega + k(s_1 \sin \phi_1 - s_3 \sin \phi_3)\rho] \sum_{m=1}^\infty e^{-m^2 \pi^2 D_B t / L_{eff}^2} L_m(\mu_1, \mu_3) \quad (4A.1)$$

The phase factor of (4.20) can be expanded to first order as:

$$\begin{aligned}
\mu_1 - \mu_2 &= -\frac{a}{(a^2 + R^2)^{3/2}}(x\Delta x + y\Delta y) \\
&= -\mu^2 s \left(\cos \phi \frac{\Delta x}{a} + \sin \phi \frac{\Delta y}{a} \right)
\end{aligned} \tag{4A.2}$$

and

$$\begin{aligned}
s_1 \sin \phi_1 - s_2 \sin \phi_2 &= \frac{y_1}{\sqrt{a^2 + R_1^2}} - \frac{y_2}{\sqrt{a^2 + R_2^2}} \\
&= \frac{y}{\sqrt{a^2 + R^2}} - \frac{y - \Delta y}{\sqrt{a^2 + (\bar{R} - \Delta \bar{R})^2}} = \frac{\Delta y}{\sqrt{a^2 + R^2}} - y \frac{\bar{R} \cdot \Delta \bar{R}}{(a^2 + R^2)^{3/2}} \\
&= \mu \frac{\Delta y}{a} - \sin \phi \mu s^2 \left(\cos \phi \frac{\Delta x}{a} + \sin \phi \frac{\Delta y}{a} \right)
\end{aligned} \tag{4A.3}$$

So the Equation (4A.1) becomes

$$\begin{aligned}
I_{coh}(\bar{R}) &= \int_0^\infty d^2 \bar{R}_1 \int_0^\infty d^2 \bar{R}_{13} \frac{\exp\left(-\frac{R_{13}^2}{4D_B t}\right)}{(a^2 + R_1^2)(a^2 + R_1^2 + \rho^2 - 2\rho R_1 \cos \phi_1)} \\
&\times \cos\left(A \frac{\Delta x}{a} + B \frac{\Delta y}{a}\right) \sum_{m=1}^\infty e^{-m^2 \pi^2 D_B t / L_{eff}^2} L_m(\mu_1, \mu_3)
\end{aligned} \tag{4A.4}$$

with

$$\begin{aligned}
A &\equiv -\mu^2 s \cos(\phi) k w - \sin(\phi) \mu s^2 \cos(\phi) k \rho \\
B &\equiv -\mu^2 s \sin(\phi) k w + (\mu - \sin^2 \phi \mu s^2) k \rho
\end{aligned} \tag{4A.5}$$

Inserting $\Delta \bar{R} = (R \cos \phi, R \sin \phi)$, we have

$$\begin{aligned}
I_{coh}(\bar{R}) &= \int_0^{2\pi} d\phi \int_0^\infty R dR e^{-\frac{R^2}{4D_B t}} e^{i \frac{R}{a} (A \cos \phi + B \sin \phi)} [\dots] \\
&= \int_0^\infty R dR e^{-\frac{R^2}{4D_B t}} \int_0^{2\pi} d\phi e^{i \sqrt{A^2 + B^2} \frac{R}{a} [\cos(\phi - \vartheta)]} [\dots] \\
&= \int_0^\infty R dR e^{-\frac{R^2}{4D_B t}} J_0\left(\sqrt{A^2 + B^2} \frac{R}{a}\right) [\dots] \\
&= 2Dt e^{-\frac{A^2 + B^2}{a^2} Dt}
\end{aligned} \tag{4A.6}$$

where J_0 is a Bessel function of the first kind. For brevity [...] refers to the additional factors

$$\frac{\sum_{m=1}^{\infty} e^{-m^2 \pi^2 D_B t / L_{eff}^2} L_m(\mu_1, \mu_3)}{(a^2 + R_1^2)(a^2 + R_1^2 + \rho^2 - 2\rho R_1 \cos \phi_1)} \quad \text{and} \quad \cos \vartheta \equiv A / \sqrt{A^2 + B^2}. \quad \text{The last step in (4A.6) is}$$

accomplished via the Bessel function integral identity (Gradshteyn and Ryzhik 2000)

$$\int_0^{\infty} dR \, R e^{-R^2 \zeta} J_0\left(\frac{R}{\beta}\right) = \frac{1}{4\zeta} e^{-\frac{\beta^2}{4\zeta}}. \quad (4A.7)$$

The factor $A^2 + B^2$ is quite complicated. Expanding, it becomes

$$(\mu^2 s k w)^2 + \mu^2 (k \rho)^2 [\sin^2 \phi s^4 + 1 - 2 \sin^2 \phi s^2] + (2\mu^3 s^3 \sin \phi - 2\mu^3 s \sin \phi) k \rho k w. \quad (4A.8)$$

In experimental situations, great efforts are made to have detection parallel to the sample face,

thus setting $w = 0$. Applying this to (4A.8) gives $\mu^2 (k \rho)^2 [\sin^2 \phi s^4 + 1 - 2 \sin^2 \phi s^2]$, and

thus (4A.4) becomes Equation (4.23), reproduced here:

$$I_{coh}(\bar{R}) = C \int_0^{\infty} dR R \int_0^{2\pi} d\phi \frac{\exp\left(\mu_1^2 \frac{(k\rho)^2 D_B t}{a^2} [s^4 \sin^2 \phi + 1 - 2s^2 \sin^2 \phi]\right)}{(a^2 + R^2)(a^2 + R_3^2 + \rho^2 - 2\rho R_3 \cos \phi_3)} \sum_{m=1}^{\infty} e^{-\frac{m^2 \pi^2 D_B t}{L_{eff}^2}} L_m(\mu_1, \mu_3)$$

where C is a multiplicative factor.

5. The Anderson Mobility Gap

5.1. Introduction

The concept of Anderson localization (introduced briefly in Section 2.5 of this thesis) was first proposed by Philip Anderson in 1958 (Anderson 1958). The system that was described involved a lattice on which electrons could hop from site to site. The energies of the sites have a disordered distribution, and for strong enough disorder, the electron eigenstates become localized in space, in that the envelope of the wavefunction decays exponentially in space. Equivalently, one can fix the disorder strength and vary the energy of the electrons. Particles in states with low energy are expected to be localized, whereas those with high enough energy (for 3D, and for not too strong disorder) can remain delocalized. There is thus some critical energy, also called the *mobility edge*, at which there is a transition between localized and delocalized states (Wölfle and Vollhardt 2010). For 3D quantum systems (in the orthogonal universality class⁸), there is only one such critical energy, above/below which the system is localized/delocalized.

In contrast, localization of classical waves in 3D is only expected to occur in some intermediate band of energy (or frequency). This is because localization is an extreme case of strong scattering, and for classical waves, the strength of scattering depends mainly on the frequency of the waves and the structure of the medium. At low frequencies where the wavelength is large compared to the scatterer size, the frequency dependence of Rayleigh scattering means that scattering is weak ($k\ell_s \gg 1$), so localization is unlikely. At high frequencies where wavelength is small compared with scatterer size or separation, the weak scattering condition is again reached, and localization is also unlikely. Strong scattering, and hence the possibility of localization, only occurs at intermediate frequencies somewhere in between. Thus, the localization regime for classical waves is expected to be bounded by two mobility edges (MEs), with conventional diffusion occurring both below the lower ME and

above the upper ME. To date, previous works with classical waves in 3D have only ever been able to detect at most one mobility edge, due to substantial experimental challenges (Hu et al. 2008; Hildebrand et al. 2014; Hildebrand 2015).

In this chapter, I present the first experimental measurements to span an entire Anderson localization regime for classical waves, including the two mobility edges on either side of it; we term this regime a *mobility gap*. These observations were accomplished through the comparison of a large amount of experimental data with predictions from the local self-consistent (SC) theory of localization. I used both transmission and backscattering measurements to measure the localization length ξ all the way through the mobility gap, thereby determining the location of the two accompanying mobility edges on either side of it. The use of the dynamic CBS effect to study localization is completely novel, and suggests a path towards a measurement of the critical exponent governing the Anderson transition.

5.1.1. The experimental search for localization of classical waves in 3D

The first experimental investigations of localization of classical waves in 3D used light waves. These measurements focussed on the static (time-integrated) CBS profile (Wiersma et al. 1997; Schuurmans et al. 1999). However, in stationary experiments it is notoriously difficult to exclude absorption, which can mimic (or even obscure) the effects of localization. For this reason, measurements which are both spatially and time-resolved have become increasingly popular to search for signatures of localization, as absorption-independent quantities may be calculated (Weaver and Lobkis 2000; Chabanov, Stoytchev, and Genack 2000).

My experimental methods enable measurements that are resolved in space, time, and frequency. These measurements are: the dynamic CBS effect in reflection, and the dynamic transverse intensity profile in transmission, which were both introduced in the context of

conventional diffusion in Chapter 4. Both of these techniques measure the spreading of wave energy in the transverse direction in the sample (parallel to the slab face). In transmission, this spreading is directly measured via the dynamic transverse intensity profile width $w_\rho^2(t)$. In the diffuse regime, the spatial intensity profile is Gaussian, so the transverse width depends on the Boltzmann diffusion coefficient D_B as $w_\rho^2(t) = 4D_B t$ (as introduced in Chapter 4). In the localization regime, the spreading of the wave pulse through the sample is hindered by interference effects, so $w_\rho^2(t)$ is expected to deviate from a linear dependence on time, eventually saturating to a constant value. This *transverse confinement* of wave energy has been observed by the group of Page et al. for localized ultrasound in monodisperse, slab-shaped samples (Hu et al. 2008). This technique was also employed in recent attempts to observe localization of light in 3D, but these measurements were severely limited by nonlinear effects, such as fluorescence, whose signatures mimic those of localization (Sperling et al. 2016)¹⁷.

Similarly to $w_\rho^2(t)$, the dynamic coherent backscattering profile $I(\rho, t)$ is independent of absorption if *at each time* the intensity profiles are normalized to 1 (i.e. the ratio $I(0, t)/I(\rho, t)$ is measured). The shape of $I(\rho, t)$, not the amplitude, is the most sensitive to wave scattering processes inside the medium. The measurement of dynamic CBS is in fact directly related to $w_\rho^2(t)$; the width of the backscattering cone is the Fourier transform of the transmitted transverse

¹⁷ Note that, in acoustics, fluorescence does not exist. I do not anticipate that other nonlinear effects will affect my data. In reflection, the input intensity is very low (conversely to the optics experiments by Sperling et al.), especially taking into account the source-sample distance and the wave spreading due to diffraction. In transmission, the input intensity is higher, but we have not seen evidence of nonlinearity for brazed samples or for granular samples where nonlinearities should be higher.

width¹⁸; $\Delta\theta^{-2}(t) \propto w(t)^2$. Thus, both $w_p(t)$ and $\Delta\theta^{-2}(t)$ increase with time, indicating a spreading of the transverse confinement profile in transmission and a *narrowing* of the CBS profile in backscattering. From this we can intuit that in the localization regime, the behaviour of $\Delta\theta^{-2}(t)$ should deviate from a linear increase just as that of $w_p^2(t)$ does. It could be expected that near localization, $\Delta\theta^{-2}(t)$ should increase more slowly, possibly saturating at long times. In this thesis the first observation of such behaviour is reported and confirmed with theory.

5.1.1.1. Potential localization regimes in my mesoglass samples

The ballistic measurements and amplitude transmission coefficient, presented in Sections 3.2.5 and 3.2.6, are valuable for making a preliminary estimate of where (at which frequencies) we might observe conventional diffusion, versus where we might observe Anderson localization. By comparing these results with theoretical predictions and previous measurements of localization, we can decide on the frequency range at which to concentrate subsequent analysis.

In Section 3.1.1.2, it was observed that L1 and L2 are polydisperse, helping to randomize the bead positions. Importantly, the polydispersity also lessens the depth and width of the band gaps (shown in Figure 3.25) compared to monodisperse samples. It is probable that a higher degree of brazing in L1 and L2 also contributes to this effect. Thus in the transmission gaps of L1 and L2, which we will call *pseudo-gaps*, transmission is lessened, but is not absent. At the lower edge of pseudo-gaps, the density of states is lower, and these frequencies are thus reasonable candidates to show Anderson localization effects (Lee 2014; van Tiggelen 1999). In

¹⁸ The diffuse halo profile in transmission is $\exp(-\rho^2/w^2)$. In reflection, in the far-field approximation ($\theta \approx q_\perp/k$), the width of the (Gaussian) diffuse halo in backscattering, $\exp(-q^2/\Delta\theta^2)$ is related to w as $\Delta\theta^{-2} = k^2 w^2/4$. In the diffuse regime, $w^2 = 4Dt$, so $\Delta\theta^{-2} = k^2 w^2/4 = k^2(4Dt)/4 = k^2 Dt$. This makes sense, since the full width at half maximum (FWHM) of the CBS profile is $\text{FWHM} \propto 1/k\sqrt{Dt}$ (the proportionality factor must be calculated from Equation (4.23)).

previously-studied monodisperse samples where localization was observed, signals were too low in the middle of band gaps to be able to observe the complete localization regime and the expected upper mobility edge; the polydispersity of L1 and L2 is expected to improve transmission all the way through the pseudo-gaps.

By varying frequency, the ‘disorder’ of the system is varied; this is how we access both diffuse and localized regimes. In this thesis, the gap around 1.2 MHz was studied in order to observe the Anderson localization regime and its accompanying mobility edges. Although this (and any other) gap may correspond to an Anderson mobility gap, this can not be stated with any certainty without detailed measurements and comparison to theory.

5.2. The local self-consistent theory of localization

As introduced in Section 2.5.2, the principal idea of the self-consistent (SC) theory of Anderson localization is that the diffusion coefficient becomes renormalized over time by successive scattering events in a disordered medium. In 2000, van Tiggelen et al. extended this analysis to finite, open media by introducing a position-dependent diffusion coefficient (van Tiggelen, Lagendijk, and Wiersma 2000; Skipetrov and van Tiggelen 2006). In this *local SC theory* the diffusion coefficient is now renormalized by leakage at the sample boundaries, as well as by multiple scattering events. The position-dependence of D was later justified using diagrammatic perturbation theory (Cherroret, Skipetrov, and van Tiggelen 2010). In 2008, the local SC theory was compared to experimental measurements of ultrasound transmitted through slab-shaped samples to observe Anderson localization in 3D (Hu et al. 2008). Its application to this specific case has been since refined by myself and others at the Ultrasonics Laboratory (Cobus, Skipetrov, et al. submitted.; Hildebrand 2015). In this thesis, predictions of the local SC

theory are compared to experimental data of both transmitted and reflected ultrasound. This constitutes the first comparison of the local SC theory with experimental data in reflection from a 3D sample.

5.2.1. Outline of local SC theory calculations

The calculation of both transmitted and reflected classical waves from a slab sample is based on the self-consistent equations for the intensity Green's function

$$C(\vec{r}, \vec{r}', \Omega) = \frac{4\pi}{c} \left\langle G(\vec{r}, \vec{r}', \omega_0 + \Omega/2) G^*(\vec{r}, \vec{r}', \omega_0 - \Omega/2) \right\rangle \quad (5.1)$$

and the frequency- and position-dependent diffusion coefficient

$$\frac{1}{D(\vec{r}, \Omega)} = \frac{1}{D_B} + \frac{12\pi}{k^2 \ell_B^*} C(\vec{r}, \vec{r}, \Omega) \quad (5.2)$$

where D_B and ℓ_B^* are the (Boltzmann) diffusion coefficient and the transport mean free path that would be observed in the system for conventional diffusion (in the absence of localization effects). The theory is generalized to the case of anisotropic scattering, i.e. $\ell_B^* > \ell$. The scattering mean free path is denoted in this section as simply ℓ , for brevity.

$C(\vec{r}, \vec{r}, \Omega)$ represents the *return probability*; the probability for a wave to return to a spot \vec{r} that it has previously visited. Now constructive interference from recurrent scattering is being taken into account, unlike in the $\mathbf{\Gamma} \approx \mathbf{L} + \mathbf{C_M}$ approximation typically used to describe coherent backscattering.

On length scales larger than one transport mean free path, $C(\vec{r}, \vec{r}, \Omega)$ is a solution to the stationary diffusion equation

$$\left[-i\Omega - \nabla_{\vec{r}} \cdot D(\vec{r}, \Omega) \nabla_{\vec{r}} \right] C(\vec{r}, \vec{r}', \Omega) = \delta(\vec{r} - \vec{r}') \quad (5.3)$$

In Equations (5.2) and (5.3), $C(\vec{r}, \vec{r}, \Omega)$ must be the same, and thus one looks for a ‘self-

consistent' solution for $C(\vec{r}, \vec{r}', \Omega)$ (Götze 1979; Vollhardt and Wölfle 1980b; Vollhardt and Wölfle 1992).

We define the mobility edge (ME) in terms of the Ioffe-Regel criterion (discussed in Section 2.5.3); a ME is at the critical value $k\ell = (k\ell)_c = 1$. To define the localization length ξ , we first consider an infinite 3D medium, where D is position-independent. This is most convenient in Fourier space:

$$C(\vec{r}, \vec{r}', \Omega) = \frac{1}{(2\pi)^3} \int d^3\vec{q} C(q, \Omega) e^{-i\vec{q}(\vec{r}-\vec{r}')} \quad (5.4)$$

and, from Equation (5.3),

$$C(q, \Omega) = [-i\Omega + q^2 D(\Omega)]^{-1} \quad (5.5)$$

Since Equation (5.3) is only valid for length scales larger than a mean free path, the integral in Equation (5.4) must be similarly constrained. This is done by performing the integral in Equation (5.4) over the transverse component \vec{q}_\perp of the 3D momentum $\vec{q} = \{\vec{q}_\perp, q_z\}$ up to a maximum value of $q_\perp^{\max} = \mu/\ell_B^*$, with $\mu \sim 1$:

$$C(\vec{r}, \vec{r}', \Omega) = \frac{1}{(2\pi)^2} C(\vec{r}, \vec{r}', \Omega) = \frac{1}{(2\pi)^3} \int_{-\infty}^{\infty} dq_z \int_0^{q_\perp^{\max}} dq_\perp dq_\perp C(q_\perp, q_z, \Omega) \quad (5.6)$$

The value of μ is related to the position of the ME. We can see this by combining Equations (5.2), (5.4) and (5.5) and calculating the diffusion coefficient:

$$D(0) = D_B \left[1 - \frac{3\mu}{(k\ell_B^*)^2} \right] \quad (5.7)$$

Thus at the ME $k\ell = (k\ell)_c = 1$, $\mu = \frac{1}{3}(\ell_B^*/\ell)^2$. When fitting data with theory, we do not know $(k\ell)_c$ a priori, so we will adjust $(k\ell)_c$ (as a fit parameter) to obtain the best fit to the data having $\mu = \frac{1}{3}(k\ell)_c^2(\ell_B^*/\ell)^2$.

To define the localization length ξ , Equations (5.1) and (5.2) can be solved for a point source at $\vec{r}' = 0$ and $t' = 0$, in the long-time limit where $D(\Omega) = -i\Omega\xi^2$. In the localization regime $k\ell < (k\ell)_c$, this gives

$$\xi = \frac{6\ell}{(k\ell)_c^2} \left(\frac{\ell}{\ell_B^*} \right) \frac{\chi^2}{1 - \chi^4} \quad (5.8)$$

where $\chi \equiv k\ell/(k\ell)_c$. In our experiments, k , ℓ , and ℓ_B^* are determined before the main fitting procedure, $(k\ell)_c$ is determined from the fitting procedure itself, and Equation (5.8) provides a direct link between $(k\ell)_c$ and ξ . Here we use ξ as the main parameter to come out of the fitting of experimental data. In the diffuse regime $k\ell > (k\ell)_c$, ξ is negative, which does not have physical significance. In the diffuse regime, the absolute value of ξ is the *correlation length* associated with intensity fluctuations in the sample.

Subsequent calculations are performed explicitly for a finite system. For a disordered 3D slab of thickness L confined between the planes $z = 0$ and $z = L$, boundary conditions are added to Equations (5.1) and (5.2):

$$C(\vec{r}, \vec{r}', \Omega) - z_0 \frac{D(\vec{r}, \Omega)}{D_B} (\hat{n} \cdot \nabla) C(\vec{r}, \vec{r}, \Omega) = 0 \quad (5.9)$$

where \hat{n} points inward, normal to the surface of the slab at a point \vec{r} on a surface, and the extrapolation length is the same as that introduced in the diffusion theory of Section 4.2.1; $z_0 = (2/3)l_B^*(1 + R)/(1 - R)$. Equations (5.9) and (5.6) are then solved iteratively to

produce a result for $D(z, \Omega)$. Transmission and reflection coefficients $T(q_{\perp}, \Omega)$ and $R(q_{\perp}, \Omega)$ are then calculated from

$$R(q_{\perp}, \Omega) = D(z, \Omega) \frac{\partial}{\partial z} C(q_{\perp}, z, z' = \ell_B^*, \Omega) \Big|_{z=0} \quad (5.10)$$

and similarly for transmission.

5.3. Comparison of experimental data with self-consistent theory

To observe Anderson localization, experimental data in both transmission and backscattering geometries were acquired. Transverse confinement experiments were performed on samples L1 and L2, with a frequency range of around 700 – 1.3 MHz (see Section 3.2.2 for details). CBS experiments were performed on samples L1 and L2, over frequency ranges of 700 – 1.3 MHz and 1.0 – 1.8 MHz, respectively (see Section 3.2.3 for details). Then, SC fitting of these data was performed for experimental frequencies around the 1.2 MHz pseudo-gap – this is a region which is a good candidate to show localization, and for which there exists both transmission and backscattering data.

The main parameter we desire to measure via the fitting procedure is the localization (correlation) length ξ . As mentioned in the previous section, we also do not know the position (frequency) of the mobility edge, so $(k\ell)_c$ is a free fit parameter which is adjusted to find the best fit value. We fix $k\ell$, and *at each frequency* of the experimental data, the value of $(k\ell)_c$ is estimated from the resulting best fit. Then ξ may be directly calculated from Equation (5.8). Here we will use ξ as the main parameter to characterize how close the system is to a mobility edge: at a ME, ξ diverges.

5.3.1. SC theory for a very thick sample

The thickness of sample L2 prohibits several methods which were employed to study L1, such as the characterization using ballistic measurements. This thickness also limits the amount of SC theory that may be calculated for sample L2. Since it calculates $D(z, \Omega)$ for every $(0 \leq z \leq L)$, the entire calculation takes more time for larger L . Sample L2 is so thick that to generate enough theory sets for good fitting results (for a large range of ξ values) would be prohibitively time-consuming¹⁹. However, in the backscattering geometry, measurements are not as sensitive to the far side of the sample as they are in transmission. Near the localization regime, backscattered waves may spend a long time in a thick sample without reaching the far side. This means that for the range of times experimentally available in my experiments, the CBS effect is not sensitive to sample thickness. Thus, theory for backscattered waves from sample L1 may also be used for L2, for the range of times experimentally available. By extension, the critical and localized regimes may be studied in arbitrarily thick samples, which is useful for many applications in which transmission measurements are not possible. Thus, for this work, SC theory that was calculated for sample L1 was also used to fit sample L2, without any need for adjustment or modification of either theory or experiment. The fitting of CBS data with theory is performed completely separately for L1 and L2.

5.3.2. Fortran and matlab calculations

Numerical solutions to local SC theory were written in Fortran by Sergey Skipetrov, and have since been modified by Lauren Hayward, Fabrice Lemoult, Kurt Hildebrand, and myself.

¹⁹ Several SC calculations for sample L2 were performed, which each lasted almost one month. To fit data with SC theory a large set of calculations is required, a process which is unfeasible for sample L2.

The Fortran code performs the calculations outlined in Section 5.1.1, resulting in $T(q_{\perp}, \Omega)$ and $R(q_{\perp}, \Omega)$. Code has been written (originally in Mathematica by Segey Skipetrov, translated into Matlab and modified by Fabrice Lemoult and myself) to transform these functions into the time-domain (Fourier transform) and, in the case of transmission, into the near-field (Laplace transform), giving intensity $I_T(t/\tau_d, \rho)$, where ρ denotes position on the sample face (perpendicular to the source axis). In reflection no Laplace transform is needed since the experiments are in the far-field, so the result $I_R(t/\tau_d, \theta)$ can be directly calculated; in reflection, $\sin \theta = q_{\perp}/k_0$, where $k_0 = 2\pi f/v_0$ and $v_0 \approx 1500$ m/s is the speed of sound in water. The time-dependence of the theoretical predictions for intensity is scaled by the diffusion time, τ_D .

The most important parameter involved in calculating SC predictions near the Anderson transition is the localization (correlation) length ξ . The calculations are performed over a wide range of ξ values, and then compared to experimental data to determine the best value of ξ . To be able to distinguish between localized and diffuse regimes using ξ , the SC theory calculations employ the parameter L/ξ , which from Equation (5.8) gives $L/\xi < 0$ in the diffuse regime. Fortran calculations of transmitted intensity were performed for the following values of L/ξ : $\{-12, -10, -7, -6, -5, -4, -3, -2.75, -2.5, -2.25, -2, -1.75, -1.5, -1.25, -1, -0.75, -0.6, -0.5, -0.4, -0.3, -0.2, -0.1, 0, 0.1, 0.2, 0.3, 0.4, 0.5, 0.6, 0.75, 1, 1.25, 1.5, 1.75, 2, 2.25, 2.5, 2.75, 3, 4\}$. Calculations of reflected intensity were performed for many, but not all of these values²⁰.

Most remaining input parameters to the theory were determined by measurements of ballistic propagation through sample L1 (Section 3.2.5) and are therefore fixed in the fitting

²⁰ My modification of the Fortran code to output reflected intensity, as well as transmitted intensity, was not implemented until after many of the transmitted intensity calculations had already been completed. Each calculation takes on average around a week, running on the WestGrid computing cluster, with more localized theory taking much longer to finish.

procedure. These are summarized in Table 5.1.

The transport mean free path, ℓ^* , cannot be determined from ballistic measurements, and must be “guessed” by the user. To determine the value of ℓ^* in my system (L1), Fortran calculations were performed for values of ranging from 1.1 - 10 mm, and fit to a few representative frequencies of experimental data. Almost all of the best fits were for $\ell^* = 4$ mm or $\ell^* = 3$ mm. There did not appear to be a relationship between ℓ^* and frequency, and for all frequencies the reduced chi-square values were slightly lower for the $\ell^* = 4$ mm theory sets.

Frequency range (MHz)	1.17 – 1.25
$k\ell_s$	2.9
ℓ_s (mm)	1.1
ℓ^* (mm)	4
L (mm)	25
R (reflection coefficient)	0.67
m (number of steps across sample thickness)	2001
Number of α values (α is the Laplace transform of time)	800
Number of u -values (number of points in spatial frequency domain)	800

Table 5.1: Input parameters for SC Fortran calculations for sample L1.

For example, at $f = 1.175$ MHz, the best fit was for the theory set with $L/\xi = -8$ and $\ell^* = 4$ mm, giving a goodness-of-fit of $\chi^2 = 1.3$. Other theory sets with $L/\xi = -8$ but different values of ℓ^* gave goodness-of-fit values of $\chi^2 = 1.4$ for $\ell^* = 3$ mm, $\chi^2 = 1.4$ for $\ell^* = 1.5$ mm, and $\chi^2 = 1.7$ for $\ell^* = 6$ mm. These values are all within one χ^2 of each other, and gave almost identical fits by eye. Thus, the transport mean free path was estimated to be $\ell^* = 4$ mm for the entire frequency range under consideration (1.17 MHz to 1.27 MHz).

5.3.3. Self-consistent theory fitting procedure

An extensive collection of code for loading, manipulating, fitting and viewing of theory and data was developed by me and Kurt Hildebrand. This code constitutes a major advance over the previous method used by Hu et al., where fits were performed by hand for each individual frequency and theory set (Hu et al. 2008). The new fitting procedure is automated to perform all fitting in one go, and incorporates improvements such as weighting fits with experimental uncertainty. All of this analysis was performed with Wavemetrics software IGOR Pro.

The fitting of experimental data with SC theory was carried out completely separately for transmission (TC data/theory) and reflection (CBS data/theory). The fitting procedures are, however, very similar. For each frequency f of experimental data, the experimental data are compared to each theory set using a weighted non-linear least-squares fitting. This comparison is performed simultaneously over all times and positions. Best fit values are chosen based on the reduced chi-square, χ_{red}^2 (a goodness-of-fit measure). Thus, by finding the best theory set for each frequency, we measure L/ξ as a function of frequency. This in turn enables the identification of the mobility edge, where $L/\xi = 0$ (ξ diverges).

5.3.3.1. Fitting transverse confinement data with SC theory

Fitting transverse confinement data with SC theory is performed simultaneously over both $I(\rho, t)$ and $w_\rho^2(t)$ profiles for a certain experimental frequency, with all times and positions being fit at once. Some representative results for data from sample L1 are shown in Figure 5.1. Due to some known inaccuracies with the fortran calculation results, data for the very earliest times were not included in the fitting. Data for late times (after $400 \mu s$), where echoes off of the emission transducer were visible in the averaged TOF profiles, were not included in the fits.

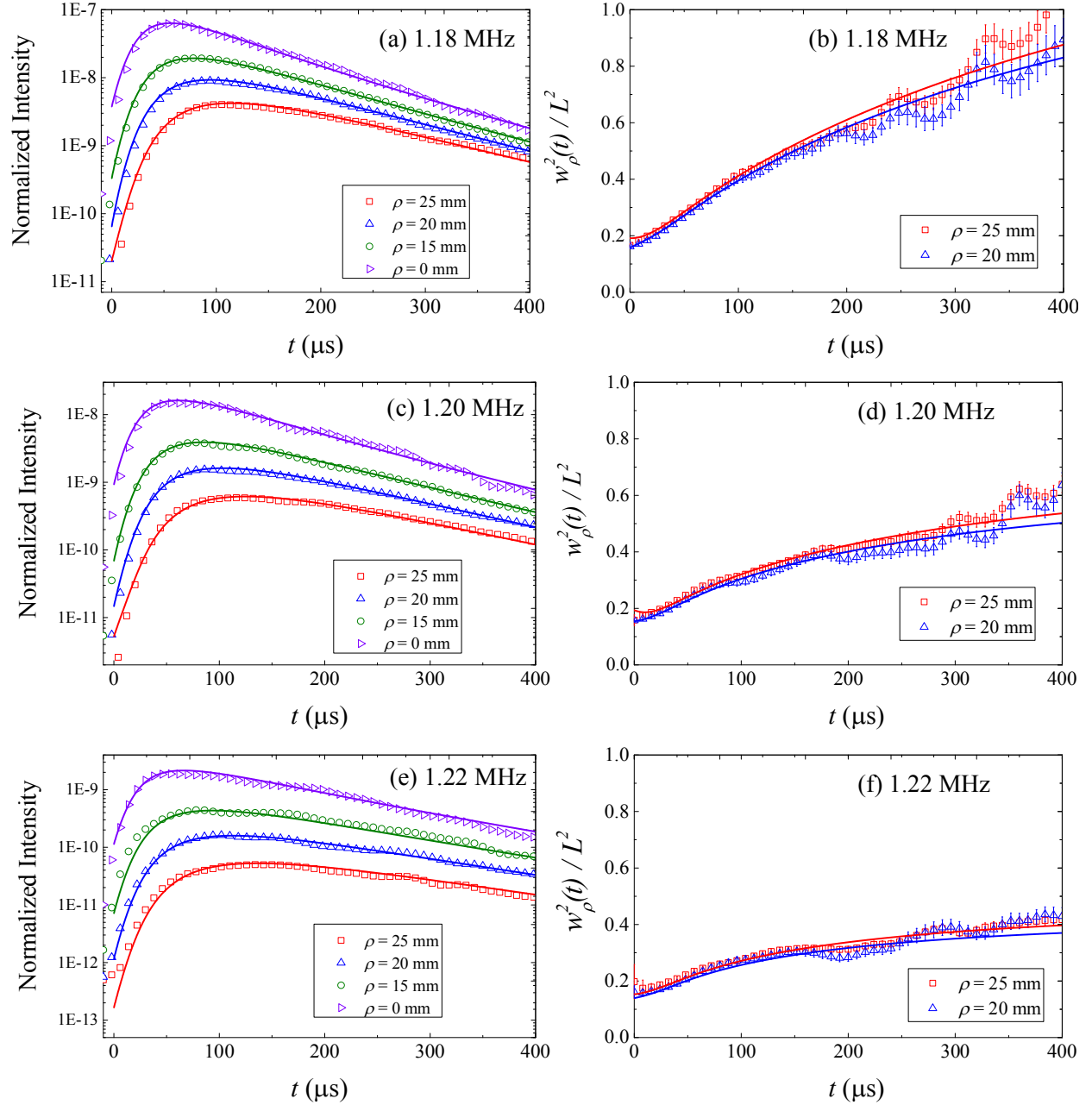


Figure 5.1: Transverse confinement results: solid lines are the best fits of our self-consistent theory to experimental data (symbols), shown for three different frequencies: (a,b) 1.18 MHz (diffuse regime), (c,d) 1.20 MHz (mobility edge), (e,f) 1.22 MHz (localized regime). For clarity, only every 100 data points are shown. Uncertainties reflect the deviation from the average over configurational disorder. Left: Temporal evolution of transmitted intensity, for four different ρ values. Uncertainties are smaller than data points. Right: Temporal evolution of the transverse width squared, $w_\rho^2(t)$, for two different ρ values. Due to large thickness of our sample, the $w_\rho^2(t)$ traces show a greater overlap than previously reported for similar samples (Hu et al. 2008). The transverse width for $\rho = 15$ mm has higher uncertainties, thus contributing less to the global fits. For clarity, it is not shown here, as it overlaps with the traces for other ρ values.

As illustrated in Figure 5.1, the behaviour of both $I(\rho, t)$ and $w_\rho^2(t)$ (symbols) is well-described by SC theory predictions (lines). Excellent fits are obtained for all frequencies. Both theory and data show clear signatures of renormalized diffusion and localization. As the localization regime is approached (as frequency is increased from 1.18 MHz to 1.22 MHz), $I(\rho, t)$ decays less rapidly and $w_\rho^2(t)$ traces become less linear, approaching saturation at long times in the localization regime. This behaviour has been observed for ultrasound in similar samples (Hu et al. 2008; Hildebrand 2015). Even at 1.18 MHz, where waves are not localized, subdiffusive behaviour is evident in Figure 5.1, where $w_\rho^2(t)$ deviates from linearity at long times.

The effect of frequency filtering of the data (see Section 3.2.4) has an effect on the early-time behaviour of both $I(\rho, t)$ and $w_\rho^2(t)$; as can be seen in Figure 5.1, $w_\rho^2(t)$ does not approach zero at $t = 0$. This effect is accounted for in our fitting procedure by the convolution of the theory curves with a pulse with width determined by the filter width. Free parameters in the transmission fitting were τ_D and absorption time τ_A . Since $w_\rho^2(t)$ profiles are independent of absorption, τ_A is determined from the fits of $I(\rho, t)$ alone. Results, shown in Figure 5.2, demonstrate low absorption values for sample L1 over the frequency range of interest, which are similar to values found for similar monodisperse slab samples (Hu et al. 2008).

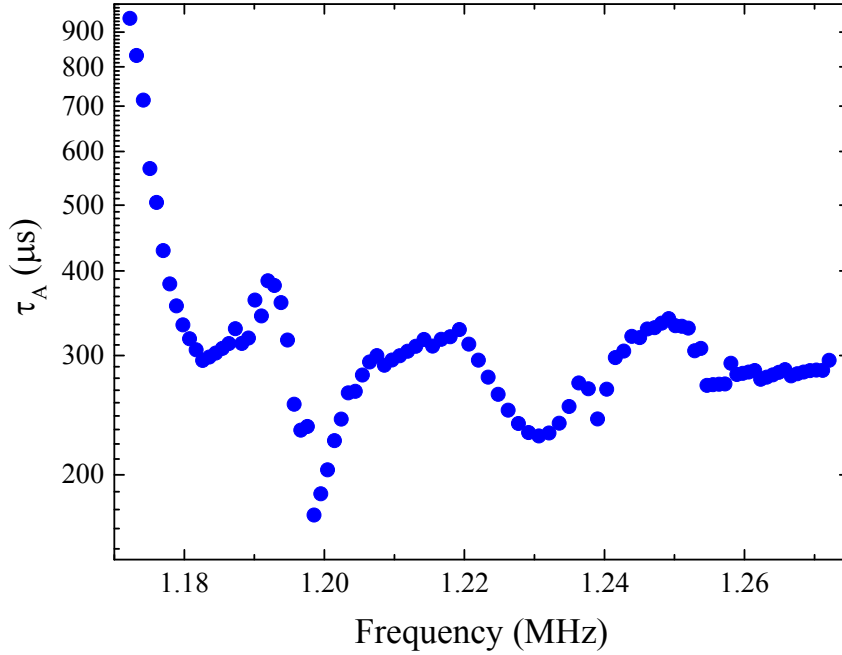


Figure 5.2: Absorption time τ_A of ultrasound in sample L1 as a function of frequency, determined from self-consistent theory fitting of TOF data.

Although the L2 transmission data could not be fit with SC theory, it is possible to make a rough characterization of the behaviour of $w_\rho^2(t)$ by fitting these curves with a power law. At the mobility edge, this quantity has been predicted to obey a power law of the form $w_\rho^2(t) \propto t^{0.5}$, for relatively short times, and to saturate in the long-time limit (Cherroret, Skipetrov, and van Tiggelen 2010). Figure 5.3 shows $w_\rho^2(t)$ from sample L2 at three representative frequencies. Dashed lines are power law fits to the data over the time range 100 – 600 μs (weighted by the experimental uncertainty and averaged over results from both $\rho = 20$ mm and $\rho = 25$ mm). At 1.20 MHz, the data are described by a power law of the form $t^{0.45}$, which is consistent with this frequency being close to (probably slightly higher than) a mobility edge.

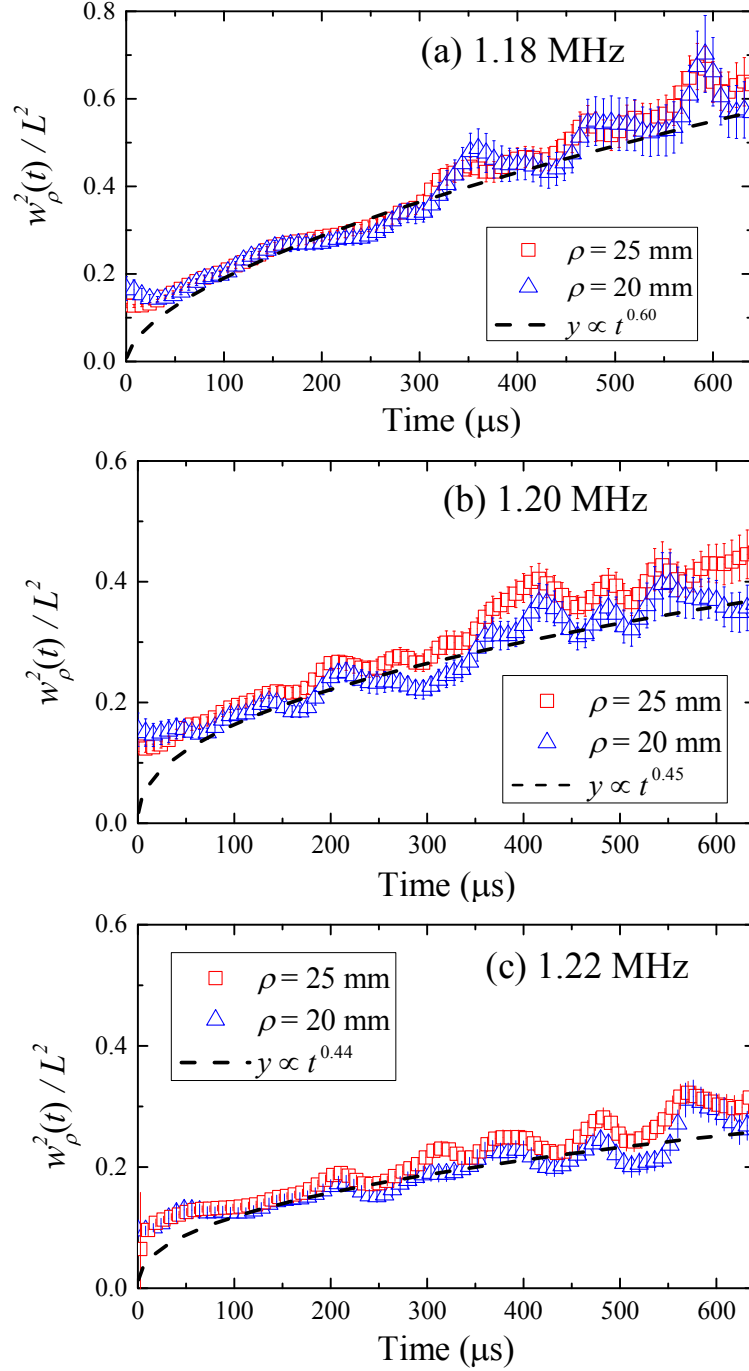


Figure 5.3: $w_\rho^2(t)$ profiles for sample L2 for (a) 1.18 MHz (diffuse regime); (b) 1.20 MHz (mobility edge), and (c) 1.22 MHz (localized regime). Shown are experimental data (symbols) with power law fits, weighted by experimental uncertainties (dashed lines). Fit results (e.g. $y \propto t^{0.60}$ for 1.18 MHz) have been averaged over the power law fits for both $\rho = 20$ mm and $\rho = 25$ mm; for clarity, only fits for $\rho = 20$ mm are shown.

5.4. The Anderson mobility gap probed by coherent backscattering

The inhibition of wave propagation due to localization effects severely limits the magnitude of the transmitted signals, motivating the development of techniques to observe localization in the reflection geometry. A promising tool for these types of measurements is the coherent backscattering (CBS) effect, which for decades has been used to measure transport parameters of disordered media in the diffuse regime. As has been experimentally observed for various types of diffuse waves and scattering media [11–14], the width of the static (time-integrated) CBS profile is directly related to the transport mean free path, ℓ^* . The dynamic (time-dependent) CBS profile provides opportunities to measure additional quantities. As was shown in Chapter 4, for relatively weak scattering where the diffusion approximation is valid, comparison of the dynamic CBS profile with predictions from theory can directly yield quantities such as the Boltzmann diffusion coefficient D_B .

In the localization regime, the CBS effect has also been well-studied, but with less success. Some of the first experimental attempts to observe Anderson localization of classical waves in 3D focused on measurements of the static CBS profile (Wiersma et al. 1997; Schuurmans et al. 1999). However, in stationary experiments it is notoriously difficult to exclude absorption, which can mimic (or even obscure) the effects of localization. For this reason, measurements which are both spatially and time-resolved (such as transverse confinement) have become increasingly popular to search for signatures of localization. As well as offering the advantage of the reflection geometry (over transmission), dynamic CBS profiles have a shape which is independent of absorption (Weaver 1993; Chabanov, Stoytchev, and Genack 2000), and are thus useful in situations in which absorption is difficult to exclude. To my knowledge, no dynamic CBS profiles have yet been compared with theory for very strong scattering (i.e. beyond the

diffusion approximation). In this section, I present the first measurements of the dynamic CBS effect of elastic waves in the localization regime in thick 3D samples. Furthermore, I compare these data with SC theory to probe the Anderson mobility gap.

5.4.1. Experimental backscattering measurements

The dynamic CBS effect from samples L1 and L2 was measured using ultrasonic arrays, as detailed in Section 3.2.3. Figure 5.4 shows the resulting CBS profiles as a function of time and source-detector angle. As observed in the diffuse regime, the dynamic CBS ‘cones’ become narrower as time evolves. For frequencies near the 1.2 MHz pseudo-gap, however, the cones narrow much less rapidly than they do for diffuse frequencies. Recall that in the diffuse regime, the width of the dynamic CBS profile evolves as $\Delta\theta^{-2}(t) \sim Dt$. For Anderson localization, $\Delta\theta^{-2}(t)$ is expected to increase less rapidly and eventually saturate at long times (Skipetrov and van Tiggelen 2006). My experimental data from both samples L1 and L2 display this behaviour, as shown in Figure 5.4. The localization regime is represented by the data at frequency 1.22 MHz; this has been determined from the results of SC theory fitting to TC data (previous section) and to CBS data, presented later in this section.

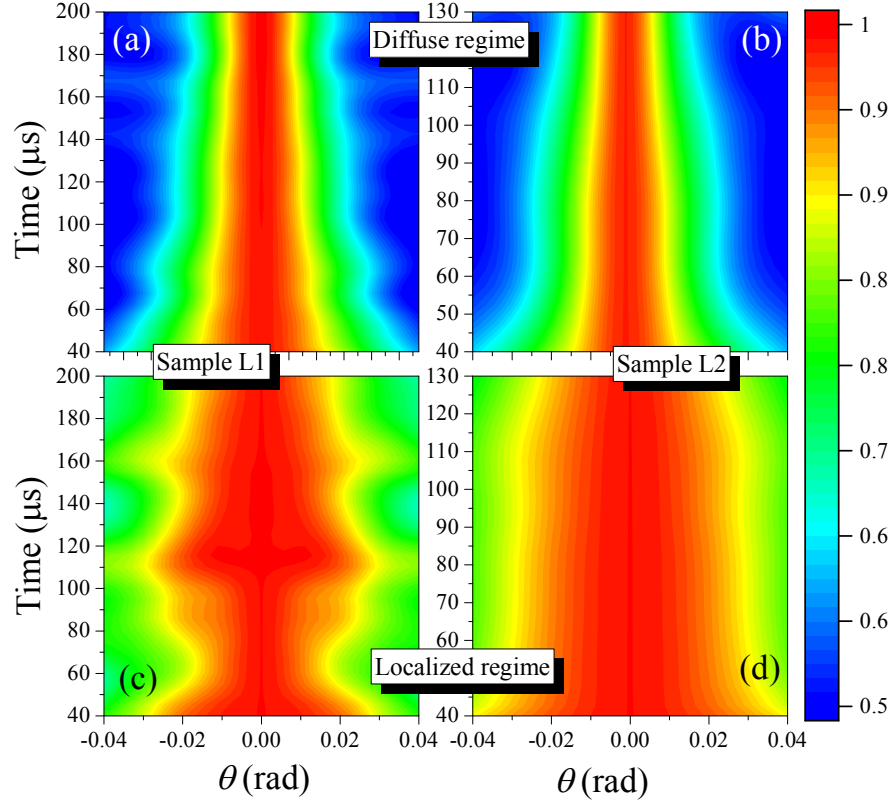


Figure 5.4: Experimental dynamic CBS profiles as a function of both time and angle for samples L1 (a,c) and L2 (b,d). Results are shown in the diffuse regime (1.65 MHz for L1, 2.5 MHz for L2) (a,b) and in the localized regime (1.22 MHz) (c,d). The profiles narrow quite rapidly in the diffuse regime (a,b), but are almost constant (notwithstanding the fluctuations in (c), discussed in the text) over the accessible range of times in the localized regime (c,d).

From Figure 5.4, it is clear that data for L1 in the localized regime display a large amount of fluctuations in both time and space. In the critical and localized regime fluctuations are to be expected, however, the fluctuations shown here cause the SC fitting of L1 CBS data to be more difficult than the same process for L2 data. The fluctuations are more extreme for L1 than for L2 because a greater amount of averaging was performed for the backscattering experiment for L2. Twice as many array elements were available for the experiment on L2, resulting in increased spatial averaging. Despite the large fluctuations, however, the SC fitting of CBS data from L1 is robust (especially for frequencies below 1.23 MHz – see the following sections). This is because many points in time *and* space can be fit simultaneously, in contrast to transmission data which

only have four points in space, corresponding to the different ρ values in the TC experiment.

In order to fit the experimental CBS profiles with theory, the backscattering data presented in this thesis have had the recurrent scattering contribution removed from the total backscattered intensity. Chapter 6 of this thesis describes how, for very strong scattering, recurrent scattering processes increase the apparent background intensity level compared to the peak value. Theory predicts the background level to be exactly one half the peak value. For data near the localized regime (e.g. Figure 5.5 (a-c,e,f)), the profiles are very wide even at late times, so the range of angles experimentally available is not wide enough to show clearly where the background level is. Thus, the recurrent scattering contribution was removed (see Section 6.2.1.1 for more details).

5.4.2. Fitting dynamic CBS profiles with SC theory

The SC theoretical predictions for $I_R(t/\tau_D, \theta)$ are valid in the far field. Our data are also valid in the far-field limit, defined for diffuse waves by the condition $a^2 \gg D_B t$, where a is the sample-array distance. In the diffuse regime for sample L1 (1.65 MHz), $D_B = 0.7 \pm 0.1 \text{ mm}^2/\mu\text{s}$, and the longest times recorded were $210 \mu\text{s}$, so the approximation is valid. This limit should be even better obeyed in the localized regime where the diffuse halo spreads more slowly.

All input parameters and calculation details for SC theory in backscattering are the same as they are for transmission, described in Section 5.3.2. Similarly to transverse confinement fitting, the fitting of CBS profiles with SC theory is performed simultaneously over all times and positions. For each frequency f , the 2D experimental matrix $I(\theta, t)$ is compared to all theoretical matrices $I(\theta, t/\tau_D)$. The fit with the lowest χ_{red}^2 is chosen as the best for that frequency, giving a measurement of $\xi(f)$.

Figure 5.5 shows representative results of theory fits to CBS data for both L1 and L2.

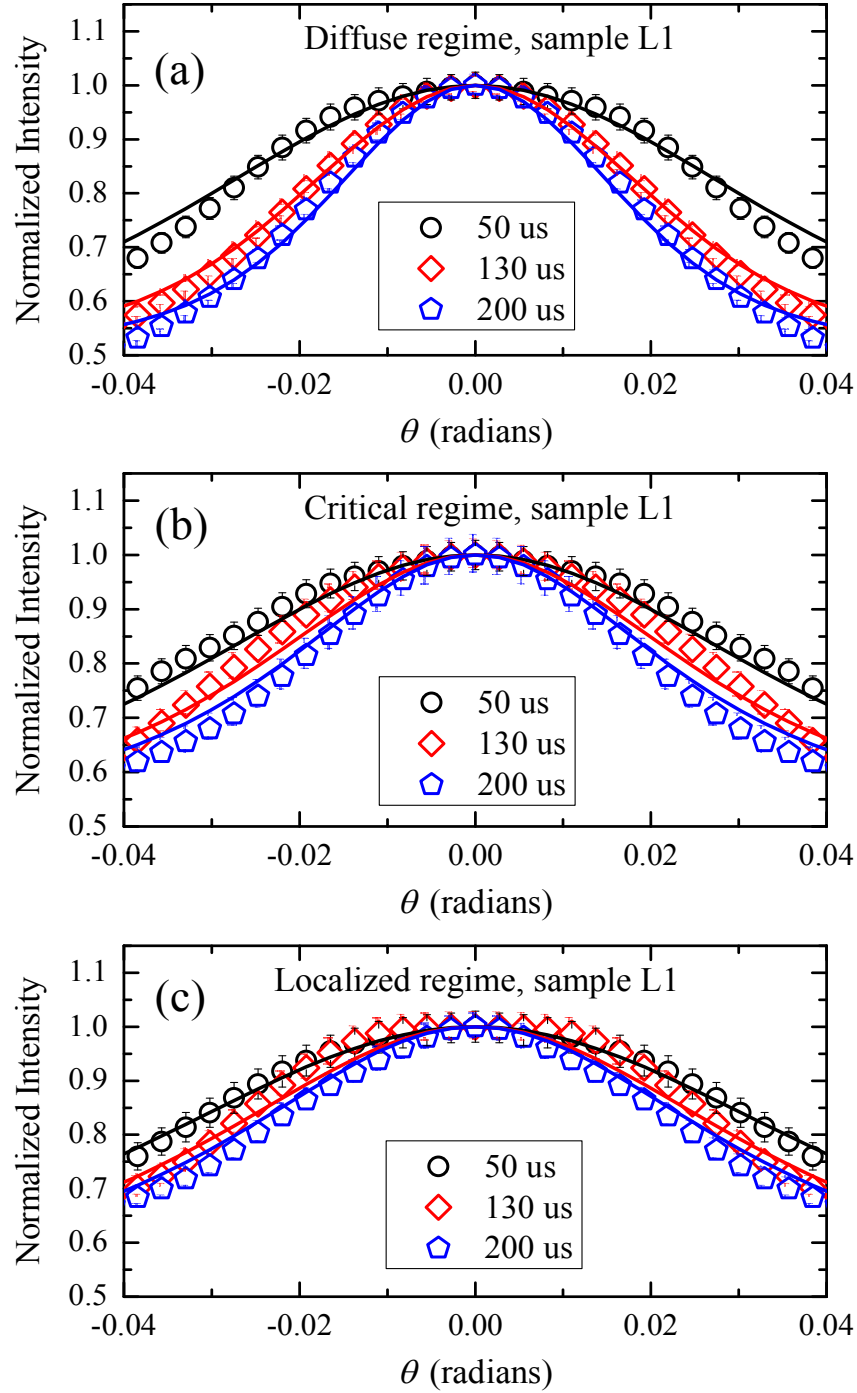
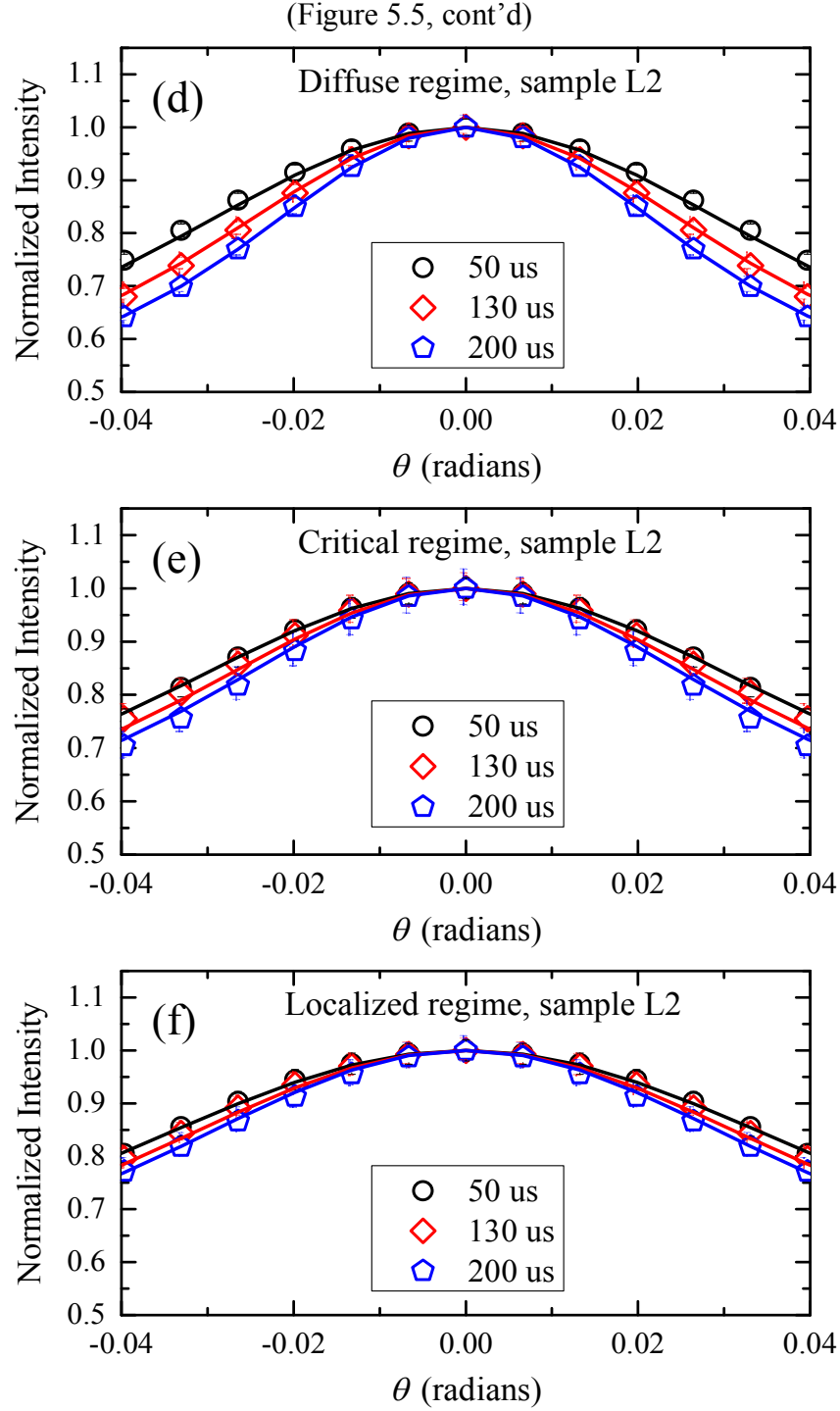


Figure 5.5: Dynamic CBS profiles from samples L1 (top) and L2 (bottom) for three different frequencies: (a), (d) 1.18 MHz in the diffuse regime; (b), (e) near 1.20 MHz at a ME; and (c), (f) 1.22 MHz in the localization regime. For each plot three representative times are shown, illustrating the difference in the rate of profile narrowing between diffuse and localized regimes. Solid lines are best fits of the self-consistent theory to the data (symbols).



Both the experimental and theoretical CBS profiles show a subtle difference in long-time behaviour between diffuse and localized regimes. Profiles shown in Figure 5.5 (a,d) exhibit the narrowing predicted by diffusion theory. As the localization regime is approached (1.18 MHz to

1.20 MHz, to 1.22 MHz), this narrowing slows. This slowing down is expected as the localization regime is approached because, as discussed previously, the inverse width squared of the CBS peak, $\Delta\theta^{-2}$, is proportional to the width of the diffuse halo, w , at the surface of the sample. In the localization regime, the diffuse halo is confined to a space on the order of ξ , and thus its growth in time eventually saturates upon reaching this limit. Therefore the corresponding $\Delta\theta^{-2}$ also stops growing and saturates at long times. This behaviour is illustrated in Figure 5.6 for both experimental data and theoretical fits.

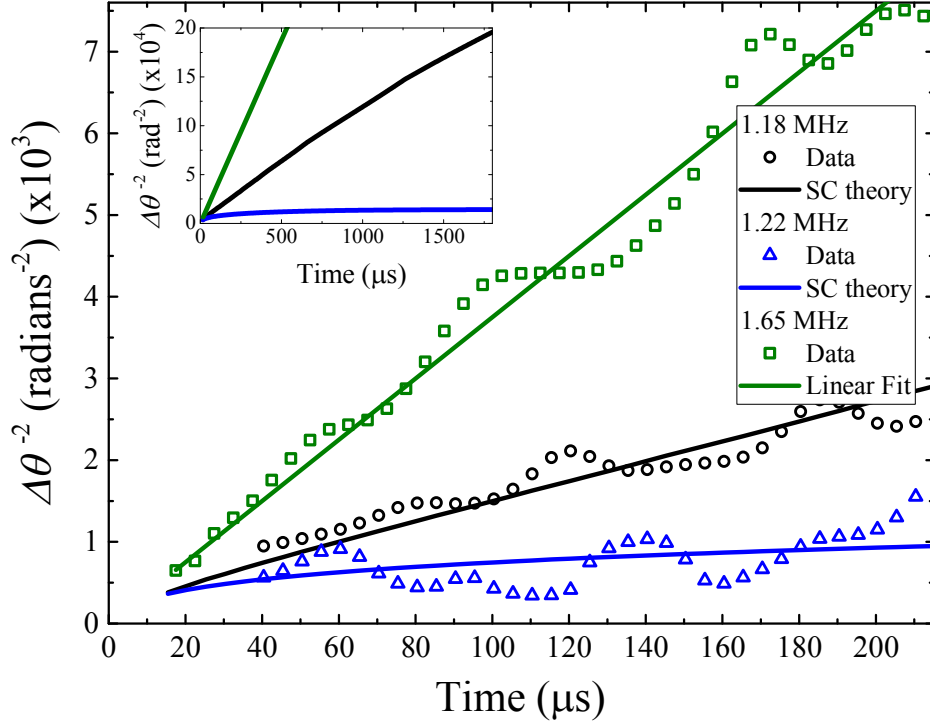


Figure 5.6: The reciprocal of the square of the half width at half maximum of dynamic CBS profiles, $\Delta\theta^{-2}(t)$. Experimental results (symbols – error bars are smaller than symbols sizes) are shown with theoretical predictions of theory (lines) for three representative frequencies: $f = 1.65$ MHz (diffuse regime, fit with theory for diffuse elastic waves, $D_B = 0.7 \pm 0.1 \text{ mm}^2/\mu\text{s}$ extracted from the fit (Section 4.4)), $f = 1.18$ MHz (subdiffusion, fit with SC theory), and $f = 1.22$ MHz (Anderson localization, fit with SC theory). The inset shows theoretical predictions for longer times.

The inset of Figure 5.6 also shows that the long-time behaviour at 1.18 MHz is subdiffuse; the diffusion coefficient exhibits a slow renormalization causing $\Delta\theta^{-2}(t)$ to deviate from

linearity. Since this behaviour is more pronounced at very long times, it is not easily observable in our experimentally-measured $\Delta\theta^{-2}(t)$. However, this observation supports the hypothesis put forward in Chapter 4 that slight subdiffusion is present at frequencies which show very strong scattering, but are not immediately beside a mobility gap. Note that the theory shown in Figure 5.6 for 1.65 MHz (diffuse regime) is simply a straight line, as predicted by diffusion theory.

For each fit of one set of SC theory predictions (one input value of L/ξ) to one set of experimental data (one f). Free parameters in the transmission fitting were τ_D and the incoherent background level. In principle, the background level should be exactly 0.5 (for profiles normalized to 1) since the recurrent scattering contribution to backscattering intensity has been removed. However, the recurrent scattering removal was not perfect, so background intensity level was allowed to vary freely for the SC fitting so as not to distort the results and reliability of my measurement of $\xi(f)$. For both samples L1 and L2, and for almost all frequencies, best fits gave a background of within 10% of 0.5.

5.5. Identification of Anderson mobility edges

One of the goals of this chapter is to precisely identify the location of a mobility edge (ME), i.e. the exact frequency at which the Anderson transition occurs ($L/\xi = 0$). I furthermore desire to characterize the behaviour of L/ξ near a ME, as it is this type of approach which could give information about the critical exponents ν . The measurement of L/ξ as a function of frequency allows the identification of the MEs by finding the experimental frequency which best matches the SC theory set with $L/\xi = 0$. However, since both experimental frequency and L/ξ are discrete sets, this may not be the ‘true’ frequency which matches $L/\xi = 0$, or, equivalently, a theory set which best matches a particular experimental frequency may not represent the ‘true’ value of L/ξ for that frequency. To determine the true L/ξ for a certain frequency in this

fashion, one could calculate a large number of theory sets which differ by very small values of L/ξ . However, this not an elegant solution, and furthermore, computing a great many theory sets takes considerable time and effort. Here I present a method to determine the true value of L/ξ for each frequency. This method also has the advantage of giving an uncertainty estimate for the measurement of L/ξ for each frequency.

5.5.1. Parabola-fitting method

For a particular frequency, the theory set that best matches the experimental data is that which gives the minimum χ^2 according to the method of least-squares. However, this only determines the best match ξ for a particular frequency amongst the theory sets which have been calculated. A better estimate of the ‘true’ value of ξ for each frequency can be found by considering the entire $\chi^2(\xi)$. The concept is this:

The method of least-squares defines a *probability function* $P(a_j)$ which gives the probability, as a function of dependent variable/s a_j , that the experimental data belongs to a particular parent set – a particular set of theoretical predictions. For a sufficiently large data set, the probability function is a Gaussian:

$$P(a_j) = Ae^{-\chi^2/2} \quad (5.11)$$

where $\chi^2 \propto (a_j - a'_j)^2 / \sigma_j^2$, and a'_j is the value of a_j that minimizes χ^2 . To determine a best fit, one seeks to maximize the probability function, which is equivalent to minimizing χ^2 , i.e. finding $a_j = a'_j$ such that $\partial\chi^2/\partial a_j = 0$. Thus, near a local minimum in a_j , χ^2 is a quadratic function of that parameter. Thus the ‘true’ value of a'_j is found at the minimum of this quadratic function of χ^2 , and its uncertainty is given by the curvature of the function near the minimum;

$$\sigma_j^2 = 2 \left(\frac{\partial^2 \chi^2}{\partial a_j^2} \right)^{-1} \quad (5.12)$$

For each frequency of experimental data, the SC theory fitting procedure returns a χ^2 for each theory set, i.e. $\chi^2(\xi)$. Representative results for $\chi^2(\xi)$ are shown in Figure 5.7. By fitting a parabola to a few points around the minimum value of χ^2 , the true minimum and its uncertainty can be found.

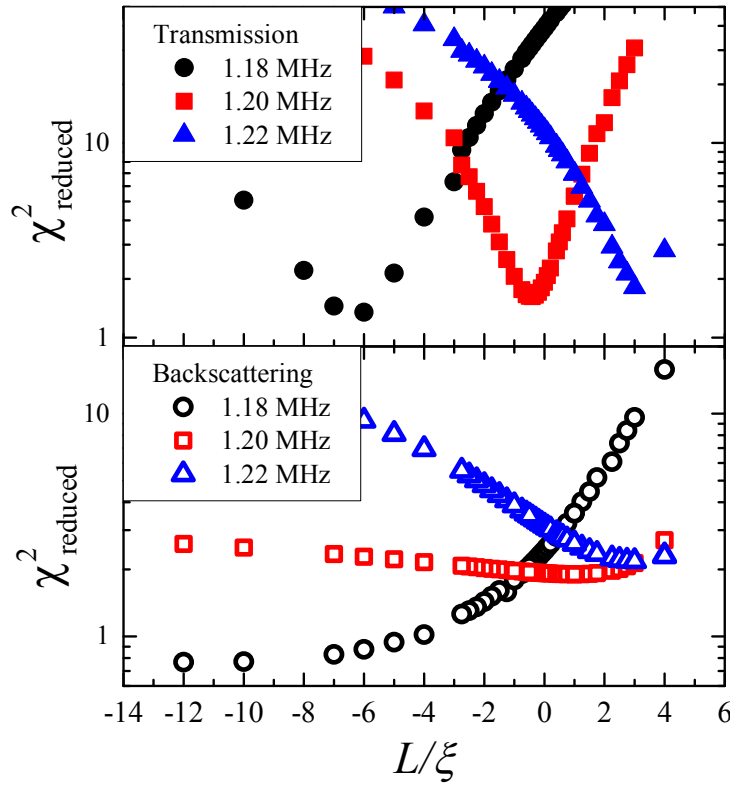


Figure 5.7: χ_{red}^2 vs L/ξ for three different frequencies. Transmission results (left vertical axis) have less uncertainty from the fitting than do backscattering results (right vertical axis).

For transmission results, the parabola-fitting gives an estimation of the actual value of L/ξ which has a very small uncertainty (see, for example, Figure 5.8). This uncertainty is an underestimation of the uncertainty introduced in the entire fitting process, as it does not take into account the inherent uncertainty in the input parameters such as R . However, a comprehensive

study of the certainty and effect on fitting results of each input parameter would be a massive undertaking and is beyond the scope of this project. In stating my results and conclusions I am careful to account for experimental uncertainties and estimations such as the inherent uncertainty in input parameters for SC theory.

5.6. Results for the Anderson mobility gap

Results from SC fitting of data for both L1 and L2 are shown in Figure 5.8. An Anderson mobility gap is clearly identified, bounded by its accompanying mobility edges at 1.198 ± 0.001 MHz (lower ME) and 1.243 ± 0.007 MHz (upper ME). These values were determined by the combination of the three sets of measurements shown in Figure 5.8.

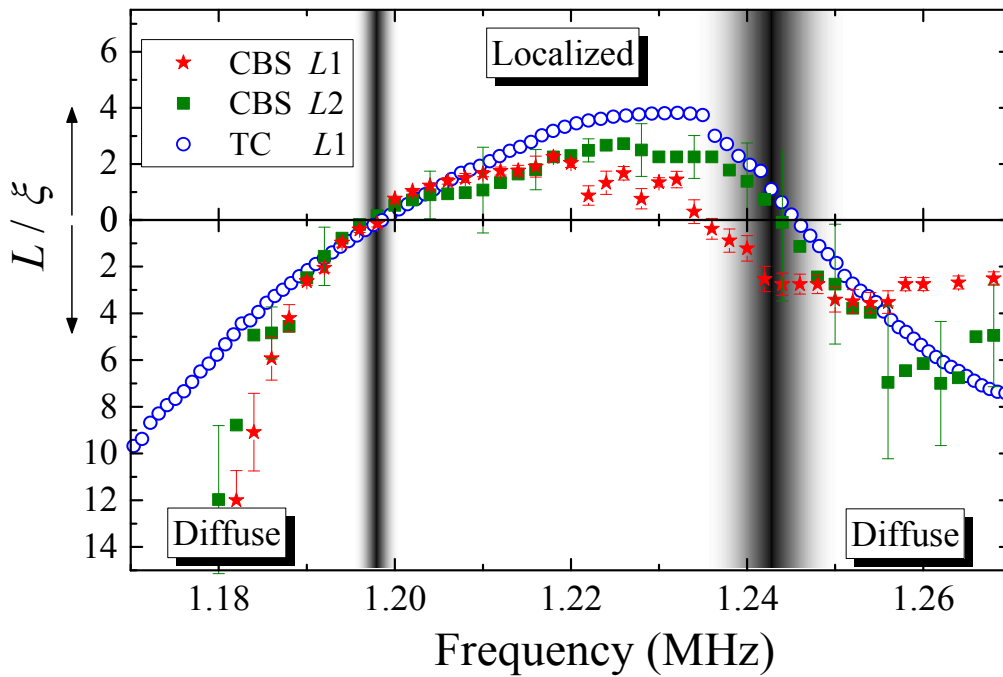


Figure 5.8: Ratio of sample thickness L to the localization (correlation) length ξ , obtained by fitting SC theory to experimental CBS profiles (sample L1, - red stars; sample L2 – green squares) and transverse confinement (TC) data (sample L1 – open circles). Error bars are smaller than symbol size for TC results. Fuzzy vertical gray lines show the resulting estimates of the positions of mobility edges. Thanks to J. H. Page for help with the creation of this figure.

Figure 5.9 shows the localization (correlation) length ξ as a function of frequency; inside the mobility gap ξ reaches a minimum value of 6.5 mm, 3.8 times smaller than the sample thickness. This plot emphasizes the divergence of ξ as the mobility edge is approached.

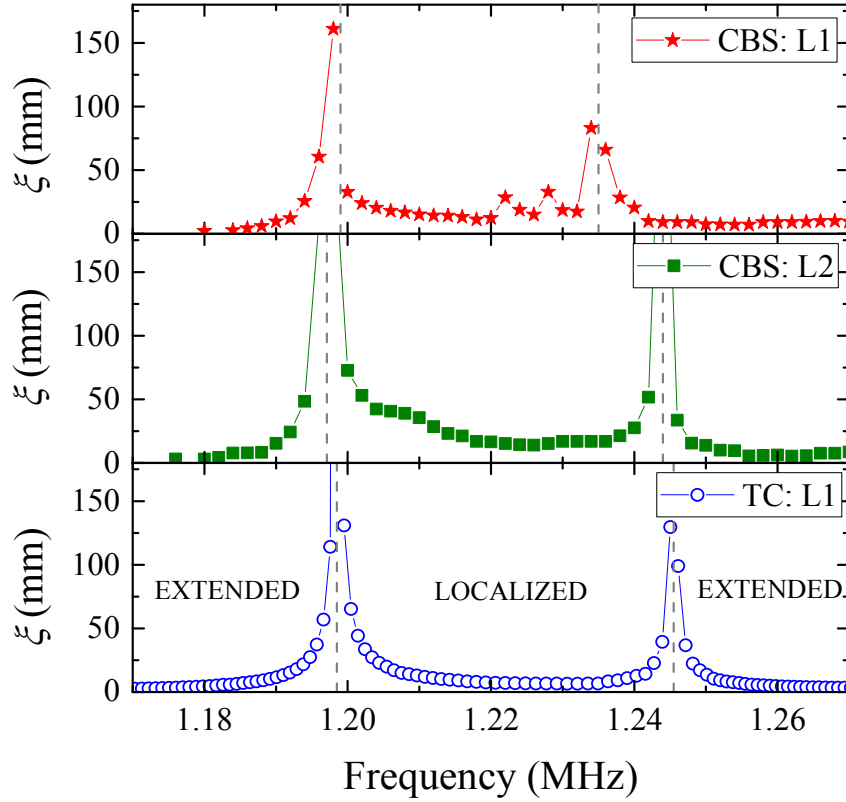


Figure 5.9: Localization (correlation) length ξ as a function of frequency, obtained by fitting SC theory to experimental CBS profiles (sample L1, top; sample L2 – center) and transverse confinement (TC) data for sample L1 (bottom). At each mobility edge, ξ diverges. Dotted vertical lines indicate our estimates of mobility edge positions. Figure created by J. H. Page.

5.6.1. The Boltzmann diffusion coefficient

The diffusion time τ_D was a free fit parameter in the SC theory fitting of TC and CBS data. The diffusion time was allowed to vary freely for all transmission and backscattering fitting. Physically, τ_D may be described as the typical time required for a wave to traverse the sample via conventional diffusion, and is given by $\tau_D = (L + 2z_0)^2 / \pi^2 D_B$ (Skipetrov and van

Tiggelen 2006). Thus, the measurement of τ_D from our fit results allows us to estimate the Boltzmann diffusion coefficient D_B as a function of frequency. Results for τ_D and D_B are shown in Figure 5.10.

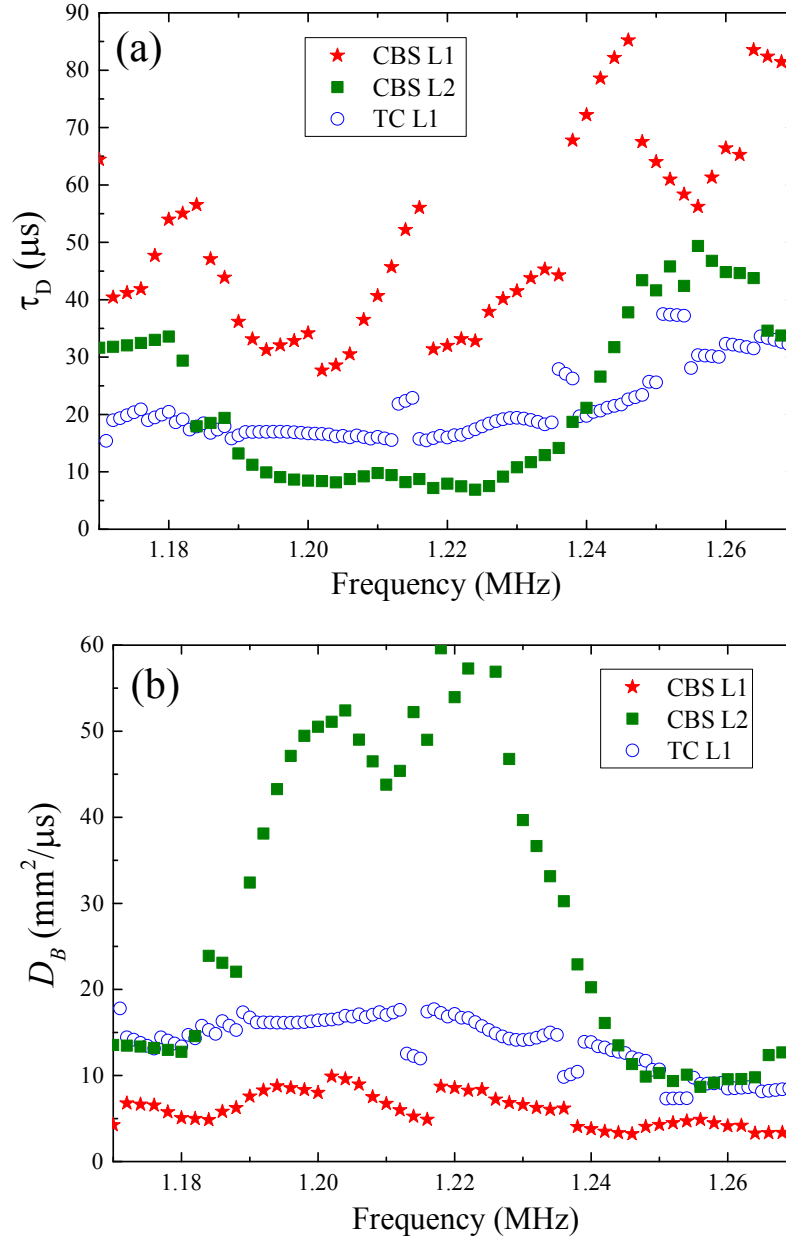


Figure 5.10: The diffusion time τ_D (a) and Boltzmann diffusion coefficient D_B (b), estimated from SC fitting. Results are from TC fitting of L1 (open circles), and CBS fitting of L1 (stars) and L2 (solid squares).

The frequency dependence of τ_D from transmission fitting (open blue circles in Figure

5.10(a)) is supported by visual inspection of the time-dependence of the transmitted intensity. Figure 5.11 shows $I(0, t)$ for several representative frequencies spanning the 1.2 MHz pseudo-gap. The peak arrival time of the average transmitted intensity is much later at frequencies above the pseudo-gap. This makes intuitive sense; for larger values of τ_D , $I(\rho, t)$ curves would be expected to arrive later and decay slower. This behaviour is observed in the transmitted intensity through L1 and L2; as frequency is increased from 1.18 MHz to 1.24 MHz, τ_D increases (Figure 5.10), and $I(\rho, t)$ profiles arrive later and decay more slowly (Figure 5.11).

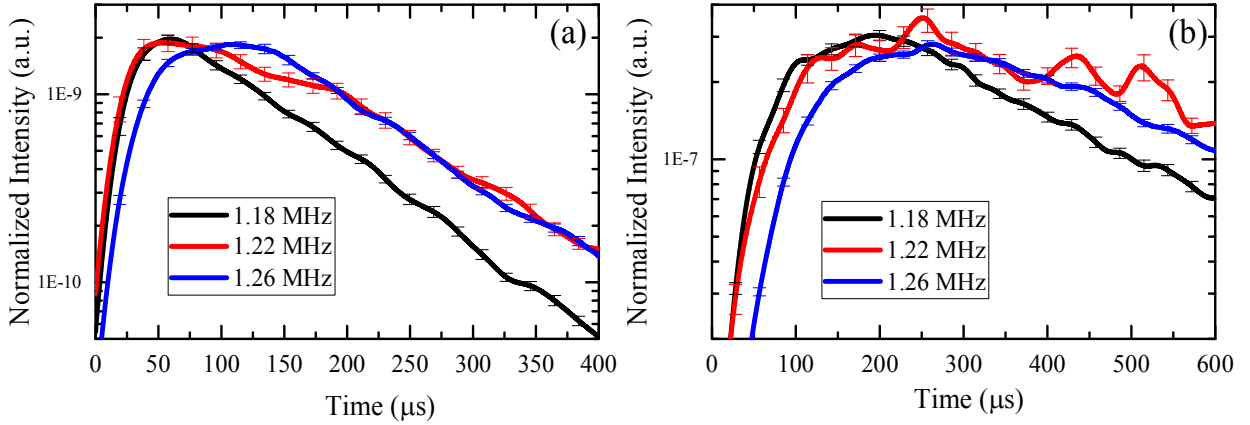


Figure 5.11: On-axis time-of-flight profiles for samples L1 (a) and L2 (b). Three frequencies are shown; 1.18 MHz (diffusive regime below mobility gap), 1.22 MHz (localized regime), and 1.26 MHz (diffusive regime above mobility gap). Above the mobility gap, profiles arrive much slower than below the mobility gap, implying a larger diffusion time τ_D . For each plot (a) and (b) the transmitted intensities have been normalized to have approximately the same peak value, to better highlight their time-dependence. Experimental uncertainties are only shown for a relatively few points, for clarity.

As previously discussed, τ_D is introduced in SC theory as a convenient way of scaling the time-dependence of the theoretical predictions, but it may not be a very relevant parameter in the context of backscattering from thick, strongly-scattering samples such as L1 and L2. In backscattering for thick samples, data are measured over an earlier time range (relative to the diffusion time), and are therefore expected to be insensitive to sample thickness. It is instructive to examine the time scales at play for our experimental geometry. We may estimate that the

initial transmitted pulse through L2 arrives around $t_{firstarrival} = L/v_g \sim 13 \mu\text{s}$. The peak of transmitted intensity through L2 does not even arrive until at least $200 \mu\text{s}$ after the incident pulse (Figure 5.11), or $\sim 187 \mu\text{s}$ after the ballistic pulse (were it measurable). In contrast, the latest time observed in backscattering from sample L2 is $130 \mu\text{s}$. Therefore, backscattering is measured for a range of times that are less than the typical time for waves to cross the sample, confirming that the backscattering data for L2 are insensitive to sample thickness.

From D_B , we can make an indirect estimate of the energy velocity, since $v_E = 3D_B/\ell^*$. Results are shown in Figure 5.12. The large values of D_B reported in this chapter (as compared to $D_B = 0.7 \text{ mm}^2/\mu\text{s}$ found in the diffuse regime) imply anomalously large values for the energy velocity $v_E = 3D_B/\ell^*$ throughout the frequency regime studied. This observation is consistent with previous results on similar samples (Hu et al. 2008; Hildebrand 2015), motivating further theoretical work to understand the behaviour of v_E in the localized regime.

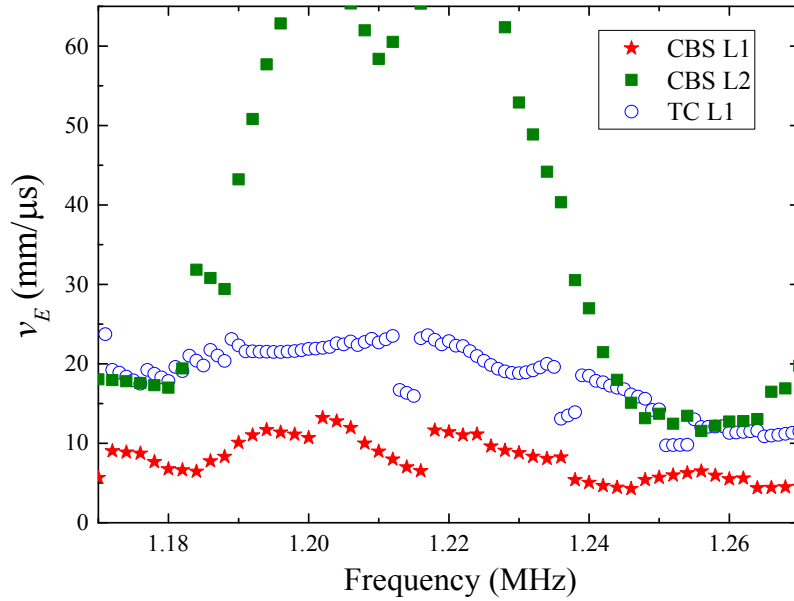


Figure 5.12: Energy velocity v_E estimated from the Boltzmann diffusion coefficient D_B .

5.6.2. Observations on thick samples

As discussed, the thickness of L2 prohibits the calculation of enough SC theory to fit the data with theory. This thickness also means that waves take much longer to propagate through the sample. My dynamic transverse profile measurements for L2 were able to record times longer than 600 μs , which is a significant experimental achievement. However, as can be seen in the TOF profiles of Figure 5.11 (b), there is still only a limited range of times available relative to the time of the first peak, which is related to τ_D (Skipetrov and van Tiggelen 2006). Thus, the most obvious indicators of localization, e.g. the saturation of $w_\rho^2(t)$, risk occurring at a time that is outside of the range of times experimentally available to us, and therefore transmission data for such a thick sample may not be very illuminating for the study of localization, within the range of times that are experimentally possible. In reflection, however, there is no difference in arrival time between thin and thick samples, suggesting an important advantage of backscattering measurements for thick samples.

5.6.3. Critical exponent estimation

Figure 5.8 suggests that the critical exponent ν of the localization transition may be estimated from the expected behaviour of Equation (2.60): $\xi(f) \propto |f - f_c|^{-\nu}$ for f near f_c . We may apply this relation to the results in Figure 5.8, as shown in the figures below for each independent set of measurements. Figure 5.13 shows L1 transmission data, and Figure 5.14 shows L1 and L2 backscattering data.

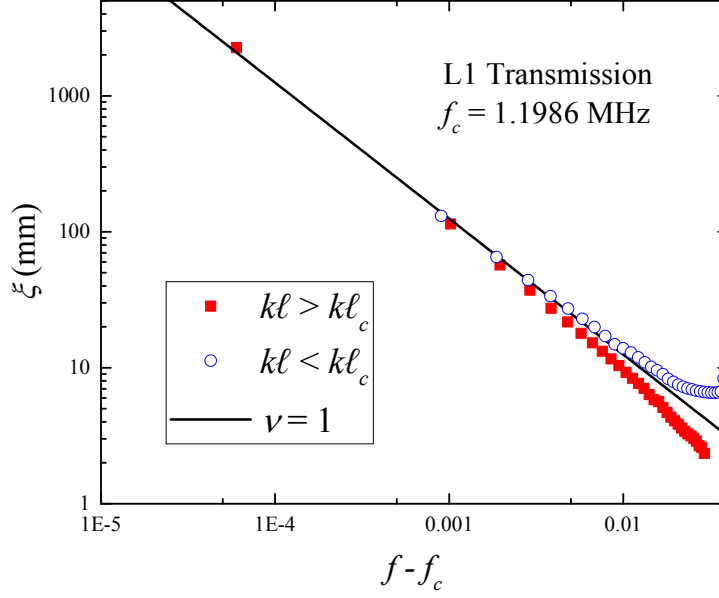


Figure 5.13: The localization (correlation) length ξ measured in transmission from L1, plotted as a function of distance from the lower ME $f - f_c$ where $f_c = 1.1986$ MHz. The approach to the ME is shown for frequencies lower than the ME ($k < k\ell_c$), and for frequencies above the ME (the localization regime, with $k\ell > k\ell_c$). The power law of $\nu = 1$ predicted by SC theory is shown (black line). A power law of $\nu = 1.06$ provides a slightly better description of the data (not shown). Figure courtesy of J. H. Page.

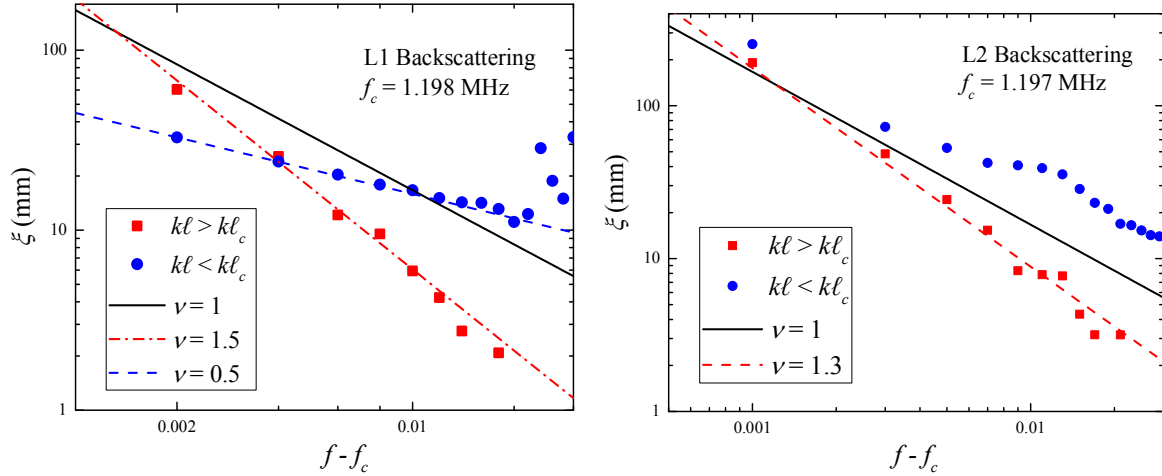


Figure 5.14: The localization (correlation) length ξ measured in backscattering, plotted as a function of distance from the lower ME $f - f_c$. The approach to the ME is shown for frequencies lower than the ME ($k\ell < k\ell_c$), and for frequencies above the ME (the localization regime, with $k\ell > k\ell_c$). The power law of $\nu = 1$ predicted by SC theory is shown (black line). (a) For sample L1, $f_c = 1.1986$ MHz. Depending on the side (lower or higher frequency) from which the ME is approached, the best fit is closer to either $\nu = 1.5$ or $\nu = 0.5$. (b) For sample L2, $f_c = 1.197$ MHz, and for $k\ell > k\ell_c$ the best fit is around $\nu = 1.3$. Figure courtesy of J. H. Page.

The transmission data shown in Figure 5.13 show convincing power law behaviour, and a power law with $\nu = 1$ describes the behaviour of the data well near the mobility edge. Results for backscattering show much more scatter. This analysis yields a rough estimate of $\nu \approx 1 \pm 0.5$ (weighing the transmission and backscattering data evenly). However, this analysis may be inescapably biased due to the fact that SC theory assumes $\xi \propto (1 - k\ell/k\ell_c)^{-1}$, i.e. it predicts that $\nu = 1$. This value is far from the generally accepted value of $\nu \approx 1.6$. However, our analysis points the way to better estimations of ν , with the development of more objective theoretical predictions.

5.7. Conclusion

The work in this chapter constitutes the first experimental observation of an Anderson mobility gap for classical waves. In particular, I have measured ξ over the entire localization regime and identified the two accompanying mobility edges. My method of fitting SC theory to experimental data enables very precise determination of the ME positions, especially in transmission. Furthermore, my measurement and analysis of the dynamic CBS profiles constitutes a completely original and promising method of probing criticality and localization. I employed observations of the CBS effect to characterize the Anderson mobility gap in very thick samples, demonstrating an advantage of backscattering measurements over those in transmission. These results also confirm that SC theory correctly describes the coherent backscattering of classical waves in the critical and localized regimes. More generally, my methods and results suggest new possibilities for the characterization of strongly scattering and/or localizing media using dynamic coherent backscattering. While the estimate of the critical exponent ν is likely subject to limitation due to the assumptions of SC theory, our observations will prompt further theoretical development and inspire new discussion in this area.

**Appendix 5A : Anderson mobility gap probed by dynamic coherent
backscattering**

Anderson mobility gap probed by dynamic coherent backscattering

L. A. Cobus,¹ S. E. Skipetrov,^{2,3} A. Aubry,⁴ B. A. van Tiggelen,^{2,3} A. Derode,⁴ and J. H. Page¹

¹*Department of Physics and Astronomy, University of Manitoba, Winnipeg, Manitoba R3T 2N2, Canada*

²*Université Grenoble Alpes, LPMMC, F-38000 Grenoble, France*

³*CNRS, LPMMC, F-38000 Grenoble, France*

⁴*Institut Langevin, ESPCI ParisTech, CNRS UMR 7587, Université Denis Diderot - Paris 7, 1 rue Jussieu, 75005 Paris, France*

(Dated: March 29, 2016)

We use dynamic coherent backscattering to study one of the Anderson mobility gaps in the vibrational spectrum of strongly disordered three-dimensional mesoglasses. Comparison of experimental results with the self-consistent theory of localization allows us to estimate the localization (correlation) length as a function of frequency in a wide spectral range covering bands of diffuse transport and a mobility gap delimited by two mobility edges. The results are corroborated by transmission measurements on one of our samples.

A quantum particle is trapped in a three-dimensional (3D) disordered potential if its energy E is lower than the so-called mobility edge (ME) E_c . As was discovered by Philip Anderson in 1958, quantum interferences may increase E_c to values that are much larger than the classical percolation threshold, an energy below which a classical particle would be trapped [1, 2]. The link between E_c and the statistical properties of disorder has been recently studied in experiments with ultracold atoms in random optical potentials [3, 4]. In contrast to quantum particles, classical waves—light or sound—may be Anderson localized by disorder only in a band of intermediate energies (or frequencies), the impact of disorder becoming weak in both high- and low-frequency limits [5, 6]. One thus expects a mobility ‘gap’ delimited by two MEs instead of a single ME. This is due to the difference between dispersion relations of quantum and classical waves [7, 8]. Resonant scattering may further complicate the spectrum by shifting the mobility gap or splitting it into several narrower ones. Mobility gaps can also exist for quantum particles when the disordered potential is superimposed on a periodic one—a common situation for electrons in crystals with impurities [9]. In the present Letter we report the first experimental observation of a mobility gap for classical waves. To this end we take full advantage of experimental techniques available for classical waves but very difficult, if not impossible, to put in practice for quantum particles and, in particular, for electrons in disordered conductors. We perform frequency-, time-, position- and angular-resolved ultrasonic reflection and transmission experiments in strongly disordered ‘mesoglasses’—elastic networks of brazed aluminum beads. The results are compared with the self-consistent theory of localization to precisely locate the two MEs and to estimate the localization length ξ throughout the mobility gap. ξ diverges at the MEs, as expected.

Among the many definitions of Anderson localization, two of them rely either on the exponential decay of eigenmodes at large distances or the vanishing of diffusion

[10]. However, strictly speaking, both only apply in an infinite disordered medium, and not in experiments which involve finite samples with often open boundaries. In the latter case, waves can leak through the sample boundaries to the surrounding medium; hence, the eigenmodes no longer decay exponentially at large distances (because waves propagate freely outside the sample), and the transport is no longer blocked completely, even though wave diffusion is suppressed exponentially. This is why important efforts were devoted in recent years to study signatures of Anderson localization in finite 3D samples that can be seen as representative portions of infinite disordered media in which waves would be Anderson localized. The most impressive successes were achieved for quantities measured in transmission where time- and position-resolved measurements of wave intensity allowed unambiguous observation of Anderson localization of elastic waves [11], without complications due to absorption. However, an important shortcoming of such measurements is the weakness of transmitted signals that decay exponentially with sample thickness L making the regime of very strong localization $L/\xi \gg 1$ inaccessible. Even in the diffuse regime, the transmitted intensity may become so weak that the measured signal is dominated by other, presumably weak phenomena (e.g., nonlinear effects or fluorescence in optics) which can be misinterpreted as a signature of Anderson localization [12, 13].

To circumvent the difficulties of transmission experiments, we develop a new approach to Anderson localization of waves based on time- and angular-resolved reflection measurements. The total reflection coefficient of a thick disordered sample is close to unity because almost all the incident energy is reflected, allowing for comfortable signal levels even deep in the localized regime. For a plane wave incident upon a slab of weakly disordered medium, $k\ell \gg 1$, the average reflection coefficient $R(\theta)$ is known to be almost Lambertian, but with a two-fold enhancement within a narrow angular range $\Delta\theta \sim (k_0\ell^*)^{-1}$ around the exact backscattering direction $\theta = 0$ [14–18]. Here k and k_0 are the wave numbers inside and outside

the sample, respectively, and ℓ and ℓ^* are the scattering and transport mean free paths. If the incident wave is a short pulse, the shape $R(\theta, t)$ of this coherent backscattering (CBS) peak evolves in time whereas its relative amplitude remains constant [19–21]. The width $\Delta\theta$ of the CBS peak decreases with time according to $\Delta\theta^2 \propto 1/Dt$, where D is the wave diffusion coefficient, as can be easily found from the solution of the diffusion equation [18]. CBS is a very general phenomenon due to constructive interferences of partial waves that follow time-reversed paths in a disordered medium. It was observed for light in suspensions of small dielectric particles [14–16] and clouds of cold atoms [22], sound [20, 21], seismic [23] and matter [24] waves. Being an interference phenomenon, CBS seems natural to use as a probe of Anderson localization. However, the stationary (time-integrated) CBS peak was predicted to be only weakly affected by localization effects, with the most pronounced effect being the rounding of its tip which can also be due to absorption [25]. Optical experiments confirmed the rounding of the tip [26, 27], but the conclusion that this behaviour was caused by Anderson localization of light [27] was not supported by transmission measurements performed on the same or similar samples [28, 29]. In this context, the dynamic CBS is more promising as a probe of Anderson localization because its shape is independent of absorption on average, and its width $\Delta\theta$ explicitly depends on the diffusion coefficient D . In a different context, recent theoretical work suggests that dynamic CBS of cold atoms in a random potential may serve as a probe of Anderson transition [30].

In this Letter we report measurements of CBS from two of our mesoglass samples composed of aluminum beads brazed together (volume fraction $\sim 55\%$) to form an elastic network. The samples have the shape of slabs with cross-sections of $230 \times 250 \text{ mm}^2$ much larger than thicknesses $L_1 = 25 \pm 2 \text{ mm}$ and $L_2 = 38 \pm 2 \text{ mm}$ of samples L1 [see Fig. 1(a)] and L2, respectively. They were waterproofed so that experiments could be performed in a water tank with immersion transducers or transducer arrays and the pores between the beads held under vacuum during all measurements. The samples are similar to those used in previous studies [11, 31], but instead of being monodisperse have a mean bead diameter of 3.93 mm with a polydispersity of about 20%, which helps to randomize bead positions. The samples also have stronger elastic bonds between beads than previous samples, visible in Fig. 1(b). These differences influence the frequency dependence of amplitude transmission coefficient, shown in Fig. 1(c). Coupling between the individual resonances of the beads leads to frequency bands of relatively high transmission whose widths depend on the coupling strength [11, 32], but these bands are narrow enough in our samples to cause transmission dips to appear in between. The depth and width of the dips are lessened by

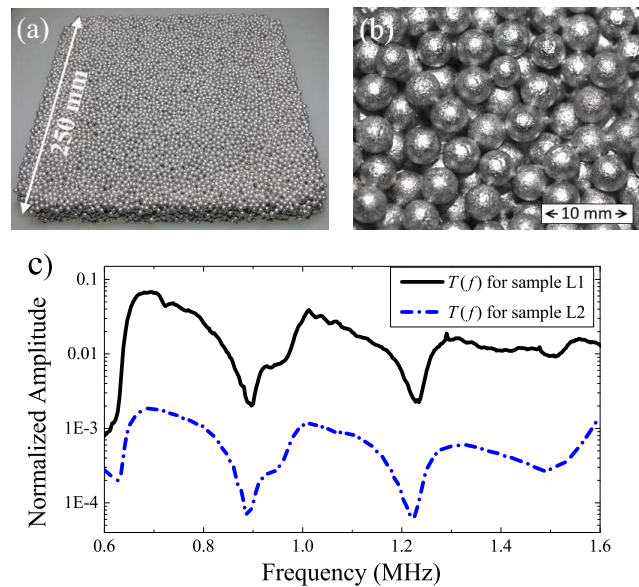


FIG. 1. (a) Sample L1. (b) Bead structure of sample L1. (c) Amplitude transmission coefficient of ultrasonic waves through samples L1 and L2 as a function of frequency.

the polydispersity and greater inter-bead bond strength compared with the monodisperse samples.

These dips may correspond to Anderson mobility gaps but one has to study the nature of wave transport in the corresponding frequency ranges to claim anything with certainty. Here we report a detailed study of wave transport around the transmission dip at 1.23 MHz . Ultrasound is very strongly scattered near this frequency; we have measured the product $k\ell$ as small as $k\ell \lesssim 3$. More details of sample L1 can be found in a previous work [33]. Sample L2 is too thick and too strongly scattering for many of the conventional methods of sample characterization in transmission to work. As no detectable coherent signal could be transmitted through L2 in the frequency range of interest, measurements of k and ℓ from the coherent pulse [34] are not possible. However, both samples were fabricated using the same technique and have very similar composition, so that estimates from coherent measurements on sample L1 are expected to be a good approximation for L2 as well.

We measure the backscattered intensity using ultrasonic transducer arrays, placed in the diffuse far field of the samples (for details, see the Supplemental Material [36]). A time-dependent ‘response matrix’ was gathered by emitting with each element in turn, and recording the time-dependent backscattered field with all elements [21, 33]. An average over configurations of disorder was performed by translating the array parallel to the sample surface and acquiring the response matrices for different positions. To obtain results as a function of both time t and frequency f , the data were filtered using a Gaussian envelope of standard deviation 0.015 MHz , centered

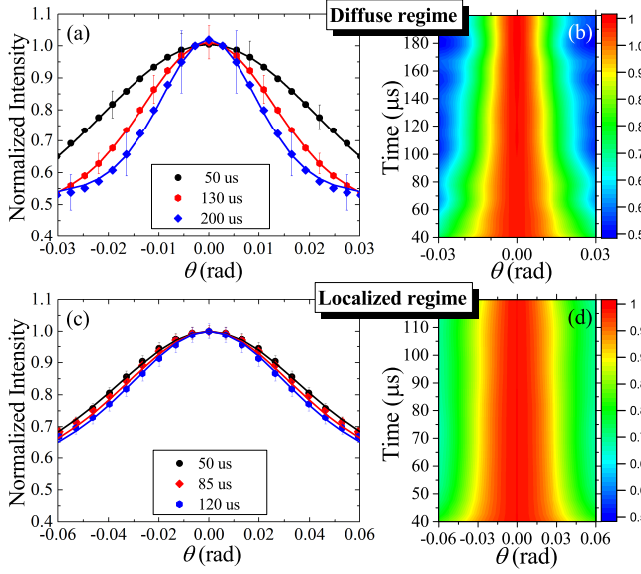


FIG. 2. Dynamic CBS profiles in the diffuse regime (1.65 MHz) (a,b) and in the localized regime (1.22 MHz) (c,d). The results in (a,b) are for sample L1, and in (c,d) for sample L2 (note the different angular scales). In (a,c) theoretical fits (lines) and experimental data (symbols) are shown for three representative times. In (a), the data are fitted using diffusion theory, giving diffusion coefficient $D = D_B = 0.7 \text{ mm}^2/\mu\text{s}$ [35], whereas in (c) SC theory is used, giving $\xi = 16.5 \text{ mm}$. Additional examples are shown in the Supplemental Material [36]. In (b,d) experimental CBS profiles are shown as a function of both time and angle. The profile narrows quite rapidly in the diffuse regime (b), but is almost constant over the accessible range of times in the localized regime (d).

around f . As has been previously reported [33], these backscattering data show significant contributions from recurrent scattering due to the signal entering and leaving the sample near the same spot [33, 37]. Recurrent scattering complicates the analysis of CBS peaks, as it is difficult to determine the (roughly flat) background intensity level corresponding to large angles θ . The recurrent scattering contribution was removed from the total backscattered intensity following the approach developed previously [33].

To eliminate the effect of absorption, the time-dependent CBS profiles $R(\theta, t)$, where θ is the angle between source and receiver elements of the ultrasonic array, are normalized by $R(0, t)$ [36]. Analogously to transverse confinement measurements in transmission [11], absorption cancels in the ratio $R(\theta, t)/R(0, t)$. Representative profiles $R(\theta, t)/R(0, t)$ are shown in Fig. 2.

To obtain a quantitative description of our data, we use the self-consistent (SC) theory of Anderson localization with a position-dependent diffusion coefficient $D(z, \Omega)$ presented in Refs. [38, 39]. First, $D(z, \Omega)$ is determined from an iterative solution of the self-consistent equations for each depth z inside the sample ($0 \leq z \leq L$).

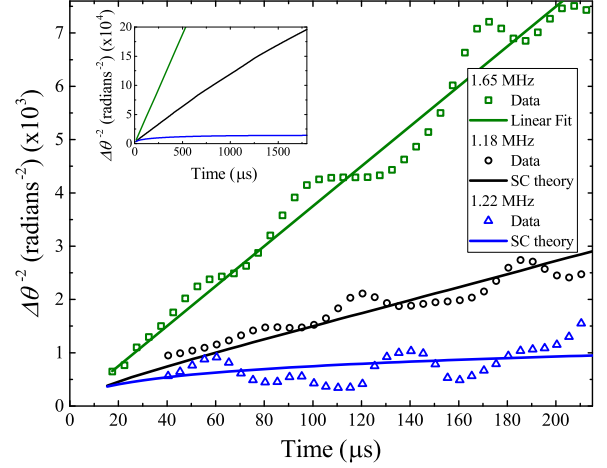


FIG. 3. Experimental results (symbols) and theoretical predictions (lines) for sample L1. Plotted is the reciprocal of the square of the half width at half maximum of the CBS peaks, $\Delta\theta^{-2}(t)$ (error bars are smaller than symbol sizes). Three representative frequencies are shown: $f = 1.65 \text{ MHz}$ (diffuse regime, diffusion coefficient $D_B = 0.7 \text{ mm}^2/\mu\text{s}$ extracted from the fit), $f = 1.18 \text{ MHz}$ (slower diffusion as a ME is approached; correlation length $\xi = 2.1 \text{ mm}$), and $f = 1.22 \text{ MHz}$ (Anderson localization; localization length $\xi = 12.5 \text{ mm}$). The inset shows theoretical predictions for longer times.

Second, the two-dimensional spatial Fourier transform of the intensity Green's function $C(q_\perp, z, z' = \ell_B^*, \Omega)$ is calculated using this $D(z, \Omega)$. Here ℓ_B^* is the transport mean free path in the absence of Anderson localization effects. Finally, the CBS profile $R(\theta, t)$ is obtained as a Fourier transform of $R(q_\perp, \Omega) = D(z = 0, \Omega) \partial C(q_\perp, z, z' = \ell_B^*, \Omega) / \partial z|_{z=0}$ where $q_\perp = k_0 \sin \theta$ [36]. Fits to the experimental data obtained from this theory are shown in Fig. 2(c). We refer the reader to Ref. [36] for the details of the fitting procedure. For a given frequency f , important outcomes of the fitting procedure are the location of f with respect to the ME f_c (indicating whether wave transport at f is extended or localized) and the value of the localization length ξ that characterizes the closeness to a ME and the extent of localization effects [40].

CBS profiles shown in Fig. 2(a,b) exhibit the narrowing with time predicted by the diffusion theory. However, when approaching $f = 1.20 \text{ MHz}$ and beyond, the narrowing of CBS profiles slows down considerably (see Fig. 2(c,d) and Fig. S1 of Ref. [36]). Such a slowing down is expected when a ME of the Anderson transition is approached and crossed because the width of the CBS peak $\Delta\theta$ behaves, roughly speaking, as the inverse width of the diffuse halo at the surface of the sample. The latter grows without limit in the diffuse regime but cannot exceed a value on the order of the localization length ξ in the localized regime. Hence, the corresponding CBS pro-

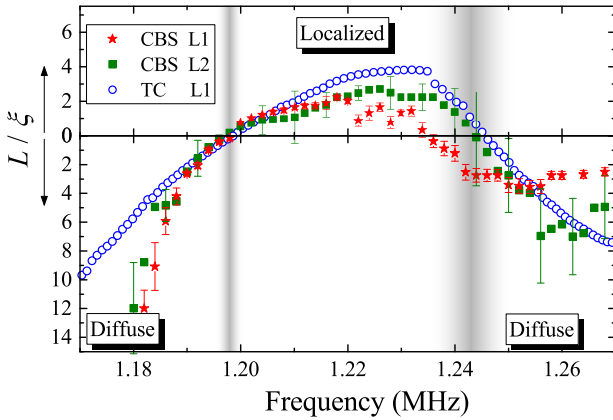


FIG. 4. The ratio of sample thickness L to the localization (correlation) length ξ obtained from fits to experimental CBS profiles (sample L1—red stars, sample L2—green squares) and transverse confinement (TC) data (sample L1—open circles). Error bars represent variations of L/ξ that increase the reduced χ^2 by unity; error bars are smaller than symbol size for transmission results. Fuzzy vertical gray lines show our estimates of mobility edges.

file stops shrinking and its width $\Delta\theta$ saturates. This is illustrated in Fig. 3 where the different types of behavior can be clearly distinguished.

We performed systematic fits of SC theory to our data for frequencies from 1.17 to 1.27 MHz for both samples L1 and L2, thereby determining the frequency dependencies of the localization (correlation) length ξ . The results are shown in Fig. 4 where MEs at approximately 1.20 and 1.24 MHz are indicated by fuzzy vertical gray lines. The Anderson mobility gap is clearly visible in between, whereas the wave transport is diffusive for frequencies below 1.20 and above 1.24 MHz. Other and possibly multiple mobility gaps can exist in our samples outside the frequency range from 1.17 to 1.27 MHz that we explored. It is important to note that although the position of the Anderson mobility gap that we have found coincides with one of the dips in the transmission spectra of Fig. 1(c), the latter is not sufficient to claim the existence of the former. Indeed, a dip in transmission can simply correspond to spectral regions with a low density of states—precursors of band gaps in larger samples. It is important to prove that the wave transport corresponds to strongly suppressed diffusion that is consistent with Anderson localization, in order to claim an Anderson mobility gap. This is achieved here by comparing experimental results with SC theory of localization.

To support our conclusions based on CBS measurements, we performed complementary experiments and analysis in transmission on sample L1. We used the technique of transverse confinement, which has been previously established as an unambiguous method of observing localization [11]. The experimental method and compari-

son of measurements with SC theory have been presented in detail in Refs. [11, 41, 42]. As can be seen in Fig. 4, the results of transmission and reflection experiments agree reasonably well. From the combination of these measurements we estimate the position of MEs to be 1.198 ± 0.001 MHz and 1.243 ± 0.007 MHz. Inside the mobility gap the measured localization length reaches a minimum of 6.5 mm (3.8 times smaller than sample thickness). The CBS results fluctuate much more with frequency, as do the CBS profiles themselves, especially around the upper ME where the position of the ME is less clear than for the lower ME. While large fluctuations are to be expected in this regime, the precision of future measurements could be improved with a greater amount of configurational averaging, longer measurement times, and a wider angular array aperture.

Figure 4 may be used to estimate the critical exponent of the localization transition ν because one expects $\xi(f) \propto |f - f_c|^{-\nu}$ for f in the vicinity of a ME f_c . As can be seen in Fig. 4, L/ξ looks approximately linear as a function of f when it crosses the axis $L/\xi = 0$, leading to $\nu \approx 1$. It should be understood, however, that this result has large uncertainties due to the spread of data points in Fig. 4 (especially at the upper ME). In addition, Fig. 4 is obtained by fitting the experimental data with SC theory which is known to yield $\nu = 1$ in contradiction with numerical calculations [43] and may thus bias the result. More work is needed to obtain accurate estimates of ν for the localization transitions reported here.

In conclusion, we have employed the dynamic CBS effect to demonstrate an Anderson mobility gap in the spectrum of ultrasound scattered in a 3D strongly disordered elastic network. Performing our measurements in reflection instead of transmission as in previous works [11, 31] ensured a sufficiently strong signal throughout the mobility gap, even for a very thick sample. This is a significant advance, as previous experiments were only able to reveal a single mobility edge [31]. Fits to the data by the self-consistent theory of localization yielded precisely the locations of the two mobility edges that serve as bounds of the mobility gap, and the localization length ξ as a function of frequency. We were able to corroborate these results via transmission measurements on one of our samples. This work demonstrates the potential of dynamic CBS experiments to study localization effects in thick samples where transmission measurements are difficult or impossible, allowing us to access the deeply localized regime where $\xi \ll L$. The thickness-independence of backscattering in a wide range of times provides an important advantage in the investigation of critical behavior where the elimination of finite-size effects is desired. This approach, made possible by a combination of modern experimental techniques with a careful theoretical description, can be extended to other classical waves (light, microwaves) as well.

We thank the Agence Nationale de la Recherche

for financial support under grant ANR-14-CE26-0032 LOVE and CNRS for support in the framework of a France-Canada PICS project Ultra-ALT. J.H.P. and L.A.C. acknowledge the support of NSERC (Discovery Grant RGPIN/9037-2001, Canada Government Scholarship, and Michael Smith Foreign Study Supplement), the Canada Foundation for Innovation and the Manitoba Research and Innovation Fund (CFI/MRIF, LOF Project 23523). A.A. and A.D. benefited from funding by LABEX WIFI (Laboratory of Excellence ANR-10-LABX-24), within the French Program Investments for the Future under Reference No. ANR-10-IDEX-0001-02 PSL*.

-
- [1] P. W. Anderson, Phys. Rev. **109**, 1492 (1958).
 - [2] E. Abrahams, ed., *50 Years of Anderson Localization* (World Scientific, Singapore, 2010).
 - [3] S. S. Kondov, W. R. McGehee, and B. Zirbel, J. J. De-Marco, Science **334**, 66 (2011).
 - [4] F. Jendrzejewski, A. Bernard, L. Müller, P. Cheinet, V. Josse, M. Piraud, L. Pezzé, L. Sanchez-Palencia, A. A., and P. Bouyer, Nat. Phys. **8**, 398 (2012).
 - [5] S. John, Phys. Rev. Lett. **53**, 2169 (1984).
 - [6] S. John, Phys. Today **44**, 32 (1991).
 - [7] B. A. Van Tiggelen, A. Lagendijk, A. Tip, and G. F. Reiter, EPL **15**, 535 (1991).
 - [8] B. A. van Tiggelen and E. Kogan, Phys. Rev. A **49**, 708 (1994).
 - [9] P. M. Chaikin and T. C. Lubensky, *Principles of Condensed Matter Physics* (Cambridge University Press, Cambridge, 1995).
 - [10] B. A. Van Tiggelen, in *Diffuse Waves in Complex Media*, edited by J. P. Fouque (Kluwer Academic Publishers, Dordrecht, 1999) pp. 1–60.
 - [11] H. Hu, A. Strybulevych, J. H. Page, S. E. Skipetrov, and B. A. van Tiggelen, Nat. Phys. **4**, 945 (2008).
 - [12] T. Sperling, L. Schertel, M. Ackermann, G. Aubry, C. M. Aegerter, and G. Maret, New J. Phys. **18**, 013039 (2016).
 - [13] S. E. Skipetrov and J. H. Page, New J. Phys. **18**, 021001 (2016).
 - [14] Y. Kuga and A. Ishumaru, J. Opt. Soc. Am. A **1**, 831 (1984).
 - [15] M. P. Van Albada and A. Lagendijk, Phys. Rev. Lett. **55**, 2692 (1985).
 - [16] P. E. Wolf and G. Maret, Phys. Rev. Lett. **55**, 2696 (1985).
 - [17] E. Akkermans, P. E. Wolf, and R. Maynard, Phys. Rev. Lett. **56**, 1471 (1986).
 - [18] E. Akkermans and G. Montambaux, *Mesoscopic Physics of Electrons and Photons* (Cambridge University Press, Cambridge, 2007).
 - [19] R. Vreeker, M. Van Albada, R. Sprik, and A. Lagendijk, Phys. Lett. A **132**, 51 (1988).
 - [20] G. Bayer and T. Niederdränk, Phys. Rev. Lett. **70**, 3884 (1993).
 - [21] A. Tourin, A. Derode, P. Roux, B. A. van Tiggelen, and M. Fink, Phys. Rev. Lett. **79**, 3637 (1997).
 - [22] G. Labeyrie, F. de Tomasi, J.-C. Bernard, C. A. Müller, C. Miniatura, and R. Kaiser, Phys. Rev. Lett. **83**, 5266 (1999).
 - [23] E. Larose, L. Margerin, B. A. van Tiggelen, and M. Campillo, Phys. Rev. Lett. **93**, 048501 (2004).
 - [24] F. Jendrzejewski, K. Müller, J. Richard, A. Date, T. Plisson, P. Bouyer, A. Aspect, and V. Josse, Phys. Rev. Lett. **109**, 195302 (2012).
 - [25] B. A. van Tiggelen, A. Lagendijk, and D. S. Wiersma, Phys. Rev. Lett. **84**, 4333 (2000).
 - [26] D. S. Wiersma, P. Bartolini, A. Lagendijk, and R. Righini, Nature **390**, 671 (1997).
 - [27] F. J. P. Schuurmans, M. Megens, D. Vanmaekelbergh, and A. Lagendijk, Phys. Rev. Lett. **83**, 2183 (1999).
 - [28] T. van der Beek, P. Barthelemy, P. M. Johnson, D. S. Wiersma, and A. Lagendijk, Phys. Rev. B **85**, 115401 (2012).
 - [29] J. Gómez Rivas, R. Sprik, A. Lagendijk, L. D. Noordam, and C. W. Rella, Phys. Rev. E **63**, 046613 (2001).
 - [30] S. Ghosh, D. Delande, C. Miniatura, and N. Cherroret, Phys. Rev. Lett. **115**, 200602 (2015).
 - [31] W. K. Hildebrand, A. Strybulevych, S. E. Skipetrov, B. A. van Tiggelen, and J. H. Page, Phys. Rev. Lett. **112**, 073902 (2014).
 - [32] J. A. Turner, M. Chambers, and R. L. Weaver, Acustica **84**, 628 (1998).
 - [33] A. Aubry, L. A. Cobus, S. E. Skipetrov, B. A. van Tiggelen, A. Derode, and J. H. Page, Phys. Rev. Lett. **112**, 043903 (2014).
 - [34] J. H. Page, P. Sheng, H. P. Schriemer, and I. Jones, Science **271**, 634 (1996).
 - [35] The diffusion theory used here (to be published in a future work) is for acoustic waves in a 3D medium, similar to that presented for 2D in Ref. [21].
 - [36] See Supplemental Material at the end of this document for details of our theoretical model and fitting procedure.
 - [37] D. Wiersma, M. P. van Albada, B. A. van Tiggelen, and A. Lagendijk, Phys. Rev. Lett. **74** (1995).
 - [38] S. E. Skipetrov and B. A. van Tiggelen, Phys. Rev. Lett. **96**, 043902 (2006).
 - [39] N. Cherroret and S. E. Skipetrov, Phys. Rev. E **77**, 046608 (2008).
 - [40] ξ plays the role of correlation length in the diffuse regime.
 - [41] J. H. Page, in *Nano Optics and Atomics: Transport of Light and Matter Waves*, edited by R. Kaiser, D. Wiersma, and L. Fallani (International School of Physics 'Enrico Fermi', Course CLXXXIII, IOS, Amsterdam; SIF, Bologna, 2011) pp. 95–114.
 - [42] W. K. Hildebrand, *Ultrasonic waves in strongly scattering disordered media: understanding complex systems through statistics and correlations of multiply scattered acoustic and elastic waves*, Doctoral thesis, University of Manitoba (2015).
 - [43] K. Slevin and T. Ohtsuki, New J. Phys. **16**, 015012 (2014).

Supplemental material

INTRODUCTION

This document provides further information on the experimental techniques, the self-consistent theory for backscattered intensity, and the procedure used to fit the predictions of this model to experimental data. Representative values of the best-fit parameters are also presented and discussed.

EXPERIMENTAL METHOD

In this section, we give additional details on the backscattering experiments that we performed to demonstrate a robust new approach for investigating 3D Anderson localization. As emphasized in the letter, time- and angle-resolved backscattering experiments have several important advantages compared with the transmission measurements used in previous studies, enabling investigations of Anderson localization all the way through any mobility gap. Access to the deeply localized regime, where $\xi \ll L$, obviously requires that the signals emerging from the medium be large enough to be measurable. In transmission, this requirement is difficult, if not impossible, to satisfy. In previous works, transmission through the samples was so greatly reduced inside the transmission dips (where a mobility edge was demonstrated) that measurements were not possible all of the way through the mobility gap, the most deeply localized regime was inaccessible, and the upper mobility edge could not be identified [S1, S2]. By contrast, the reflection geometry that we employ here capitalizes on the distinct advantage that backscattered ultrasound is not affected by this limitation, allowing arbitrarily thick samples to be studied, and a complete investigation of the entire localization regime to be carried out. In addition, backscattering measurements are independent of sample thickness over a significant range of times before the detected signals have been able to reach and travel back from the far side of the sample. This not only simplifies the interpretation of the current backscattering measurements but will also enable future investigations of critical behaviour in which finite size effects can be eliminated. It is these considerations that motivated the design of our backscattering experiments, and have led to the significant progress in the investigation of 3D Anderson localization that is highlighted in the conclusions of our letter.

Given these advantages of backscattering measurements, one might wonder why we have focused on dynamic coherent backscattering rather than near-field detection of the time-dependent transverse intensity profile at the surface of the sample. Such dynamic transverse profile measurements would be expected to give

the same type of (absorption-free) information on localization as was obtained previously in transmission [S3], but with all of the additional advantages of the reflection geometry. While this is true in principle, we found that practical limitations preclude effective measurements of this type in reflection. Specifically, near-field measurements in reflection are extremely problematic because the placement of transducers at the sample surface leads to spurious reflections between the generator, sample surface, and detector. In addition, the generation and detection transducers get in the way of each other, making measurements difficult and data for some positions simply inaccessible. We also tried making measurements of the near-field transverse profile through the use of ultrasonic arrays in direct contact with the sample surface, but these were plagued by crosstalk between transducer elements during emission, which interfered with the detection of the interesting signals that have penetrated inside the sample. In addition, placing an array in contact with the sample complicates the boundary conditions. In contrast, coherent backscattering enables the spatial Fourier transform of the entire spatial intensity profile to be measured *in the far-field* with a single ultrasonic transducer array, making it the perfect tool to investigate the growth (or not) of the transverse width in reflection.

The backscattering experiments, as well as the transmission measurements used to corroborate the results for sample L1, were carried out by immersing water-proofed samples and transducers in a large water tank. The pores between the brazed beads in the samples were held under vacuum, thus ensuring that ultrasonic transport inside the sample was confined to the elastic bead network, and that both backscattering and transmission experiments were performed under the same conditions (apart from placement and type of ultrasonic emitters and detectors used). Thus, although both longitudinal and transverse elastic waves are present inside our solid samples, the emitted and measured signals for all experiments have longitudinal polarization (acoustic waves in water).

In backscattering, the response matrix was measured for sample L1 (L2) using 64 (128) elements of a linear ultrasonic array with a central frequency of 1.6 (1.0) MHz, capable of emitting/detecting signals for a frequency range of 0.6 - 1.9 MHz (0.5 - 1.4 MHz). Utmost care was taken to ensure that all possible contributions due to stray background signals were eliminated from the backscattering data by systematically searching for such contributions, removing them where possible, and analysing the data only over the range of times where valid data, uncontaminated by stray signals, were detected. For example, careful placement of the array and sample, the design of a support system for the sample that eliminated spurious reflections, as well as checks with (temporarily inserted) reflecting or opaque objects, were used to ensure that effects from the edges of samples were negligible. The use of short pulses and a large water

tank ensured that reflections from the sides of the tank arrived after the backscattered signals from the sample. The data were analyzed only for times greater than 40 μs (to discard any vestiges of specular reflections from the sample surface and single scattering, which might have persisted despite the sophisticated filtering technique that were used to remove these contributions [S4]) and for times less than 200 (120) μs for L1 (L2) (to reject contributions from echoes between the array and sample). Similar care was employed to ensure that only multiply scattered signals from inside the sample were analyzed for the transmission measurements on L1 (see Refs. [S1, S2] for details on similar transmission experiments).

For configurational averaging of the backscattering data, the array was translated parallel to the sample, acquiring response matrices at 302 (66) different positions. The distance between the array and sample was 182 (136) mm, so that the backscattering experiments were carried out in the far field, which for diffuse waves is defined by the condition $a \gg \sqrt{D_B t}$ (a is the sample-array distance, D_B is the Boltzmann diffusion coefficient, t is time). In the diffuse regime (e.g., 1.65 MHz for sample L1), D_B for sample L1 has been measured to be approximately 0.7 mm²/ μs , and the longest times experimentally available to us are 210 μs , so the approximation of $a = 182 \text{ mm} \gg \sqrt{0.7 \times 210} \approx 12 \text{ mm}$ is valid. In the localized regime, the dynamic spreading of the diffuse halo is less, so that the far-field limit is even better respected.

After filtering the recurrent scattering contribution, the bandwidth-limited time-dependent CBS profiles $R(\theta, t)$ were extracted from the conventional multiple scattering contribution to the response matrix. The dynamic CBS profiles were normalized to eliminate the influence of absorption by dividing $R(\theta, t)$ by $R(0, t)$, since at time t the effect of absorption on the numerator and denominator of this ratio is the same, and therefore cancels. Typical results near the lower mobility edge are shown in Fig. S1, where the data are compared with theoretical predictions as described in the next two sections.

SELF-CONSISTENT THEORY FOR DYNAMIC COHERENT BACKSCATTERING

Our theoretical model to describe the dynamic coherent backscattering (CBS) of ultrasound is based on the equations of self-consistent (SC) theory of Anderson localization with a position- and frequency-dependent diffusion coefficient $D(\mathbf{r}, \Omega)$ as derived in Ref. [S5]. In these equations, the scattering mean free path ℓ should be replaced by ℓ_B^* —the transport mean free path in the absence of localization effects—to account for the scattering anisotropy of our samples ($\ell_B^* > \ell$).

To define the mobility edge (ME) and the localization length, we first analyze SC equations in the infinite 3D medium where D becomes independent of position. For

the stationary ($\Omega = 0$) diffusion coefficient we obtain

$$D = D_B \left[1 - \frac{3\mu}{(k\ell_B^*)^2} \right], \quad (\text{S1})$$

where D_B is the (Boltzmann) diffusion coefficient in the absence of localization effects and an upper cut-off $q_\perp^{\text{max}} = \mu/\ell_B^*$ (with $\mu \sim 1$) was introduced in the integration over the transverse momentum $q_\perp = \{q_x, q_y\}$ in order to regularize the integral. Here we break the symmetry between q_\perp and q_z to anticipate the experimental geometry of a disordered slab perpendicular to the z axis. A ME of the Anderson transition at $k\ell = (k\ell)_c$ corresponds to $\mu = \frac{1}{3}(k\ell)_c^2(\ell_B^*/\ell)^2$. In the localized regime $k\ell < (k\ell)_c$, an analytic solution of the equations of SC theory can be obtained for a point source emitting a short pulse at $\mathbf{r}' = 0$ and $t' = 0$, in the long-time limit. We obtain an intensity Green's function

$$C(\mathbf{r}, \mathbf{r}', t \rightarrow \infty) = \frac{1}{4\pi\xi^2|\mathbf{r} - \mathbf{r}'|} \exp(-|\mathbf{r} - \mathbf{r}'|/\xi), \quad (\text{S2})$$

where the localization length is

$$\xi = \frac{6\ell}{(k\ell)_c^2} \left(\frac{\ell}{\ell_B^*} \right) \frac{p^2}{1 - p^4}, \quad (\text{S3})$$

and $p = k\ell/(k\ell)_c$.

To describe the experimental data, we solve the equations of SC theory in a slab of thickness L with boundary conditions derived in Ref. [S5], where the extrapolation length

$$z_0 = \frac{2}{3}\ell_B^* \frac{1 + R}{1 - R} \quad (\text{S4})$$

depends on the internal reflection coefficient R . To this end, we Fourier transform the SC equations in the transverse plane $\boldsymbol{\rho} = \{x, y\}$ and discretize the remaining ordinary differential equation for $C(q_\perp, z, z', \Omega)$ on a grid for $z \in [0, L]$ [S6]. A sufficiently fine discretization is also introduced for q_\perp and Ω , and the resulting system of linear equations with a tridiagonal matrix of coefficients is solved numerically using a standard routine `zgtsl` from LAPACK library [S7] for $D(z, \Omega) = D_B$. A new value of $D(z, \Omega)$ is then obtained from the return probability

$$C(\mathbf{r}, \mathbf{r}' = \mathbf{r}, \Omega) = \frac{1}{2\pi} \int_0^{q_\perp^{\text{max}}} dq_\perp q_\perp C(q_\perp, z, z' = z, \Omega), \quad (\text{S5})$$

and the solution is iterated until convergence, i.e., $D(z, \Omega)$ does not change by more than a very small amount, typically less than $(5 \times 10^{-5})\%$, from one iteration to the next. Transmission and reflection coefficients $T(q_\perp, \Omega)$ and $R(q_\perp, \Omega)$ are then calculated as

$$R(q_\perp, \Omega) = D(z, \Omega) \left. \frac{\partial}{\partial z} C(q_\perp, z, z' = \ell_B^*, \Omega) \right|_{z=0} \quad (\text{S6})$$

and similarly for $T(q_\perp, \Omega)$. We obtain the time-dependent intensity profiles in transmission $T(\boldsymbol{\rho}, t)$ and

reflection $R(\boldsymbol{\rho}, t)$ by a double inverse Fourier transform of $T(q_\perp, \Omega)$ and $R(q_\perp, \Omega)$, respectively. The dynamic CBS profile $R(\theta, t) = R(q_\perp = k_0 \sin \theta, t)$ follows from the observation that the CBS shape is given by the Fourier transform of the ‘diffuse intensity halo’ at the sample surface [S8].

FITTING SELF-CONSISTENT THEORY TO EXPERIMENTAL BACKSCATTERING DATA

The theory for $R(\theta, t)$ developed in the previous section is valid in the far field, where $\sin \theta = q_\perp/k_0$. Here $k_0 = 2\pi f/v_0$ and $v_0 \approx 1500$ m/s is the speed of sound in water. This is the appropriate limit for comparing with the experimental data, since our backscattering experiments are performed in the far-field (discussed in the first section of this Supplemental Material).

Near the localized regime, backscattered waves may spend a long time in a thick sample without reaching the far side. This means that for a range of times less than twice the typical time for waves to cross the sample, which can be estimated from the peak in the time-dependent transmission, the CBS effect is not sensitive to sample thickness. This is significant because calculations for very thick samples can be prohibitively time-consuming, so the modeling of backscattering in the localized regime is more convenient when there is no explicit dependence on sample thickness. In other words, theory for backscattered waves from a thin sample may also be used for a thicker sample, provided that the range of times investigated is short enough. Here we calculate SC theory for sample L1 and can compare it to experimental CBS profiles of both L1 and L2.

Most input parameters for the calculation of SC theory were determined from measurements performed in separate experiments and could thus be fixed in the fitting procedure. These (fixed) parameters are: scattering mean free path $\ell = 0.9$ mm, reflection coefficient $R = 0.67$, and wave vector $k = 2\pi f/v_p$, with phase velocity $v_p = 2.8$ mm/ μ s, giving $k\ell = 2.7$ for $f = 1.2$ MHz. The remaining parameter, the transport mean free path $l_B^* = 4$ mm, was determined from SC fitting of transverse confinement (transmission) data from sample L1.

The most important parameter involved in SC theory calculations of $R(\theta, t)$ in the vicinity of an Anderson transition is the localization (correlation) length ξ . As this parameter is unknown a priori, theoretical predictions for $R(\theta, t)$ are calculated for a large range of ξ values from the diffuse to localized regimes (and back again). These values of ξ are determined from $k\ell$ and its critical value at the transition $(k\ell)_c$ using Eq. (S3), with $k\ell$ fixed at the experimentally estimated value for $f = 1.2$ MHz. For each frequency f of experimental data, the experimental CBS matrix $R(\theta, t)$ is fitted with every theory set. All fits are least-squares comparisons between the 2D matrices

from experiment and theory, $R(\theta, t)$, using the reduced χ^2 to determine the best-fit values of ξ . All times and θ values are fit simultaneously. This fitting procedure was performed with Wavemetrics software IGOR Pro. By finding the best-fit theory set for each f , the frequency-dependence of the localization (correlation) length $\xi(f)$ was determined. This, in turn, enabled the locations of the two MEs, f_{c1} and f_{c2} , to be determined (these are the frequencies where ξ diverges).

Representative fit results for both samples are shown in Fig. S1, showing the quality of the fits in the diffuse regime at a frequency below the first localization transition [Fig. S1(a),(d)], at the first mobility edge [Fig. S1(b),(e)], and in the mobility gap [Fig. S1(c),(f)]. In all cases, the experimental data are well-described by the SC theory: the narrowing of CBS profiles with time is reduced as the ME is reached [Fig. S1(b),(e)], and in the localized regime CBS profiles change even less with time [Fig. S1(c),(f)], with the width approaching a constant at long times.

The Boltzmann diffusion coefficient D_B was a free fit parameter, yielding $D_B(f)$ after the entire fitting process. For sample L1, $D_B \approx 10 \pm 7$ mm² μ s⁻¹ below 1.24 MHz, and $D_B \approx 5 \pm 2$ mm² μ s⁻¹ above 1.24 MHz (from transmission and reflection measurements). The frequency-dependence of $D_B(f)$ is supported by visual inspection of the time-dependence of the transmitted intensity in these regimes, and these values of D_B are similar to the results of previous measurements in similar samples [S2, S3]. For sample L2, the fitting results gave values of D_B ranging from $D_B \sim 13 - 61$ mm² μ s⁻¹ below 1.24 MHz (peaking in the localized regime) and $D_B \sim 9$ mm² μ s⁻¹ above 1.24 MHz. However, for such a thick sample as L2, the backscattering data are not very sensitive to D_B over the experimentally accessible range of times, so that these estimates for sample L2 are not likely to be very accurate, although they are still consistent with surprisingly large values of D_B , as has been found for other samples in the localized regime. Such values imply anomalously large values of the energy velocity v_E [S3], motivating future work to seek a theoretical understanding of v_E in the localized regime.

The only other fit parameter was the background intensity level, which was also allowed to vary freely. For both samples L1 and L2, and for almost all frequencies, best fits gave a background of within 10% of the value of 0.5 which would be expected after the removal of the recurrent scattering contribution. This variation of the background intensity results from the challenges of completely removing the recurrent scattering contribution, especially at early times where recurrent scattering dominates the backscattered intensity; by allowing the background intensity to be a free fit parameter, we were able to ensure that these background fluctuations did not degrade the reliability of our determination of the frequency dependence of the localization (correlation) length.

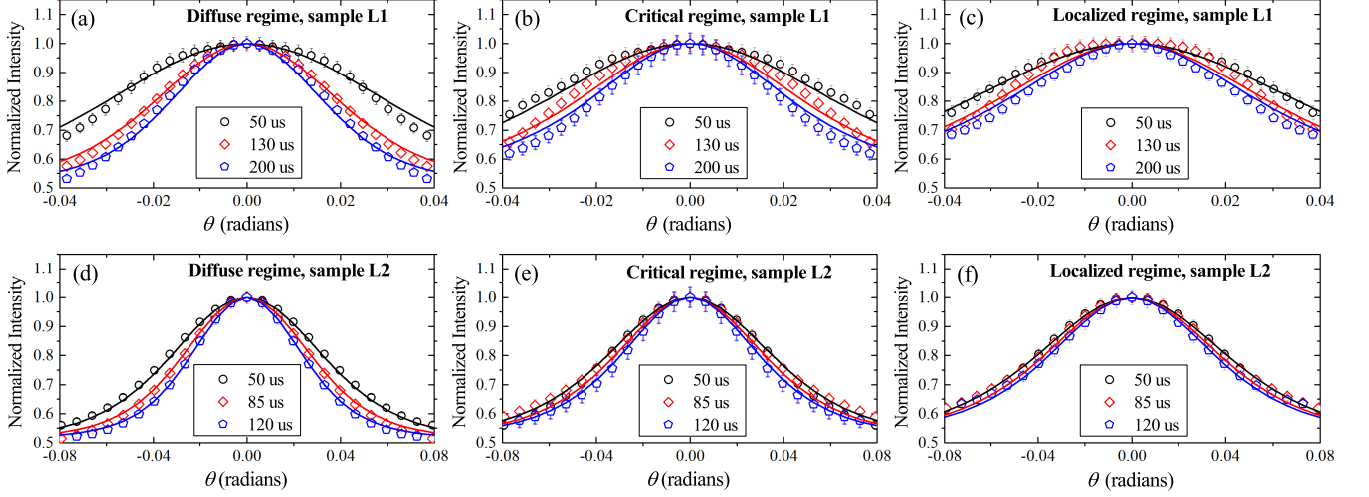


FIG. S1. Dynamic CBS profiles from samples L1 (top) and L2 (bottom) for three different times, and for three different frequencies: (a),(d) 1.18 MHz in the diffuse regime (correlation length $\xi = 2.1 \pm 0.2$ mm for L1 and 3.2 ± 0.9 mm for L2); (b),(e) near 1.20 MHz at a ME (ξ diverges); and (c),(f) 1.22 MHz in the localized regime ($\xi = 12 \pm 1$ mm for L1 and 16 ± 3 mm for L2). Solid lines are best fits of SC theory to the data (symbols). Note that the horizontal scales are different between (a,b,c) and (d,e,f), and that a different range of times is presented. It is also important to note that ξ should not necessarily be the same for both samples at exactly the same frequency.

-
- [S1] W. K. Hildebrand, A. Strybulevych, S. E. Skipetrov, B. A. van Tiggelen, and J. H. Page, Phys. Rev. Lett. **112**, 073902 (2014).
- [S2] W. K. Hildebrand, *Ultrasonic waves in strongly scattering disordered media: understanding complex systems through statistics and correlations of multiply scattered acoustic and elastic waves*, Doctoral thesis, University of Manitoba (2015).
- [S3] H. Hu, A. Strybulevych, J. H. Page, S. E. Skipetrov, and

- B. A. van Tiggelen, Nat. Phys. **4**, 945 (2008).
- [S4] A. Aubry, L. A. Cobus, S. E. Skipetrov, B. A. van Tiggelen, A. Derode, and J. H. Page, Phys. Rev. Lett. **112**, 043903 (2014).
- [S5] N. Cherroret and S. E. Skipetrov, Phys. Rev. E **77**, 046608 (2008).
- [S6] The actual calculation is performed in dimensionless variables, but we omit this technical detail here for the purpose of clarity.
- [S7] <http://www.netlib.org/lapack/>.
- [S8] E. Akkermans and G. Montambaux, *Mesoscopic Physics of Electrons and Photons* (Cambridge University Press, Cambridge, 2007).

6. Recurrent Scattering

6.1. Introduction to recurrent scattering

Recurrent scattering is often described in terms of scattering diagrams as a “loop” scattering process, where the wave returns to the same scatterer more than once (this concept was introduced in terms of diagrammatic scattering theory in Section 2.3.1). However, it is more accurate to define recurrent scattering in terms of the probability of a wave returning within a mean free path of a spot it has previously visited (van Tiggelen, Wiersma, and Lagendijk 1995). In most multiple scattering phenomena, recurrent scattering is negligible compared to other lower-order processes. Recurrent scattering events become important only when the *return probability* – the probability of a wave returning near a spot it has previously visited – is significantly high. Such circumstances tend to arise only in the strong scattering regime, where the diffusion approximation may not fully describe wave transport. Scattering strength may be characterized by the product of wave vector and scattering mean free path, $k\ell_s$. For small $k\ell_s$, i.e. $k\ell_s \sim 1$, scattering is strong and interference effects are important in describing wave behaviour.

As it is by nature a backscattering phenomenon, recurrent scattering is most easily studied in the reflection geometry. The first direct experimental observation of recurrent scattering of classical waves was presented by Wiersma et al. via measurements of static CBS profiles (Wiersma et al. 1995). Specifically, the group showed that the *enhancement factor*, which is the ratio of intensity at the top of the CBS cone to the incoherent intensity, deviated from 2 due to recurrent scattering. In the heuristic discussion of CBS (Section 2.4), the CBS cone was stated to show an enhancement of 2 in the exact backscattering direction. This implies that the enhancement factor is also always exactly 2. However, this is not necessarily the case experimentally, since there are coherent contributions to intensity which are angle-independent,

and thus add to the observed ‘incoherent’ background, reducing the enhancement factor. One of these contributions is recurrent scattering. In addition, experiments have shown that in general, the reduction in enhancement factor is only observable in strongly scattering media (van Albada, van der Mark, and Lagendijk 1987; Wiersma et al. 1995). We may explain this fact by examining the enhancement factor more carefully using diagrammatic theory.

We can now rewrite the reducible vertex function in terms of the vertices defined in Section 2.3.1: $\mathbf{\Gamma} = \mathbf{R} + \mathbf{U} = \mathbf{R} + \mathbf{C} + \mathbf{S}$. At exact backscattering (source-receiver angle $\theta = 0$), we have $S(\vec{r}_1 \approx \vec{r}_2 \approx \vec{r}_3 \approx \vec{r}_4)$ and $C_0 = R_0$ from reciprocity (subscript 0 denotes exact backscattering). Here, the *experimental* enhancement factor Ξ is given by the ratio

$$\Xi = \frac{\text{total intensity}}{\text{incoherent intensity}} = \frac{R_0 + C_0 + S'_0}{R_0 + S'_0} = 2 - \frac{S'_0}{R_0 + S'_0}. \quad (6.1)$$

where S'_0 indicates that single-scattering contributions (the term I) are not included²¹ (van Tiggelen, Wiersma, and Lagendijk 1995). Thus, recurrent scattering processes are mostly responsible²² for the occurrence of $\Xi < 2$. These contributions are entirely absent from the diffusion approximation picture²³. Figure 6.1 shows experimentally-measured enhancement factors for backscattered light: the enhancement factor decreases as scattering strength increases. (Note that in this experiment, single-scattering contributions were carefully removed.) This effect illustrates the idea that recurrent scattering events are important in the strong scattering regime. This fact was described theoretically in Section 2.3.1, where recurrent scattering events were

²¹ The last step follows, since $C_0 = R_0$, by adding and subtracting S'_0 in the numerator.

²² It has also been suggested that non-linear effects, such as the presence of nonlinear point-scatterers, could modify the enhancement factor (Wellens 2009), but this has yet to be conclusively shown in experiment.

²³ Note that the same calculation done with *only* ladder and most-crossed diagrams gives $\Xi = 2$ (Akkermans and Maynard 1985).

shown to be one of the set of diagrams which are ignored by the diffusion approximation $\mathbf{U} \sim l$.

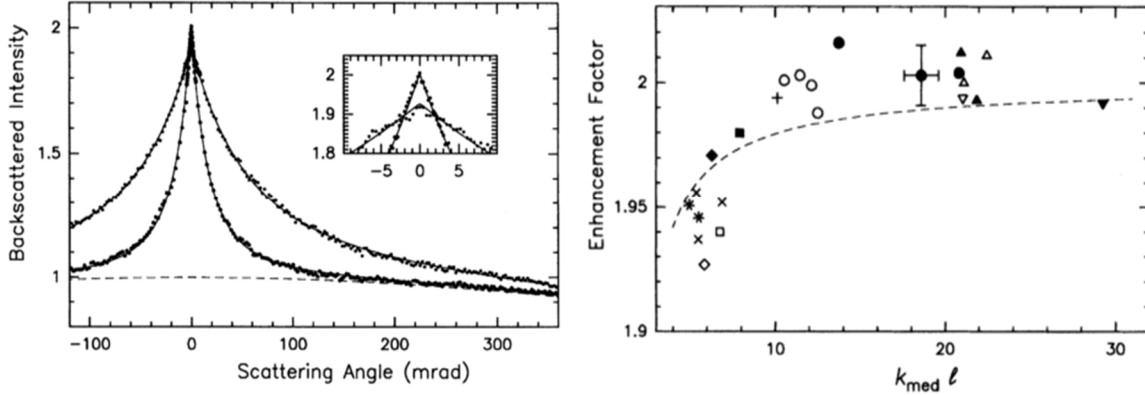


Figure 6.1: (Left) Backscattered intensity plotted against scattering angle. Narrow cone: BaSO₄ sample, $k_{med} l^* = 22.6 \pm 1.0$, where k_{med} is the wave vector of light in the medium. Broad cone: TiO₂ sample, $k_{med} l^* = 5.8 \pm 1.0$. Solid and dashed lines are, respectively, coherent and incoherent contributions from diffusion theory. Insert: top of both cones. The enhancement factor for the broad cone is less than 2. (Right) Enhancement factor plotted against $k_{med} l^*$. The enhancement factor is less than 2 for $k_{med} l^* \leq 10$. Used with permission (Wiersma 1995).

Beyond ‘mere’ strong scattering, it is clear that an increased return probability is directly linked with the phenomenon of Anderson localization. With more recurrent scattering, waves spend a longer time in the sample and transport slows down. This link between recurrent scattering and localization is shown clearly in the equations for the self-consistent theory of localization – an increase in return probability results in the renormalization (decrease) of the diffusion coefficient $D(\Omega, \vec{r})$ from the purely diffusive Boltzmann diffusion coefficient D_B (see Equation. (5.2), Section 5.2.1).

In this chapter, I show that experimental measurements of the return probability can be used to study Anderson localization. The recurrent scattering contribution to backscattered intensity is obtained via a numerical method of separating recurrent scattering and ‘conventional’ multiple scattering processes. This constitutes the first experimental study of *dynamic* recurrent scattering on its own, as well as the first ever experimental study of recurrent scattering in the critical and localized regimes. We also show that this recurrent/multiple scattering separation is

necessary to our studies of coherent backscattering (the work presented in Section 5.4), because the decrease in enhancement factor due to recurrent scattering complicates the fitting of theory to experimental CBS cones.

6.2. Surface recurrent scattering effects on the coherent backscattering profile

Using ultrasonic arrays, the backscattered field was measured from samples L1 and L2 as detailed in Section 3.2.3. The backscattered intensity as a function of angle, time and frequency was calculated as detailed in Section 4.2.3. Results are shown in Figure 6.2 for two representative frequencies. The total backscattered intensity (black circles) has the same shape as would be expected for a CBS profile, *but* it has a reduced enhancement factor. In other words, since ultrasound is so strongly scattered in these mesoglasses, the recurrent scattering contribution to total backscattered intensity is non-negligible. This effect is clearly visible by eye even in the diffuse regime (1.65 MHz, Figure 6.2a) - the background intensity level is more than half of the peak value. In the localized regime (1.23 MHz, Figure 6.2b) it is not so evident what the enhancement factor is, since the cones are so broad even at these late times that the background level is not easily discernable. This becomes a problem when trying to fit theory to these data. Theoretical CBS profiles have background levels of 0.5 times the peak value. During the fitting process, the background level may be allowed to vary to account for any deviations from 0.5, but *only if the background is visible*. Thus, in order to fit CBS profiles with theory, recurrent scattering had to be removed from the experimental data. This process is detailed in Section 6.2.1.1. Results are shown in Figure 6.2, where the recurrent scattering and conventional multiple scattering processes are shown with the original total intensity profiles. Only the conventional multiple scattering profiles (e.g. the curves represented by blue pentagons in Figure 6.2) were used in the analysis of Chapter 5.

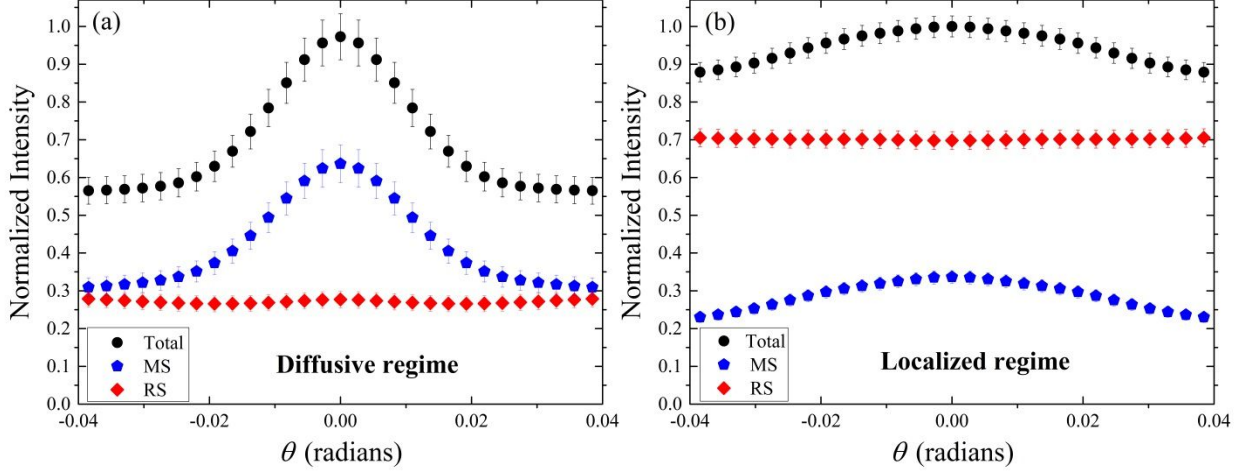


Figure 6.2: Backscattered intensity profiles at time $t = 200\mu\text{s}$ from sample L1. Total backscattered intensity (black circles) consists of contributions from recurrent and single scattering (RS, red diamonds) and conventional multiple scattering (MS, blue pentagons). The RS contribution in the diffuse regime (a) at 1.65 MHz is less than that in the localization regime (b) at 1.23 MHz. Profiles are all normalized to the peak value of total backscattered intensity. Some uncertainties are smaller than symbols sizes.

6.2.1. Recurrent scattering and the memory effect

Backscattering experiments conducted with ultrasonic arrays enable the measurement of the *propagation matrix*. As discussed in Section 2.3.2, the propagation matrix contains all relevant information about the system composed of the sources, the medium through which the waves travel, and the detectors. For random heterogeneous media, it is thus naturally described by *random matrix theory* (RMT). The manipulation of the propagation matrix based on RMT is the basis for some sophisticated studies of multiple scattering media. It has been used to fully describe the transmission modes of a complex system (Genack 2011; Gérardin et al. 2014), for selective target detection through an aberrating layer (Prada et al. 1996; Popoff et al. 2011), wave focussing across a highly scattering slab (Popoff et al. 2010; Kim et al. 2012), and optimized control of wave transport in diffusive media (Shi, Davy, and Genack 2015; Gérardin et al. 2014).

Another RMT approach to complex media was shown to separate the single and conventional multiple scattering contributions to backscattered intensity (Aubry and Derode

2009b; Aubry and Derode 2009a; Shahjahan et al. 2014). Pioneered by Aubry et al. in 2009, the original intent of this technique was to isolate singly-scattered signals to improve target detection through a multiple-scattering medium. However, the signatures of recurrent scattering in the propagation matrix are the same as those of single scattering. Figure 6.3 shows the experimentally-measured propagation matrix \mathbf{K} (consisting of the Green's functions K_{ij} describing the propagation from source i , through the sample, and to detector j) at times $t = 15 \mu\text{s}$ and $t = 200 \mu\text{s}$. Contrary to the speckle pattern for transmission of Figure 2.1, the backscattered speckle patterns of Figure 6.3 do not appear random. Instead, they display a deterministic coherence along its antidiagonals. These coherences in \mathbf{K} are caused by the *memory effect* in backscattering.

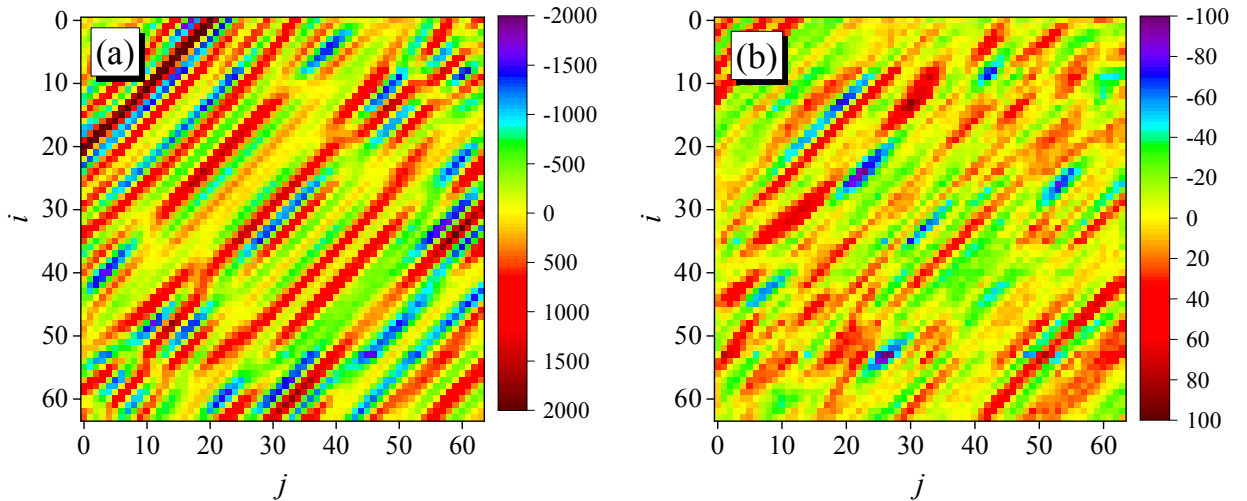


Figure 6.3: Propagation matrices \mathbf{K} for time $t = 15 \mu\text{s}$ (a) and $t = 200 \mu\text{s}$ (b). Antidiagonal coherences persist for long times, far past the range of times in which single scattering is possible.

Originally discovered in optics (Freund, Rosenbluh, and Feng 1988; Feng et al. 1988), the memory effect describes how the rotation of an incident beam by an angle θ causes the resulting speckle to be shifted by the same angle θ in transmission, or $-\theta$ in backscattering. This means that the speckle pattern retains some ‘memory’ about the incident beam, even for a

very strongly scattering sample. For single scattering, the memory effect persists over the entire angular domain, i.e. the *angular correlation width* $\Delta\theta = \pi/2$. For multiple scattering, the effect is limited to a much smaller range of $\Delta\theta \sim \lambda/W$ where W is the spatial extent of the wave spreading in the sample (Akkermans and Montambaux 2007). The signature of the memory effect on a propagation matrix is that of coherences along the antidiagonals (Aubry et al. 2014; Aubry and Derode 2009b), as shown in Figure 6.3. At early times, the coherences are due to the effects of single scattering. However, at very late times ($t = 200 \mu\text{s}$, Figure 6.3(b)), the coherences remain, despite there being no possibility of their resulting from single scattering. These coherences are caused by recurrent scattering, which, involving paths which begin and end near the same spot on the sample surface, exhibits the same angular range as single scattering.

6.2.1.1. The separation of recurrent and multiple scattering

The memory effect gives an opportunity to separate single/recurrent scattering (SS/RS) from the ‘conventional’ multiple scattering (MS), by taking advantage of the signature of the antidiagonal coherences (Aubry and Derode 2009a; Aubry and Derode 2011; Aubry et al. 2014; Aubry and Derode 2009b). This process is outlined here, and described in detail by Aubry et al. (Aubry et al. 2014) (this work is included in this thesis as Appendix 6A).

The ‘filter’ of single/recurrent scattering from conventional multiple scattering will be referred to here as the RS-MSF²⁴. The method consists of four steps:

1. Rotation and separation

The propagation matrix \mathbf{K} is rotated, and separated into two submatrices $\mathbf{A}^{(1)}(t)$ and $\mathbf{A}^{(2)}(t)$. The submatrices contain the antidiagonals of \mathbf{K} . The coherences that can be seen in

²⁴ The filter was adapted for the strong scattering regime by Alexandre Aubry (Aubry et al. 2014). Its use in this project is thanks to the collaboration with and support of Dr. Aubry.

Figure 6.3 now lie along the columns of $\mathbf{A}^{(q)}$, where $q = 1, 2$. The matrices $\mathbf{A}^{(q)}$ are made up of two components that we want to separate:

$$\mathbf{A} = \mathbf{A}_R + \mathbf{A}_M \quad (6.2)$$

where \mathbf{A}_R represents the SS/RS contribution to backscattered intensity, and \mathbf{A}_M is the MS contribution. Theoretically, the SS/RS contribution can be expressed as

$$\mathbf{A}_R[l, m] = \exp\left[j \frac{kp^2}{4a}(s-r)^2\right] r_m \quad (6.3)$$

where k is the wave number in water and r_m is a random coefficient. The variables s and r are related to the indices of \mathbf{A}_R as $l = (s-r)/2 + (N+3)/4 + 1$ for $\mathbf{A}^{(1)}[l, m]$ and $l = (s-r-1)/2 + (N+3)/4$ for $\mathbf{A}^{(2)}[l, m]$, where N is the number of rows/columns of the original propagation matrix (i.e. the number of ultrasonic array elements). Equation (6.3) gives the theoretical dependence of \mathbf{A}_R on index l . Conversely, the MS contribution does not display such a dependence, and has only a short-range correlation between its lines.

2. Separation of signal and noise

A singular value decomposition (SVD) of $\mathbf{A}^{(q)}$ is performed in the frequency domain:

$$\mathbf{A} = \mathbf{U} \mathbf{\Lambda} \mathbf{V}^\dagger = \sum_{q=1}^p \lambda_q \mathbf{U}^{(q)} \mathbf{V}^{(q)\dagger}. \quad (6.4)$$

$\mathbf{\Lambda}$ is a square diagonal matrix containing the (real and positive) singular values λ_q in decreasing order, and \mathbf{U} and \mathbf{V} are square unitary matrices with columns $\mathbf{U}^{(q)}$ and $\mathbf{V}^{(q)}$ that correspond to the singular vectors associated with each λ_q .

Conceptually, the SVD separates the $\mathbf{A}^{(q)}$ matrices into two subspaces: a *signal* subspace \mathbf{S} and a *noise* subspace \mathbf{N} . The signal subspace is a matrix with long-range correlation between its rows and/or columns, while the noise subspace is a random matrix with only short- or

medium-range correlations between its rows/columns. The signal subspace is given by largest singular values (and their corresponding singular vectors), and the noise subspace is given by the smallest singular values.

To discriminate between signal and noise subspaces, we need to determine the value (rank) of λ_q that separates the subspaces. For our experimental geometry the job is simple, as we can use the paraxial approximation that $a \gg Np$, where a is the sample-array distance and p is the pitch of the individual elements. Thus only the first singular value and vector, λ_1 and $\mathbf{U}^{(1)}$, are associated with the signal subspace. The subspaces can be calculated by:

$$\begin{aligned}\mathbf{S} &= \mathbf{U}^{(1)} \mathbf{U}^{(1)\dagger} \mathbf{A} \\ \mathbf{N} &= \mathbf{A} - \mathbf{U}^{(1)} \mathbf{U}^{(1)\dagger} \mathbf{A}\end{aligned}\tag{6.5}$$

3. A correction for strongly scattering media

We have seen that the RS contribution displays the same signatures as SS, and that these contributions may be separated from those of MS. This is due to the memory effect, which causes long-range correlations for SS/RS, but relatively short ones for MS. For MS, the memory effect is limited to the area of $\Delta\theta \sim \lambda/W$ where W is the spatial extent of the wave spreading in the sample. In the diffusion approximation, $W \propto \sqrt{D_B t}$, so the correlation angle $\Delta\theta$ quickly becomes small as time progresses. However, for subdiffusive or localized behaviour, the wave energy spreads much more slowly, so there may be a significant memory effect in the multiple scattering subspace.

This issue was dealt with by Aubry et al. via the development of a correction for the RS-MSF (Aubry et al. 2014).

4. The final step is the reconstruction of \mathbf{K}_M and \mathbf{K}_R by re-rotating $\mathbf{S}^{(q)}$ and $\mathbf{N}^{(q)}$. An inverse Fourier transform can (if desired) return the data back to the time-domain.

Some representative results of the RS-MSF filter applied to my experimental data are shown in Figure 6.4.

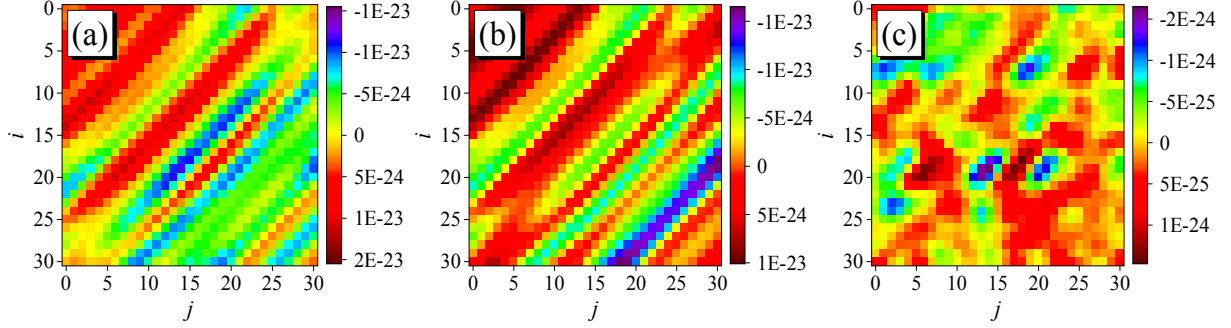


Figure 6.4: Propagation matrices from L1 after the RS-MSF process, shown for frequency $f = 1.65$ MHz and time $t = 150 \mu\text{s}$. Even for this late time and diffuse frequency, the total backscattered intensity (a) is clearly dominated by the recurrent scattering contributions (b). After RS-MSF is applied, the conventional multiple scattering contribution (c) has mostly recovered the random appearance that would be expected for a speckle pattern for incoherent waves.

Using only \mathbf{K}_M , the coherent backscattering profiles can now be calculated²⁵ free of RS effects (giving, e.g., the data represented by blue pentagons in Figure 6.2). The recurrent scattering on its own, however, also holds valuable information about wave behaviour inside the medium. This RS-MSF technique has enabled the first experimental study of RS on its own, and furthermore, the first characterization of RS in the critical and localized regimes (Aubry et al. 2014).

6.3. Recurrent scattering in the Anderson mobility gap

Figure 6.5 shows the time-evolution of the recurrent scattering (RS) ratio I_R/I (I is total

²⁵ Actually, if the desired quantity is $I(\theta, t)$, step 4 is not necessary, as $I(\theta, t)$ can be computed by summing \mathbf{S} and/or \mathbf{N} directly over the appropriate indices. Since with every rotation and re-rotation of matrices some elements are lost (Aubry and Derode 2009b), this is a worthwhile approach to take. Note that this is the reason that there are only 61 θ values for CBS intensity profiles, and only 31 θ values in the matrices shown in Figure 6.4, while the original propagation matrices have 64 rows and columns.

backscattered intensity) in the diffuse regime (1.65 MHz), the critical regime (1.20 MHz), and the localized regime (1.23 MHz). At early times ($t \lesssim 40 \mu\text{s}$) the backscattered intensity is almost completely composed of single scattering and specular reflections from the sample surface. After $50 \mu\text{s}$ the RS ratio decreases. In the diffuse regime the RS contribution to total intensity quickly becomes small. In the critical and localized regime the RS ratio remains high even for late times, and has a particularly slow decay at the mobility edge (1.20 MHz). This observation supports the idea that RS plays an important role in the discussion of Anderson localization.

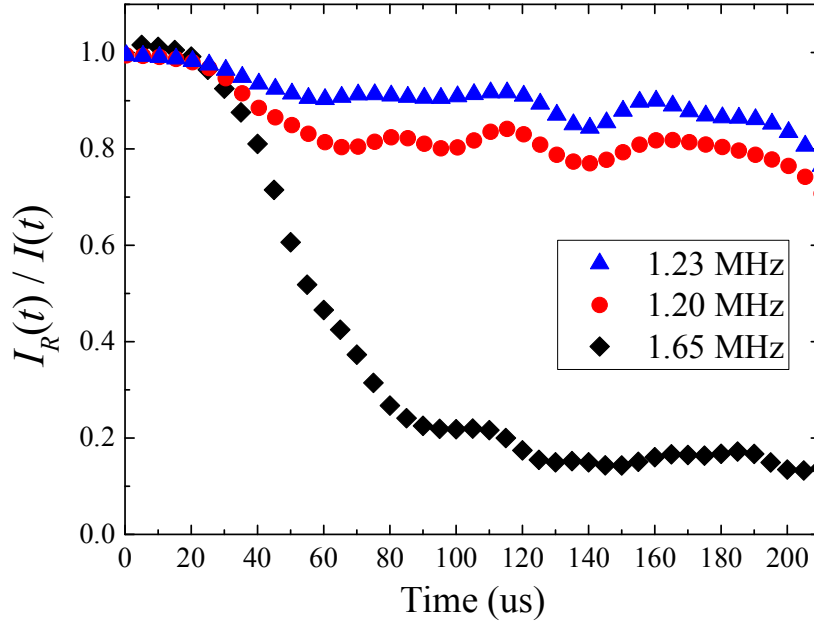


Figure 6.5: Time dependence of the RS to total intensity ratio $I_R(t)/I(t)$ in the diffuse regime (1.65 MHz, black diamonds), the critical regime (1.20 MHz, red circles), and the localized regime (1.23 MHz, blue triangles).

The decay of RS with time has particular significance in the study of localization. For times less than twice the Thouless time $\tau_D = L^2/D_B \sim 100 \mu\text{s}$, the medium can be considered semi-infinite, backscattered waves having not had the time to interact with the opposite sample face. In this case, the return probability measured at the sample surface should decay as a power law: in the diffuse regime, $I_R \propto 1/t^{5/2}$ for a point source (Douglass et al. 2011). In the

localized regime, for times earlier than $t < \xi^2/D_B$ (this is a different time scale than in the diffuse case, since the waves may not have spread throughout the entire sample), return probability should decay as $I_R \propto 1/t^2$ (Douglass et al. 2011; Skipetrov and van Tiggelen 2006). At longer times ($t > 2\tau_D$), the finite sample thickness becomes a factor, so the rate of decay should be similar to that of transmission; exponential in the diffuse regime (Page et al. 1995; Johnson et al. 2003) and slower than exponential in the localized regime (Hu et al. 2008).

Figure 6.6 shows the experimentally-measured recurrent scattering $I_R(t)$ from L1.

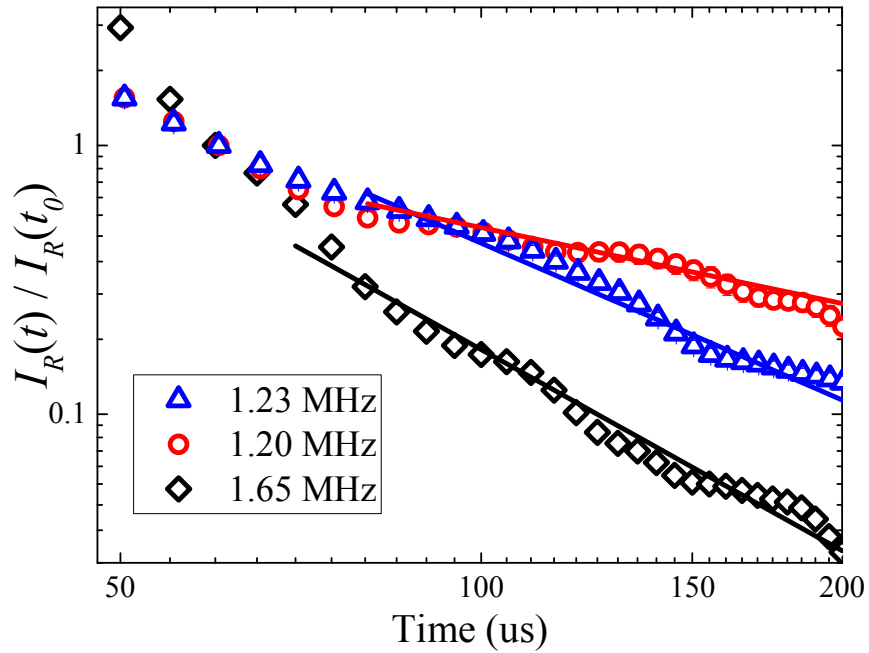


Figure 6.6: Time dependence of the RS intensity $I_R(t)$ normalized by their values at time $t_0 = 60 \mu s$, $I_R(t_0)$. Data shown are from sample L1, at the same three frequencies as in Figure 6.5. The corresponding power law fits (solid lines) give $I_R(t) \propto t^{-2.49 \pm 0.08}$ in the diffuse regime, $I_R(t) \propto t^{-0.94 \pm 0.04}$ at the mobility edge, and $I_R(t) \propto t^{-1.94 \pm 0.06}$ in the localized regime.

At all frequencies, $I_R(t)$ is well described by a power law $1/t^\alpha$ between $85 \mu s$ and $100 \mu s$ (these fits are weighted by experimental uncertainties, given by the standard deviation of the configurational average). In the diffuse regime (1.65 MHz), the expected $\alpha = 5/2$ behaviour is observed. In the localization regime (1.23 MHz), the predicted decay of $\alpha = 2$ is obtained. In

between the diffuse and localized regimes, a shift in α can be observed from 5/2 to 2. *However*, at the mobility edge of 1.20 MHz, I_R decays unexpectedly slowly, giving a value of $\alpha \approx 1$.

Interestingly, the transition between $I_R(t) \sim t^{-2.49 \pm 0.08}$ at 1.65 MHz, $I_R(t) \sim t^{-0.94 \pm 0.04}$ at 1.20 MHz and $I_R(t) \sim t^{-1.94 \pm 0.06}$ at 1.23 MHz does not occur for the upper ME around 1.24 MHz, where the result of $\alpha \approx 1$ at the ME is not observed. This may have a physical significance; it has been shown that the local density of states probably differs between the upper and lower MEs of a mobility gap (Lee 2014). As discussed in earlier chapters, the LDOS is expected to be much higher at the lower edge of a band gap than at the upper edge (our upper ME). This could cause a physical difference in wave behaviour between upper and lower MEs. It is also possible that the significant fluctuations and low signal-to-noise at those frequencies are obscuring the results, as was observed for the fitting of CBS data with SC theory (Section 5.4).

The same quantity $I_R(t)$ from sample L2 is shown in Figure 6.7. Frequency 1.15 MHz is shown as an example of a ‘diffuse’ frequency, although its proximity to the localization regime suggests that transport is probably subdiffusive. At all frequencies, $I_R(t)$ is well described by a power law $1/t^\alpha$ between 60 μ s and 125 μ s (these fits are weighted by experimental uncertainties, given by the standard deviation of the configurational average). These data do not agree as well with theoretical predictions as do the data from sample L1 (Figure 6.6). However, the general trend is still obeyed; in the localization regime (1.23 MHz), a decay of $\alpha \approx 1.7$ is obtained, and in between the diffuse and localized regimes, a shift upwards in α can be observed.

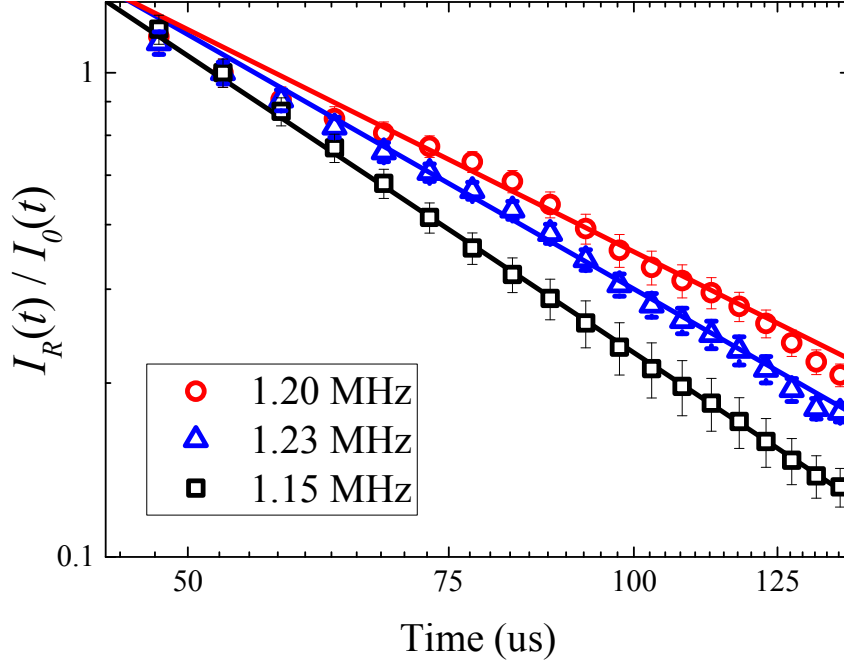


Figure 6.7: Time dependence of the RS intensity $I_R(t)$ normalized by their values at time $t_0 = 53 \mu\text{s}$, $I_R(t_0)$. Data shown is for L2. The corresponding power law fits (solid lines) give $I_R(t) \propto t^{-2.04 \pm 0.01}$ at 1.15 MHz, $I_R(t) \propto t^{-1.52 \pm 0.05}$ at the mobility edge (1.20 MHz), and $I_R(t) \propto t^{-1.74 \pm 0.04}$ in the localized regime (1.23 MHz).

At the mobility edge of 1.20 MHz, I_R decays unexpectedly slowly, giving a value of $\alpha \approx 1.5$. Although the limitation in the range of times available for this data set may impact the accuracy of this power law fitting, the results agree qualitatively with the surprising results from sample L1 data, that is, the observation of a surprisingly slow decay of $I_R(t)$ at the lower ME. Theoretical predictions for the decay of the return probability do not give a separate prediction for the mobility edge (only predictions for the diffuse and localized cases). Our striking result shows that further theoretical work is required.

6.4. Statistics of the propagation matrix

The RMT approach to the propagation matrix goes far beyond the recurrent scattering separation presented in this chapter. The statistical distribution of the singular values of a random matrix can be predicted based on the properties of the matrix. A random matrix \mathbf{K} whose

antidiagonals are strongly correlated would be expected to resemble a Hankel matrix, an $N \times N$ random matrix whose antidiagonals are equal (Aubry and Derode 2009b). The distribution of the singular values of \mathbf{K} could also be expected to resemble a Hankel distribution. This effect has been demonstrated experimentally for weakly scattering media (Aubry and Derode 2010; Aubry and Derode 2009b). Here, we would expect the same effect, since the propagation matrices measured from samples L1 and L2 show very strong antidiagonal correlations (Figure 6.3). We find that their singular values do indeed show Hankel-like distributions for most frequencies. Near the mobility edge, however, large deviations from the theoretical predictions were observed, especially around 1.2 MHz (Aubry et al. 2014). In the next paragraph we consider the mechanism leading to those large singular values.

For weakly scattering media containing several well-separated reflecting objects, the largest singular of \mathbf{K} values may be associated with the most brightly reflecting objects. Each corresponding singular vector can be interpreted physically as the wavefront which, if sent from the array of transducers, would cause a wave to converge to that object. This interpretation can be applied in the real-world to produce powerful target detection and imaging techniques (Prada and Fink 1994; Popoff et al. 2011). Instead of physically emitting a singular vector from the ultrasonic array to focus to a target, this backfocussing can be performed numerically. For a medium in which single scattering dominates, this technique enables the imaging of each bright reflecting target.

Sample L1 is very strongly scattering, and does not consist of bright, well-resolved individual scatterers. Nonetheless, if the singular vectors corresponding to the two largest singular values for \mathbf{K} from L1 are backpropagated, target-like images are produced (Figure 6.8).

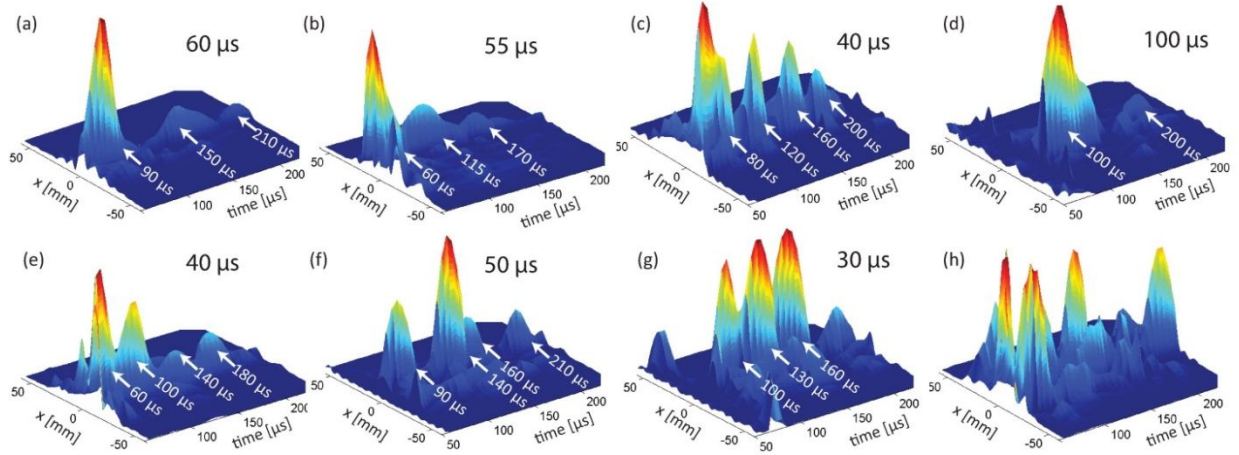


Figure 6.8: ‘Hotspots’ (the numerical backpropagation of singular vectors from the propagation matrix) of sample L1 at frequency 1.20 MHz. Peaks correspond to intense recurrent scattering paths inside the sample. Shown are different configurations of disorder (array positions) (plots (a-h)). For different configurations of disorder, the backfocussing produces peaks at different (but regular) time windows – these time intervals are marked on each plot (a-h) (Aubry et al. 2014).

If single scattering were the dominant process, the observation of a single peak would indicate a brightly reflecting object, whose distance inside the sample would correspond to the time required for a wave to travel between the array and the object. Instead, for sample L1 at the first ME (1.2 MHz), distinct peaks are observed to occur at regular time intervals, as shown in Figure 6.8. We interpret these peaks as the intensity which travels along recurrent scattering paths having their start and end points near the sample surface. The regular time intervals at which the intensity returns would therefore correspond to the length of the recurrent scattering path inside the sample. For \mathbf{K} matrices acquired at different array positions (i.e. different configurations of disorder), these *hotspots* exhibit different recurring time intervals, which supports the interpretation that the peaks correspond to recurrent scattering paths of different distances inside the sample.

6.5. Conclusion

We have observed a significant contribution of recurrent scattering to total backscattered intensity from slab mesoglasses L1 and L2. Usually practically non-existent for weakly-scattering media, this high RS contribution indicates the presence of very strong scattering in these samples. This observation agrees qualitatively with our previous estimate of $k\ell \sim 1$, but is subject to fewer assumptions and is directly observable by inspecting the propagation matrix at long times (e.g. Figure 6.3).

Via the RS-MSF, the contribution of recurrent scattering to total backscattered intensity was studied for the first time on its own. In particular, the return probability as a function of time was examined, and experimental results were supported by theoretical predictions in both the diffusive and localized regimes. However, at the lower mobility edge of 1.20 MHz, a strikingly slow return probability decay was observed, which is different than the theoretical predictions for both diffuse and localized regimes. Our observation may indicate the presence of related processes at the mobility edge, motivating further theoretical work to understand such behaviour. Certainly, additional measurements of multifractality and possibly C_0 correlations (Hildebrand et al. 2014) for samples L1 and L2 may be interesting.

This work constitutes the first study of RS in the critical and localized regimes. As recurrent scattering is directly linked to the scattering processes which accompany Anderson localization, this work represents a valuable and direct new method of investigating the critical and localized regimes.

**Appendix 6A : Recurrent scattering and memory effect at the Anderson
localization transition**

Recurrent Scattering and Memory Effect at the Anderson Localization Transition

A. Aubry,^{1*} L. A. Cobus,² S. E. Skipetrov,³ B. A. van Tiggelen,³ A. Derode,¹ and J. H. Page²

¹*Institut Langevin, ESPCI ParisTech, CNRS UMR 7587, Université Denis Diderot—Paris 7, 1 rue Jussieu, 75005 Paris, France*

²*Department of Physics and Astronomy, University of Manitoba, Winnipeg, Manitoba R3T 2N2, Canada*

³*Université Grenoble I/CNRS, Laboratoire de Physique et Modélisation des Milieux Condensés UMR 5493, B.P. 166, 38042 Grenoble, France*

(Received 12 June 2013; published 28 January 2014)

We report on ultrasonic measurements of the propagation operator in a strongly scattering mesoglass. The backscattered field is shown to display a deterministic spatial coherence due to a remarkably large memory effect induced by long recurrent trajectories. Investigation of the recurrent scattering contribution directly yields the probability for a wave to come back close to its starting spot. The decay of this quantity with time is shown to change dramatically near the Anderson localization transition. The singular value decomposition of the propagation operator reveals the dominance of very intense recurrent scattering paths near the mobility edge.

DOI: 10.1103/PhysRevLett.112.043903

PACS numbers: 42.25.Dd, 43.20.Gp, 71.23.An

In a disordered medium, a classical approach is to consider the trajectory followed by a wave as a Brownian random walk. After a few scattering events, the spatiotemporal evolution of the mean intensity is governed by the diffusion equation. The relevant parameters are the scattering mean free path l_s , the transport mean free path l^* , and the Boltzmann diffusion coefficient D_B . However, this classical picture neglects interference effects that may resist the influence of disorder. In particular, constructive interference between reciprocal multiple scattering (MS) paths enhances the probability for a wave to come back close to its starting point as compared to classical predictions: this phenomenon is known as weak localization. Hence, interference can slow down and eventually stop the diffusion process, giving rise to Anderson localization (AL) [1–5]: instead of spreading diffusely from the source, a wave packet remains localized in its vicinity on a length scale given by the localization length ξ . The transition at a mobility edge between diffuse and localized behavior is predicted to exist only in three-dimensional media and occurs when the scattering is sufficiently strong, i.e., when $kl_s \sim 1$ (with k the wave number in the scattering medium) [2]. Several experiments in optics have shown deviations from diffuse behavior in three-dimensional strongly scattering samples [6–8]. However, the most direct proof of three-dimensional classical wave localization was first established in acoustics, by observing the transverse confinement of energy in a *mesoglass* consisting of an elastic network of aluminium beads [9]. More recently, this transverse confinement method [9] has also been used in optics [10].

In this Letter, we investigate some new mesoscopic aspects of AL, taking advantage of ultrasonic technology. More precisely, we adopt a matrix formalism which is particularly appropriate since the ultrasonic wave field can

be controlled by an array of independent transducers acting both as sources and receivers (Fig. 1). The Green's functions K_{ij} , obtained by emitting a wave from an array element i and recording the backscattered field at an element j , constitute the propagation matrix \mathbf{K} . This matrix provides many fundamental insights into the medium under investigation. One can, for instance, extract from \mathbf{K} the single- and multiple-scattering components [11–13], the diffusive halo and the coherent backscattering cone [14], or even determine the open scattering channels [15,16].

In this study, the propagation matrix is investigated in the strongly scattering regime ($kl_s \sim 1$). Surprisingly, the backscattered field displays a deterministic coherence along the antidiagonals of \mathbf{K} in a way similar to single scattering [11], but at much longer times of flight. We argue that recurrent scattering (RS) paths account for this long-range coherence and establish the link with the memory effect

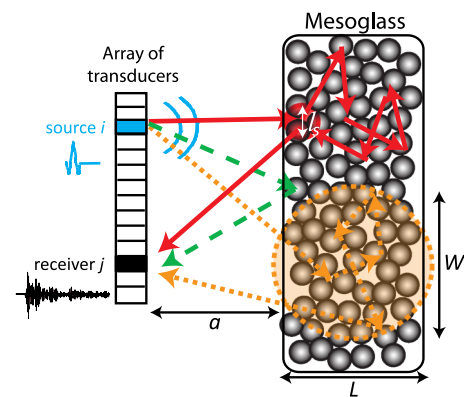


FIG. 1 (color online). Experimental setup. Examples of a single scattering path (green dashed arrows), of a RS path (red solid arrows) and of a conventional MS path (orange dotted arrows) are drawn.

[17,18]. By RS paths, we mean any scattering path that begins and ends at positions separated by less than one mean free path. A matrix method is then applied to extract the RS contribution from the backscattered wave field. This yields a quantitative measurement of the probability for a wave to return to its starting spot. A slowing down of the decay of this return probability with time is observed near the localization transition, in qualitative agreement with theory [4]. At the mobility edge, the measured decay is actually slower than anticipated from the self-consistent (SC) theory of localization [4]. This surprising behavior coincides with the emergence of very intense RS paths that dominate the singular value spectrum of \mathbf{K} . These observations offer new insights into key aspects of three-dimensional AL that have not been accessible to experimental investigation previously.

Our random scattering sample is a mesoglass similar to those used in a previous work [9]. It is made from 3.93 mm mean diameter aluminium beads brazed together at a volume fraction of approximately 55%. The cross section ($230 \times 250 \text{ mm}^2$) of the slab-shaped sample is much larger than its thickness $L = 25 \text{ mm}$. Unlike the samples in Ref. [9], there is a polydispersity of about 20% in the size of the beads, and different brazing conditions resulted in stronger elastic bonds between the beads, thereby modifying the scattering properties of the sample. From measurements at 0.9 MHz of the coherent pulse crossing the sample [19], we estimate the longitudinal phase velocity $v_p \approx 2.8 \text{ mm}/\mu\text{s}$ and the mean free path $l_s \approx 1.3 \text{ mm}$ [19]. This leads to a product of wave number k and mean free path $kl_s \lesssim 3$. Above 1 MHz, the coherent pulse becomes too small to measure accurately in this thick sample, consistent with even stronger scattering and smaller values of kl_s . By performing transverse confinement measurements [9], we find that the waves are localized between 1.2 and 1.25 MHz (mobility edges), with $\xi < L$ in the middle of this band.

The experimental setup (Fig. 1) uses $N = 64$ elements of a linear ultrasonic array in the 1–2 MHz frequency range. The array pitch p is 0.5 mm. The array is immersed in water, at a distance $a = 182 \text{ mm}$ from the waterproofed sample. N^2 time-dependent responses are measured by sending a pulse from element i and recording the scattered wave field at element j (see Fig. 1), for all i and j . To perform a time-frequency analysis, these signals are filtered by a Gaussian envelope of standard deviation of 0.015 MHz centered around a given central frequency f . A set of matrices $\mathbf{K}(t, f)$ is obtained at each time-frequency pair. This operation was repeated for 302 different realizations of disorder by moving the array in a plane parallel to the sample surface.

Figure 2(a) displays a typical example of the matrix \mathbf{K} obtained at frequency $f = 1.25 \text{ MHz}$ and time $t = 185 \mu\text{s}$ much exceeding the mean free time $l_s/v_p \approx 1 \mu\text{s}$, deep in the MS regime. Surprisingly, despite its overall random

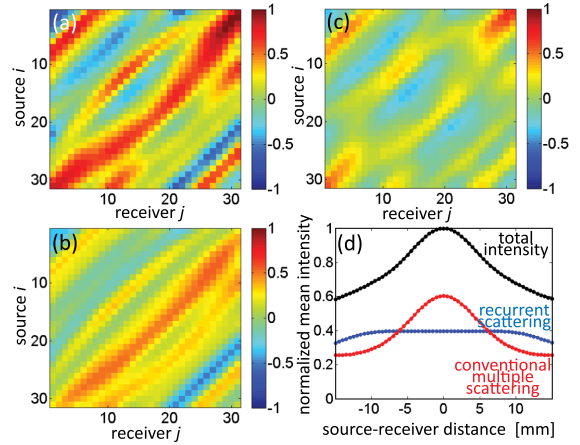


FIG. 2 (color online). (a) Real part of the matrix \mathbf{K} at time $t = 185 \mu\text{s}$ and frequency $f = 1.25 \text{ MHz}$ for a given realization of disorder. (b) Real part of the RS contribution \mathbf{K}_R . (c) Real part of the conventional MS contribution \mathbf{K}_M . (d) Spatial mean intensity profiles at the same time and frequency.

appearance, the matrix \mathbf{K} exhibits a clear coherence along its antidiagonals. This result should be considered in the context of previous studies [11,20] that dealt with much weaker scattering ($kl_s \sim 100$). In these media, the antidiagonal coherence was proven to be associated with the single scattering contribution and insensitive to disorder. It can also be understood as a manifestation of the well-known memory effect. This phenomenon was discovered in optics in the late eighties [17,18] and has recently received renewed interest in the context of ultrasonic and optical imaging [12,21–24]. When an incident plane wave is rotated by an angle θ , the speckle image measured in transmission or in backscattering in the far field of the sample is shifted by the same angle θ (or $-\theta$ in reflection), as long as θ does not exceed a certain threshold, namely the angular correlation width $\Delta\theta$. In the single scattering regime, the memory effect actually spreads over the whole angular spectrum ($\Delta\theta = \pi/2$) [17,18]. This accounts for the fact that the signals K_{ij} are coherent along the same antidiagonal, as long as only single scattering takes place. Indeed two pairs of array elements (i_1, j_1) and (i_2, j_2) on the same antidiagonal obey $i_1 + j_1 = i_2 + j_2$. Changing the direction of emission amounts to changing i_1 into i_2 . Consequently, in reflection the resulting speckle will be tilted so that the signal that was received in j_1 will be coherent with the new signal in $j_2 = j_1 - (i_2 - i_1)$. When MS takes place, the correlation width $\Delta\theta$ is greatly restricted. Therefore the K_{ij} 's are no longer expected to exhibit this remarkable antidiagonal coherence, and are expected to emerge as random and only short-range correlated [11,20]. However, Fig. 2(a) clearly contradicts this simple picture. It indicates that the matrix \mathbf{K} corresponding to the strongly MS regime shares the spatial coherence of the matrix corresponding to the single scattering regime, though at much longer times of flight.

Another surprising result is shown by Fig. 2(d) which displays the mean backscattered intensity as a function of the distance between the source i and the receiver j at the same time and frequency as in Fig. 2(a). In the MS regime ($v_p t \gg l_s$) and far from localization ($kl_s \gg 1$), the intensity backscattered at the source is expected to be twice as large as the intensity far from the source: this is the coherent backscattering phenomenon [25–28]. Although we do indeed obtain this coherent backscattering peak, the enhancement factor is clearly smaller than 2. We interpret this as a sign of a large contribution from RS (red arrows in Fig. 1). RS, just like single scattering, contributes to the background intensity that is independent of the distance between source and receiver. The interference between a wave and its reciprocal counterpart is indeed always constructive for these two contributions. A reduction of the enhancement factor due to RS was previously observed experimentally, but in a much lower proportion and not as a function of time [29,30].

The very large RS contribution seen in our experiment sheds new light on the long-range spatial coherence observed in Fig. 2(a). In the strongly scattering regime, the backscattered field can be decomposed into a sum of two terms: (i) A RS contribution (red arrows in Fig. 1) that displays the same statistical properties as the single scattering one. This contribution accounts for the deterministic coherence along the antidiagonals of \mathbf{K} in Fig. 2(a). (ii) A *conventional* MS contribution (orange arrows in Fig. 1) for which the first and last scattering events are separated by more than one mean free path. In this case, the memory effect is restricted to the angular width of the backscattering cone [31,32].

Previous studies have taken advantage of the memory effect to separate single and multiple scattering [11–13]. Here, the previous method is significantly extended [33] to enable \mathbf{K} [Fig. 2(a)] to be separated into a RS component \mathbf{K}_R [Fig. 2(b)] and a conventional MS component \mathbf{K}_M [Fig. 2(c)]. Once the separation of these two contributions is performed, one can compute the corresponding mean backscattered intensity [Fig. 2(d)]. Whereas RS leads to a flat intensity profile, the conventional MS intensity exhibits a coherent backscattering cone. The recovery of an enhancement factor close to two demonstrates that RS was indeed responsible for reducing the enhancement factor seen for the total intensity I [30] [Fig. 2(d)].

The RS intensity I_R is directly related to the probability P_R for a wave to return to the spot at which it entered the scattering sample. From a theoretical point of view, this return probability is a key quantity in the description of the renormalization of the diffusion constant in the SC theory of localization [3,4]. Figure 3(a) shows the time evolution of the RS ratio I_R/I at $f = 1.2$ MHz (critical regime), $f = 1.225$ MHz (localized regime), and $f = 1.8$ MHz (diffuse regime), with I the total backscattered intensity. After a plateau close to 100% that lasts until $t = 50 \mu\text{s}$ due to

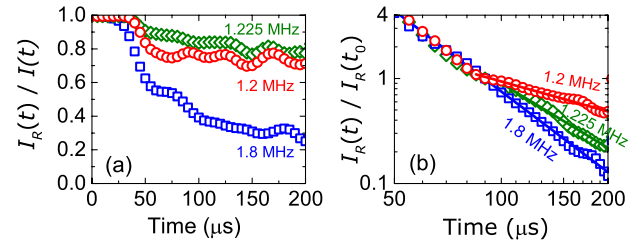


FIG. 3 (color online). (a) Time evolution of the RS ratio I_R/I at $f = 1.2$ MHz (red circles), $f = 1.225$ MHz (green diamonds), and $f = 1.8$ MHz (blue squares). (b) Time evolution of the RS intensities $I_R(t)$, normalized by their values at time $t_0 = 90 \mu\text{s}$, at the same three frequencies, shown in a log-log scale. The corresponding fits with a power law (continuous lines) yield $I_R(t) \propto t^{-2.55 \pm 0.13}$ at 1.8, $I_R(t) \propto t^{-2.04 \pm 0.18}$ at 1.225 and $I_R(t) \propto t^{-0.95 \pm 0.23}$ at 1.2 MHz.

specular echoes from the sample surface (see green arrows in Fig. 1), the RS ratio starts to decrease with time. This ratio is highest at 1.225 MHz, and has a particularly slow decay at $f = 1.2$ MHz, with I_R/I being still above 70% at $t = 200 \mu\text{s}$ (i.e., after 450 scattering events) for both frequencies. The large predominance of RS paths at frequencies near 1.225 MHz strongly suggests it to be a crucial element in any discussion of AL.

The decay of the RS intensity with time bears particular signatures of AL. For times of flight smaller than twice the Thouless time $\tau_D = L^2/D_B \sim 100 \mu\text{s}$, the medium can be considered as semi-infinite in a backscattering configuration. In that case, a power law decay is expected for the return probability at the surface of the sample: $I_R(t)$ should decrease as $1/t^{5/2}$ in the diffuse regime [8] and, for $t > \xi^2/D_B$, as $1/t^2$ in the localized regime [4,8]. At longer times of flight ($t > 2\tau_D$), the finite sample size should come into play so that the decay becomes similar to that of time-dependent transmission, i.e., exponential in the diffuse regime [34,35] and nonexponential in the localized regime [7,9].

Figure 3(b) displays the typical time dependence of $I_R(t)$ in the 1–2 MHz frequency range. At all frequencies, $I_R(t)$ can be described by a power law $1/t^\alpha$ between 85 and $200 \mu\text{s}$. We recover the exponent $\alpha = 5/2$ at 1.8 MHz, characteristic of the diffuse regime, and observe its shift to 2 at 1.225 MHz as expected in the localized regime. Furthermore, we observe a strikingly slower decay at $f = 1.2$ MHz, which corresponds to a mobility edge and where α reaches a value close to 1. Further theoretical work on the Anderson transition in open media is needed to account for this unexpected behavior. As the exponent α is linked to the dimension of available space in which the waves propagate, it might be related to previously observed [36] and theoretically predicted [37–40] multifractal properties of the wave function. In the literature, transmission measurements have also shown some deviations from SC theory in the localized regime [41] due to long-lived

resonant modes [42]. Interestingly, as discussed below, the discrepancy with SC theory in backscattering coincides with the emergence of very intense RS paths close to the mobility edge.

We now investigate the effect of RS on the statistical properties of the random matrix \mathbf{K} . First, we study the statistical properties of the singular values of \mathbf{K} and compare them with the predictions of random matrix theory (RMT). The singular value decomposition (SVD) consists in writing $\mathbf{K} = \mathbf{U}\mathbf{\Lambda}\mathbf{V}^\dagger$, where \mathbf{U} and \mathbf{V} are unitary matrices and $\mathbf{\Lambda}$ is a diagonal matrix whose nonzero elements λ_i are called the singular values of \mathbf{K} . They are real, positive, and arranged in decreasing order. In the case of random matrices whose antidiagonals are either constant or strongly correlated (Hankel matrices), the statistical distribution of singular values, particularly the strongest ones, can be calculated and compared to experimental measurements [11,20]. In the present situation, given the substantial memory effect, one would expect the singular values to follow Hankel-like distributions, as was observed in previous work dealing with weaker scattering [11,20]. However, the present experimental results show that this is clearly not the case for the first two singular values, especially around 1.2 MHz. Figure 4(a) displays the average of the three largest singular values, $\langle\lambda_{i=1,2,3}\rangle$, as a function of frequency at a given time $t = 150 \mu\text{s}$ [43]. The $\langle\lambda_i\rangle$ are compared to the theoretical values expected for Hankel random matrices [20]. As we will now discuss, the spectacular discrepancy between the first two singular values and RMT predictions around 1.2 MHz is related to the dominance of intense RS paths in the backscattered wave field.

Singular vectors can be given a physical interpretation: they are the invariants of the time reversal operator $\mathbf{K}\mathbf{K}^\dagger$. In a weakly scattering regime, there is a one-to-one correspondence between single scattering paths and eigenvectors of \mathbf{K} associated with nonzero singular values [44,45]: each singular vector of \mathbf{K} corresponds to the wave front

that, if sent as such from the array, would focus onto the corresponding scatterer. By contrast, in strongly scattering media, the physical meaning of singular vectors and the result of their back propagation will be different, and may reveal unusual phenomena. Figure 4(b) shows the time evolution of the numerical back propagation of \mathbf{V}_1 at the sample surface for one realization of disorder. Once again, we observe remarkable behavior around 1.2 MHz: \mathbf{V}_1 back-focuses on the same particular location at regular time intervals (every $40 \mu\text{s}$), as if it were associated with a particular *dynamic hot spot*. The corresponding peaks are of same duration as the incident pulse ($\sim 10 \mu\text{s}$). In the strongly scattering regime, near the localization transition, we argue that the largest singular values of \mathbf{K} are associated with predominant RS paths, whose entry and exit points appear as specific hot spots at the surface of the sample. For the realization of disorder considered in Fig. 4(b), the occurrence of the same hot spot every $40 \mu\text{s}$ could indicate that it corresponds to successive round trips along a RS path of no less than 90 scattering events. Note that the emergence of dynamic hot spots has been observed in other configurations of disorder with different regularly spaced intervals of time ranging from $30 \mu\text{s}$ to $100 \mu\text{s}$ [33]. From a practical point of view, the selective and independent excitation of RS paths can open new perspectives for manipulation of wave fields in complex media. In an amplifying medium, for example, one could select the scattering paths to be amplified and thus control the random laser process [46].

In conclusion, we have shown how new information on the dynamics of Anderson localization can be obtained using the mesoscopic reflection matrix approach. The long-range spatial coherence of the RS contribution has been directly observed and its link with the memory effect has been established. A sophisticated matrix manipulation method has been further developed to separate this contribution from the conventional MS background, enabling RS to be examined experimentally on its own for the first time. Thus we are able not only to demonstrate that the contribution of RS to the total backscattered intensity is strikingly large near the Anderson transition, but also to investigate the dynamics of the return probability for waves within the scattering medium. In particular, a dramatic slowing down in the decay of the return probability has been found near the mobility edge, with a power-law exponent α that is smaller than expected, motivating new theoretical work to understand this behavior quantitatively. The emergence of very intense RS paths, which are revealed by our analysis of the singular values of the backscattering matrix, is another novel feature of our results, and provides support for the idea that RS plays a very important role near the mobility edge.

A. A. and A. D. are grateful for funding provided by the Agence Nationale de la Recherche (ANR-11-BS09-007-01, Research Project DiAMAN) and by LABEX WIFI

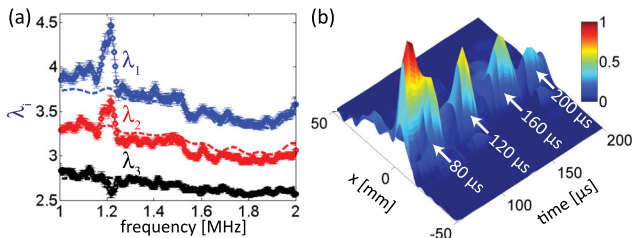


FIG. 4 (color online). (a) Average of the first three singular values $\langle\lambda_i\rangle$ versus frequency at time $t = 150 \mu\text{s}$. The experimental results (circles) are compared to the RMT predictions (lines). Error bars correspond to \pm the standard error in the mean. (b) Back propagation of the first singular vector at the sample surface computed at each time for one realization of disorder at frequency $f = 1.2 \text{ MHz}$. x represents the coordinate along the surface.

(Laboratory of Excellence ANR-10-LABX-24) within the French Program “Investments for the Future” under reference ANR-10-IDEX-0001-02 PSL*. J. H. P. and L. A. C. acknowledge the support of NSERC (Discovery Grant RGPIN/9037-2011, Canada Government Scholarship, and Michael Smith Foreign Study Supplement), the Canada Foundation for Innovation and the Manitoba Research and Innovation Fund (CFI/MRIF, LOF Project 23523).

*alexandre.aubry@espci.fr

- [1] P. W. Anderson, *Phys. Rev.* **109**, 1492 (1958).
- [2] E. Abrahams, P. W. Anderson, D. C. Licciardello, and T. V. Ramakrishnan, *Phys. Rev. Lett.* **42**, 673 (1979).
- [3] D. Vollhardt and P. Wölfle, *Phys. Rev. Lett.* **48**, 699 (1982).
- [4] S. E. Skipetrov and B. A. van Tiggelen, *Phys. Rev. Lett.* **96**, 043902 (2006).
- [5] A. Lagendijk, B. A. van Tiggelen, and D. S. Wiersma, *Phys. Today* **62**, 24 (2009).
- [6] D. S. Wiersma, P. Bartolini, A. Lagendijk, and R. Righini, *Nature (London)* **390**, 671 (1997).
- [7] M. Störzer, P. Gross, C. M. Aegerter, and G. Maret, *Phys. Rev. Lett.* **96**, 063904 (2006).
- [8] K. M. Douglass, S. John, T. Suezaki, G. A. Ozin, and A. Dogariu, *Opt. Express* **19**, 25320 (2011).
- [9] H. Hu, A. Strybulevych, J. H. Page, S. E. Skipetrov, and B. A. van Tiggelen, *Nat. Phys.* **4**, 945 (2008).
- [10] T. Sperling, W. P. Bührer, C. M. Aegerter, and G. Maret, *Nat. Photonics* **7**, 48 (2013).
- [11] A. Aubry and A. Derode, *Phys. Rev. Lett.* **102**, 084301 (2009).
- [12] A. Aubry and A. Derode, *J. Appl. Phys.* **106**, 044903 (2009).
- [13] A. Aubry and A. Derode, *J. Acoust. Soc. Am.* **129**, 225 (2011).
- [14] A. Aubry and A. Derode, *Phys. Rev. E* **75**, 026602 (2007).
- [15] S. M. Popoff, G. Lerosey, R. Carminati, M. Fink, A. C. Boccara, and S. Gigan, *Phys. Rev. Lett.* **104**, 100601 (2010).
- [16] M. Kim, Y. Choi, C. Yoon, W. Choi, J. Kim, Q.-H. Park, and W. Choi, *Nat. Photonics* **6**, 583 (2012).
- [17] I. Freund, M. Rosenbluh, and S. Feng, *Phys. Rev. Lett.* **61**, 2328 (1988).
- [18] S. Feng, C. Kane, P. A. Lee, and A. D. Stone, *Phys. Rev. Lett.* **61**, 834 (1988).
- [19] J. H. Page, P. Sheng, H. P. Schriemer, I. Jones, X. Jing, and D. A. Weitz, *Science* **271**, 634 (1996).
- [20] A. Aubry and A. Derode, *Waves Random Complex Media* **20**, 333 (2010).
- [21] E. G. van Putten, D. Akbulut, J. Bertolotti, W. L. Vos, A. Lagendijk, and A. P. Mosk, *Phys. Rev. Lett.* **106**, 193905 (2011).
- [22] S. M. Popoff, G. Lerosey, R. Carminati, M. Fink, A. C. Boccara, and S. Gigan, *New J. Phys.* **13**, 123021 (2011).
- [23] O. Katz, E. Smal, and Y. Silberberg, *Nat. Photonics* **6**, 549 (2012).
- [24] J. Bertolotti, E. G. van Putten, C. Blum, A. Lagendijk, W. L. Vos, and A. P. Mosk, *Nature (London)* **491**, 232 (2012).
- [25] Y. Kuga and A. Ishimaru, *J. Opt. Soc. Am. A* **1**, 831 (1984).
- [26] M. P. Van Albada and A. Lagendijk, *Phys. Rev. Lett.* **55**, 2692 (1985).
- [27] P.-E. Wolf and G. Maret, *Phys. Rev. Lett.* **55**, 2696 (1985).
- [28] A. Tourin, A. Derode, P. Roux, B. A. van Tiggelen, and M. Fink, *Phys. Rev. Lett.* **79**, 3637 (1997).
- [29] D. S. Wiersma, M. P. van Albada, B. A. van Tiggelen, and A. Lagendijk, *Phys. Rev. Lett.* **74**, 4193 (1995).
- [30] B. A. van Tiggelen, D. A. Wiersma, and A. Lagendijk, *Europhys. Lett.* **30**, 1 (1995).
- [31] I. Freund, M. Rosenbluh, and R. Berkovits, *Phys. Rev. B* **39**, 12403 (1989).
- [32] E. Akkermans and G. Montambaux, *Mesoscopic Physics of Electrons and Photons* (Cambridge University Press, Cambridge, England, 2006).
- [33] See Supplemental Material at <http://link.aps.org/supplemental/10.1103/PhysRevLett.112.043903> for a detailed description of the recurrent scattering filter and more information on recurrent scattering hot spots.
- [34] J. H. Page, H. P. Schriemer, A. E. Bailey, and D. A. Weitz, *Phys. Rev. E* **52**, 3106 (1995).
- [35] P. M. Johnson, A. Imhof, B. P. J. Bret, J. G. Rivas, and A. Lagendijk, *Phys. Rev. E* **68**, 016604 (2003).
- [36] S. Faez, A. Strybulevych, J. H. Page, A. Lagendijk, and B. A. van Tiggelen, *Phys. Rev. Lett.* **103**, 155703 (2009).
- [37] F. Wegner, *Z. Phys. B* **36**, 209 (1980).
- [38] F. Evers and A. D. Mirlin, *Rev. Mod. Phys.* **80**, 1355 (2008).
- [39] J. T. Chalker and G. J. Daniell, *Phys. Rev. Lett.* **61**, 593 (1988).
- [40] V. E. Kravtsov, A. Ossipov, and O. M. Yevtushenko, *J. Phys. A* **44**, 305003 (2011).
- [41] Z. Q. Zhang, A. A. Chabanov, S. K. Cheung, C. H. Wong, and A. Z. Genack, *Phys. Rev. B* **79**, 144203 (2009).
- [42] C. S. Tian, S. K. Cheung, and Z. Q. Zhang, *Phys. Rev. Lett.* **105**, 263905 (2010).
- [43] Prior to averaging over different realizations of disorder, the singular values have been normalized by their quadratic mean.
- [44] C. Prada and M. Fink, *Wave Motion* **20**, 151 (1994).
- [45] S. M. Popoff, A. Aubry, G. Lerosey, M. Fink, A. C. Boccara, and S. Gigan, *Phys. Rev. Lett.* **107**, 263901 (2011).
- [46] N. Bachelard, J. Andreasen, S. Gigan, and P. Sebbah, *Phys. Rev. Lett.* **109**, 033903 (2012).

Supplementary material: Recurrent scattering and memory effect at the Anderson localization transition

A. Aubry,¹ L. A. Cobus,² S. E. Skipetrov,³ B. A. van Tiggelen,³ A. Derode,¹ and J. H. Page²

¹*Institut Langevin, ESPCI ParisTech, CNRS UMR 7587,*

Université Denis Diderot - Paris 7, 1 rue Jussieu, 75005 Paris, France

²*Department of Physics and Astronomy, University of Manitoba, Winnipeg, Manitoba R3T 2N2, Canada*

³*Université Grenoble 1/CNRS, Laboratoire de Physique et Modélisation des Milieux Condensés UMR 5493, B.P. 166, 38042 Grenoble, France*

RECURRENT SCATTERING FILTER

This section describes the method to separate the recurrent scattering (RS) and the conventional multiple scattering (MS) contributions. Our approach is inspired by previous studies that have shown how to separate single scattering (SS) and MS in weakly scattering media [S1–S3]. RS actually displays the same statistical properties as SS, *i.e.* a deterministic spatial coherence along the antidiagonals of the array response matrix \mathbf{K} , which is a manifestation of a long-range memory effect. The idea is to take advantage of this property to filter RS from the conventional MS background. However, albeit more restricted, a memory effect also exists for the MS contribution [S4, S5]. For the matrix \mathbf{K} , this implies that the MS far-field speckle exhibits a finite correlation length δ [S6, S7], which can be expressed in units of the array pitch p as

$$\delta \sim \lambda_w a / [pW(t)], \quad (\text{S1})$$

with λ_w the wavelength in water, a the array-sample distance and $W(t)$ the dynamic size of the diffusive halo as a function of time. In a weakly scattering regime, the diffusive halo grows quickly enough ($W(t) \propto \sqrt{Dt}$, with D the diffusion constant) to consider the multiple scattering field as fully uncorrelated. The separation of SS and MS is then relatively easy [S1–S3]. In a strongly scattering regime, the diffusive halo grows much more slowly and can even saturate at the Anderson transition. Hence, the separation between RS and conventional MS is more tricky but still possible.

The method used for this separation consists of a four-step process:

- Rotation of the matrix $\mathbf{K}(t)$ and construction of two submatrices $\mathbf{A}^{(1)}(t)$ and $\mathbf{A}^{(2)}(t)$.
- Singular value decomposition (SVD) of matrices $\mathbf{A}^{(q)}$ (with $q = 1, 2$) in the frequency domain. $\mathbf{A}^{(q)}$ is decomposed as the sum of two matrices: $\mathbf{A}^{(q)} = \mathbf{S} + \mathbf{N}$, where \mathbf{S} and \mathbf{N} correspond to the signal subspace mainly associated with RS and the noise subspace associated with conventional MS.
- Correction of the signal and noise subspaces to obtain estimators of the RS and MS contributions in the time domain: $\hat{\mathbf{A}}_{\mathbf{R}}^{(q)}(t)$ and $\hat{\mathbf{A}}_{\mathbf{M}}^{(q)}(t)$. This correction is based on energy arguments.
- Construction from $\hat{\mathbf{A}}_{\mathbf{R}}^{(q)}(t)$ and $\hat{\mathbf{A}}_{\mathbf{M}}^{(q)}(t)$ of RS and MS matrix estimators $\hat{\mathbf{K}}_{\mathbf{R}}(t)$ and $\hat{\mathbf{K}}_{\mathbf{M}}(t)$.

The first, second and fourth steps (rotation of data, SVD of antidiagonals) have already been presented in a previous study

[S3] and will be briefly recalled. The third step constitutes the important new extension of the previous method. This novel step is necessary to tackle the medium-range correlations of the MS field in the strongly scattering regime.

Matrix rotation

A rotation of matrix data is performed as depicted in Fig. S1(a)-(b). It consists in building two matrices $\mathbf{A}^{(1)}$ and $\mathbf{A}^{(2)}$ from matrix \mathbf{K} :

$$\mathbf{A}^{(1)} = [A_{lm}^{(1)}] \text{ of dimension } (2M - 1) \times (2M - 1),$$

$$\text{such that } A^{(1)}[l, m] = K[l + m - 1, m - l + 2M - 1] \quad (\text{S2})$$

$$\mathbf{A}^{(2)} = [A_{lm}^{(2)}] \text{ of dimension } (2M - 2) \times (2M - 2),$$

$$\text{such that } A^{(2)}[l, m] = K[l + m, m - l + 2M - 1] \quad (\text{S3})$$

with $M = (N + 3)/4$. Here $N = 61$, so $M = 16$ is an even number. This rotation of data is illustrated in Fig. S1. Fig. S1(a) shows an example of matrix \mathbf{K} measured experimentally at a given time t . Fig. S1(b) displays the matrix $\mathbf{A}^{(1)}$ obtained after the rotation of data described above. The columns of matrices $\mathbf{A}^{(1)}$ and $\mathbf{A}^{(2)}$ correspond to the antidiagonals of \mathbf{K} . Therefore the coherence of recurrent scattering now manifests itself along the columns of $\mathbf{A}^{(1)}$ and $\mathbf{A}^{(2)}$. $\mathbf{A}^{(1)}$ contains the antidiagonals for which the source index s and the receiver index r are of same parity, such that $l = (s - r)/2 + M + 1$ and $m = (s + r)/2 - M + 1$ are integers. $\mathbf{A}^{(2)}$ contains the antidiagonals for which s and r are of opposite parity, such that $l = (s - r - 1)/2 + M$ and $m = (s + r + 1)/2 + M$ are integers. In the next subsection, we will no longer make the difference between matrices $\mathbf{A}^{(1)}$ and $\mathbf{A}^{(2)}$ because they are filtered in the same way. They will both be called \mathbf{A} . P is the dimension of \mathbf{A} . For matrix $\mathbf{A}^{(1)}$, $P = 2M - 1$; for matrix $\mathbf{A}^{(2)}$, $P = 2M - 2$. Because of spatial reciprocity, \mathbf{K} is symmetric ($k_{sr} = k_{rs}$). Thus, \mathbf{A} also exhibits a symmetry: each line of its upper part is identical to a line of its lower part.

Singular value decomposition of \mathbf{A}

A Fourier analysis of the matrix $\mathbf{A}(t)$ is first performed by means of a discrete Fourier transform (DFT). This yields a set

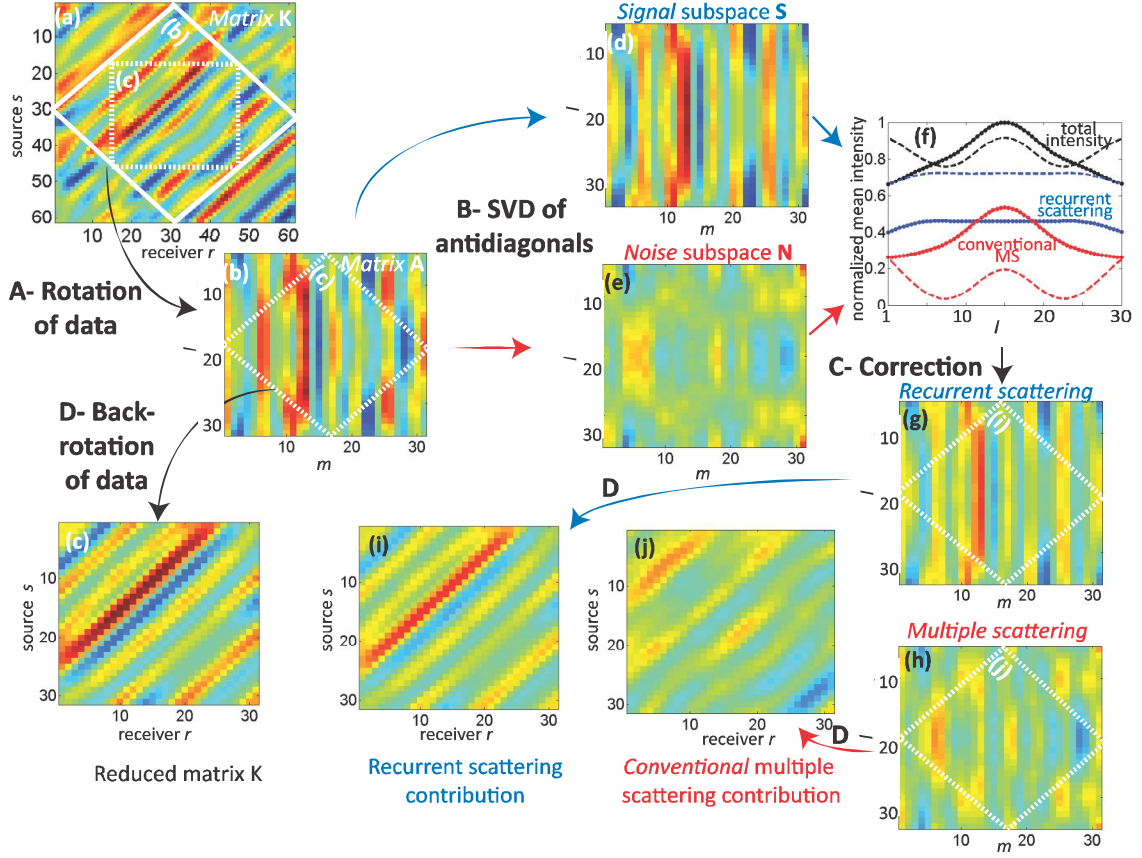


FIG. S1: Different steps for the separation of RS and MS illustrated for a representative example of the matrix \mathbf{K} at a given time $t = 185 \mu\text{s}$ and frequency $f = 1.25 \text{ MHz}$. (a) Measured matrix \mathbf{K} . (b) Matrix $\mathbf{A}^{(1)}$ deduced from \mathbf{K} by rotation of data. (c) Reduced matrix \mathbf{K} deduced from \mathbf{A} by back-rotation of data. (d) Signal subspace \mathbf{S} of \mathbf{A} [Eq. (S9)]. (e) Noise subspace \mathbf{N} of \mathbf{A} [Eq. (S10)]. (f) Intensity profiles of antidiagonal matrices: total intensity I (continuous black line), signal subspace intensity I_S (blue dashed line), noise subspace intensity I_N (red dashed line), $I_S + I_N$ (black dashed line), estimated RS intensity \hat{I}_R (blue continuous line), estimated MS intensity \hat{I}_M (red continuous line). (g) Estimated RS antidiagonal matrix $\hat{\mathbf{A}}_R$. (h) Estimated MS antidiagonal matrix $\hat{\mathbf{A}}_M$. (i) Estimated RS matrix $\hat{\mathbf{K}}_R$. (j) Estimated MS matrix $\hat{\mathbf{K}}_M$.

of matrices $\mathbf{A}(f)$ at each frequency f . The matrix \mathbf{A} contain a SS/RS component (matrix \mathbf{A}_R) and MS component \mathbf{A}_M that we want to separate:

$$\mathbf{A} = \mathbf{A}_R + \mathbf{A}_M \quad (\text{S4})$$

Using the paraxial approximation to describe the wave propagation outside of the scattering sample and assuming point-like scatterers, the SS/RS contribution can be expressed as [S1–S3]

$$A_R[l, m] = \exp \left[j \frac{k_w p^2}{4a} (s - r)^2 \right] r_m \quad (\text{S5})$$

with k_w the wave number in water and r_m a random coefficient. Remember that $l = (s - r)/2 + M + 1$ for $A^{(1)}[l, m]$ and that $l = (s - r - 1)/2 + M$ for $A^{(2)}[l, m]$. Hence, each column of the matrix \mathbf{A}_R exhibits a known dependence as a function of index l (parabolic phase term) which is the manifestation of a long-range memory effect. On the contrary, the

MS contribution does not display such a deterministic behavior. It can be expressed as a correlated random wave field:

$$A_M[l, m] = c_l d_m \quad (\text{S6})$$

where c_l and d_m are random coefficients. The memory effect gives rise to a correlation between the lines of \mathbf{A}_M . This correlation can be quantified with the coefficient $\Gamma[l'] = \langle c_l c_{l+l'}^* \rangle$. We define the correlation length δ as the typical length scale of this correlation. In the experimental conditions of the Letter, a typical value for δ is of 4 array pitches.

As in Ref. S3, a singular value decomposition (SVD) of the matrix \mathbf{A} can be performed to separate SS/RS from MS. The SVD decomposes a matrix into two subspaces: a *signal* subspace (a matrix characterized by a long-range correlation between its lines and/or columns) and a *noise* subspace (a random matrix with possibly some short or medium-range correlations between its entries). When the SVD is applied to the matrix \mathbf{A} , we expect the *signal* subspace (*i.e.*, the largest sin-

gular values) to correspond to the SS/RS contribution (\mathbf{A}_R) and the *noise* subspace (*i.e.*, the smallest singular values) to correspond to the MS contribution (\mathbf{A}_M).

The SVD of matrix \mathbf{A} is given by

$$\mathbf{A} = \mathbf{U} \mathbf{\Lambda} \mathbf{V}^\dagger = \sum_{q=1}^P \lambda_q \mathbf{U}^{(q)} \mathbf{V}^{(q)\dagger} \quad (\text{S7})$$

where the symbol \dagger stands for transpose conjugate. \mathbf{A} is a square diagonal matrix of dimension N , containing the real positive singular values λ_q in a decreasing order ($\lambda_1 > \lambda_2 > \dots > \lambda_P$). \mathbf{U} and \mathbf{V} are square unitary matrices of dimension N . Their respective columns $\mathbf{U}^{(q)}$ and $\mathbf{V}^{(q)}$ correspond to the singular vectors associated with each singular value λ_q .

A general issue is to determine which rank of singular value separates the *signal* subspace from the *noise* subspace [S3]. However, the paraxial approximation can be made here since the array-sample distance a is much larger than the transverse size of the array Np . The SS/RS contribution is then given by Eq. (S5) and \mathbf{A}_R is of rank 1. Hence, only the eigenspace associated with the first singular value λ_1 corresponds to the signal subspace. For point-like scatterers, the elements of $\mathbf{U}^{(1)}$ are given by

$$u_l^{(1)} = \exp \left[j \frac{k_w p^2}{4a} (s-r)^2 \right] / \sqrt{P} \quad (\text{S8})$$

with $l = (s-r)/2 + M + 1$ for $\mathbf{A}^{(1)}$ and $l = (s-r-1)/2 + M$ for $\mathbf{A}^{(2)}$. In practice, due to the directivity of transducers and the finite size of scatterers, the modulus of $\mathbf{U}^{(1)}$ is not perfectly uniform. Consequently, a SVD of \mathbf{A} is needed to estimate the SS/RS subspace with the best precision. The signal (\mathbf{S}) and noise (\mathbf{N}) subspaces are thus given by,

$$\mathbf{S} = \mathbf{U}^{(1)} \mathbf{U}^{(1)\dagger} \mathbf{A} \quad (\text{S9})$$

$$\mathbf{N} = \mathbf{A} - \mathbf{U}^{(1)} \mathbf{U}^{(1)\dagger} \mathbf{A} \quad (\text{S10})$$

An example of the result provided by the SVD of \mathbf{A} is shown in Fig. S1. The signal and noise subspaces deduced from \mathbf{A} [Fig. S1(b)] are shown in Fig. S1(d) and (e), respectively. Ideally, \mathbf{S} should be devoid of conventional MS. However, the latter contribution is not strictly orthogonal to the SS/RS subspace, especially as the MS field exhibits medium-range correlations. Hence, a post-treatment is needed to correct this contamination of the signal subspace by MS.

Correction of the signal and noise subspaces

An inverse discrete Fourier transform is first performed to return to the time domain. This yields the signal and noise

subspaces as a function of time t , $\mathbf{S}(t)$ and $\mathbf{N}(t)$. The partial mixing of RS and MS in noise and signal subspaces can be pointed out by investigating the intensity profiles I_S and I_N as a function of l which is directly related to the distance between the source s and the receiver r :

$$I_S[l] = \langle |S_{lm}|^2 \rangle \text{ and } I_N[l] = \langle |N_{lm}|^2 \rangle \quad (\text{S11})$$

where the symbol $\langle \dots \rangle$ denotes an ensemble average. We have checked that these mean intensities are indeed independent of m . An example of the intensity profiles obtained at a given time t is shown in Fig.S1(f). Whereas the intensity profile I_S associated with the signal subspace is a flat plateau characteristic of single/recurrent scattering, the intensity profile I_N does not display an intensity profile typical of multiple scattering, *i.e.* a coherent backscattering peak on top of a flat incoherent background. This is because a part of the MS contribution emerges along the signal subspace. One can also note that the sum of I_S and I_N is not equal to the total intensity $I[l] = \langle |A_{lm}|^2 \rangle$ computed from the matrix \mathbf{A} . Although the subspaces \mathbf{S} and \mathbf{N} are orthogonal in the frequency domain, they are not necessarily so in the time domain.

To investigate the coupling between RS and MS eigenspaces, \mathbf{S} and \mathbf{N} can be expressed as a function of \mathbf{A}_R and \mathbf{A}_M by substituting Eq. (S4) into Eqs. (S9) and (S10). This yields

$$\mathbf{S} = \mathbf{A}_R + \mathbf{U}^{(1)} \mathbf{U}^{(1)\dagger} \mathbf{A}_M \quad (\text{S12})$$

$$\mathbf{N} = \mathbf{A}_M - \mathbf{U}^{(1)} \mathbf{U}^{(1)\dagger} \mathbf{A}_M \quad (\text{S13})$$

This last pair of equations points out the coupling term $\mathbf{U}^{(1)} \mathbf{U}^{(1)\dagger} \mathbf{A}_M$.

We now derive the expressions of the noise and signal matrix elements $N[l, m]$ and $S[l, m]$, as well as the corresponding intensities $I_N[l]$ and $I_S[l]$. An expression for the noise matrix entries $N[l, m]$ can be found by substituting Eq. (S6) into Eq. (S13):

$$N[l, m] = \left[c_l - u_l^{(1)} \sum_{i=1}^P u_i^{(1)*} c_i \right] d_m \quad (\text{S14})$$

The intensity $I_N[l]$ [Eq. (S11)] can then be deduced:

$$I_N[l] = \left[\langle |c_l|^2 \rangle - 2\text{Re} \left\{ u_l^{(1)} \sum_{i=1}^P u_i^{(1)*} \Gamma[l-i] \right\} + \left| u_l^{(1)} \right|^2 \sum_{i=1}^P \sum_{j=1}^P u_i^{(1)*} u_j^{(1)} \Gamma[i-j] \right] \langle |d_m|^2 \rangle \quad (\text{S15})$$

Making the approximation that $\Gamma[i] = 0$ for $|i| > \delta$ and assuming that $2a/k_w \gg p^2 \delta^2$ (valid in our experiment), then

$u_i^{(1)*} u_j^{(1)} \sim 1/P$ for $|i-j| < \delta$ and the last equation becomes

$$I_N[l] = \left[\langle |c_l|^2 \rangle - \frac{2}{P} \sum_{i=1}^P \Gamma[l-i] + \frac{1}{P^2} \sum_{i=1}^P \sum_{j=1}^P \Gamma[i-j] \right] \langle |d_m|^2 \rangle \quad (\text{S16})$$

Finally, if $P \gg \delta$ (which is the case in our experiment),

$\sum_{i=1}^P \sum_{j=1}^P \Gamma[i-j] \sim 2P \sum_{m=0}^{\delta} \Gamma[m]$. It then follows that

$$I_N[l] = \underbrace{\langle |c_l|^2 \rangle}_{I_M[l]} + \underbrace{\frac{2}{P} \left[- \sum_{i=1}^P \Gamma[l-i] + \sum_{m=0}^{\delta} \Gamma[m] \right]}_{C_N[l]} \langle |d_m|^2 \rangle \quad (\text{S17})$$

This expression (S17) shows explicitly that $I_N[l]$ is given by the sum of the conventional MS intensity I_M and a coupling term C_N . If we consider the case $l = 1$, we can see that C_N vanishes and that $I_N[l = 1] \simeq I_M[l = 1]$.

An expression for the signal matrix elements $S[l, m]$ can also be found by substituting the expression for \mathbf{A}_R [Eq. (S5)] and \mathbf{A}_N [Eq. (S6)] into Eq. (S12):

$$S[l, m] = u_l^{(1)} r_m + u_l^{(1)} \sum_{i=1}^P u_i^{(1)*} c_i d_m \quad (\text{S18})$$

One can then derive the corresponding intensity $I_S[l]$ [Eq. (S11)]

$$I_S[l] = \underbrace{\left| u_l^{(1)} \right|^2 \langle |r_m|^2 \rangle}_{I_R[l]} + \underbrace{\left\langle 2\text{Re} \left\{ r_m^* \sum_{i=1}^P u_i^{(1)*} c_i \sum_m d_m \right\} + \left| u_l^{(1)} \sum_{i=1}^P u_i^{(1)*} c_i d_m \right|^2 \right\rangle}_{C_S[l]} \quad (\text{S19})$$

with I_R the recurrent scattering intensity and C_S a coupling term due to the residual multiple scattering intensity in the signal subspace. If we make the approximation that $\left| u_l^{(1)} \right|^2 \sim P^{-1}$ [Eq. (S8)], C_S can be considered constant over l .

To estimate the residual multiple scattering contribution

C_S , one can use the fact that the sum of I_R and I_M should be equal to the total intensity $I = \langle |a_{lm}|^2 \rangle$

$$I[l] = I_R[l] + I_M[l] \quad (\text{S20})$$

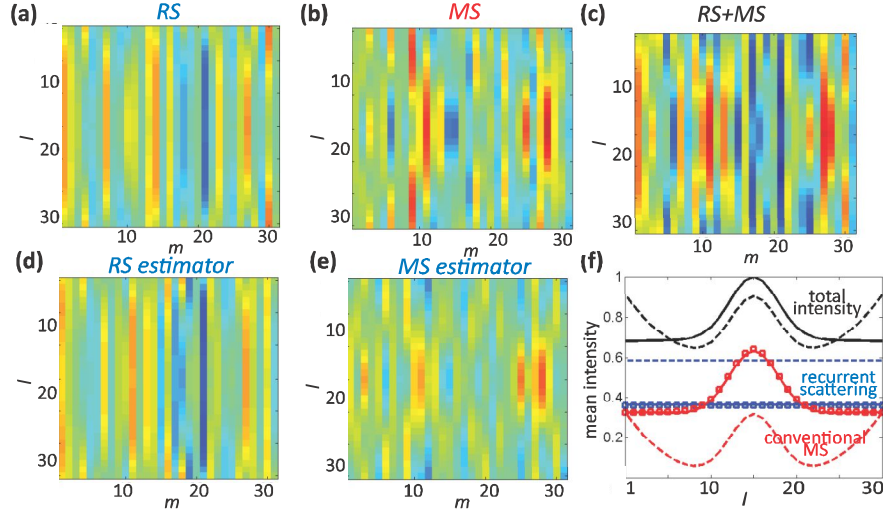


FIG. S2: Numerical validation of the RS/MS separation method. (a) Example of simulated RS matrix \mathbf{A}'_R . (b) Example of simulated MS matrix \mathbf{A}'_M . (c) Corresponding matrix $\mathbf{A}' = \mathbf{A}'_R + \mathbf{A}'_M$. (d) Estimated RS matrix $\hat{\mathbf{A}}'_R$. (e) Estimated MS matrix $\hat{\mathbf{A}}'_M$. (f) Intensity profiles (continuous line): I_R (blue), I_M (red) and I (black) - Estimated intensity profiles before correction (dashed lines): I_S (blue), I_N (red) and $I_N + I_S$ (black). Estimated intensity profiles after correction (square symbols): \hat{I}_R (blue) and \hat{I}_N (red).

Using Eqs. (S17)-(S19), we obtain

$$C_S + C_N[l] = I_S[l] + I_N[l] - I[l] \quad (\text{S21})$$

Considering the last equation when $l = 1$ and recalling that $C_N[l = 1] \simeq 0$ allows one to calculate the coefficient C_S

$$C_S \simeq I_S[l = 1] + I_N[l = 1] - I[l = 1] \quad (\text{S22})$$

Once C_S is known, one can deduce estimators for the RS intensity and the conventional MS intensity:

$$\hat{I}_R[l] = I_S[l] - C_S \quad (\text{S23})$$

$$\hat{I}_M[l] = I[l] - I_S[l] - C_S \quad (\text{S24})$$

This operation is illustrated in Fig. S1(f). We check that \hat{I}_M displays a profile typical of multiple scattering: a coherent backscattering peak on top of a flat incoherent background with an enhancement factor close to 2.

Estimators for the matrices \mathbf{A}_R and \mathbf{A}_M can be obtained by renormalizing \mathbf{S} and \mathbf{N} such that $\hat{I}_R[l] = \langle |\hat{A}_R[l, m]|^2 \rangle$ and $\hat{I}_M[l] = \langle |\hat{A}_M[l, m]|^2 \rangle$. This renormalization yields

$$\hat{\mathbf{A}}_R = \alpha \mathbf{S}, \quad \hat{\mathbf{A}}_M = \mathbf{A} - \alpha \mathbf{S}, \quad (\text{S25})$$

with $\alpha = \sqrt{1 - C_S/I_S[1]}$

This operation is illustrated in Fig. S1. $\hat{\mathbf{A}}_R$ and $\hat{\mathbf{A}}_M$ shown in Figs. S1(g)-(h) are obtained following the renormalization of \mathbf{S} and \mathbf{N} [Figs. S1(d)-(e)].

Back-rotation of data

The last step is the reverse of the first one. From $\hat{\mathbf{A}}_R$ and $\hat{\mathbf{A}}_M$, two estimators of the matrices \mathbf{K}_R and \mathbf{K}_M , of dimension $(2M - 1) \times (2M - 1)$, are built [see Fig. S1(i)-(j)] with a change of coordinates, back to the original system:

- if $(s - r)/2$ is an integer, then, $\hat{K}_{R,M}[s, r] = \hat{A}_{R,M}^{(1)}[(s - r)/2 + M, (s + r)/2]$
 - if $(s - r)/2$ is not an integer, then, $\hat{K}_{R,M}[s, r] = \hat{A}_{R,M}^{(2)}[(s - r - 1)/2 + M, (s + r - 1)/2]$
- $\hat{\mathbf{K}}_R$ and $\hat{\mathbf{K}}_M$ are estimators of the RS contribution and of the conventional MS contribution, respectively.

Numerical validation of the RS/MS separation method

In order to validate our approach, a numerical test has been performed by generating random matrices with the same statistical properties as the experimental antidiagonal matrices.

The RS antidiagonal matrix \mathbf{A}_R has been simulated numerically as follows. The procedure first consists in generating numerically a line vector \mathbf{R} whose elements are circularly symmetric complex Gaussian random variables with zero mean. Then a matrix \mathbf{A}'_R is built by multiplying the column vector $\mathbf{U}^{(1)}$ [Eq. (S8)] with the random line vector \mathbf{R} [Eq. (S5)]. One can show that the matrix $\mathbf{A}'_R = \mathbf{U}^{(1)}\mathbf{R}$ exhibits the same correlation properties as the experimental RS antidiagonal matrix \mathbf{A}_R . The parameters that appear in the expression of vector $\mathbf{U}^{(1)}$ [Eq. (S8)] are chosen to be the same as in the experiment: $a = 182$ mm, $p = 0.5$ mm, $f = 1.2$ MHz. An example of numerical matrix \mathbf{A}'_R thus obtained is shown in Fig. S2(a).

As for the conventional MS contribution, the correlation coefficient Γ_l is first assumed to follow a Gaussian dependence $\Gamma_l = \exp(-l^2/\delta^2)$. We will consider a correlation length of 4 array pitches ($\delta = 4$), a typical value in our experiment. From this correlation coefficient, one can build a covariance matrix \mathbf{J} whose coefficients are given by $J_{ij} = \Gamma_{i-j}$. The next step consists in generating numerically a random column

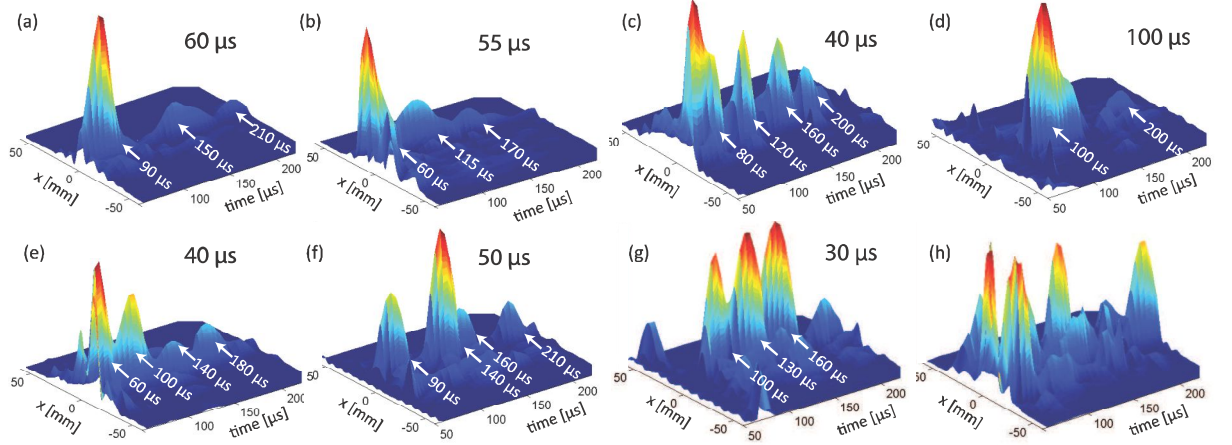


FIG. S3: Backpropagation of the first singular vector versus time at the sample surface for eight realizations of disorder at frequency $f = 1.2$ MHz. x represents the coordinate along the surface.

vector \mathbf{R}' whose elements are circularly symmetric complex Gaussian random variables with zero mean. Then, a correlated random vector \mathbf{B} is built from \mathbf{R}' , such that

$$\mathbf{B} = \mathbf{J}^{1/2} \mathbf{R}' \quad (\text{S26})$$

One can show that the entries of \mathbf{B} exhibit the correlation coefficient Γ_l . The antidiagonals should also exhibit the features of spatial reciprocity and of coherent backscattering in the MS regime. To that aim, a new column vector $\mathbf{C} = [c_l]$ is built by summing $\mathbf{B} = [b_l]$ and its flipped counterpart $\mathbf{B}' = [b_{P-l}]$ such that:

$$c_l = b_l + b_{P-l} \quad (\text{S27})$$

This vector \mathbf{C} is finally multiplied by a random line vector \mathbf{D} to yield a matrix $\mathbf{A}'_{\mathbf{M}} = \mathbf{C} \times \mathbf{D}$ [Eq. (S6)]. This matrix thus generated displays the same properties as the experimental MS matrix $\mathbf{A}_{\mathbf{M}}$. An example of numerical matrix $\mathbf{A}'_{\mathbf{M}}$ is shown in Fig. S2(b). As expected, it displays medium-range correlations along its columns. It also exhibits the feature of spatial reciprocity since each line of its upper part is identical to a line of its lower part: $A'_{\mathbf{M}}[l, m] = A'_{\mathbf{M}}[P-l, m]$. The corresponding intensity profile $I_{\mathbf{M}}[l]$ has been calculated by averaging $|A'_{\mathbf{M}}[l, m]|^2$ over m and over 1000 different realizations. $I_{\mathbf{M}}$ is displayed in Fig. S2(f) and exhibits a coherent backscattering cone whose line shape is governed by the correlation coefficient Γ_l .

Once the matrices $\mathbf{A}'_{\mathbf{R}}$ and $\mathbf{A}'_{\mathbf{M}}$ are obtained, one can build the matrix \mathbf{A}' [Fig. S2(c)] as the sum of the RS and MS contributions [Eq. (S4)]. The corresponding intensity profile $I[l] = \langle |A'_{\mathbf{R}}[l, m]|^2 + |A'_{\mathbf{M}}[l, m]|^2 \rangle$ is shown in Fig. S2(f). It displays a coherent backscattering peak with a linewidth and an enhancement factor similar to experimental results [see Fig. S1(f)].

The previously described RS/MS separation method has been tested on randomly generated antidiagonal matrices \mathbf{A} . To that aim, we have projected the matrix \mathbf{A}' over the RS

eigenvector $\mathbf{U}^{(1)}$ which yields the signal subspace $\mathbf{S} = \mathbf{U}^{(1)} \mathbf{U}^{(1)\dagger} \mathbf{A}'$ and the noise subspace $\mathbf{N} = \mathbf{A}' - \mathbf{S}$. The corresponding intensity profiles are shown in dashed lines in Fig. S2(f). As for experimental data, the noise subspace does not provide an intensity profile typical of multiple scattering (flat incoherent background). However, once the correction given by Eq. (S23) is applied [square symbols in Fig. S2(f)], the mean intensity profiles $I_{\mathbf{R}}$ and $I_{\mathbf{M}}$ are nicely recovered.

As for the estimators of the RS and MS matrices $\hat{\mathbf{A}}'_{\mathbf{R}}$ and $\hat{\mathbf{A}}'_{\mathbf{M}}$, the agreement is not as good as for the intensity profiles but still acceptable. The RS and MS estimators shown in Figs. S2(d)-(e) are compared to the RS and MS matrices $\mathbf{A}'_{\mathbf{R}}$ and $\mathbf{A}'_{\mathbf{M}}$ [Figs. S2(a)-(b)]. The averaged degree of similarity between those matrices reaches values of 90% and 80% for RS and MS, respectively.

This numerical test validates our method under the conditions of our experiment. One has to remember that two main conditions have to be fulfilled for the RS/MS separation method to be successful: $2a/k_w \gg p^2 \delta^2$ and $P \gg \delta$.

RECURRENT SCATTERING HOT SPOTS

In the Letter, the singular value decomposition of the matrix \mathbf{K} has been investigated. A one-to-one correspondence has been demonstrated between the highest singular values and predominant recurrent scattering paths around 1.2 MHz. The first singular vector \mathbf{V}_1 back-focuses on the same particular location at regular time intervals (every 40 μs for the example shown in the Letter). Our hypothesis is that this hot spot corresponds to the entry/exit point of a RS path at the surface of the sample. The occurrence of the same hot spot periodically in time seems to indicate that it corresponds to successive round trips along the same RS path.

The goal of this supplementary material is to demonstrate that this result is not specific to the configuration of disorder considered in the Letter. To that aim, the backpropagation

of \mathbf{V}_1 is shown in Fig. S3 for eight other configurations of disorder. Except in Fig. S3(h), \mathbf{V}_1 back-focuses on particular locations at regular time intervals [Figs. S3(a)-(f)]. These time intervals depend on the realization of disorder, with values ranging from 30 μs [Fig. S3(g)] to 100 μs [Fig. S3(d)]. The variation of this time interval according the realization of disorder strongly suggests that these hot spots are not due to specular reflections from the front and back sample boundaries, since then the intervals would be the same whatever the configuration of disorder. Note that in Fig. S3(f), \mathbf{V}_1 back-focuses onto two different locations: $x = 12.5$ mm at times $t = 90$ and 160 μs , and $x = 9$ mm at times $t = 140$ and 210 μs . The emergence of these two hot spots separated by the same interval of time could indicate that they share parts of the same recurrent scattering path.

-
- [S1] A. Aubry and A. Derode, Phys. Rev. Lett. **102**, 084301 (2009).
 - [S2] A. Aubry and A. Derode, J. Appl. Phys. **106**, 044903 (2009).
 - [S3] A. Aubry and A. Derode, J. Acoust. Soc. Am. **129**, 225 (2011).
 - [S4] I. Freund, M. Rosenbluh, and S. Feng, Phys. Rev. Lett. **61**, 2328 (1988).
 - [S5] S. Feng, C. Kane, P. A. Lee, and A. D. Stone, Phys. Rev. Lett. **61**, 834 (1988).
 - [S6] I. Freund, M. Rosenbluh, and R. Berkovits, Phys. Rev. B **39**, 12403 (1989).
 - [S7] E. Akkermans and G. Montambaux, Mesoscopic Physics of Electrons and Photons (Cambridge University Press, London, 2006).

7. Statistics and Multifractality Near the Mobility Edge

7.1. Introduction

The scaling theory of localization explains how, in principle, the effects of localization can be probed by examining the behaviour of waves on different length scales (see Section 2.5.1). However, this theory does not take into account fluctuations, which is a significant limitation because fluctuations are expected to be especially strong near the critical point (Krachmalnicoff et al. 2010; Mirlin 2000). This thesis has demonstrated that near the Anderson transition, the localization length ξ is difficult to measure due to huge fluctuations, which are a source of uncertainty in the experimental data. However, the fluctuations themselves can be used to probe the critical and localized regimes. This chapter demonstrates such a technique, based on measurements of the multifractal spatial structure of the wave function intensity. I present measurements of the spatial variations of the speckle pattern which are expected to show one or more Anderson localization transitions. These systems are slab sample L1 and similarly-constructed cubic-shaped aluminum-brazed samples. As it is a measure of spatial fluctuations which are enhanced in the critical regime, multifractal (MF) analysis is a natural tool for an investigation of the localization transition. A recent theoretical advance suggests that experimentally-measured signatures of MF from cubic samples of varying sizes could enable the measurement of the critical exponent ν . The first steps towards this ambitious goal are reported here, and promising results are presented.

7.2. Introduction to multifractality²⁶

Multifractality is a sensitive measure of the spatial structure of wavefunctions. This means that the moments of transmitted intensity depend on the system size L in a nontrivial way (Evers and

²⁶ (Rodriguez et al. 2011; Evers and Mirlin 2008)

Mirlin 2008; Faez et al. 2009). This dependence can be determined either by varying system size, L , or by dividing the system into boxes of size b , and varying b , as shown in Figure 7.1.

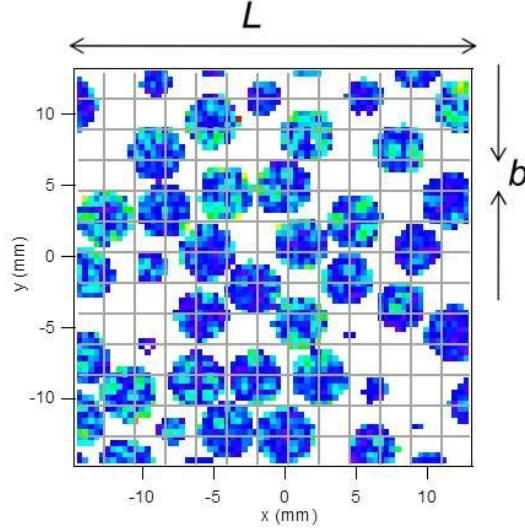


Figure 7.1: For a fixed system size, the spatial structure of the transmitted speckle pattern can be probed by dividing up the speckle map into boxes of size b . Shown here is a map of intensity transmitted through a cubic aluminum brazed sample (these types of samples are discussed further in Section 7.4).

The scaling of the moments of intensity is measured by the *generalized inverse participation ratio* (GIPR):

$$P_q = \sum_{i=1}^N \left[\int_{B_i} \hat{I}(\vec{r}) d^d \vec{r} \right]^q \quad (7.1)$$

where $\hat{I}(\vec{r}) = |\psi^2(\vec{r})| / \int |\psi^2(\vec{r})| d^d \vec{r}$. The integral over B_i denotes a summation of intensity inside a particular box B_i of linear size b , with $\lambda \ll b \ll L$, where λ is the wavelength. This box-summing concept is sketched in Figure 7.1, where in this case $L = L_g$, as L_g is the linear size of the speckle pattern on the surface of the sample, and $d = 2$ since the spatial structure in a plane is analysed. By carrying out this procedure on the entire sample surface, and varying b , the dependence of P_q on b can be measured. The GIPR scales with L/b as

$$\langle P_q \rangle \sim (L/b)^{-\tau(q)}. \quad (7.2)$$

The exponent $\tau(q)$ is often used to define the fractal dimension of a system D_q via $\tau_q = D_q(q - 1)$. For extended states, $D_q = d$, where d is the system dimension. For localized states $D_q = 0$. A single, non-integer value of D_q would imply that the wavefunctions exhibit a (single) fractal structure. For critical states, D_q is a nontrivial *function* of q , indicating that the spatial structure of wavefunctions is *multifractal*.

By separating $\tau(q)$ into its ‘conventional’ (diffuse) and anomalous parts, we can write

$$\tau_q \equiv d(q - 1) + \Delta_q, \quad (7.3)$$

where Δ_q is defined as the *anomalous fractal dimension*. For extended states, $\Delta_q = 0$ (for $L \rightarrow \infty$ or $\lambda \rightarrow 0$). At criticality, τ_q is a continuous function of q , indicating that the wavefunction structure is multifractal. This (nonlinear) dependence of τ_q on q can be characterized using the *singularity strengths* α_q , defined as:

$$\alpha_q = d\tau_q/dq \quad (7.4)$$

The GIPR are proportional to the moments of the distribution function of the intensities, $\mathcal{P}(I_B)$. This distribution, also called the *probability density function* (PDF), scales with L/b at criticality as

$$\mathcal{P}(\ln I_B) \sim (L/b)^{-d+f(\alpha)}. \quad (7.5)$$

where $\alpha \equiv \ln I_B / \ln(L/b)$ and $I_B \equiv \int_{B_i} \hat{I}(\vec{r}) d^d \vec{r}$. The second term in the exponent, $f(\alpha)$, is called the singularity spectrum, and is the fractal dimension of the set of points \vec{r} where the wavefunction intensity scales as $I(\vec{r}) \sim L^{-\alpha}$.

While the wavefunctions are, strictly speaking, only predicted to be multifractal exactly at the critical point, they are expected to remain multifractal on either side of the transition (on a

range smaller than the correlation length ξ) (Cuevas and Kravtsov 2007; Rodriguez et al. 2011; Faez et al. 2009). This idea is supported by the common observation of very high wavefunction fluctuations as the transition is approached, and by recent work showing that wave functions exhibit strong multifractality (MF) near the Anderson transition (Faez et al. 2009). This experimental study by Faez et al. measured multifractal aspects of ultrasound in 3D, in samples similar to my samples L1 and L2. Figure 7.2 shows the results for Δ_q in the localized regime near the critical point, compared with optical measurements for diffuse waves. The data show the expected parabolic shape (Faez et al. 2009), and are relatively flat in the diffuse regime and curved in the localized regime. The data also confirm the predicted symmetry relation for Δ_q :

$$\Delta_q = \Delta_{1-q} . \quad (7.6)$$

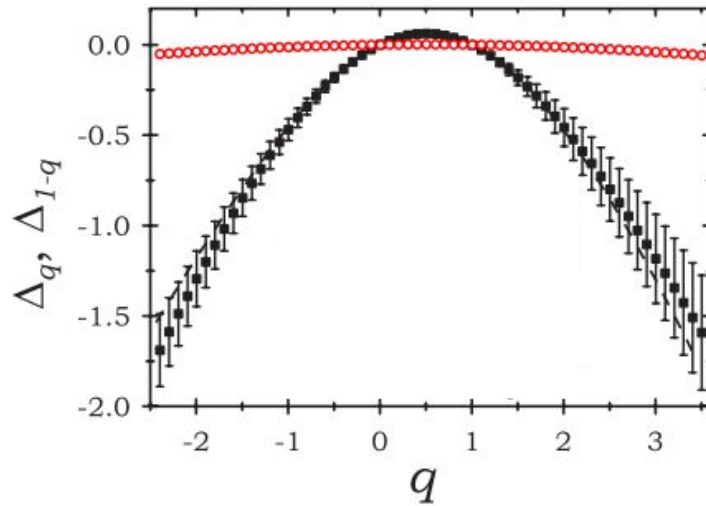


Figure 7.2: The measured anomalous exponents Δ_q from ultrasound in a brazed aluminum bead slab mesoglass. The ultrasonic results in the localized regime (black squares) are compared with optical measurements in the diffuse regime (red circles). The dashed line shows the results in the localized regime, mirrored about $q = 1/2$. The agreement between black squares and dashed line supports the predicted symmetry relation of Equation (7.6). Figure courtesy of John H. Page.

7.2.1. Multifractality and finite-size scaling

The expectation that multifractality will persist away from the critical point suggests that

the phase transition itself could be studied using multifractal quantities. Recently, Rodriguez et al. have extended the multifractal theory summarized in the previous section to the vicinity of the critical point (Rodriguez et al. 2010; Rodriguez et al. 2011). They have done this by combining multifractal analysis with finite-size scaling concepts. Their theoretical model (supported by numerical simulations) which is applicable throughout the entire critical regime, suggests that critical parameters at the Anderson transition may be measured from the probability density function (PDF) and/or the generalized inverse participation ratio (GIPR). The main ideas of the extended theory are summarized very briefly below, and described in detail by Rodriguez et al.

At the critical point (and in the thermodynamic limit $L \rightarrow \infty$), the GIPRs obey the scaling law of Equation (7.2), reproduced here:

$$\langle P_q \rangle \sim \lambda^{\tau(q)}$$

where $\lambda \equiv b/L$. Close to the transition, the GIPRs are expected to depend on the ratio of L and b to the localization (correlation) length ξ . This is justified using renormalization group (RG) arguments. This concept is also fundamental to scaling theory, where the width of localized modes, γ , scales as $\gamma \propto \exp(-L/\xi)$ (Equation (2.57)). Thus, the scaling law for the GIPRs can be written more generally as

$$\langle P_q \rangle(W, L, b) \sim \lambda^{\tau(q)} P_q(L/\xi, b/\xi) \quad (7.7)$$

with $\xi = \xi(W)$ and W is the disorder parameter. At the critical point W_c the correlation length diverges according to the critical exponent ν :

$$\xi \propto |W - W_c|^{-\nu} \quad (7.8)$$

Combining Equations (7.7) and (7.8) recovers the L/b invariance of the GIPR at the critical point (Equation (7.2)). It is important to note that in this theory, sample size L is assumed to be

equivalent to the linear size of the grid, L_g , over which transmitted speckle is measured. For our experiments these quantities are not equivalent. In previous work on slab-shaped samples (including Section 7.3 in this thesis), sample size L was not relevant in the comparison with theory, so the relation $\lambda = b/L_g$ was used. For the finite-size scaling analysis presented here, we keep the definition of $\lambda \equiv b/L$, as clearly the physical sample dimensions must be involved in the RG method begun at Equation (7.7).

Away from the transition, the GIPRs depend on L , b , and disorder W . To quantify this dependence, Equation (7.7) can be rearranged as

$$\tilde{\tau}_q(W, L, \lambda) = \tau_q + \frac{q(q-1)}{\ln \lambda} B_q(L/\xi, b/\xi) \quad (7.9)$$

where the function B_q is related to the original GIPRs P_q . This enables the definition of generalized anomalous scaling exponents

$$\tilde{\Delta}_q \equiv \tilde{\tau}_q - d(q-1) \quad (7.10)$$

which will obey the scaling law

$$\tilde{\Delta}_q(W, L, \lambda) = \Delta_q + \frac{q(q-1)}{\ln \lambda} B_q(L/\xi, b/\xi). \quad (7.11)$$

Similarly, the PDF may be approximated throughout the critical regime using a generalized version of the singularity spectrum, $\tilde{f}(\alpha)$:

$$\mathcal{P}(\ln I_B; W, L, b) \propto (L/b)^{-d + \tilde{f}(\ln I_B; W, L, b)}. \quad (7.12)$$

As the thermodynamic limit $\lambda \rightarrow 0$ is approached at the critical point, Equation (7.12) reduces to the standard expression of Equation (7.5). For fixed λ , the PDF is scale invariant at the transition. Using Equations (7.4) and (7.9), we can see that the generalized α obeys a scaling

law similar to that of Δ_q ;

$$\tilde{\alpha}_q(W, L, \lambda) = \alpha_q + \frac{1}{\ln \lambda} A_q(L/\xi, b/\xi) \quad (7.13)$$

It can be shown that the mean value of the PDF, $\langle \alpha \rangle$, and the position of its maximum, obey the same scaling law as Equation (7.13).

This multifractal theory applies over the entire critical regime. Two applications of the theory to experimental data are immediately evident (Rodriguez et al. 2011):

1. By varying disorder and system size, but fixing λ , the critical parameters of the Anderson transition can be measured. This analysis was performed for numerical simulations by Rodriguez et al. Results for the PDF are shown in Figure 7.3. As the Anderson transition is crossed from the diffusive (metal) to localized (insulator) regime, the PDF broadens and its center shifts. The rate at which the center shifts depends *only* on sample size.

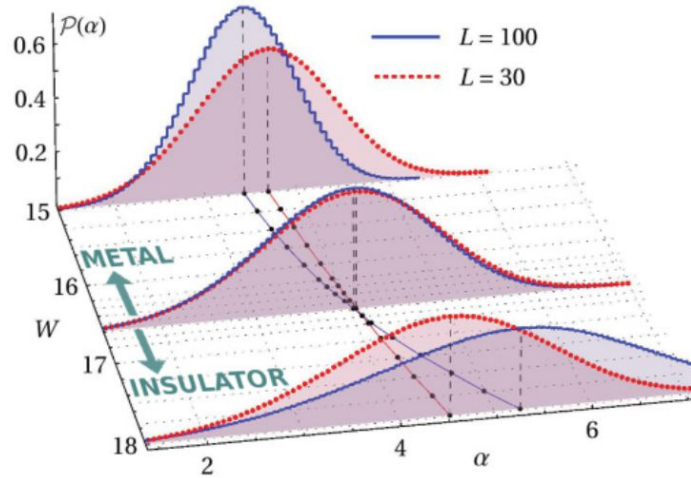


Figure 7.3: Numerical simulations of the probability density $\mathcal{P}(\ln I_B; W, L, b)$ as a function of disorder, W , across the Anderson transition for a fixed λ . Results are shown for two system sizes L . In this figure, $\alpha \equiv \ln I_B / \ln \lambda$. Used with permission (Rodriguez et al. 2010).

In other words, multifractal quantities such as the PDF and GIPR exhibit finite-size scaling

behaviour close to the Anderson transition. For fixed L/b , both Δ_q and the PDF show :

a) Scale-invariance at the critical point

b) Finite-size scaling behaviour away from the transition

The theory predicts that

c) As the mobility edge is approached, Δ_q and the mean of the PDF will shift at a rate which depends on L .

The theory would allow the fitting of experimental data with disorder and system size for a simultaneous estimate of critical parameters W_c , which is determined by f_c for my experiments in the SC theory analysis in Section 5.1.1 of this thesis, and ν . An example of how this type of analysis could be applied to my experimental data is presented in Section 7.5.4 of this chapter.

2. To go further with the analysis, the theory would allow the fitting of experimental data with disorder, system size *and* box size. This would yield, in addition to f_c and ν , an estimate of the scale-invariant multifractal exponents Δ_q and α . This technique was demonstrated for numerical data by Rodriguez et al. in 2011.

In this work, I would like to see if the shift in the Δ_q and $\langle\alpha\rangle$ as the ME is approached (points 1a-c, above) can be observed experimentally. This measurement will be extremely challenging, as it requires samples of different sizes in which the mobility edge occurs at the same frequency, and enough samples (realizations of disorder) to provide an adequate configurational average. Success with this first experimental step, however, will lead to more sophisticated fitting of the data with the theory (point 2, above), which could simultaneously pinpoint the frequency of the mobility edge *and* provide an unambiguous experimental

measurement of ν for classical waves in a 3D medium.

7.3. Speckle statistics in a slab mesoglass

In Chapter 5 of this thesis, fluctuations in the averaged transmitted and backscattered dynamic intensity were observed near the critical regime (e.g. Figure 6.6 and Figure 5.5, and accompanying text). For a more direct quantification of the spatial fluctuations in transmitted intensity, the variance σ^2 (the square of the standard deviation) can be examined. This quantity can be measured experimentally by acquiring speckle maps of transmitted field in the following way.

7.3.1. Field mapping

A field map is used to study the speckle pattern of transmitted waves near (within 1-2 λ) the surface of the sample. In these experiments, the source is kept stationary and the detector scans over a relatively large grid on the opposite sample face. In this way, a speckle pattern near the output face of the sample (such as that shown in Figure 2.1) is acquired. To ensure that results are not dependent on a particular source point (and to acquire more points for statistical analysis), several speckle maps are recorded with the source point at different positions on the sample surface. Further experimental details are given in Section 3.2.2.

7.3.2. Variance from speckle maps

Figure 7.4 shows $\sigma^2(f)$ of the normalized transmitted intensity $\hat{I}(f) \equiv I(f)/\langle I(f) \rangle$ through sample L1. The variance is calculated from the experimental speckle maps measured in transmission, as described in the previous section. Five different maps were acquired, each with a different source position. The configurationally-averaged variance $\langle \sigma^2(f) \rangle$ is the average of the variance from each map. The difference in the level of this quantity and the ‘overall variance’,

$\sigma^2(f)$, calculated over all data from all maps, is most likely due to C_0 correlations. These correlations are related to the fluctuations of the density of states at the source position, and have been shown to increase significantly near a mobility edge (Hildebrand et al. 2014). In Figure 7.4 the difference between $\langle \sigma^2 \rangle$ and σ^2 is most markedly observed near MEs (1.2 MHz and 0.88 MHz, which is almost certainly a ME). This concept is in keeping with the theme of enhanced fluctuations near the localization regime.

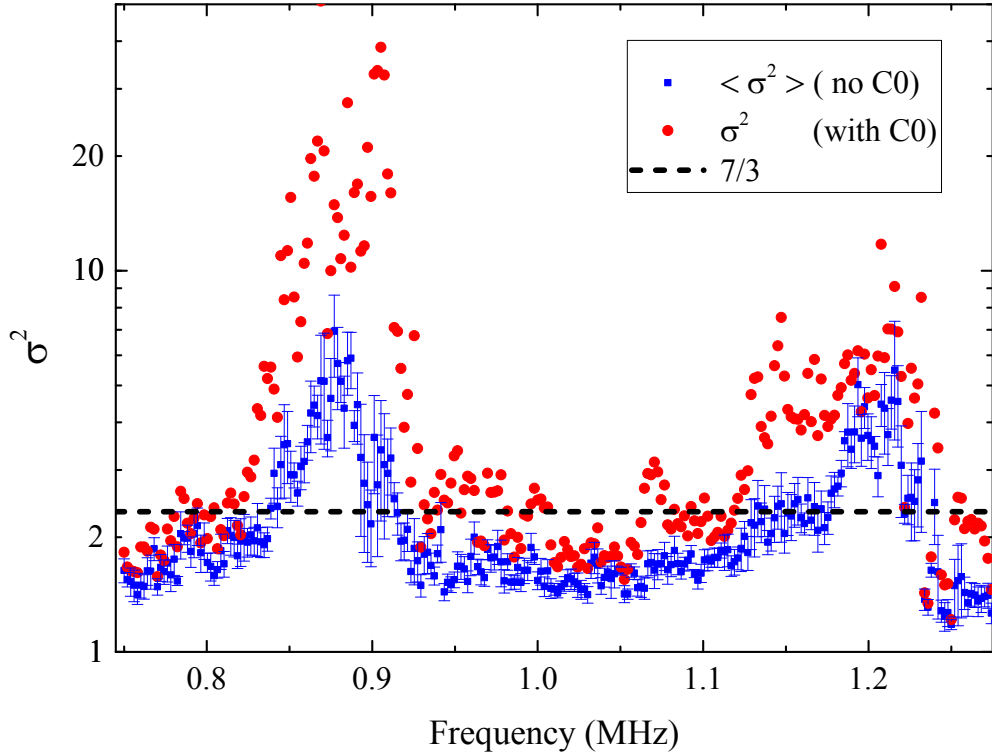


Figure 7.4: Variance of normalized transmitted intensity speckle maps for sample L1. Configurationally-averaged $\langle \sigma^2 \rangle$ (black squares) is generally lower than σ^2 which includes data from all source positions (red circles), especially near critical regimes, due to the presence of significant C_0 correlations. Error bars for $\langle \sigma^2 \rangle$ indicate the deviation from the mean over the variance from each individual speckle map. Every second point for $\langle \sigma^2 \rangle$ is omitted, for clarity.

The large variance at the lower ME of 1.20 MHz indicates the presence of huge fluctuations of transmitted intensity, in agreement with previous observations in this thesis and for similar samples. At no frequency is $\langle \sigma^2 \rangle = 1$ recovered, which is the expected value for

purely diffuse behaviour. The exception is near 1.25 – 1.3 MHz, where the presence of noise in these experimental measurements dominates (see Figure 7.6 and accompanying text). Even at 1.0 – 1.1 MHz, where the probability of purely diffuse behaviour is highest, $\sigma^2 > 1$. It is probable that wave transport is subdiffusive all the way through the 1.0 MHz passband. In any case, Fig. 7.4 shows that the magnitude of variance depends on how the variance is measured, so that care must be used in trying to establish a criterion for locating a mobility edge based on a particular value of the variance.

Figure 7.4 also enables a tentative comparison of the data with one of the criteria for localization, outlined in Section 2.5.3: variance of transmitted intensity $\langle \sigma^2 \rangle = 7/3$ at the mobility edge (so $\langle \sigma^2 \rangle > 7/3$ for localization). However, this criterion was established for quasi 1D systems, and may not be valid in 3D.

7.3.3. Multifractality

As a first approach to observing multifractality near a mobility edge, I have calculated the anomalous exponent Δ_q for my slab mesoglass L1. This quantity is calculated from transmission speckle maps. The analysis is similar to that detailed by Faez et al. (Faez et al. 2009). For these experimental data, the appropriate length scale to compare with b is L_g , the linear size of the grid over which the speckle map was measured (as shown in Figure 7.1), and not the actual sample size. The GIPRs are calculated directly from the speckle map (Equation (7.1)), for a range of box sizes b . From the configurationally-averaged GIPRs, the anomalous fractal dimension Δ_q can be directly calculated. Results are shown in Figure 7.5 for diffuse (1.0 MHz) and localized (1.2 MHz) regimes. The data in the localized regime are very similar to that for the monodisperse sample shown in Figure 7.2, but the conventional diffusive behaviour is not recovered: the Δ_q at 1 MHz depend more heavily on q than would be expected in the diffuse

regime. The reason for this may be that waves at 1 MHz are not purely diffusive. Being at the center of a pass band, 1 MHz is presumed to be the ‘most’ diffuse frequency out of the available range for the measured transmitted speckle map (0.75 to 1.28 MHz), but this fact has not been independently confirmed (as was done, for example, at 250 kHz in Chapter 4). However, it is definitely not localized, and is shown in Figure 7.5 and Figure 7.6 to be at least somewhat diffusive.

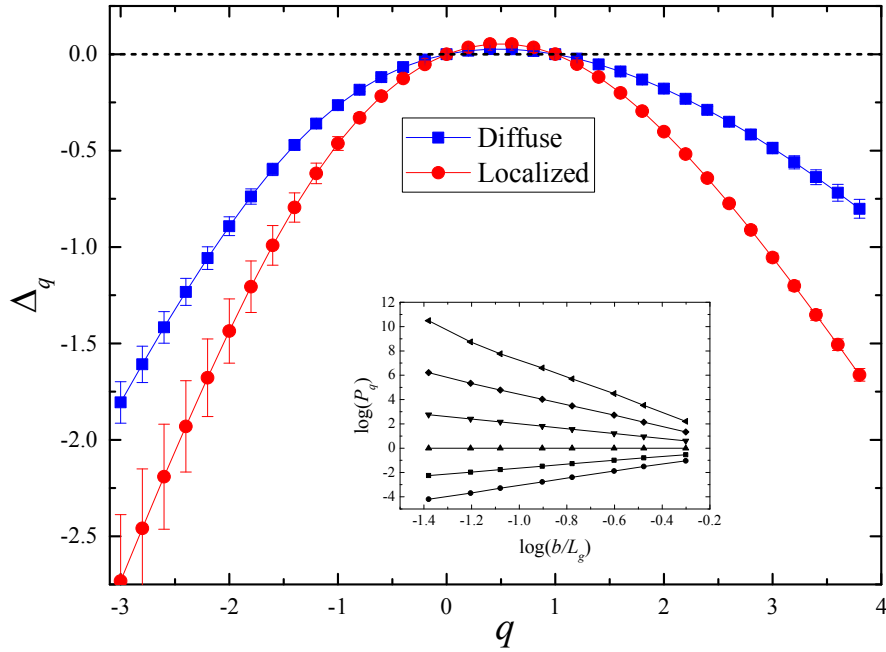


Figure 7.5: Anomalous fractal exponents Δ_q for the diffuse regime (1 MHz, blue squares) and localized regime (1.20 MHz, red circles). The logarithm of the GIPRs are shown in the inset, for a range of $q = \{-2, -1, 0, 1, 2, 3\}$, in descending order (the uppermost line is for $q = -2$, the lowest line is for $q = 3$). Linear fits of $\langle \log(P_q) \rangle$ enable the direct calculation of Δ_q from Equations (7.2) and (7.3). Uncertainties for Δ_q are given by the uncertainty in the linear fits of $\langle \log(P_q) \rangle$ vs $\log(b/L_g)$.

Figure 7.6 shows the frequency dependence of $\Delta_{q=2}$. For $q = 2$, the Δ_q decrease as the critical point is approached, as predicted by theory (Rodriguez et al. 2011; Evers and Mirlin 2008). We can observe that there is probably also a localization regime near 0.88 MHz, a frequency range which was not included in the time-consuming self-consistent theory fitting approach of Chapter

5. The brief results presented here suggest that the relatively simple approach of multifractal analysis could, with further development, be used to locate localized regimes.

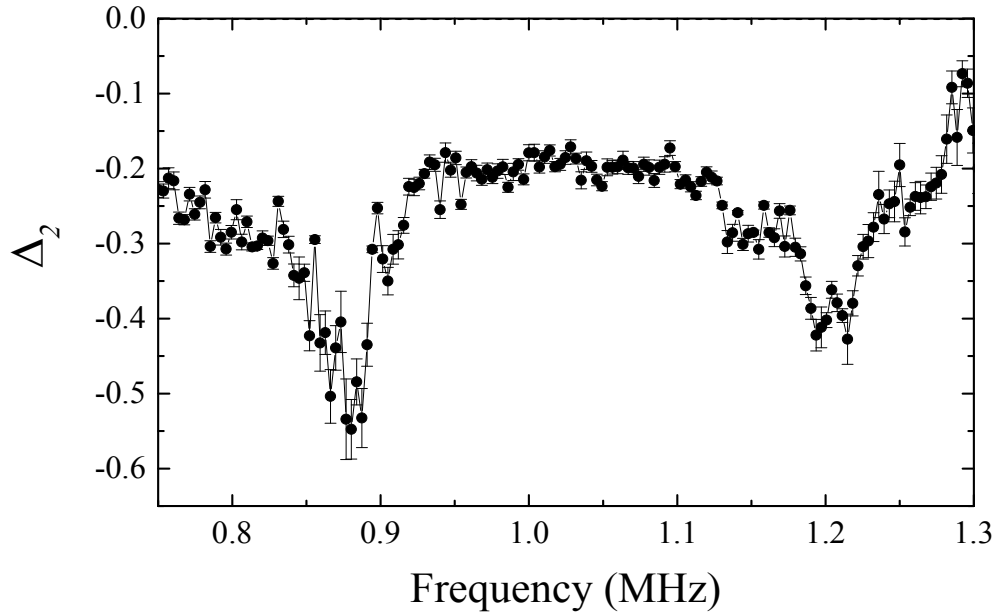


Figure 7.6: Anomalous fractal exponents Δ_2 as a function of frequency. There is a clear dip at 1.2 MHz, the lower mobility edge for this sample. The noise dominates after around 1.25 MHz for this measurement. The spike around 1.3 MHz is due to signals from a local radio station (frequency 1290 kHz), which are picked up clearly by our water tank experiments (this is visible as a spike in the transmission coefficient shown in Figure 3.25).

7.3.3.1. The effect of noise

It is clear from Figure 7.5 that the predicted symmetry relation for the Δ_q (Equation (7.6)) is not obeyed for the data from sample L1. This was found to be due to the influences of noise. Noise affects negative q values more, since in Equation (7.1) the reciprocal of very small values is being calculated. Thus, excessive noise has the effect of increasing the GIPRs, especially for small b where the noise cannot be completely averaged away. This causes a decrease in Δ_q values. This effect can be demonstrated by calculating the anomalous fractal exponents for

matrices of pseudo-random noise²⁷, as shown in Figure 7.7. This figure also demonstrates that a larger grid size (i.e. more points in the configurational average of the GIPRs) can help to alleviate this effect. One can anticipate from this plot that only for an extremely large grid will Δ_q approach 0 for all q (and obey the predicted symmetry relation), which would be intuitively expected for purely uncorrelated speckle.

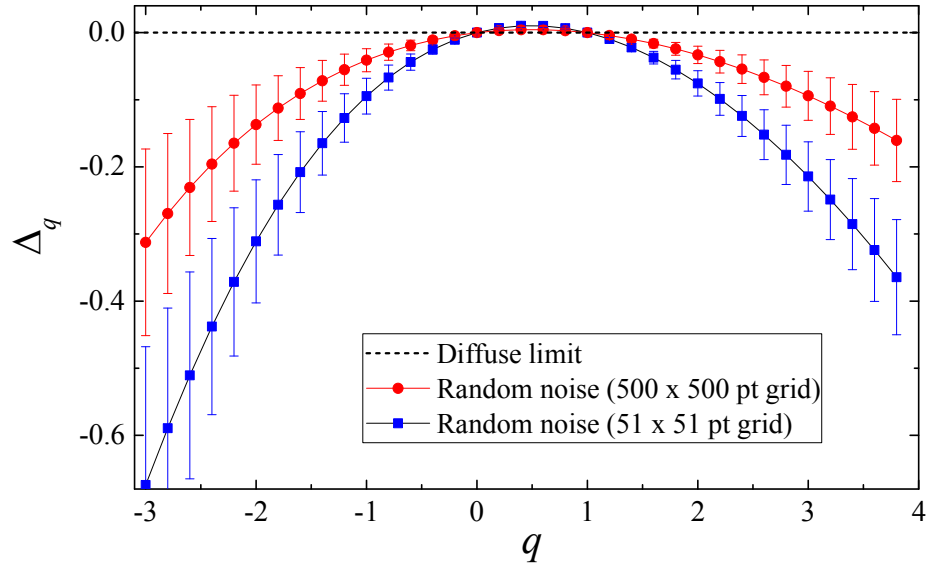


Figure 7.7: Anomalous exponent Δ_q calculated for matrices of pseudo-random values²⁷. Values for negative q are lower than for positive q . Uncertainties are given by the standard deviation from the mean over all grid points.

Conclusions that can be drawn from this simple example are that positive q values are more reliable than negative ones. Noise, which in the case examined here may have some correlations, causes Δ_q to decrease for all q , except very near to $q = 1/2$: the parabola shape of Δ_q is ‘bent’ inwards. This observation demonstrates that the Δ_q are very sensitive to any correlations, as well as the effect of waves being diffuse or localized. For practical experimental

²⁷ These matrices are filled with numbers between the typical minimum values of transmitted speckle intensity for L1, given by the pseudo-random number generator function *enose* in Wavemetrics IGOR software.

purposes, it is clear that noise can distort the results for Δ_q , motivating the development of careful noise discrimination techniques.

7.4. Experiments on cubic mesoglasses

Multifractal behaviour was observed in slab mesoglasses in the critical regime in the previous section by keeping L constant and varying b . Next, we are interested in investigating the sample-size dependence of two measures of multifractality (the GIPR and PDF) by varying L . To this end, I have constructed cubic samples similar to the slab mesoglasses, but which are smaller and exist in a range of sizes. This section details the experimental measurement of ultrasound through these samples, and the comparison of these results with predictions from the finite-size scaling theory of Section 7.2.1. I report significant differences in several different statistical quantities between cube and slab-shaped samples.

7.4.1. Construction of brazed cubic samples

Cubic samples were made of aluminum beads (diameter 4.11 mm) brazed together to form porous 3D disordered networks. This brazing technique is the same as that described in Section 3.1.1. Each sample is cube-shaped, with volume L^3 and linear size $L = 2$ cm, 3 cm, 4 cm, 5 cm, and 6 cm (Fig. below). Several cubes of each size were made to provide opportunity for greater configurational averaging. Thus, since each sample represents a different configuration of disorder, it is important to achieve the same ‘strength’ of brazing (Lee 2014) (i.e. the same size of ‘necks’ connecting individual beads) for all samples. To this end, individual molds for the cubic samples were fashioned so that many different samples, of varying sizes, could be brazed at the same time. Several sets of samples were brazed in this fashion, using the same conditions such as furnace heating profile, pressure, etc. For each cube, one face was sanded flat for laser

interferometry measurements. Representative samples are shown in Figure 7.8. Details on brazing conditions and finished samples are provided in Section 3.1.1.

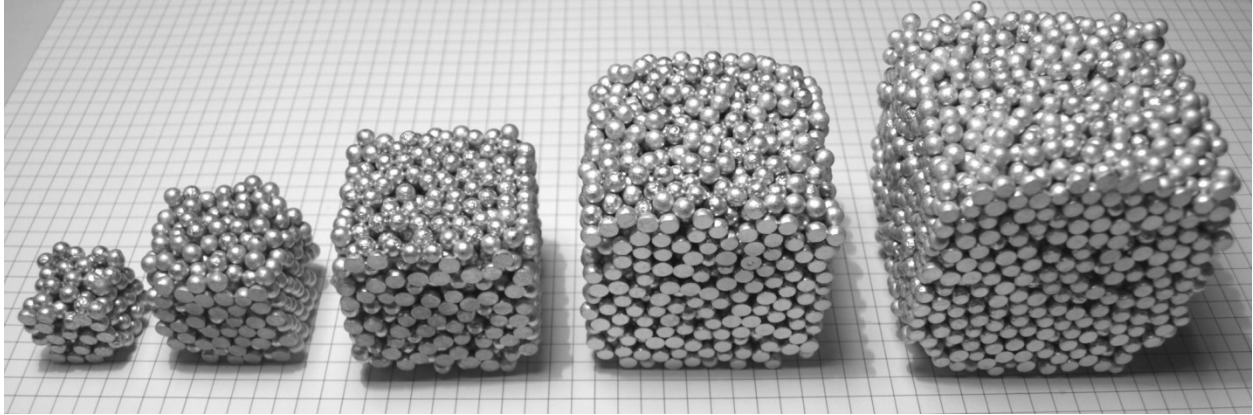


Figure 7.8: Cubic aluminum-sintered samples shown against a background grid of 0.5 x 0.5 cm squares. One representative sample is shown for each size L : left to right: 2 cm, 3 cm, 4 cm, 5 cm, 6 cm. In this picture, the nearest face of each sample is the flat output face, on which acoustic vibrations are measured with a laser interferometer.

7.4.2. Measurements of vibrations on the sample surface

The transmission of acoustic waves through each cubic sample was experimentally measured using an acoustic transducer as the source, and a laser interferometer as the detector. The laser ultrasonic receiver (*TEMPO-2D*, produced by *Bossa Nova Technologies*) is a photorefractive interferometer. A probe beam is incident on the sample (as shown in Figure 7.9). The light reflected back from the sample surface enters the interferometer and is mixed with a reference beam in a photorefractive crystal. This generates a local oscillator beam, which then interferes with the signal beam on a photodetector, producing a photocurrent proportional to the displacement of the sample surface.

The experimental setup around the sample is shown in Figure 7.9. A quasi-point source was constructed by gluing an aluminum cone to a small contact-coupled ultrasonic transducer with a central frequency of 1 MHz (CrystalBond 555 was used, as the hardened glue may be simply dissolved in warm water). The tip of the cone is the diameter of one bead. For each

experiment, the cone tip was placed into contact with an individual bead on the sample surface, which was partially sanded flat for better contact. The transducer emits a long chirp spanning a wide range of frequencies. A laser interferometer measures the acoustic vibrations at the opposite sample surface over a wide range of times and frequencies. Both sample and source are placed on a motorized stage. By translating the stage relative to the interferometer, a two-dimensional (2D) scan of the vibrations on the sample face was recorded.



Figure 7.9: The experimental setup for a representative 5 cm cube. The transducer, glued to an aluminum cone (far right) is placed into firm contact with one bead on the input sample surface (right side of sample). The laser interferometer (left) scans the opposite face of the sample, recording a map of the transmitted speckle intensity as a function of time.

These experiments were performed on many different samples, and, for each sample, several experiments were performed with the source in contact with different spots on the input face. By changing the source position, the input signal is coupled to different modes of the sample. Thus, configuration averaging was performed over experiments on different samples of the same size, *and* on experiments on the same sample with differing source positions.

7.4.2.1. Details of signal generation and detection

An Arbitrary Wave Generator (AWG) generates the input signal (in this case a wideband chirp), which is amplified by a linear amplifier (*E&I Broadband Power Amplifier, Model 2200L*)

and sent to the contact-coupled transducer. The laser interferometer records the vibrations normal to the surface, on the opposite face of the sample. For the analysis presented here only out-of-plane signals were used. Signals were acquired using a Gage Compuscope CS14200/CSE1621 digital oscilloscope card, which allows for fast onboard averaging. The Gage card is synchronized in time with the output of the AWG. Acquired signals were downloaded from the Gage card by Matlab in real-time. Thus, additional averaging was possible by performing multiple acquisitions and averaging them together in Matlab.

The entire generation and detection process is controlled by a sophisticated set of software developed mostly by Cody Friesen, and modified by Eric Jin Ser Lee and myself. This software also controls the motors which translate the sample and source parallel to the interferometer, and includes a complex autofocus routine for the interferometer. This routine ensures that signal is only collected where an acceptable amount of light is reflected back into the interferometer (Friesen 2011). This means that in a scan of a sample surface, voids or areas which are very rough are neglected, decreasing the time required to complete an entire scan.

7.4.2.2. Data processing

With each acquired signal, two additional measurements are also taken: (1) a calibration value, which depends on the total amount of collected light for that point, and (2) the *in-plane accuracy*, which is a measure of the angular dependence of the reflected light. A small in-plane accuracy indicates that a relatively large percentage of reflected light is not parallel to the incident beam axis.

The magnitude of an acquired signals is in volts. The signal is converted to displacement in nanometers by dividing it by the calibration signal. The calibration signal can be used to reject those points which are not within the plane of the acquisition grid scan, i.e. areas which are voids,

or too rough for a decent measurement. The in-plane accuracy can also be used to identify areas from which a large proportion of backscattered light is reflected at an angle to the probe beam. For instance, at the edge of a bead, the in-plane error is often quite high, if light is scattered sideways from the edge, or if only some of the probe beam is in contact with the bead. Here, measurements of normal displacement are not as reliable. Thresholding of the raw data using both the calibration signal and the in-plane accuracy was used to reject signals at rough surfaces or at bead edges.

The data from a scan are immediately Fourier-transformed into intensity as a function of frequency, and calibration and in-plane error thresholding performed. Figure 7.10 shows the average transmitted intensity through a 5 cm sample. Band gaps are clearly visible. They appear at very similar frequencies as the pseudo-gaps of the slab mesoglasses (shown in Figure 3.25), which is not surprising since the cubic and slab samples have similar bead sizes.

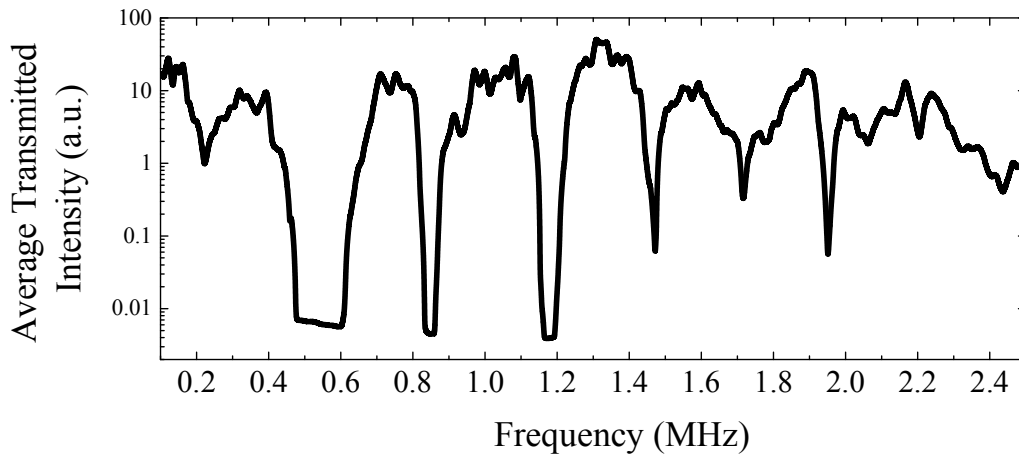


Figure 7.10: Average transmitted intensity through a 5 cm cube (other sizes very similar). Pass bands are due to the coupling of individual bead resonances.

Figure 7.11 shows transmitted amplitude from a scan of a 5 cm cube, for a few representative frequencies. These data have been normalized by the calibration signal, and both the calibration and in-plane error have been used to discriminate between polished bead surfaces

and voids/rough spots on bead edges. These void areas are given a value of not-a-number (NaN) (white areas in Figure 7.11), so that such data are not included in any statistical analysis.

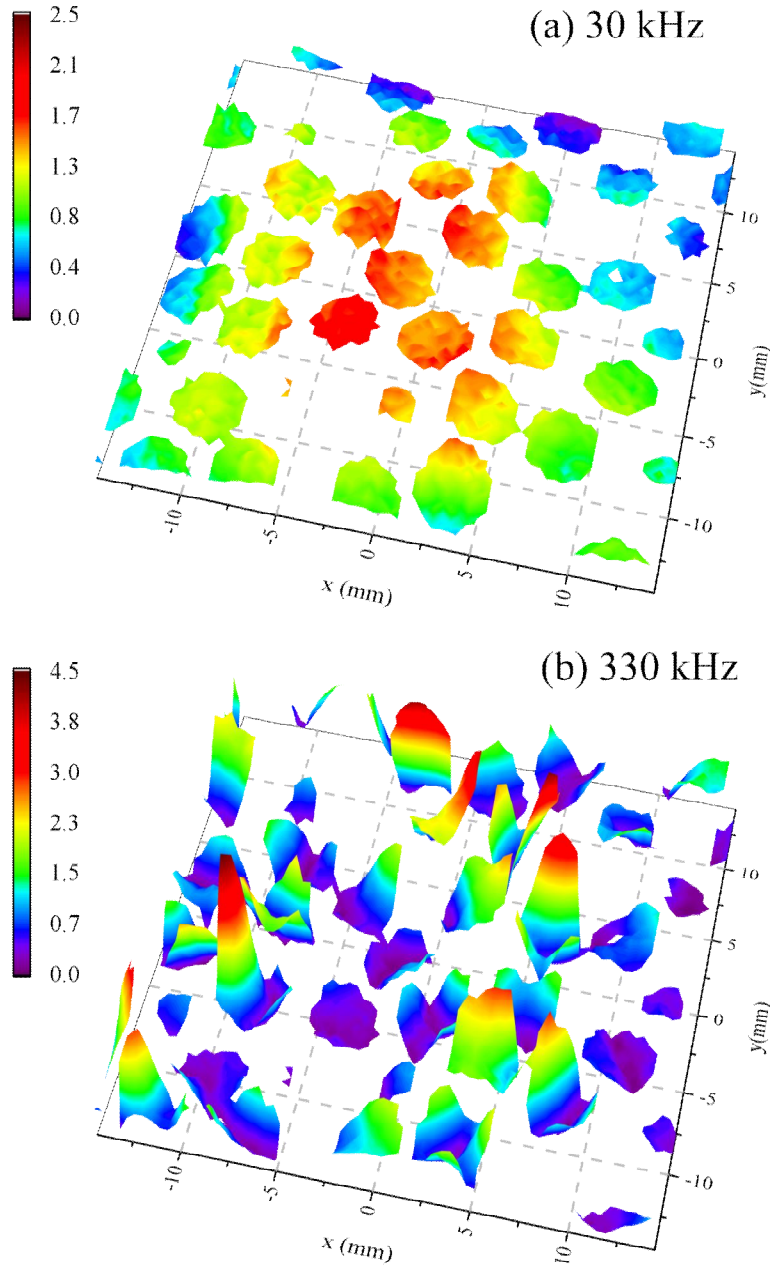
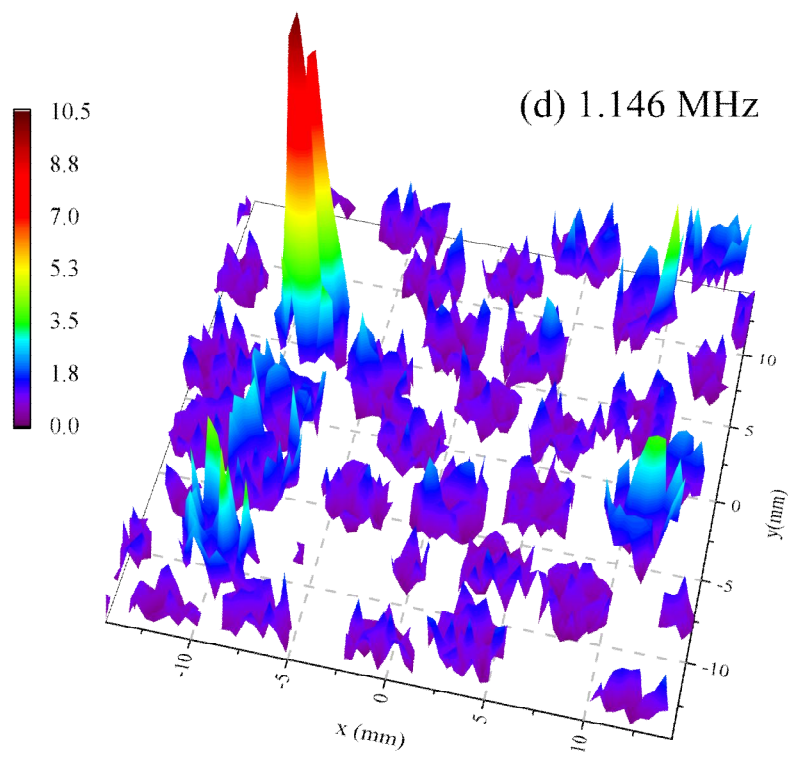
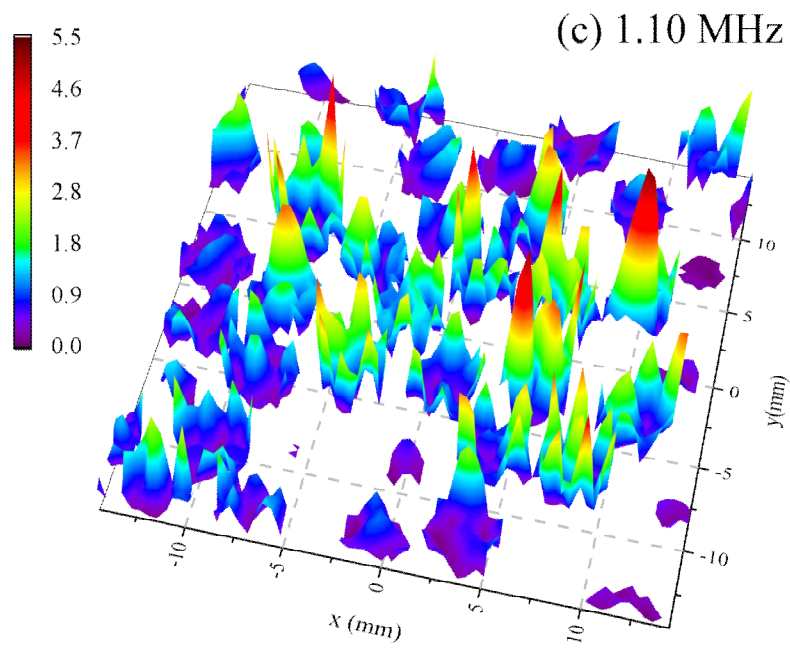
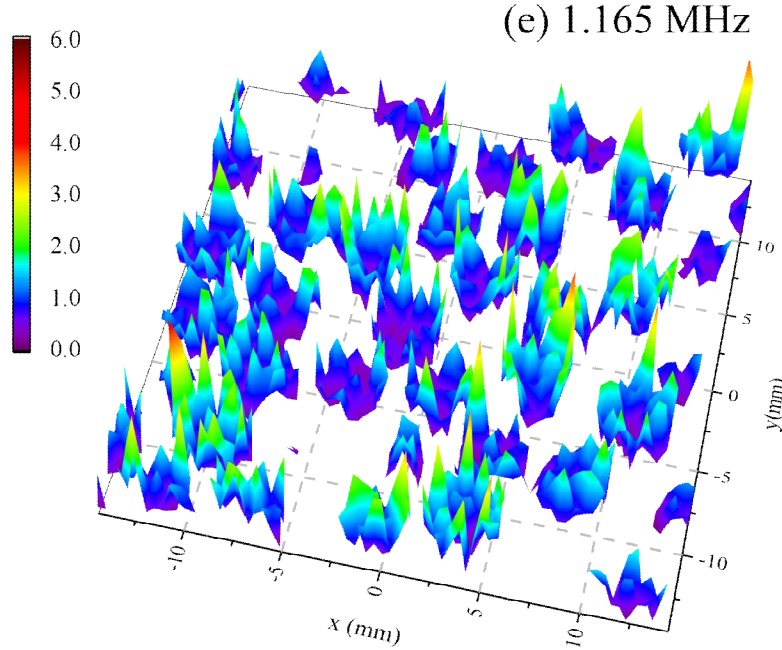


Figure 7.11: Transmitted amplitude through a 5 cm cube, measured by a laser interferometer. Units on colour scales are nm normalized by the average transmitted amplitude at each frequency. Data are shown for several representative frequencies. The approximate spatial extent of acoustic modes in the sample is visible by eye: at 30 kHz (a) and 330 kHz (b), wavelength is much larger than bead size, and modes spread across the entire sample. Around 1.1 to 1.2 MHz (c,d), wavelength is comparable to bead size, and at 1.165 MHz (e), wavelength is smaller than bead size.

(Figure 7.11, cont'd)



(Figure 7.11, cont'd)



In the monodisperse cubic samples, strong scattering can be expected for frequencies where wavelength is comparable to bead size. Thus, frequencies around the band gap near 1.2 MHz were chosen to be investigated for signs of localization. Indeed, at 1.146 MHz, a single spatially localized mode can be observed by eye in Figure 7.11 (d) (and similar behaviour is observed for many other samples). While this in itself is not evidence of Anderson localization, the existence of spatially confined modes near a lower band gap edge is extremely suggestive of localized waves (Hu et al. 2008). This estimate is supported by the fact that in the slab samples L1 and L2, Anderson localization was observed near the pseudo-band gap at around 1.2 MHz (Chapter 5). Thus, the frequencies around the 1.2 MHz band gap are studied in this work.

7.5. Speckle statistics from cubic mesoglasses

Although *average* transmitted intensity through the cubes is similar for different samples and source points (resembling that shown in Figure 7.10), transmitted modes inside band gaps such as that shown in Figure 7.11 (d) are not observed for every source point. In other words, not every input and output point can couple to a localized mode. This means that C_0 correlations are significant, as was observed for sample L1 (see Figure 7.4 and accompanying text). A large C_0 effect is encouraging in a search for a ME, but it also means that a large number of experiments, and careful noise discrimination, are required for meaningful statistical analysis of the speckle maps from the brazed cubes.

7.5.1. Variance

For each frequency and source position, normalized variance of intensity fluctuations σ^2 was calculated in the same way as it was for the speckle maps from L1 (Section 7.3). Results are shown in Figure 7.12, averaged over different source positions and configurations of disorder²⁸.

Variance at pass band edges shows a dramatic increase, indicating large fluctuations. Waves at these frequencies are good candidates to show localized behaviour. The prediction of $\sigma^2 \approx 7/3$ at a ME, along with the expectation that the DOS is small at the upper edge of a pass band, gives an indication of where mobility edges may be expected for these samples.

²⁸ Variance and multifractal quantities were averaged over the following different samples and scans (input position): for 2 cm samples, 3 scans in total on 3 different samples, for 4 cm samples, 3 scans in total on 2 different samples, for 5 cm samples, 7 scans in total on 2 different samples, and for 6 cm samples, 3 scans in total on 2 different samples.

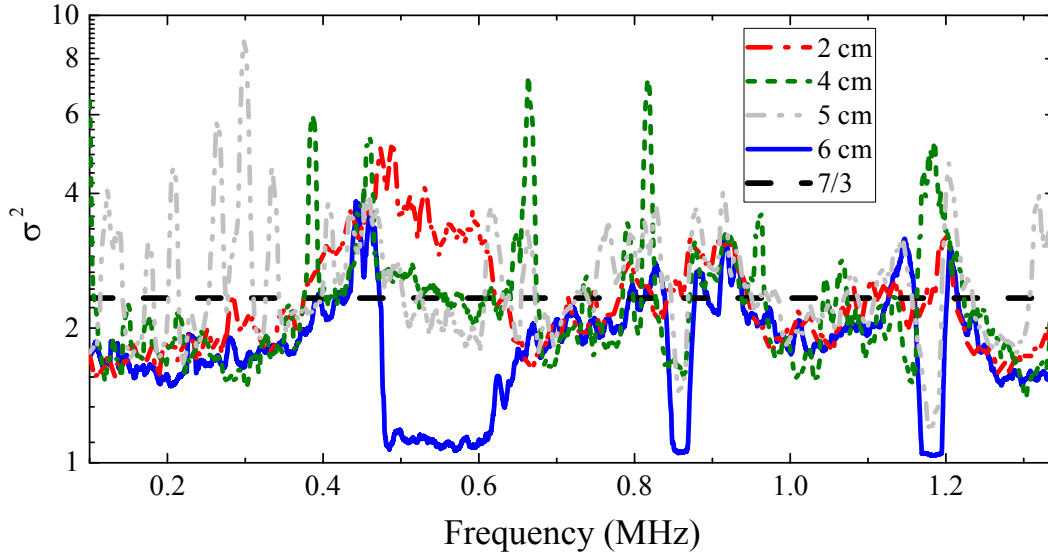


Figure 7.12: Average variance as a function of frequency. Values of $\sigma^2 \rightarrow 1$ for some sizes (e.g. 6 cm) are due to noise inside band gaps as described in Section 7.5.2. The reason for the spikes in variance for the 5 cm sample at lower frequencies are unknown.

7.5.2. Noise discrimination

The most interesting statistics were found in the frequencies at the lower edge of the 1.2 MHz band gap – more specifically, around 1.14 to 1.18 MHz. However, SNR at these frequencies is very low, and noise effects were found to seriously interfere with the desired statistical analysis. Therefore, *for each scan*, the following method was used to discriminate between signal and noise:

1. The average intensity level inside the band gap is found, and any point in the scan where the intensity level is lower than that threshold is set to NAN (illustrated in Figure 7.13).

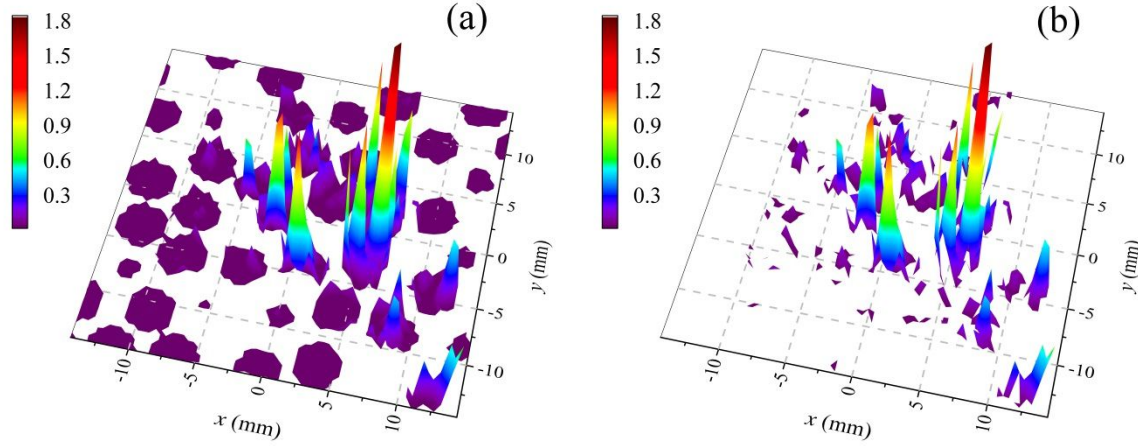


Figure 7.13: Intensity maps of one 5 cm cube at 1.1538 MHz, normalized by the total average intensity. (a) shows all points, and (b) shows only points for which intensity is above the average level inside the 1.2 MHz band gap (the result of the first intensity level thresholding procedure). Only the points in (b) are used in subsequent analysis.

Since each scan is different, and the output speckle map depends greatly on the source position, the intensity thresholding helps to shield configurationally-averaged quantities from noise, and to obtain accurate statistics farther into the band gap than would otherwise be possible. For example, in Figure 7.14, for different source positions on the same sample, very different maps result. For some frequencies near the band gap (e.g. 1.1538 MHz, shown in Figure 7.14), almost no signal is transmitted through the sample for some source positions. Neglecting these points enables more accurate statistical analysis which only includes those points which are above the noise. In the example of Figure 7.14, ‘scan 2’ of Cube 5b (right) would hardly contribute at all to resulting statistics at this frequency. Note that setting these points to NAN is different from setting them to zero, as NANs do not contribute to any average quantities.

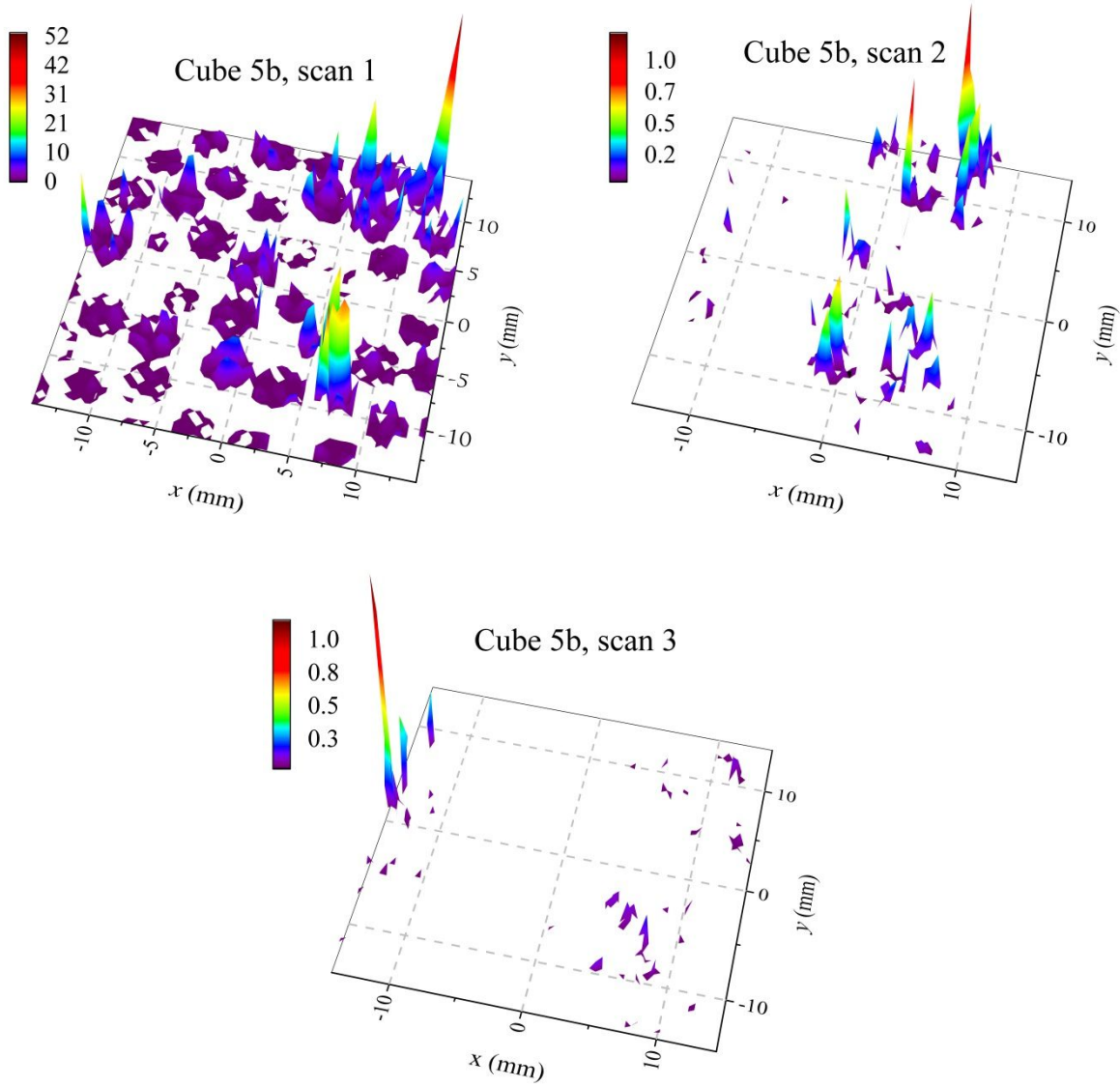


Figure 7.14: Intensity maps of one 5cm cube at 1.1538 MHz after intensity thresholding. Three maps of the same sample surface are shown, for different source positions.

2. A similar procedure is performed during the box-summing step of the analysis – for each frequency f , any box $I_b(f)$ is rejected (not counted in subsequent statistical analysis) for which the sum of intensity in the box is less than 4x the sum of intensity in that same box, averaged over a frequency range inside the neighbouring band gap (1.18 to 1.19 MHz), i.e.

$$\sum_{box} I(f) > 4 \sum_{f_{BG}} \frac{\left(\sum_{box} I(f) \right)}{N f_{BG}} \quad (7.14)$$

where f_{BG} denotes the range of frequencies inside the band gap (entirely dominated by noise for most source positions) and $N f_{BG}$ is the number of points in frequency in that range. The factor of 4 was chosen by observing in detail the effect of this box-intensity-thresholding on the subsequent analysis results.

7.5.3. Multifractality and finite-size scaling

Both the PDFs and GIPRs were calculated for the transmitted intensity through each cubic sample. These quantities were calculated separately for each scan, and then averaged together for each different cube size. Since each scan measures transmitted intensity for a unique source position, this average is an average over realizations of disorder²⁸. For the PDF calculation, boxes (such as those shown in Figure 7.1) were allowed to overlap for increased averaging (this was not possible for the GIPR calculation). This did not introduce any unexpected effects in the final results. Noise discrimination was performed as outlined in Section 7.5.2.

Results for the probability density are shown in Figure 7.15 for two representative frequencies. I observe a subtle scaling of PDF maxima with system size L , in the diffuse regime (left plot). In the plot on the right, a clear shift in PDF maxima from the diffusive regime towards criticality ($1.1 \rightarrow 1.2$ MHz) is demonstrated, and there is much less variation with system size. By varying nothing but the physical size of the sample, a difference in behaviour near the mobility edge is seen. For frequencies higher than 1.15 MHz, there is too much noise to observe definite signs of localization, i.e. a further shift of the PDF maxima such that the 6 cm PDF is furthest to the right and the 2 cm PDF is furthest to the left. However, it should in principle be possible to fit data which approaches the ME with the existing theory, and still extract the critical

exponent, seeing as it is the *rate* of the shift with disorder and system size that is important. This step is considered in the next section.

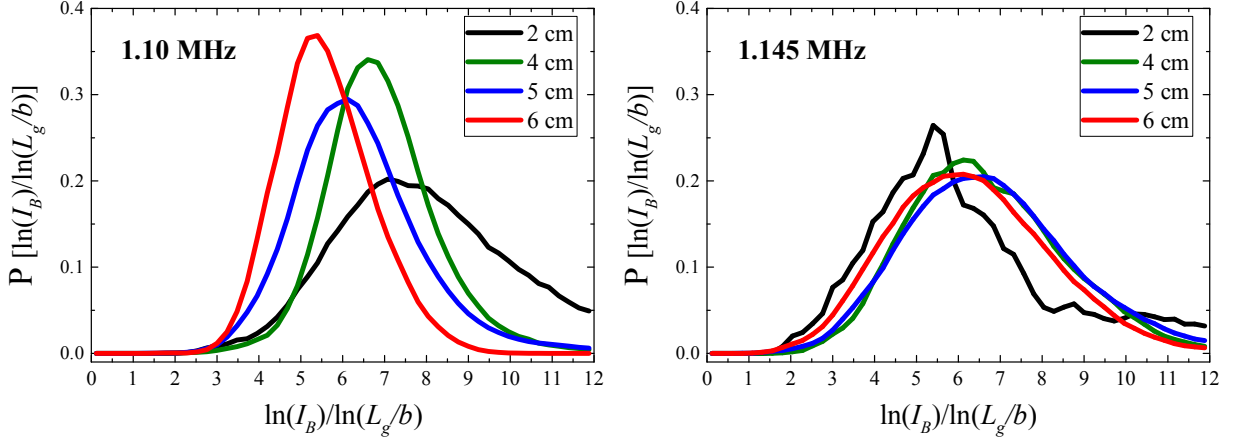


Figure 7.15: Probability Density Functions. Expected shifting of maxima is observed in the diffuse regime (left). With the approach to the mobility edge, distributions for different L shift to the right at different rates (right). At 1.145 MHz, the 2 cm curve is distorted due to noise. For both frequencies, data are averaged over a frequency range of 7.55 kHz.

Results for the GIPRs are shown in Figure 7.16 for two representative frequencies. In the theory of Rodriguez et al., the GIPRs are calculated for one box size only (Rodriguez et al. 2011; Rodriguez et al. 2010). Here, I calculate the GIPRs using the method of Faez et al. (Faez et al. 2009; Hildebrand 2015), where τ_q is calculated over a range of box sizes, and a linear fit of $\langle \log(P_q) \rangle$ vs $\log(b/L_g)$ gives Δ_q directly (this is the same method to calculate the GIPR in sample L1). I have verified that these calculations give approximately the same results, i.e. $\langle \log(P_q) \rangle$ depends linearly on $\log(b/L_g)$, and that they give values of Δ_q that are similar to the single box size method used by Rodriguez et al. The linear fitting method involves more averaging (better statistics), giving results with less uncertainty. There is a subtle difference between these methods according to the theory, but the data quality are limited by the amount of available configurational averaging and the influence of noise, precluding a detailed analysis beyond the observation of a general shift of Δ_q with f and L .

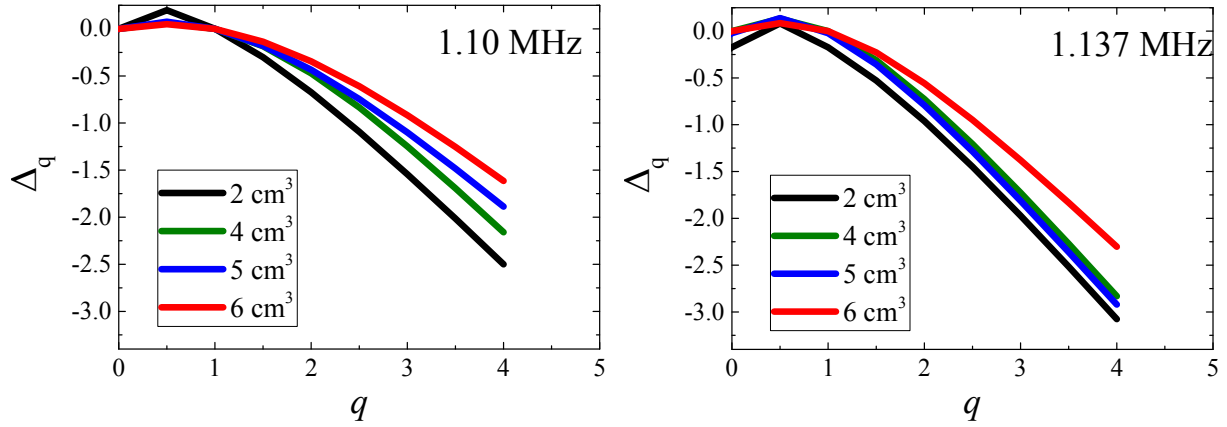


Figure 7.16: Anomalous exponents Δ_q are very low even for the diffuse regime (1.10 MHz, left, averaged over 17.75 kHz). Closer to the pass band edge, the Δ_q decrease even more and are less curved, as expected for the localization regime (right, averaged over 7.75 kHz). For negative q values, Δ_q are highly affected by noise and are therefore not shown. For each sample thickness, configurational averaging was done over 2-5 source points and/or samples.

In Figure 7.16, 1.137 MHz is the frequency the farthest into the band gap at which there is enough statistics to give clear results for Δ_q which are relatively unaffected by noise. There is a subtle shift observed between diffuse (1.10 MHz) and near-critical (1.137 MHz) regimes, in which the anomalous exponents for different sample sizes become lower (indicating an approach to localization) and closer together (implying an approach size-independence).

7.5.4. Critical exponent estimation

Although it is clear that much more configurational averaging is required to obtain accurate results from the experimental data, we can anticipate the finite-size scaling analysis to be performed on future more complete results. To get a sense of the next steps of this project, I present here the FSS analysis that will be used, and apply this theory to the data available so far.

To obtain an estimate of the critical exponent from my data, I apply the simplest possible version of the finite-scaling theory; a one-parameter finite-scaling scaling (FSS) model. This model can be applied to systems whose evolution can be described in terms of one variable only;

in this case, the variable is L/ξ . In principle, a two-parameter FSS model can also be used to analyse these data, by varying the box-size so that the PDF and Δ_q depend on both L/ξ and b/ξ , but this analysis should probably only be attempted after verifying that the one-parameter FSS gives meaningful results, and is thus beyond the scope of this project at present.

Let the function $\Gamma_q(W, L)$ denote either $\tilde{\Delta}_q(W, L, \lambda)$ or $\tilde{\alpha}_q(W, L, \lambda)$ from Equations (7.11) and (7.13). For the one-parameter FSS, the value of λ is fixed so that $\Gamma_q(W, L)$ depends on only one parameter (L/ξ). $\Gamma_q(W, L)$ can be expressed as a function of two variables; β , a relevant variable which describes the nonlinearities of the W dependence on the scaling variable (L/ξ), and η , an irrelevant variable. We can write:

$$\Gamma_q(W, L) = \zeta_q(L/\xi) \quad (7.15)$$

where ζ_q denotes the RHS of either Equation (7.11) or (7.13). The role of the irrelevant variable is to account for a shift with L of the disorder at which the $\Gamma_q(W, L)$ curves cross (away from the mobility edge, W_c). Equation (7.15) can be expanded in first order in η to obtain

$$\zeta_q^k(\beta L^{1/\nu}, \eta L^{1/\nu}) = \zeta_q^0(\beta L^{1/\nu}) + \eta L^y \zeta_q^1(\beta L^{1/\nu}). \quad (7.16)$$

The irrelevant component is a finite-size effect which should vanish for large L , so $y < 0$. The scaling function can be expanded:

$$\zeta_q^k(\beta L^{1/\nu}) = \sum_{j=0}^{n_k} a_{kj} \beta^j L^{j/\nu}, \text{ for } k = 0, 1. \quad (7.17)$$

Expanding β and η in terms of $w = W - W_c$ up to order m_β and m_η , respectively, gives

$$\beta(w) = w + \sum_{m=2}^{m_\beta} b_m w^m, \eta(w) = 1 + \sum_{m=2}^{m_\eta} c_m w^m. \quad (7.18)$$

The fitting of this model to experimental data is characterized by the fitting orders n_0 , n_1 , m_β , and m_η . The fitting should be performed using the lowest orders of these expansions as possible, while keeping high enough orders to give an acceptable goodness-of-fit. Ideally, these orders are parameters in the fitting process; the total number of free parameters would therefore be $N_p = n_0 + n_1 + m_\beta + m_\eta + 4$ (including W_c , ν , and y). For this work, the data are probably not of good enough quality to obtain meaningful fits with higher order terms. Here I will use only the lowest orders of the model. To second order, Equation (7.18) gives

$$\beta(w) = w + b_2 w^2, \quad \eta(w) = 1 + c_2 w^2 \quad (7.19)$$

To second order, Equation (7.17) is

$$\zeta_q^k(\beta L^{1/\nu}) = a_{k0} + a_{k1} \beta L^{1/\nu} + a_{k2} \beta^2 L^{2/\nu} \quad (7.20)$$

Thus, Equation (7.16) becomes

$$\begin{aligned} \zeta_q^k(\beta L^{1/\nu}, \eta L^{1/\nu}) &= \zeta_q^0(\beta L^{1/\nu}) + \eta L^y \zeta_q^1(\beta L^{1/\nu}) \\ &= a_{00} + a_{01} \beta L^{1/\nu} + a_{02} \beta^2 L^{2/\nu} + L^y (a_{10} + a_{11} \beta L^{1/\nu} + a_{12} \beta^2 L^{2/\nu}) \end{aligned} \quad (7.21)$$

The irrelevant variable is not expected to contribute meaningfully to the approximate fitting of my data. In the work of Rodriguez et al., which consists of numerical simulations involving over one million configurational averages, the shift in W that is described by η is still very small. Thus, only the lowest order in η will be kept from Equation (7.21). Here I will also replace the general disorder parameter (W), with that for our systems of ultrasound in brazed mesoglasses, frequency (f). This gives the fitting function

$$\Gamma_q(f, L) = \alpha_0 + \alpha_1 (f - f_c) L^{1/\nu} + \alpha_2 (f - f_c)^2 L^{2/\nu} + \alpha_3 L^y \quad (7.22)$$

The localization (correlation) length is related to the critical frequency f_c as $\xi \propto |\beta(f - f_c)|^{-\nu}$.

Variables α_0 , α_1 , α_2 , α_3 , and f_c are common to all data curves, while L is a fixed parameter

which is different for each data curve (since they originate from samples of different sizes). The model can be applied to either the mean value of the PDF curves, $\langle\alpha\rangle(f, L)$, or to the anomalous exponent $\Delta_q(f, L)$. Here, experimental data for $\langle\alpha\rangle(f, L)$ is fit with the model. A global fit to all curves is first performed using only the first two terms of Equation (7.22). Then, the results for the fit parameters are used as initial guesses for subsequent fits which include, one by one, the next two parameters of Equation (7.22). Fit results do not change significantly with the addition of each term, indicating an insensitivity to higher order terms and to any order of η .

Figure 7.17 shows the mean values²⁸ of the PDF of the experimental data, $\langle\alpha\rangle$, as a function of frequency and for four different cube sizes. These are the same data that are shown for two frequencies in Figure 7.15, but here have not been averaged over frequency. (Corresponding results for Δ_q are not shown as they are too noisy.) On either side of the band gap, FSS has been performed via a global fit of all (4) curves with Equation (7.22). Fits were weighted by experimental uncertainties. Performing the fit with, and without, the last two terms of Equation (7.22) changes the fit results only by a trivial amount. Free and fixed parameters are given in Table 7.1. It is important to note that the goodness-of-fit measures are not acceptable (reduced $\chi^2 \ll 1$ due to the large experimental uncertainties, and the resulting uncertainties for some fit parameters are larger than the parameter value), and that therefore the results for f_c and ν are probably not very meaningful. This analysis is shown solely as an indication of the future direction of this project. The estimates of $f_c \sim 1.5$ MHz (for the data below the bandgap) and $f_c \sim 1.1$ MHz (for the data above the bandgap) are clearly not accurate. These results indicate either that there are not enough data at the band edges to clearly show the critical behaviour of $\langle\alpha\rangle$, or that there is not a localization regime inside the band gap, so that the waves do not undergo a full transition at the band edges. However, the fit results for ν ($\nu = 1.1$ for the lower

gap edge data, and $\nu = 1.0$ for the upper gap edge data) are not unreasonable given the uncertainties in the data, since the generally accepted value is $\nu \sim 1.6$ (see Section 2.5.1).

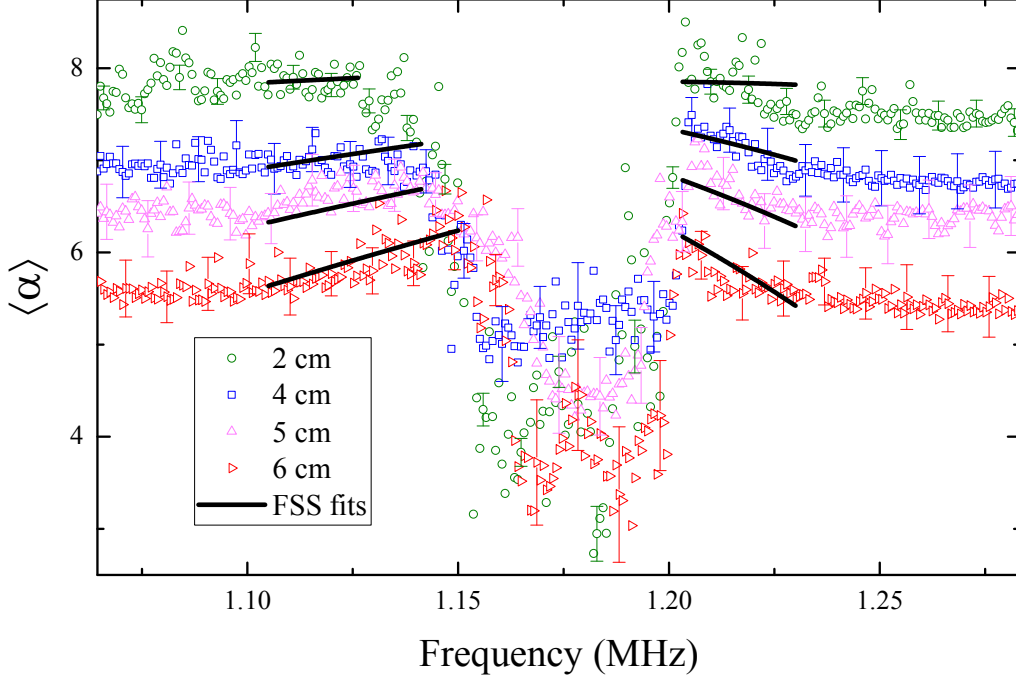


Figure 7.17: Experimentally-measured mean PDF values, $\langle \alpha \rangle$, for four different cube sizes. Global fits to the FSS model are shown, which were performed separately on each side of the band gap. For clarity only every 15th data point, and fewer error bars, are shown. Note that inside the band gap ($\sim 1.15 - 1.20$ MHz) the low $\langle \alpha \rangle$ values are due to noise.

	ν	f_c	α_0	α_1	α_2	α_3	y
Lower gap edge ($\sim 1.10 - 1.15$ MHz)							
Starting value	1.6	1.15	8	0.5	0	0	0
Results	1.1	1.5	8.3	0.03	-0.01	-0.0001	-0.001
Upper gap edge ($\sim 1.20 - 1.23$ MHz)							
Starting value	1.6	1.18	8	-0.5	0	0	0
Results	1.0	1.1	7.9	-0.1	-0.04	-0.008	0.5

Table 7.1: Starting values and results for free fit parameters from FSS model applied to the experimentally-measured $\langle \alpha \rangle$. Corresponding uncertainties for several of these parameters, and overall unacceptable goodness-of-fits, indicate that these parameters should not be taken as physically meaningful.

7.6. Conclusions and future directions

I have measured transmitted intensity through cubic samples of different sizes. The transmitted speckle patterns on the surface of the cubes show dramatic fluctuations and localized modes. To quantify these effects, I have investigated the multifractality of the transmitted intensity. A shift in the mean of the calculated PDFs shows finite-size scaling, and seems to indicate that critical regimes exist as the bandgap is approached from lower and higher frequencies. Improved statistics are needed to be able to conclusively observe a crossing over of $\langle\alpha\rangle$ or Δ_q into the localized regime. I have also fit the PDFs with a finite-size scaling model to estimate the critical exponent and critical frequencies. This analysis suggests that there may be no Anderson transition in these samples, which seems surprising in view of the significant fluctuations of transmitted intensity through the cubes at these frequencies. In general, the results so far highlight the need for a large amount of configurational averaging, especially since localized modes inside the band gap are rare and are not excited by all input points. Alternately, creating similar cubic samples which are less strongly brazed (Lee 2014) and/or polydisperse (see e.g. Section 5.1.1.1 of this thesis) could help to increase the likelihood of Anderson localization occurring, and increase the amount of signal that is transmitted in band gaps.

An important question which has not yet been addressed is whether our measured surface multifractal properties are similar to those of the bulk medium, which is what simulations generally measure (cf. (Evers and Mirlin 2008)). Another question concerning surface speckle that has not been addressed theoretically is how polarization of elastic waves influences the measured MF properties. Answering these questions, and improving signal-to-noise via different samples or greater configurational averaging, will be instrumental in obtaining an accurate experimental estimate of the critical exponent from this project.

8. A Lévy Phononic Glass

8.1. Introduction

In this thesis and in many other works, departures from conventional diffusion are used as indications that localization may be present. We have looked experimentally at how diffusion, subdiffusion, and localization are exhibited in the same sample, and how transitions between them are made. We have also seen that very careful work is required for definitive proof of critical or localized behaviour. This point is especially crucial when one considers that a whole host of scattering processes can show departures from conventional diffusion, other than localization. The description of diffusive transport as a random walk is in fact a special case of an entire class of random walk processes. These include *superdiffusion*, where transport is faster than conventional diffusion. Just as with subdiffusion, superdiffusive waves will deviate from conventional diffusive behaviour, but for superdiffusion, these deviations will not indicate an approach to localization.

We propose to investigate whether localization and superdiffusive processes can be observed in the same sample, and if so, whether there is any interplay between them. This chapter presents preliminary research on a sample which is a good candidate for the proposed project.

A generalized description of diffusion can be written simply in terms of the mean squared displacement $\langle x^2 \rangle$ as

$$\langle x^2 \rangle = Dt^\gamma \quad (8.1)$$

where D is the generalized diffusion coefficient, and γ is a parameter that governs the transport. For $\gamma = 1$, conventional diffusion is recovered, but for $\gamma < 1$ transport is subdiffusive, and for

$\gamma > 1$ transport is superdiffusive (Savo et al. 2014).

An example of superdiffusion is the *Lévy flight*. This is a process in which the steps of the random walk have a power law distribution given by

$$P(z) = \frac{1}{z^{\alpha+1}} \quad (8.2)$$

where $P(z)$ is the probability of a step of length z , and α determines the type of Lévy flight ($1 \leq \alpha < 2$). Transport is dominated by long steps (Mandelbrot 1983), so the mean step length diverges and the diffusion approximation breaks down.

Recently, Lévy flights were observed for light propagation through samples of so-called Lévy glasses (Barthelemy, Bertolotti, and Wiersma 2008). This material consisted of packed glass microspheres with a specific distribution of sizes; it was shown that a very specific distribution $P(d)$ of microsphere diameters d is required to obtain a Lévy flight of type α (Bertolotti et al. 2010):

$$P(d) = 1/d^{2+\alpha} \quad (8.3)$$

This is a fractal (self-similar) distribution, meaning that the structure is independent of length scale. Real-world samples have a finite range of possible sphere sizes, resulting in a so-called *truncated* Lévy flight; conventional diffusive behaviour is recovered on length scales larger than the largest possible step size (i.e. the largest sphere diameter). In a recent work, convincing observations of Lévy flights were made by studying the thickness-dependence of time-dependent transport through the Lévy glasses (Savo et al. 2014). The transmitted intensity was shown to decay as $T(t) \sim \exp(-t/\tau)$. The lifetime was expected to show a sample thickness dependence of $\tau \sim L^{d_w}$, thus enabling an estimate of the fractal dimension d_w of the system.

This chapter explores an analogous system which is expected to exhibit superdiffusion for acoustic waves; a Lévy phononic glass. This is a material which is engineered to show both

strong scattering of ultrasound, and to have a fractal distribution of available steps. Initial measurements on this system have been carried out, and show interesting departures from conventional diffusion. This concrete first step towards the study of superdiffusion of ultrasound lays the foundation for a more involved study of the thickness-dependence of transmission through Lévy phononic glasses.

8.2. Slab sample L0

A slab-shaped Lévy phononic glass sample ‘L0’ was constructed using the brazing technique described in Section 3.1.1. As was pointed out by Bertolotti et al., the easiest type of Lévy flight to construct is that of $\alpha = 1$. This means that the diameter distribution is $P(d) = 1/d^3$, so that equal *volumes* of different sizes of spheres are required to achieve a fractal distribution of diameters (Bertolotti et al. 2010). Sample L0 was constructed from four different aluminum bead sizes, with the final sample being composed of close to 40 g of 7.9 mm beads, 40 g of 4.11 mm beads, 41 g of 2 mm, and ~48 g of 1 mm (extra 1 mm beads were added to fill out the sides of the sample in the mold). The sample has a circular face of diameter $d \approx 23$ cm, and the thickness equals the diameter of the largest bead size; $L \approx 7.9$ mm. Additional details on sample preparation are included in Section 3.1.1. The finished sample is shown in Figure 8.1. Subsequent samples will include many more bead sizes, but since sample L0 is, in principle, statistically self-similar, sample L0 should exhibit some Lévy-like wave transport.



Figure 8.1: Sample L0, shown in its acrylic holder for ultrasonic experiments. The sample (like all others studied in this thesis) is held in the holder by a thin layer of silicone (white outer layer), which also prevents stray sound from propagating between the sample edges and the holder. The hole through which air is evacuated from the sample is visible as a white vertical line (top of figure). The final steps of adding thin plastic walls over the sample faces, and wrapping the holder in Teflon tape, were performed after this picture was taken.

8.3. Transmission through the Lévy phononic glass

Speckle maps were acquired in transmission for sample L0 following the procedure detailed in Section 7.3.1. These experiments were carried out using two different broadband focussing transducers for the input signal with central frequencies of 1 MHz and 2.25 MHz, respectively. Thus, experimental data for a wide range of frequencies is available. Unlike previous samples discussed in this thesis, it is unclear at what frequency or frequencies departures from conventional diffusion will occur for sample L0. As most of the sample is composed of smaller beads than samples L1 and L2, one would expect stronger scattering at higher frequencies, i.e. for the 2 MHz experimental data. As usual when beginning to study a

new sample, we can look for interesting features in the transmission as a function of frequency. Figure 8.2 shows the amplitude transmission coefficient for L0. There are no clear pass bands or gaps observed, but there is a clear decrease in transmitted signal from 1 MHz to 2 MHz.

For samples L1 and L2, very strong scattering was observed around 1-1.3 MHz, where the wavelength of waves entering the sample, $\lambda = v/f \sim 1.5/1.2 = 1.25$ mm is smaller than the mean bead diameter. Thus, we might expect strong scattering in L0 at wavelengths smaller than 1 mm, which is the diameter of the majority of beads in the sample (although the polydispersity makes this argument approximate at best). Thus, we expect more interesting behaviour near or above 2 MHz, where $\lambda \sim 1.5/2 = 0.75$ mm.

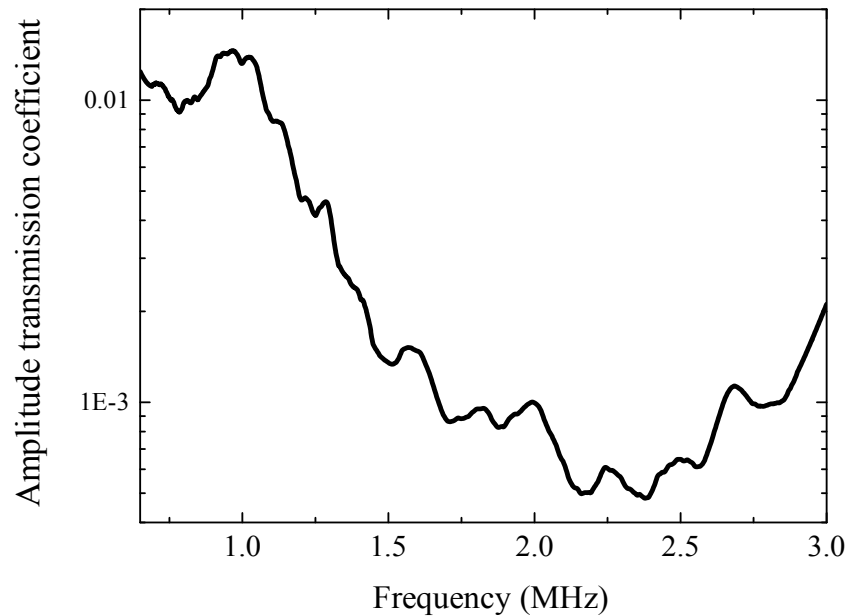


Figure 8.2: Amplitude transmission coefficient for sample L0 over the experimentally available range of frequencies. This quantity was measured using only the on-axis data from the transmitted speckle maps and normalized by the frequency dependence of the reference signal. Although only a relatively small amount of configurational averaging could be done (26 (22) points for the 1 MHz (2 MHz) experiment) this quantity is still very useful as an estimate of the frequency dependence.

Figure 8.3 shows the transmitted time-of-flight (TOF) intensity profile, averaged over all detector positions, filtered at different central frequencies. A significant ballistic component was

also anticipated, due to the small sample thickness and the presence of the 7.9 mm diameter beads, which span the entire sample thickness. However, transmission through the sample was lower than expected, including the initial coherent signal. It is surprising that the material is so opaque for this entire frequency range of 0.75 – 2.5 MHz. To obtain a sufficient amount of configurational averaging, therefore, many different maps corresponding to different source positions were obtained: 26 maps for 1 MHz, and 22 maps for 2 MHz.

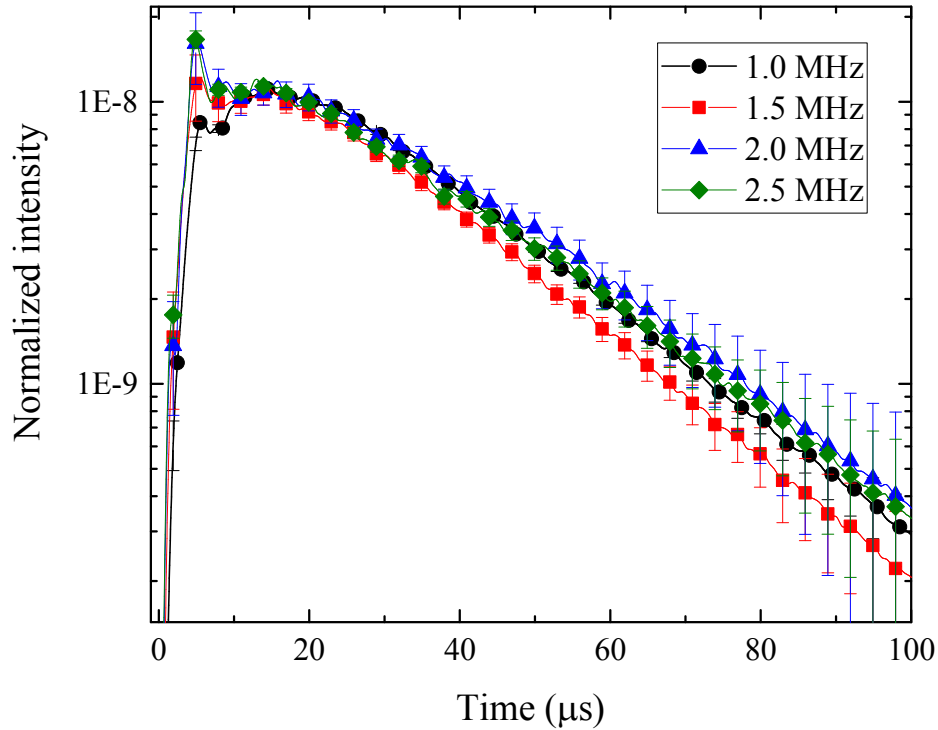


Figure 8.3: Average time-of-flight profiles through sample L0, filtered in frequency with a (relatively narrow) bandwidth of 50 kHz. The input transducer is centered at 2 MHz. The TOF profiles have been averaged over all (22) configurations of disorder, and all detector positions (ρ) on the 2D speckle map. Profiles have been normalized so that they have approximately the same peak value, for easier comparison of their time-dependence.

The weak frequency dependence is also shown in measured time-of-flight (TOF) profiles (time-dependent transmitted intensity), which hardly vary at all as a function of frequency. Thus, data were filtered in frequency with a large width of $w = 250$ kHz (see Section 3.2.4 for more details). This gives the advantage of additional averaging and lesser effects from the filter width.

The frequency filtering was performed for two central frequencies (corresponding to the central frequencies of the two input transducers): 1 MHz and 2 MHz. Data presented in this chapter are thus labeled ‘1 MHz’ and ‘2MHz’, following the convention laid out in earlier chapters of this thesis. For better statistics, a moderate amount of spatial averaging was performed; since the speckle maps are acquired on a discrete two-dimensional grid, this amounts to averaging the data over similar values of ρ . Thus for the data presented below, ρ represents a mean radial distance from the center of the grid. For all transmitted intensity profiles, the noise level is determined from the pretrigger signal and subtracted from the entire profile (as detailed in Section 3.2.2).

Figure 8.4 shows the TOF profiles for the 1 MHz data as a function of time for three different ρ values. The profiles decay much more quickly than was observed for samples L1 and L2 (see Section 4.3). At long times, the decay of the TOF profiles is well-described by a function of the form

$$y(t) = y_0 + A \frac{e^{-t/\tau}}{t} \quad (8.4)$$

which is the expected behaviour for transmitted intensity with a point source and point detector in the diffusion regime (Page et al. 1995). If the transmitted intensity is integrated over all output points, the expected long-time behaviour in the diffusion approximation is an exponential decay. This behaviour is exhibited by our data from L0 (Figure 8.4, grey squares, and Figure 8.3). The observations of what appears to be diffuse TOF profiles, however, does not mean that the behaviour is not Lévy flight-like (Savo et al. 2014).

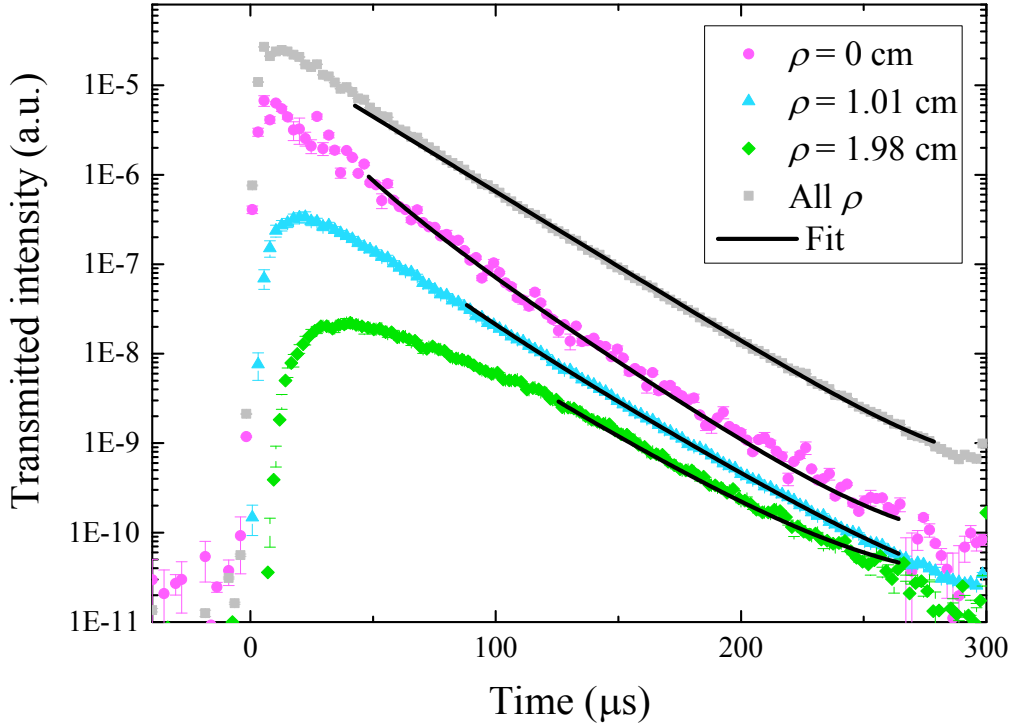


Figure 8.4: Average transmitted intensity through sample L0 at 1 MHz. Shown are TOF profiles for on-axis data ($\rho = 0$ cm, pink circles), and off-axis data ($\rho = 1.01$ cm, blue triangles, and $\rho = 1.98$ cm, green diamonds). The decay of the intensity at later times has been fit with a function of the form $y(t) = y_0 + A e^{-t/\tau}/t$ (black lines). The on-axis data displays more oscillations since less spatial averaging is possible for small ρ values in a 2D grid. After around $250 \mu\text{s}$ the TOF profiles descend into the noise level. The grey squares show transmitted intensity averaged over all output points, which displays an exponential decay at long times. Only every 30 data points are shown for clarity. Error bars represent the uncertainty in the configurational average. The $\rho = 0$ mm trace has been multiplied by 2 so that the long-time behaviour can be distinguished from the other traces.

In Figure 8.5, the same data shown in Figure 8.4 is plotted as a function of ρ for three different times. As expected, $I(\rho)$ is roughly Gaussian for all times after around $35 \mu\text{s}$. However, for earlier times ($t < 35 \mu\text{s}$) there is an additional contribution to intensity at small ρ values, and a Gaussian can not be fit to the entire intensity profile. This is illustrated in Figure 8.5 for $t = 27 \mu\text{s}$. This enhancement of intensity at small ρ and small t is not expected for diffusion, but is predicted to occur for superdiffusion (Zumofen and Klafter 1993; Drysdale and Robinson 2006) and has been observed for Lévy flights in optics (Savo et al. 2014).

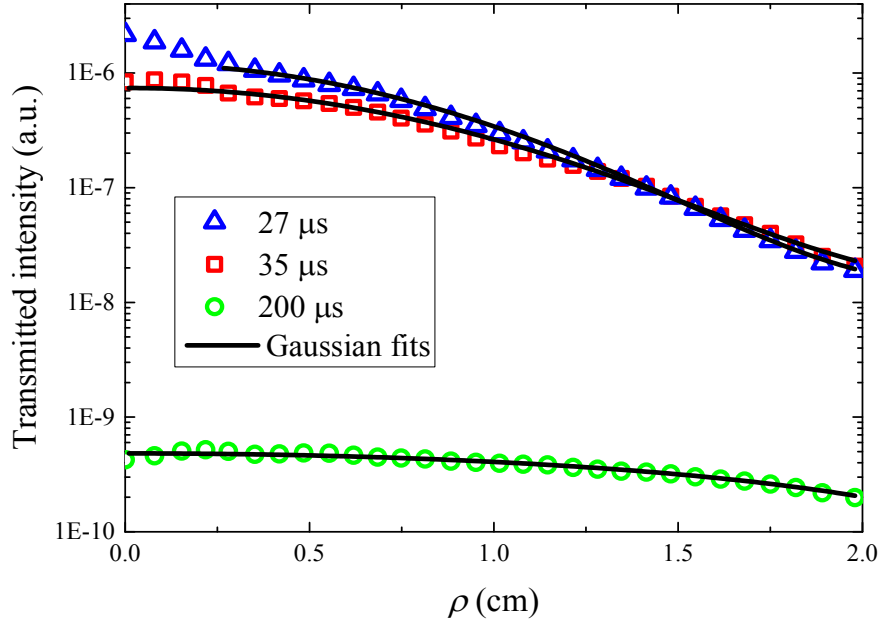


Figure 8.5: $I(\rho)$ for three different times (symbols) with Gaussian fits (black lines). Error bars (which represent the uncertainties from the configurational average) are smaller than symbols.

To further investigate the time-dependent transport of ultrasound inside L0, the transverse width may be calculated from the time- and spatially- dependent speckle maps, similarly to the calculation for the transmitted dynamic transverse profile experimental data (Equation (4.29)). Results are shown in Figure 8.6. For all frequencies and ρ values, $w_\rho^2(t)/L^2$ is only very weakly dependent on ρ , close to the behaviour found for conventional diffusion (Page et al. 1995). It also increases linearly with time for $t > 50 \mu\text{s}$ as would be expected for diffusion. However, a straight line can only be fit to the traces by allowing a substantial y-intercept $y_0 > 0.5$. As discussed in Section 4.3.1.1, a linear increase with a zero y-intercept is theoretically predicted for $w_\rho^2(t)$ for conventional diffusion, and has been observed experimentally, originally for glass bead suspensions by Page et al. (Page et al. 1995), and for aluminum-brazed samples at low frequencies in this thesis (Chapter 4). The finite size of the point source can introduce a vertical offset to $w_\rho^2(t)$ (Hu 2006), but this effect is negligible for this experiment.

The frequency filter width (see Section 3.2.4), being large, should also not cause this effect. These observations, namely $y_0 > 0$ and the kink in $w_\rho^2(t)$ at around 15-25 μs , indicate anomalous wave behaviour in sample L0 that must be related to the structure of this sample.

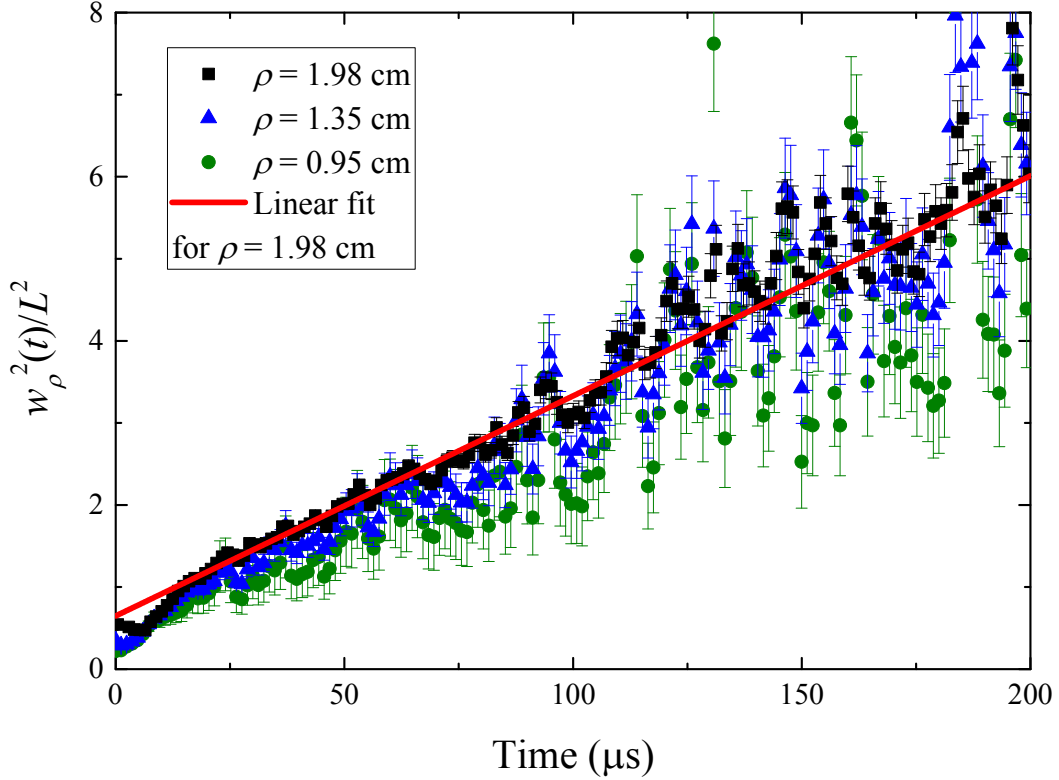


Figure 8.6: Transverse width divided by sample thickness squared for sample L0 at 1 MHz. Three representative ρ values are shown. After 50 μs , $w_\rho^2(t)/L^2$ increases linearly for all ρ values. A linear fit to the $\rho = 1.98 \text{ cm}$ trace is shown as a guide to the eye. Only every 15 data points are shown for clarity. Error bars represent the uncertainty in the spatial averaging and in the configurational average.

For the Lévy flight observations in optics, the clearest indications of superdiffusive behaviour were from the dependence of transmitted intensity on sample thickness. The research presented in this thesis is limited to one sample thickness only. However, we may simulate thickness-dependent measurements using our speckle maps, since transmitted waves that are detected at different transverse ρ values have travelled on average along longer paths, as though they had travelled through different thicknesses of the same sample. By fitting the exponential

decay of the TOF profiles with the exponential function $T(t) \sim \exp(-t/\tau)/t$, the lifetime τ was estimated for each ‘effective’ sample thickness, $\rho_{\text{eff}} \equiv \sqrt{\rho^2 + L^2}$. Results are shown in Figure 8.7. Note that the lifetimes measured are quite short compared to the expected absorption times (which, for aluminum-brazed samples, are generally on the order of $100 \mu\text{s}$) so the contribution of absorption time to the TOF time-dependence decay is negligible. Thus, it is ignored for the analysis presented here.

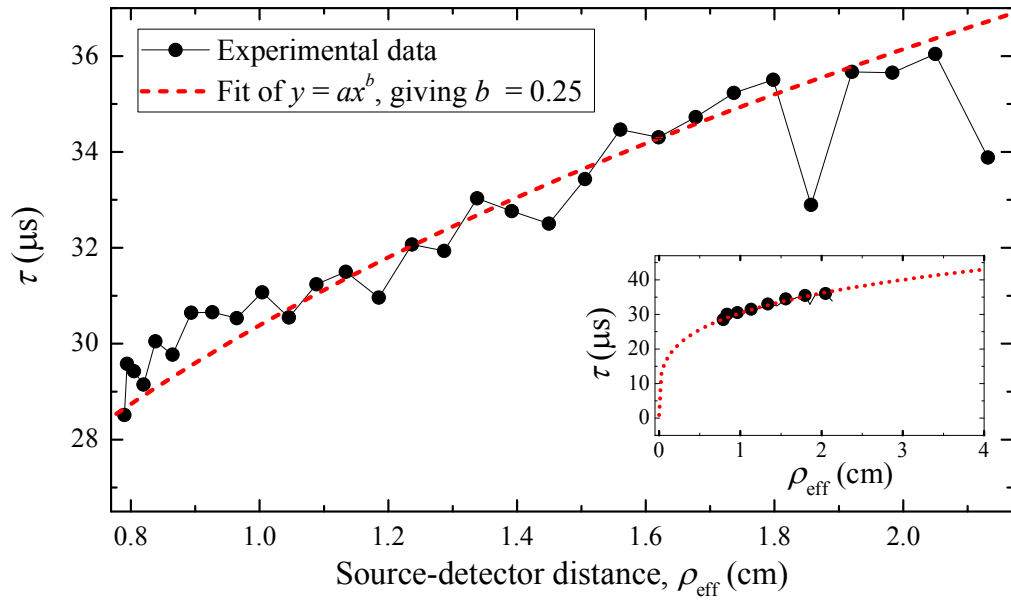


Figure 8.7: Experimental lifetime of transmitted intensity through sample L0 (black circles), as a function of ρ_{eff} . Error bars (smaller than the symbols) represent the uncertainty in the fits of the TOF profiles which were used to measure τ . A power law fit of the data (red line) gives a scaling exponent of $b = 0.25$. Inset: the same data and fit on wider horizontal and vertical scales. Only every 4th data point is shown in the inset for clarity.

For conventional diffusion, it is well known that diffusion time scales with effective sample thickness as $\tau_D \sim cL_{\text{eff}}^2$, where $L_{\text{eff}} \equiv L + 2z_0 = \rho_{\text{eff}} + 2z_0$, $z_0 = 2l^*(1 - R)/3(1 + R)$, and c is a constant. For the generalized class of diffusive processes that we consider here, the lifetime τ is expected to scale with the fractal dimension of the random walk: $\tau \sim cL_{\text{eff}}^{d_w}$. For

conventional diffusion, $d_w = 2$, for subdiffusion $d_w > 2$, and for superdiffusion $d_w < 2$. For the photonic Lévy glasses studied by Savo et al., $d_w \approx 1.3$ was measured (Savo et al. 2014).

For my phononic Lévy glass, τ vs ρ_{eff} is shown in Figure 8.7. A fit of the form $\tau \sim \rho_{\text{eff}}^b$ yields $b \approx 0.25$, which seems very small. However, for a measurement of d_w , it is necessary to use L_{eff} , which means that z_0 , and therefore l^* and R , must be known²⁹. The result for d_w is very sensitive to the values of L_{eff} . For instance, if $z_0 \approx 1.36$ cm (the value calculated for sample L1) is used, then the power law fit gives $b \approx 0.5$. To go further with this analysis will require more samples of different thicknesses and accurate determination of z_0 .

8.4. Speckle statistics of the Lévy phononic glass

As the features of $I(\rho, t)$ are rather frequency-independent, and their deviations from conventional diffusive behaviour are not very spectacular, it is now instructive to look at the statistics of the speckle maps, as was done for data near Anderson localization in Section 7.3. As can be observed by eye in Figure 8.8, the transmitted speckle maps from sample L0 show striking differences in overall intensity and distribution for different source positions. These fluctuations could be due to the C_0 effect, which measures the variation in local density of states near the source.

²⁹ Assuming that the calculation of z_0 is the same for a Lévy flight as it is for diffusion, which to my knowledge has not been proven (see also the work of Savo et al.).

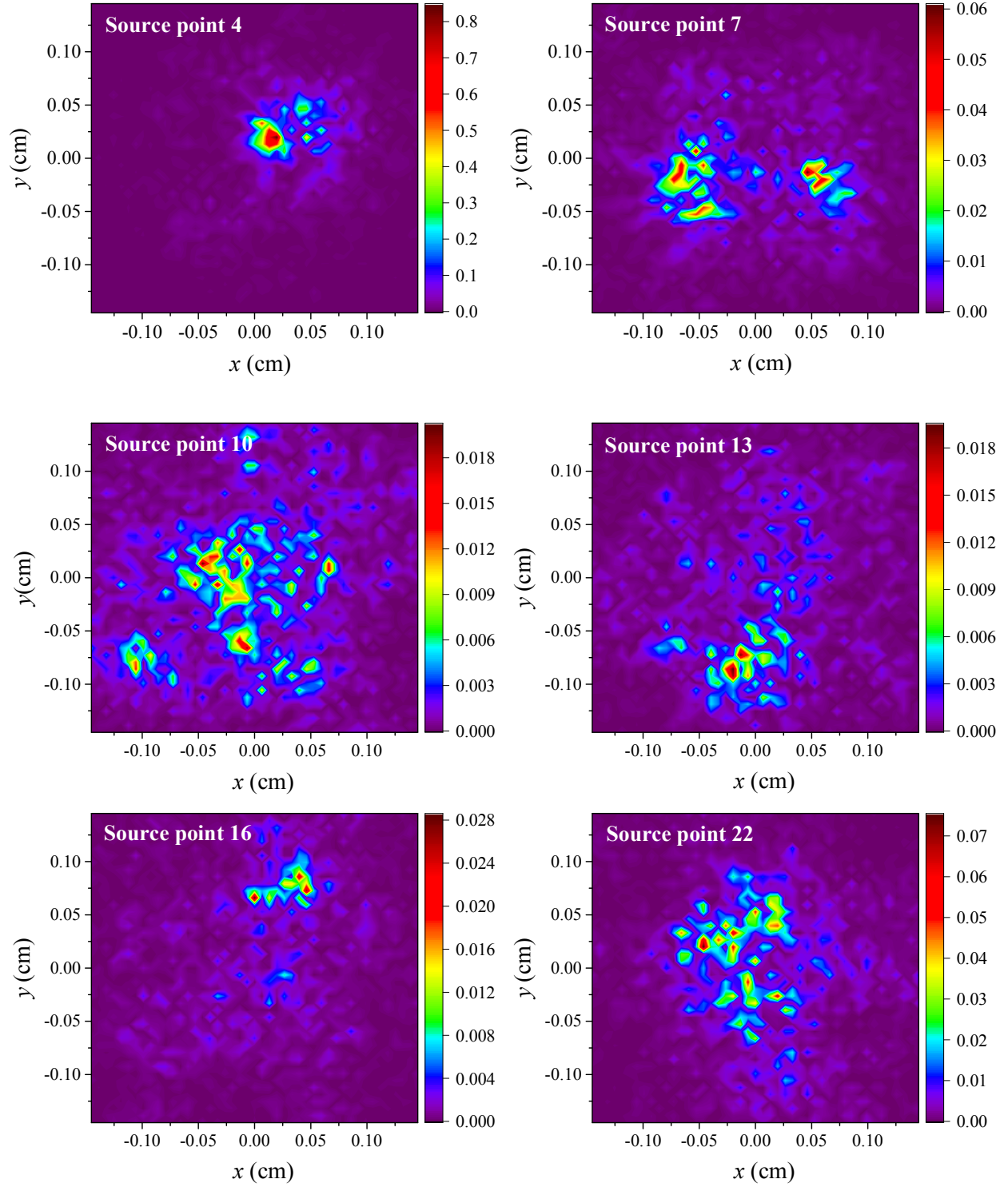


Figure 8.8: Speckle maps of transmitted intensity through sample L0 at 1 MHz. Maps for six (of 26) different source points are shown.

To quantify fluctuations in intensity, the variance σ^2 of the speckle maps was calculated

in the same two ways that are detailed in Section 7.3; (1) variance is calculated for each intensity map, and the results averaged over all maps (denoted in this thesis as $\langle \sigma^2 \rangle$), or (2) variance is calculated over all maps at once (denoted σ^2). With method 1, variations from map to map due to the coupling between the source and the input surface of the sample do not contribute, whereas method 2 is sensitive to these variations. Figure 8.9 shows the results in both the time (a) and frequency (b) domain. In both plots $\sigma^2 > \langle \sigma^2 \rangle$.

As shown in Figure 8.9 (a), the variance shows a general decrease with time. This behaviour has not been observed before in aluminum-brazed slab mesoglasses (Page 2011). In the diffuse regime, one would expect σ^2 to be independent of time. In the localization regime, a small increase with time is expected in 3D, and a large increase has been observed in quasi-1D (Wang et al. 2010).

In a previous work, a similar difference $\sigma^2 > \langle \sigma^2 \rangle$ was observed between speckle maps from a point source and plane wave source (a speckle map from a plane-wave source does not exhibit C_0 correlations). These measurements were shown to be due to significant C_0 effects, which are enhanced near the Anderson transition (Hildebrand 2015). Thus it is possible that the results in this section could be interpreted as showing a large C_0 effect.

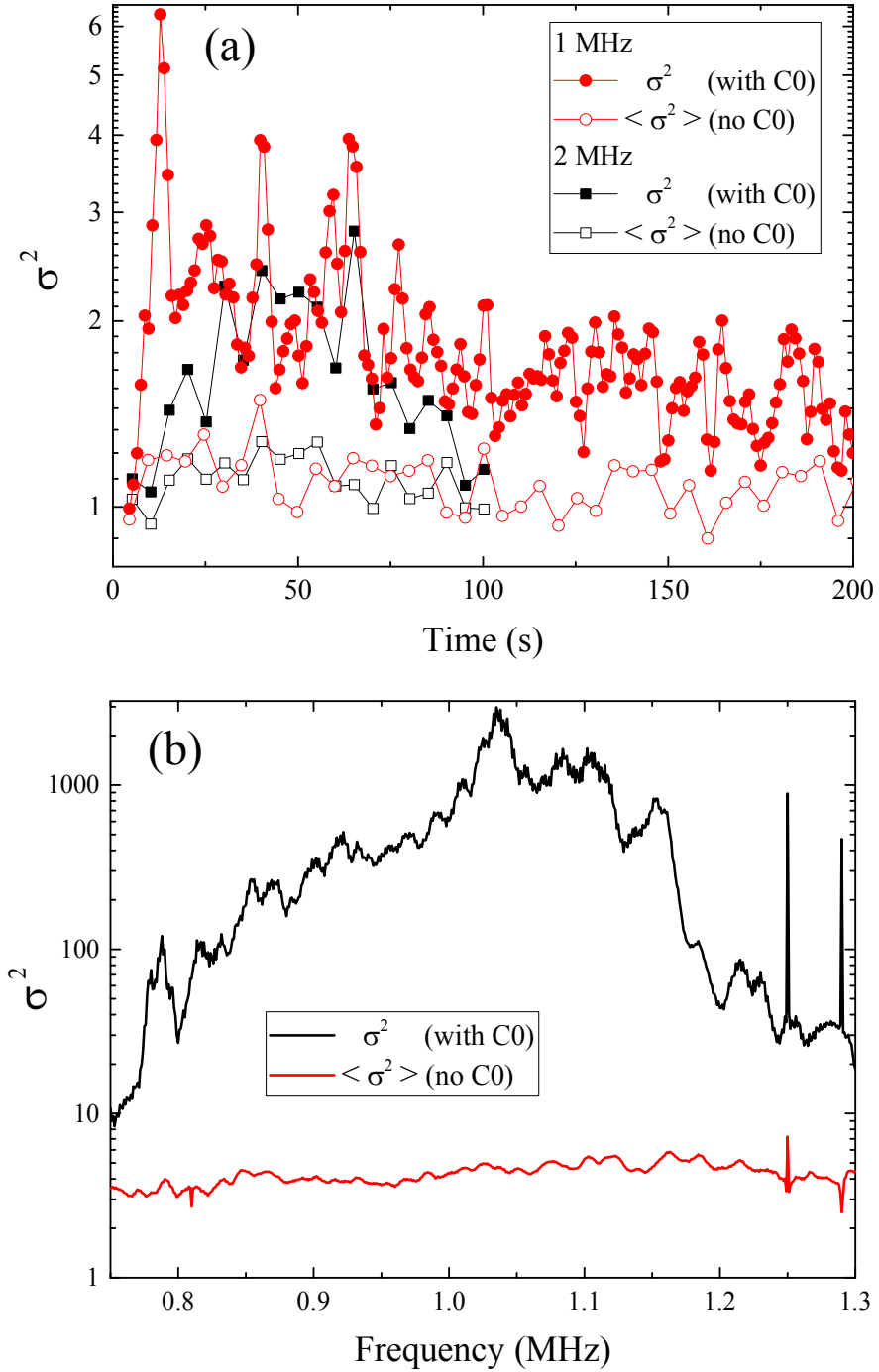


Figure 8.9: Variance of transmitted intensity speckle maps through sample L0. Shown are variance calculated over all speckle maps at once, σ^2 , and the variance calculated for each speckle map and averaged, $\langle \sigma^2 \rangle$. (a) Variance as a function of time for 1 MHz (red symbols) and 2 MHz (black symbols). Data have been filtered in frequency with a width of 250 kHz. (b) Variance as a function of frequency, for all times $0 < t < 200 \mu\text{s}$. The spikes in (b) are probably due to signals from two local radio stations (frequencies 1250 and 1290 kHz).

8.5. Conclusions and future directions

Several subtle deviations from conventional diffuse transport were experimentally measured from sample L0. The TOF profiles arrive more abruptly and decay more quickly than is generally observed for diffusion in similar 3D slab samples (Page et al. 1995; Hu 2006). The transmitted intensity shows anomalous behaviour near $t = 0$ and $\rho = 0$, which is an effect previously observed for superdiffuse light (Zumofen and Klafter 1993; Drysdale and Robinson 2006; Savo et al. 2014). Measurements of variance indicate that transmitted intensity is extremely sensitive to a change in source position, implying possibly C_0 effects. Finally, an extremely weak frequency dependence of the time-dependent transmitted intensity was observed, which is surprising as other aluminum-brazed samples show dramatic changes in wave scattering properties over this wide range of frequencies (c.f. Figure 3.25, or work by Hu et al. (2008) or Hildebrand (2015)). Perhaps considerably higher frequencies are required to obtain stronger scattering and/or Lévy-like behaviour in L0. Experiments at higher frequencies and on thicker samples (which can contain a much wider range of bead sizes, including larger ones) should be able to answer this question. In any case, samples of different thicknesses will probably be required to study superdiffusion and localization using transmission measurements.

Backscattering measurements on sample L0 would also be instructive; for a single sample, a measurement of the static CBS intensity profile can be used to calculate the fractal dimension of the system (Dogariu, Uozumi, and Asakura 1992; Burresi et al. 2012)³⁰. Dynamic CBS measurements have, to my knowledge, not been carried out for the superdiffuse regime in 3D, but would also be highly interesting.

³⁰ To do this would require that the experimental issues that arose for static CBS measurements on my other slab mesoglasses can be overcome; see Section 4.2.1.4.

9. Conclusions and future directions

In this thesis, a wide range of experimental measurements was used to observe several novel aspects of waves in random media. Since most of these interesting phenomena occur in the strong scattering regime, several samples were constructed specifically to exhibit strong scattering of ultrasound. The dimensions and structure of each sample were also designed with the experiments in mind. In particular, slab-shaped mesoglasses were constructed with much larger widths and thicknesses than those of previous samples, in order to be well-suited for backscattering measurements using ultrasonic arrays.

Diffuse, subdiffuse and localized wave behaviour in the slab mesoglasses was observed using the *dynamic CBS effect*. Results for the diffuse regime were presented first. To characterize the wave transport, the Boltzmann diffusion coefficient (D_B) was measured by fitting the dynamic CBS profiles with theory for diffuse acoustic waves in a 3D medium (van Tiggelen 2002). Results agreed with similar measurements made in transmission using more established methods. This work constitutes the first comparison of experimental dynamic CBS with the presented theory. It also illustrates the commonality between the dynamic transverse intensity profiles in reflection and in transmission. Since the CBS profile $I(\theta, t)$ is the Fourier transform of the reflected dynamic intensity profile, the width of $I(\theta, t)$ is related to the width of the intensity profile in transmission: $\Delta\theta^{-2}(t) \propto w_\rho^2(t)$. In the diffuse regime, both $w_\rho^2(t)$ and $\Delta\theta^{-2}(t)$ increase linearly with time, an effect which was established for $w_\rho^2(t)$ (Page et al. 1995) and $\Delta\theta^{-2}(t)$ (Tourin et al. 1997) separately, and observed in this thesis via reflection and transmission measurements on the same sample.

The analysis of the transmission measurements for diffuse waves at higher frequencies (1.65 MHz) shows some subtle ambiguities. They indicate slight subdiffuse behaviour, i.e. D_B appears to be renormalized (becomes smaller and smaller) at later times. The *self-consistent*

theory of localization (SC theory) describes this renormalization in terms of an increased *return probability*. This means that, due to sample disorder and strong scattering, waves have an increased probability of returning near to a spot which they have previously visited in the sample. For a ‘perfect storm’ of disorder, wavelength, and several other factors, this effect can become extreme; D_B can be successively renormalized until it approaches zero. This phenomenon is called *Anderson localization* (AL). In 3D, there is a transition between AL and the diffuse regime, occurring at the *mobility edge*. Localization is very difficult to observe experimentally, especially for 3D, as it is accompanied by large fluctuations and low transmission, and can also be confused with other effects including absorption. In this thesis, AL in 3D was studied experimentally via (absorption-independent) dynamic CBS measurements. This work constitutes the first observation of dynamic CBS in 3D in the localization regime. Results were supported by experiments in transmission, which are also fit with SC theory. Previous work has shown that, in the AL regime, $w_p^2(t)$ bends over and eventually saturates at long times (Hu et al. 2008; Cherroret, Skipetrov, and van Tiggelen 2010). Similar behaviour for $\Delta\theta^{-2}(t)$ was anticipated, and was reported here for the first time. Both CBS and the dynamic transverse intensity profile were fit with SC theory, enabling a measurement of the correlation/localization length ξ (the spatial extent of wave energy) over the entire *mobility gap* - the AL regime bounded by two mobility edges. This is the first complete experimental characterization of a mobility gap for classical waves in 3D.

Results for the average intensity in reflection could be improved by lessening the effect of fluctuations on experimental data. With a larger experimental range of angles and/or times, the dynamic CBS effect could be employed on its own to locate mobility edges and characterize the Anderson transition. In this thesis, a preliminary estimate is given for the *critical exponent* ν

which governs the transition between localized and diffuse behaviour, but it is unclear how much this analysis is biased by assumptions made by SC theory (Cobus, Skipetrov, et al. submitted). There are several promising approaches for measuring ν from the dynamic CBS data, including scaling methods similar to those presented by Ghosh et al. (Ghosh et al. 2015). In addition, since this is the first experimental reflection data for AL in 3D, there are several theoretical predictions which (with some further data manipulation) could now be experimentally investigated, including phase derivative (delay time) calculations (Schomerus, van Bommel, and Beenakker 2001; Chabanov, Stoytchev, and Genack 2000) and frequency correlations (Muskens, van der Beek, and Lagendijk 2011; Hildebrand et al. 2014).

Significant *recurrent scattering* was observed in the dynamic backscattering data near the localization regime. This contribution to backscattered intensity was found to complicate the analysis of the CBS effect. Thus, recurrent scattering was separated from these data using a matrix method originally developed for the weak scattering diffuse regime (Aubry and Derode 2009a; Aubry and Derode 2011; Aubry and Derode 2009b) and extended to the strong scattering regime (Aubry et al. 2014). However, since recurrent scattering is directly related to the return probability, it is interesting to study on its own. In this thesis, the first experimental study of the recurrent scattering contribution to backscattered intensity was presented (this work was first published by Aubry et al. in 2014). The dynamics of the return probability $R(t)$ were examined; in the diffuse and localized regimes, the behaviour of $R(t)$ agreed with theoretical predictions. At the mobility edge, a surprisingly slow decay of $R(t)$ was observed, which should stimulate further theoretical research in this area. This work implies that recurrent scattering is particularly sensitive to extraordinary scattering processes at criticality, and could potentially be used to discriminate between diffuse, critical and localized regimes without having to do complicated

theory fitting. Further experimental work (including lessening the effect of fluctuations) could investigate whether $R(t)$ could be used to measure the critical exponent.

In the strong scattering regime, and especially near localization, fluctuations of wavefunctions inside the scattering medium can be extremely large. In this thesis, experiments and post-processing techniques were designed carefully to extract meaningful measurements, but analyses were nevertheless made more complicated by remaining fluctuations. However, the calculation of some statistical quantities which measure fluctuations can take advantage of this effect to study localization. One such quantity, called *multifractality* (MF), has been previously used to investigate localization of ultrasound (Faez et al. 2009). A recent theoretical advance has shown that measurements of MF from systems of varying sizes could enable the determination of the critical exponent ν (Rodriguez et al. 2010; Rodriguez et al. 2011). In this thesis, the first steps towards performing this task experimentally were presented. Cubic samples of different sizes were created, and the transmitted intensity through many of them was measured using a laser interferometer. Careful noise discrimination was necessary to investigate critical behaviour, which is most likely to occur in a pseudo-band gap (a range of frequencies of low signal relative to the noise). The transmitted intensity on the surface of the cubes showed dramatic fluctuations and spatially-localized modes. Signatures of MF were calculated, which show sample-size dependent effects in frequency ranges on either side of a bandgap. This finite-size scaling suggests that critical regimes exist within these frequency ranges. Results so far highlight the need for a large amount of configurational averaging and a significant dependence on the position of the input signal, an effect which is prevalent near criticality. This project will, in future, involve data from many more cubic samples, resulting in more reliable averaged quantities that can be fit with theoretical predictions. This fitting procedure, which would result

in a measurement of both f_c and ν , is demonstrated on the data available so far, and is the long-term goal of this project.

This thesis ends with a step into future planned research; we propose to observe the interplay between subdiffusion, localization, and other diffusion-like processes. An example of one of these other anomalous processes is superdiffusion, in which transport may be faster than diffusion (rather than slower, like subdiffusion). Investigated in this thesis was a sample with a fractal structure, engineered to resemble those which have displayed a type of superdiffusion called a Lévy flight, for light waves (Bertolotti et al. 2010; Barthelemy, Bertolotti, and Wiersma 2008). As this is a new type of sample for ultrasound, exploratory experiments were carried out over a wide range of frequencies, and various analyses performed to provide clues as to the nature of wave transport in the sample. The results demonstrated the presence of effects that seem diffusive, as well as clear deviations from conventional diffusive behaviour. The next immediate steps of the project will be the creation of more samples of different thicknesses, with more sizes of beads for a better approximation of a fractal distribution, and possibly experiments at different frequencies. Measurements of the thickness-dependence of transmission through the samples will be instructive. On a longer time-scale, further engineering of samples will be carried out to encourage strong scattering, with the goal of inducing both localization and superdiffusion in the sample.

Anomalous wave behaviour, and Anderson localization in particular, continues to be an area of great interest and potential. The work presented in this thesis contributes important advances to the field, including new experimental observations and the development and improvement of sophisticated experimental techniques and analysis. This research and the reported conclusions are not a closed case, but suggest even more new ways forward.

References

- Abrahams, E., P. W. Anderson, D. C. Licciardello, and T. V. Ramakrishnan. 1979. "Scaling Theory of Localization: Absence of Quantum Diffusion in Two Dimensions." *Physical Review Letters* 42 (10): 673–76.
- Akkermans, E., and R. Maynard. 1985. "Weak Localization of Waves." *Journal de Physique Lettres* 46: L1045–53.
- Akkermans, E., and G. Montambaux. 2007. *Mesoscopic Physics of Electrons and Photons*. Cambridge: Cambridge University Press.
- Akkermans, E., P. E. Wolf, R. Maynard, and G. Maret. 1988. "Theoretical Study of the Coherent Backscattering of Light by Disordered Media." *Journal de Physique France* 49: 77–98.
- Anderson, P. W. 1958. "Absence of Diffusion in Certain Random Lattices." *Physical Review* 109 (5): 1492–1505.
- Anderson, P. W. 1985. "The Question of Classical Localization: A Theory of White Paint?" *Philosophical Magazine Part B* 52 (3): 505–9.
- Aubry, A., L. A. Cobus, S. E. Skipetrov, B. A. van Tiggelen, A. Derode, and J. H. Page. 2014. "Recurrent Scattering and Memory Effect at the Anderson Localization Transition." *Physical Review Letters* 112 (4): 043903.
- Aubry, A., and A. Derode. 2007. "Ultrasonic Imaging of Highly Scattering Media from Local Measurements of the Diffusion Constant: Separation of Coherent and Incoherent Intensities." *Physical Review E* 75 (2): 026602.
- Aubry, A., and A. Derode. 2009a. "Detection and Imaging in a Random Medium: A Matrix Method to Overcome Multiple Scattering and Aberration." *Journal of Applied Physics* 106 (4): 044903.
- Aubry, A., and A. Derode. 2009b. "Random Matrix Theory Applied to Acoustic Backscattering and Imaging In Complex Media." *Physical Review Letters* 102 (8): 084301.
- Aubry, A., and A. Derode. 2010. "Singular Value Distribution of the Propagation Matrix in Random Scattering Media." *Waves in Random and Complex Media* 20 (3): 333–63.
- Aubry, A., and A. Derode. 2011. "Multiple Scattering of Ultrasound in Weakly Inhomogeneous Media: Application to Human Soft Tissues." *The Journal of the Acoustical Society of America* 129 (1): 225–33.
- Aubry, A., A. Derode, P. Roux, and A. Tourin. 2007. "Coherent Backscattering and Far-Field Beamforming in Acoustics." *The Journal of the Acoustical Society of America* 121 (1): 70–77.

- Baldantoni, A., B. J. Janeway, D. C. Lauzon, M. J. Purdon, and Roland S. Timsit. 1994. ““NOCOLOKTM Sil Flux – A Novel Approach for Brazing Aluminum.”” In *SAE Technical Paper 940502*.
- Barthelemy, P., J. Bertolotti, and D. S. Wiersma. 2008. “A Lévy Flight for Light.” *Nature* 453 (7194): 495–98.
- Bayer, G., and T. Niederdränk. 1993. “Weak Localization of Acoustic Waves in Strongly Scattering Media.” *Physical Review Letters* 70 (25): 3884–87.
- Beck, J. 1999. *Internal Report*. Ultrasonics Laboratory, University of Manitoba.
- Bershadskii, A. 2003. “Multiscaling Anderson Localization of Cosmic Electromagnetic Fields.” *Physics Letters B* 559 (3-4): 107–12.
- Bertolotti, J., K. Vynck, L. Pattelli, P. Barthelemy, S. Lepri, and D. S. Wiersma. 2010. “Engineering Disorder in Superdiffusive Lévy Glasses.” *Advanced Functional Materials* 20 (6): 965–68.
- Bobowski, J. 2001. *Summer Student Report for 2000 & 2001*. Ultrasonics Laboratory, University of Manitoba.
- Buresi, M., V. Radhalakshmi, R. Savo, J. Bertolotti, K. Vynck, and D. S. Wiersma. 2012. “Weak Localization of Light in Superdiffusive Random Systems.” *Physical Review Letters* 108 (11): 110604.
- Carlslaw, H. S., and J. C. Jaeger. 1995. *Conduction of Heat in Solids*. 2nd ed. London: Oxford University Press.
- Carminati, R., J. J. Sáenz, J.-J. Greffet, and M. Nieto-Vesperinas. 2000. “Reciprocity, Unitarity, and Time-Reversal Symmetry of the S Matrix of Fields Containing Evanescent Components.” *Physical Review A* 62 (1): 012712.
- Chabanov, A. A., M. Stoytchev, and A. Z. Genack. 2000. “Statistical Signatures of Photon Localization.” *Nature* 404 (6780): 850–53.
- Cherroret, N., S. E. Skipetrov, and B. A. van Tiggelen. 2010. “Transverse Confinement of Waves in Three-Dimensional Random Media.” *Physical Review E* 82 (5): 056603.
- Cobus, L. A., S. E. Skipetrov, A. Aubry, B. A. van Tiggelen, A. Derode, and J. H. Page. “Anderson Mobility Gap Probed by Dynamic Coherent Backscattering.” *Manuscript Submitted*.
- Cuevas, E., and V. E. Kravtsov. 2007. “Two-Eigenfunction Correlation in a Multifractal Metal and Insulator.” *Physical Review B* 76 (23): 235119.

- de Wolf, D. A. 1971. “Electromagnetic Reflection from an Extended Turbulent Medium: Cumulative Forward-Scatter Single-Backscatter Approximation.” *IEEE Transactions on Antennas and Propagation* 19 (2): 254–62.
- Dogariu, A., J. Uozumi, and T. Asakura. 1992. “Enhancement of the Backscattered Intensity from Fractal Aggregates.” *Waves in Random Media* 2 (4): 259–63.
- Douglass, K. M., S. John, T. Suezaki, G. A. Ozin, and A. Dogariu. 2011. “Anomalous Flow of Light near a Photonic Crystal Pseudo-Gap.” *Optics Express* 19 (25): 25320–27.
- Drysdale, P. M., and P. A. Robinson. 2006. “Levy Random Walks in Finite Systems.” *Physical Review E* 58 (5): 5382–94.
- Edwards, J. T., and D. J. Thouless. 1972. “Numerical Studies of Localization in Disordered Systems.” *Journal of Physics C: Solid State Physics* 5 (8): 807–20.
- Evers, F., and A. D. Mirlin. 2008. “Anderson Transitions.” *Reviews of Modern Physics* 80 (4): 1355–1417.
- Faez, S., A. Strybulevych, J. H. Page, A. Lagendijk, and B. A. van Tiggelen. 2009. “Observation of Multifractality in Anderson Localization of Ultrasound.” *Physical Review Letters* 103 (15): 155703.
- Feng, S., C. Kane, P. A. Lee, and A. D. Stone. 1988. “Correlations and Fluctuations of Coherent Wave Transmission through Disordered Media.” *Physical Review Letters* 61 (7): 834–37.
- Fink, M., D. Cassereau, A. Derode, C. Prada, P. Roux, and M. Tanter. 2000. “Time-Reversed Acoustics” 1933.
- Freund, I., M. Rosenbluh, and S. Feng. 1988. “Memory Effects in Propagation of Optical Waves through Disordered Media.” *Physical Review Letters* 61 (20): 2328–31.
- Friedrich, C., and U. Wegler. 2005. “Localization of Seismic Coda at Merapi Volcano (Indonesia).” *Geophysical Research Letters* 32 (14): L14312.
- Friesen, C. 2011. *Internal Report: Laser Interferometer Documentation*. Ultrasonics Laboratory, University of Manitoba.
- Genack, A. Z. 2011. “Statistics of Modes and Transmission Channels in the Photon Localization Transition.” In *Recent Developments in Wave Physics of Complex Media*. Cargèse.
- Gérardin, B., J. Laurent, A. Derode, C. Prada, and A. Aubry. 2014. “Full Transmission and Reflection of Waves Propagating through a Maze of Disorder.” *Physical Review Letters* 113 (17): 173901.
- Ghosh, S., D. Delande, C. Miniatura, and N. Cherroret. 2015. “Coherent Backscattering Reveals

- the Anderson Transition.” *Physical Review Letters* 115 (20): 200602.
- Götze, W. 1979. “A Theory for the Conductivity of a Fermion Gas Moving in a Strong Three-Dimensional Random Potential.” *Journal of Physics C: Solid State Physics* 12 (1958): 1279–96.
- Gradshteyn, I. S., and I. M. Ryzhik. 2000. *Table of Integrals, Series, and Products*. Edited by Alan Jeffrey and Daniel Zwillinger. 6th ed. Academic Press.
- Hasselfield, M. 2003. *Internal Report: CBS Analysis*. Ultrasonics Laboratory, University of Manitoba.
- Hildebrand, W. K. 2015. “Ultrasonic Waves in Strongly Scattering Disordered Media: Understanding Complex Systems through Statistics and Correlations of Multiply Scattered Acoustic and Elastic Waves.” PhD Thesis, University of Manitoba.
- Hildebrand, W. K., A. Strybulevych, S. E. Skipetrov, B. A. van Tiggelen, and J. H. Page. 2014. “Observation of Infinite-Range Intensity Correlations Above, At, and below the Mobility Edges of the 3D Anderson Localization Transition.” *Physical Review Letters* 112 (7): 073902.
- Hu, H. 2006. “Localization of Ultrasonic Waves in an Open Three- Dimensional System.” MSc. Thesis, University of Manitoba.
- Hu, H., A. Strybulevych, J. H. Page, S. E. Skipetrov, and B. A. van Tiggelen. 2008. “Localization of Ultrasound in a Three-Dimensional Elastic Network.” *Nature Physics* 4 (12): 945–48.
- Ioffe, A. F., and A. R. Regel. 1960. “Non-Crystalline, Amorphous and Liquid Electronic Semiconductors.” *Progress in Semiconductors* 4: 237.
- Ishimaru, A. 1977. “Theory and Application of Wave Propagation and Scattering in Random Media.” *Proceedings of the IEEE* 65 (7): 1030–61.
- Jendrzejewski, F., A. Bernard, K. Müller, P. Cheinet, V. Josse, M. Piraud, L. Pezzé, L. Sanchez-Palencia, A. Aspect, and P. Bouyer. 2012. “Three-Dimensional Localization of Ultracold Atoms in an Optical Disordered Potential.” *Nature Physics* 8 (5): 398–403.
- John, S. 1984. “Electromagnetic Absorption in a Disordered Medium near a Photon Mobility Edge.” *Physical Review Letters* 53 (22): 2169–72.
- John, S., H. Sompolinsky, and M. J. Stephen. 1983. “Localization in a Disordered Elastic Medium near Two Dimensions.” *Physical Review B* 27 (9): 5592–5603.
- Johnson, P. M., A. Imhof, B. Bret, J. G. Rivas, and A. Lagendijk. 2003. “Time-Resolved Pulse Propagation in a Strongly Scattering Material.” *Physical Review E* 68 (1): 016604.

- Jonckheere, T., C. A. Müller, R. Kaiser, C. Miniatura, and D. Delande. 2000. "Multiple Scattering of Light by Atoms in the Weak Localization Regime." *Physical Review Letters* 85 (20): 4269–72.
- Kim, M., Y. Choi, C. Yoon, W. Choi, J. Kim, Q.-H. Park, and W. Choi. 2012. "Maximal Energy Transport through Disordered Media with the Implementation of Transmission Eigenchannels." *Nature Photonics* 6 (9): 583–87.
- Knothe, A., and T. Wellens. 2015. "Frequency Correlations in Reflection from Random Media." *Journal of the Optical Society of America A* 32 (2): 305–13.
- Krachmalnicoff, V., E. Castanié, Y. De Wilde, and R. Carminati. 2010. "Fluctuations of the Local Density of States Probe Localized Surface Plasmons on Disordered Metal Films." *Physical Review Letters* 105 (18): 183901.
- Kramer, B., A. MacKinnon, T. Ohtsuki, and K. Slevin. 2010. "Finite Size Scaling Analysis of the Anderson Transition." In *50 Years of Anderson Localization*, edited by E. Abrahams, 347–60. Tuck Link, Singapore: World Scientific.
- Kuga, Y., and A. Ishimaru. 1984. "Retroreflectance from a Dense Distribution of Spherical Particles." *Journal of the Optical Society of America A* 1 (8): 831–35.
- Lagendijk, A., and B. A. van Tiggelen. 1996. "Resonant Multiple Scattering of Light." *Physics Reports* 270 (3): 143–215. doi:10.1016/0370-1573(95)00065-8.
- Langer, J. S., and T. Neal. 1966. "Breakdown of the Concentration Expansion for the Impurity Resistivity of Metals." *Physical Review Letters* 16 (22): 984–85.
- Lee, E. J. S. 2014. "Ultrasound Propagation through Complex Media with Strong Scattering Resonances." PhD Thesis, University of Manitoba.
- Lemarié, G., J. Chabé, P. Szriftgiser, J. C. Garreau, B. Grémaud, and D. Delande. 2009. "Observation of the Anderson Metal-Insulator Transition with Atomic Matter Waves: Theory and Experiment." *Physical Review A* 80 (4): 043626.
- Licciardello, D. C., and D. J. Thouless. 1975. "Constancy of Minimum Metallic Conductivity in Two Dimensions." *Physical Review Letters* 35 (21): 1475–78.
- Lingevitch, J. F. 2002. "Time Reversed Reverberation Focusing in a Waveguide." *The Journal of the Acoustical Society of America* 111 (6): 2609–14.
- Lopez, M., J.-F. Clément, P. Szriftgiser, J. C. Garreau, and D. Delande. 2012. "Experimental Test of Universality of the Anderson Transition." *Physical Review Letters* 108 (9): 095701.
- Mamou, V. 2005. "Caractérisation Ultrasonore D'échantillons Hétérogènes Multiplement Diffuseurs." PhD Thesis, Université Paris 7 - Denis Diderot.

- Mandelbrot, B. B. 1983. *The Fractal Geometry of Nature*. San Francisco: W. H. Freeman.
- Match, C. 2015. *Internal Report: Propagation of Ultrasonic Waves in Complex Media: Investigation of Honeycomb Lattice*. Ultrasonics Laboratory, University of Manitoba.
- Mirlin, A. D. 2000. “Statistics of Energy Levels and Eigenfunctions in Disordered Systems.” *Physics Reports* 326: 259–382.
- Mott, N. F. 1974. *Metal-Insulator Transitions*. London: Taylor & Francis.
- Muskens, O. L., T. van der Beek, and A. Lagendijk. 2011. “Angle Dependence of the Frequency Correlation in Random Photonic Media: Diffusive Regime and Its Breakdown near Localization.” *Physical Review B* 84 (3): 035106.
- Page, J. 2011. “Anderson Localization of Ultrasonic Waves in Three-Dimensional ‘mesoglasses.’” In *Recent Developments in Wave Physics of Complex Media*. Cargèse.
- Page, J. H. 2011. “Anderson Localization of Ultrasound in 3 Dimensions.” In *Proc. International School of Physics “Enrico Fermi”, Course CLXXXIII*, edited by R Kaiser, D.S Wiersma, and L Fallani, 95–114. IOS, Amsterdam; SIF, Bologna.
- Page, J. H., H. P. Schriemer, A. E. Bailey, and D. A. Weitz. 1995. “Experimental Test of the Diffusion Approximation for Multiply Scattered Sound.” *Physical Review E* 52 (3): 3106–14.
- Page, J. H., H. P. Schriemer, I. Jones, P. Sheng, and D. A. Weitz. 1997. “Group Velocity in Strongly Scattering Media.” *Science* 271: 634–37.
- Page, J. H., P. Sheng, H. P. Schriemer, I. Jones, J. Xiaodun, and D. A. Weitz. 1996. “Classical wave propagation in strongly scattering media.” *Physica A* 241:64-71.
- Pinski, S. D., and R. A. Roemer. 2011. “Study of the Localization-Delocalization Transition for Phonons via Transfer Matrix Method Techniques.” *Journal of Physics: Conference Series* 286 (1): 012025.
- Popoff, S. M., A. Aubry, G. Lerosey, M. Fink, A. C. Boccara, and S. Gigan. 2011. “Exploiting the Time-Reversal Operator for Adaptive Optics, Selective Focusing, and Scattering Pattern Analysis.” *Physical Review Letters* 107 (26): 263901.
- Popoff, S. M., G. Lerosey, R. Carminati, M. Fink, A. C. Boccara, and S. Gigan. 2010. “Measuring the Transmission Matrix in Optics: An Approach to the Study and Control of Light Propagation in Disordered Media.” *Physical Review Letters* 104 (10): 100601.
- Prada, C., and M. Fink. 1994. “Eigenmodes of the Time Reversal Operator : A Solution to Selective Focusing in Multiple-Target Media.” *Wave Motion* 20 (94): 151–63.

- Prada, C., S. Manneville, D. Spoliansky, and M. Fink. 1996. "Decomposition of the Time Reversal Operator: Detection and Selective Focusing on Two Scatterers." *The Journal of the Acoustical Society of America* 99 (4): 2067.
- Rodriguez, A., L. J. Vasquez, K. Slevin, and R. A. Römer. 2010. "Critical Parameters from a Generalized Multifractal Analysis at the Anderson Transition." *Physical Review Letters* 105 (4): 046403.
- Rodriguez, A., L. J. Vasquez, K. Slevin, and R. A. Römer. 2011. "Multifractal Finite-Size Scaling and Universality at the Anderson Transition." *Physical Review B* 84 (13): 134209.
- Sapienza, L., H. Thyrestrup, S. Stobbe, P. D. Garcia, S. Smolka, and P. Lodahl. 2010. "Cavity Quantum Electrodynamics with Anderson-Localized Modes." *Science* 327 (5971): 1352–55.
- Savo, R., M. Burrelli, T. Svensson, K. Vynck, and D. S. Wiersma. 2014. "Walk Dimension for Light in Complex Disordered Media." *Physical Review A* 90 (2): 023839.
- Schomerus, H., K. J. H. van Bommel, and C. W. J. Beenakker. 2001. "Coherent Backscattering Effect on Wave Dynamics in a Random Medium." *Physical Review E* 63 (2): 026605.
- Schriemer, H. P. 1997. "Ballistic and Diffusive Transport of Acoustic Waves in Random Media." PhD Thesis, University of Manitoba.
- Schriemer, H. P., M. L. Cowan, J. H. Page, P. Sheng, Z. Liu, and D. A. Weitz. 1997. "Energy Velocity of Diffusing Waves in Strongly Scattering Media." *Physical Review Letters* 79 (17): 3166–69.
- Schriemer, H. P., N. G. Pachet, and J. H. Page. 1996. "Ultrasonic Investigation of the Vibrational Modes of a Sintered Glass-Bead Percolation System." *Waves in Random Media* 6: 361–86.
- Schuermans, F., M. Megens, D. Vanmaekelbergh, and A. Lagendijk. 1999. "Light Scattering near the Localization Transition in Macroporous GaP Networks." *Physical Review Letters* 83 (11): 2183–86.
- Segev, M., Y. Silberberg, and D. N. Christodoulides. 2013. "Anderson Localization of Light." *Nature Photonics* 7 (3): 197–204.
- Sepehrinia, R., M. R. R. Tabar, and M. Sahimi. 2008. "Numerical Simulation of the Localization of Elastic Waves in Two- and Three-Dimensional Heterogeneous Media." *Physical Review B* 78 (2): 024207.
- Shahjahan, S., A. Aubry, F. Rupin, B. Chassignole, and A. Derode. 2014. "A Random Matrix Approach to Detect Defects in a Strongly Scattering Polycrystal: How the Memory Effect Can Help Overcome Multiple Scattering." *Applied Physics Letters* 104 (23): 234105.
- Sheng, P. 2006. *Introduction to Wave Scattering, Localization and Mesoscopic Phenomena*.

- Edited by R. Hull, R. M. Jr. Osgood, J. Parisi, and H. Warlimont. Second Edi. Vol. 468. Berlin: Springer.
- Shi, Z., M. Davy, and A. Z. Genack. 2015. “Statistics and Control of Waves in Disordered Media.” *Optics Express* 23 (9): 12293–320.
- Skipetrov, S. E., and B. A. van Tiggelen. 2006. “Dynamics of Anderson Localization in Open 3D Media.” *Physical Review Letters* 96 (4): 043902.
- Slevin, K., and T. Ohtsuki. 2014. “Critical Exponent for the Anderson Transition in the Three-Dimensional Orthogonal Universality Class.” *New Journal of Physics* 16 (1): 015012.
- Sperling, T., L. Schertel, M. Ackermann, G. J. Aubry, C. M. Aegerter, and G. Maret. 2016. “Can 3D Light Localization Be Reached in ‘White Paint’?” *New Journal of Physics* 18 (1): 013039.
- Thouless, D. J. 1974. “Electrons in Disordered Systems and the Theory of Localization.” *Physics Reports* 13 (3): 93–142.
- Tourin, A. 1999. “Diffusion Multiple et Renversement Du Temps Des Ondes Ultrasonores.” PhD Thesis, Université Paris VII.
- Tourin, A., A. Derode, P. Roux, B. A. van Tiggelen, and M. Fink. 1997. “Time-Dependent Coherent Backscattering of Acoustic Waves.” *Physical Review Letters* 79 (19): 3637–39.
- Turner, J. A., M. E. Chambers, and R. L. Weaver. 1998. “Ultrasonic Band Gaps in Aggregates of Sintered Aluminum Beads.” *Acustica* 84: 628–31.
- van Albada, M. P., and A. Lagendijk. 1985. “Observation of Weak Localization of Light in a Random Medium.” *Physical Review Letters* 55 (24): 2692–95.
- van Albada, M. P., M. B. van der Mark, and A. Lagendijk. 1987. “Observation of Weak Localization of Light in a Finite Slab: Anisotropy Effects and Light-Path Classification.” *Physical Review Letters* 58 (4): 361–64.
- van der Mark, M. B., M. P. van Albada, and A. Lagendijk. 1988. “Light Scattering in Strongly Scattering Media: Multiple Scattering and Weak Localization.” *Physical Review B* 37 (7).
- van Tiggelen, B. A. 1999. “Localization of Waves.” In *Diffuse Waves in Complex Media*, edited by J. P. Fouque, 1–60. Kluwer Academic Publisher.
- van Tiggelen, B. A. 2002. *Private Communication*. Unpublished.
- van Tiggelen, B. A., and E. Kogan. 1994. “Analogies between Light and Electrons: Density of States and Friedel’s Identity.” *Physical Review A* 49 (2): 708–13.

- van Tiggelen, B. A., A. Lagendijk, and D. S. Wiersma. 2000. "Reflection and Transmission of Waves near the Localization Threshold." *Physical Review Letters* 84 (19): 4333–36.
- van Tiggelen, B. A., A. Lagendijk, and D. S. Wiersma. 2001. "Radiative Transfer of Localized Waves." In *Photonic Crystals and Light Localization in the 21st Century*, edited by C.M. Soukoulis. Dordrecht: Kluwer.
- van Tiggelen, B. A., and R. Maynard. 1998. "Reciprocity and Coherent Backscattering of Light." In *Wave Propagation in Complex Media*, edited by G. Papanicolaou. New York: Springer-Verlag.
- van Tiggelen, B. A., D. A. Wiersma, and A. Lagendijk. 1995. "Self-Consistent Theory for the Enhancement Factor in Coherent Backscattering." *Europhysics Letters (EPL)* 30 (1): 1–6.
- Vollhardt, D., and P. Wölfle. 1980a. "Diagrammatic, Self-Consistent Treatment of the Anderson Localization Problem in $d \leq 2$ Dimensions." *Physical Review B* 22 (10): 4666–79.
- Vollhardt, D., and P. Wölfle. 1980b. "Anderson Localization in $D \leq 2$ Dimensions: A Self-Consistent Diagrammatic Theory." *Physical Review Letters* 22 (10): 4666–79.
- Vollhardt, D., and P. Wölfle. 1992. "Self-Consistent Theory of Anderson Localization." In *Electronic Phase Transitions*, edited by W. Hanke and Y. V. Kopayev, 1st ed., 32:1–78. Tuck Link, Singapore: Elsevier Science Publishers.
- Vreeker, R., M. P. van Albada, R. Sprik, and A. Lagendijk. 1988. "Femtosecond Time-Resolved Measurements of Weak Localization of Light." *Physics Letters A* 132 (1): 51–54.
- Wang, J., A. A. Chabanov, D. Y. Lu, Z. Q. Zhang, and A. Z. Genack. 2010. "Dynamics of Mesoscopic Fluctuations of Localized Waves." *Physical Review B* 81 (24): 241101.
- Weaver, R. L. 1993. "Anomalous Diffusivity and Localization of Classical Waves in Disordered Media: The Effect of Dissipation." *Physical Review B* 47 (2): 1077–80.
- Weaver, R. L., and O. I. Lobkis. 2000. "Enhanced Backscattering and Modal Echo of Reverberant Elastic Waves." *Physical Review Letters* 84 (21): 4942–45.
- Wegner, F. 1979. "The Mobility Edge Problem: Continuous Symmetry and a Conjecture." *Zeitschrift Für Physik B* 35 (3): 207–10.
- Wellens, T. 2009. "Nonlinear Coherent Backscattering." *Applied Physics B* 95 (2): 189–93.
- Wiersma, D. S. 1995. "Light in Strongly Scattering and Amplifying Random Media." *PhD Thesis*. University of Amsterdam.
- Wiersma, D. S., P. Bartolini, A. Lagendijk, and R. Righini. 1997. "Localization of Light in a Disordered Medium." *Nature* 390 (12): 671–73.

- Wiersma, D., M. P. van Albada, B. A. van Tiggelen, and A. Lagendijk. 1995. "Experimental Evidence for Recurrent Multiple Scattering Events of Light in Disordered Media." *Physical Review Letters* 74 (21).
- Wolf, P. E., and G. Maret. 1985. "Weak Localization and Coherent Backscattering of Photons in Disordered Media." *Physical Review Letters* 55 (24): 2696–99.
- Wolf, P. E., G. Maret, E. Akkermans, and R. Maynard. 1988. "Optical Coherent Backscattering by Random Media: An Experimental Study." *Journal de Physique France* 49: 63–75.
- Wölfle, P., and D. Vollhardt. 2010. "Self-Consistent Theory of Anderson Localization." In *50 Years of Anderson Localization*, edited by Elihu Abrahams, 1st ed., 43–72. Tuck Link, Singapore: World Scientific.
- Zumofen, G., and J. Klafter. 1993. "Scale-Invariant Motion in Intermittent Chaotic Systems." *Physical Review E* 47 (2): 851–63.